UNIVERSIDAD DE GRANADA

**Tesis doctoral**
Julio 2010

# The properties of virialized dark matter halos: signals from the large scale structures

`[ PhD THESIS ]`

**Antonio José Cuesta Vázquez**
*Instituto de Astrofísica de Andalucía (CSIC)*

***Memoria de Tesis***
*presentada en la Universidad de Granada*
*para optar al grado de Doctor en Astrofísica*

Director de tesis:
**Dr. Francisco Prada Martínez**

*To my thesis adviser,*
*for making this possible.*
*Thank you Paco.*

”The eternal mystery of the world is its comprehensibility”
—Albert Einstein

# Acknowledgements

This Thesis is a compilation of the research which took place over the past four years. It was enriched from fruitful collaborations all over the world, working together with research groups at University of California at Berkeley, University of California at Santa Cruz, Harvard University, Astrophysical Institute Potsdam, Instituto de Astrofísica de Canarias, and Universidad Autónoma de Madrid, to mention some of them.

First of all, I want to thank my Thesis adviser, Dr. Francisco Prada. His never ending ambition always pushed me to become competitive enough to work with the best people in the most prestigious universities. This Thesis would not have been possible without his perseverance and patience.

I am also in debt to my teachers at University of Granada Prof. Eduardo Battaner and Prof. Estrella Florido, as my scientific career in Astrophysics would have never started without them. Thank you for making me so curious about a science named Cosmology and for encouraging me to taste the fruit of research. I must confess that I hesitated a lot, but now I can say safely that you gave me the best advice.

Besides, I am very grateful to those of you who always supported me, despite the fact that this work is sometimes very hard and leaves me with very little spare time. Needless to say, it has been very difficult to me to find an equilibrium between work and life, but some people understood my situation anyways. Here I need to mention my brother, who helped me to put any kind of family problems aside; Lupi and Fer, for being always close to me even in the most difficult moments; Estrella and María for irradiating that kind of energy that is able to change lives; and finally

Juanma and his friends for sharing with me the historical achievements of the local soccer team and the dream of the World Cup made true while I was writing the last parts of my Thesis. Somehow, all of these people highly contributed to this Thesis by making me happier about the life I decided to live. I do not want to forget here the charming city of Granada, in which I lived my whole life. Now that I am moving far away across the sea, I need to bring with me all these good memories.

I also want to acknowledge the support of my former co-workers at Instituto de Astrofísica de Andalucía (CSIC) for the help they always provided. In particular, M.Ángeles Cortés and Rafa Parra are beautiful examples of excellence in the work they do. I want to thank the people in Dr. Prada's research group, in particular to Fabio Zandanel, Miguel A. Sánchez Conde and Mattia Fornasa for helping me to write this Thesis. I owe my office mate, Antonio García, the ability to question everything in my life (even to question finishing my Thesis on time).

Finally, I want to thank Prof. Nikhil Padmanabhan at Yale University, for offering me a Postdoctoral position in which I will continue working on the most interesting topics of Physical Cosmology. I am so proud of getting this position that still I hardly can believe it. Fortunately, I believe that in the next few years large galaxy surveys are going to reveal exciting hidden properties of the Universe we live in, and my work at the SDSS collaboration will contribute a little bit to these discoveries. As science is made by people, I am convinced that everybody has to thank a lot of people for their help to creating knowledge. So thank you everybody, for making the achievements of the future come true.

# Resumen

Los halos de materia oscura proporcionan el esqueleto cósmico del Universo observado. Entender su dinámica interna es clave para comprender cómo afecta a la formación y evolución de las galaxias. En esta memoria he analizado la distribución interna de la materia oscura en halos colapsados y he estudiado algunas magnitudes dinámicas de interés usando simulaciones cosmológicas de alta resolución. La distribución en el espacio de las fases de la materia de un halo de materia oscura muestra claros patrones cinemáticos que dependen de la masa del halo, confirmando previos análisis. Estos rasgos se usan aquí para cuantificar la cantidad de materia perteneciente al halo en casquetes esféricos que muestran una velocidad radial neta nula. En promedio, la masa de los halos de materia oscura caracterizada por sobredensidades esféricas 340 veces la densidad promedio del Universo, es cercana a esta definición cinemática de la masa, si bien existe algo de dispersión. No obstante, la masa de los halos con masa similar a la Vía Láctea está típicamente subestimada, hasta un 70% de la masa virial e incluso un factor 3 en el radio virial. Las estimaciones analíticas que usan las ecuaciones de Jeans bajo la aproximación de no evolución temporal, muestran que las velocidades circulares se reproducen bien por la teoría a cualquier distancia radial siempre que no haya flujo neto de materia hacia dentro o hacia fuera en ese casquete esférico. También presentamos una aproximación analítica para el perfil de densidad promedio en halos de materia oscura, en el modelo cosmológico $\Lambda$CDM, que es preciso dentro de un 10–15% incluso para grandes distancias radiales desde $0.05R_{vir}$ hasta $10R_{vir}$ para masas de halos comprendidas entre $10^{11.5}$ y $10^{15.0}$ $h^{-1}M_{\odot}$. Proponemos una forma modificada de la aproximación de Navarro, Frenk & White (NFW): $\rho(r) = \rho_{NFW}(r) + A(r/Rvir)^{-1} + B(1 + r/Rvir)^{-1} + \bar{\rho}$. Hemos usado esta nueva aproximación para estudiar el efecto lente gravitacional débil y también para obtener una expresión analítica para el *shear* tangencial. Esto nos ha perimitido cuantificar la contribución al *shear* de las regiones más externas del perfil de densidad

de los halos de materia oscura.

En la segunda parte de esta memoria, muestro la contribución que se espera en el cielo en rayos gamma debido a la auto-aniquilación de partículas de materia oscura en el escenario comúnmente utilizado de Física de Partículas, donde el neutralino (partícula supersimétrica) es un fuerte candidato para constituir la materia oscura no bariónica. La distribución de grandes estructuras más allá del radio virial del halo de la Vía Láctea se obtiene a partir de simulaciones restringidas del Universo Local, que toman ventaja del hecho de que las estructuras grandes están menos afectadas por evolución no-lineal y por tanto pueden ser mejor restringidas en las condiciones iniciales de la simulación cosmológica. A pesar del gran número de estudios centrados en la componente galáctica, Fermi podría detectar también emisión de rayos gamma provenientes de grandes estructuras extragalácticas, como filamentos y cúmulos cercanos (por ejemplo Virgo y Coma), en particular para modelos de materia oscura que se desintegra de forma que ajusten el exceso de positrones medido por PAMELA. Este resultado añade los cúmulos de galaxias y filamentos cercanos a la lista de fuentes a observar para los telescopios Čerenkov, como MAGIC, que persiguen la detección indirecta de la materia oscura, a pesar de tener un cociente masa-luminosidad menor comparado con las galaxias enanas. También he explorado la posibilidad de un origen local para los rayos cósmicos ultraenergéticos (UHECRs, por su acrónimo en inglés), motivada por evidencias observacionales sobre una composición mixta en el espectro de los rayos cósmicos en el extremo de altas energías. Usando el catálogo de Karachentsev et al. que incluye galaxias cercanas con distancias menores que 10Mpc (es decir, pertenecientes al Volumen Local), medimos la correlación entre la muestra de sucesos de UHECRs hechos públicos hasta ahora por la colaboración Pierre Auger. Las galaxias cercanas con $D <$ 10Mpc muestran una correlación similar con los UHECRs comparada con típicos aceleradores de partículas como son los AGNs. Al igual que se muestra en esta memoria de tesis, un gran número de recientes avances teóricos y experimentales ofrecen grandes expectativas para la detección y determinación de la partícula que constituye la materia oscura. Esta tesis se ha escrito bajo la supervisión del Dr. Francisco Prada Martínez, Instituto de Astrofísica de Andalucía - CSIC.

# Summary

Dark matter halos provide the cosmic scaffolding for the observed Universe. Understanding their internal dynamics is key to understand how they affect to galaxy formation and evolution. In this dissertation I analyse the internal distribution of dark matter in collapsed halos and study some dynamical quantities of interest using high-resolution $N$-body cosmological simulations. The distribution in phase space of the matter inside the dark matter halo shows clear patterns that depend on the halo mass, confirming previous analyses. These features are used here to quantify the amount of matter in spherical shells showing no net radial velocity belonging to the halo. On average, the mass of dark matter halos characterised as spherical overdensities of 340 times the average density of the Universe is close to this kinematical definition of mass, albeit with some scatter. However, dark matter halos around the mass of the Milky Way halo are typically underestimated by up to 70% in virial mass and even a factor of 3 in virial radius. Analytical estimations using the Jeans equations under the approximation of no time evolution show that circular velocities are well reproduced by the theory at any radial distance provided there is no net infall or outflow in that spherical shell. We also present an approximation for the average density profile of dark matter halos, in the $\Lambda$CDM cosmological model, which is accurate to within 10–15% even for large radial distances from $0.05R_{vir}$ up to $10R_{vir}$ for halo masses ranging from $10^{11.5}$ to $10^{15.0}$ $h^{-1}M_{\odot}$. We propose a modified form of the Navarro, Frenk & White (NFW) approximation: $\rho(r) = \rho_{NFW}(r) + A(r/Rvir)^{-1} + B(1 + r/Rvir)^{-1} + \bar{\rho}$. We use this new approximation to study the weak gravitational lensing and to obtain an analytic expression for the tangential shear. This allows us to quantify the contribution to the shear from the outer regions of the density profile.

In the second part of the dissertation, I show the expected contribution to the gamma-ray sky due to self-annihilation and decay of dark matter particles in the usual particle physics scenario, where the neutralino is a strong candidate to constitute the non-baryonic dark matter. The distribution of large structures beyond the virial radius of the Milky Way halo is obtained from Constrained Simulations of the Local Universe, which take advantage of the fact that large scales are less affected by non-linear evolution and hence can be better constrained in the initial conditions of the simulation. Contrary to what recent analyses have focused on, Fermi might also detect $\gamma$-ray emission from extragalactic large structures, such as nearby galaxy clusters and filaments (e.g. Virgo and Coma), in particular for decaying dark matter models fitting the positron excess as measured by PAMELA. This result adds nearby galaxy clusters and filaments to the list of targets for Čerenkov telescopes, such as MAGIC, aiming for indirect detection of dark matter, despite having a lower mass-to-light ratio as compared to dwarf galaxies. We also explore the possibility of a local origin for ultra high energy cosmic rays (UHECRs), motivated by the observational evidence for mixed composition in the high-energy end of the cosmic ray spectrum. Using the catalog of Karachentsev et al. including nearby galaxies with distances less than 10 Mpc (Local Volume), we measure the strength of the correlation with the sample of UHECR events released so far by the Pierre Auger collaboration. We note that nearby galaxies with $D < 10$ Mpc show a similar correlation with UHECRs as compared to well-known particle accelerators such as AGNs. As shown in this Thesis, many recent experimental and theoretical developments are offering high expectations for the detection and the determination of the dark matter particle. This thesis has been written under the supervision of Dr. Francisco Prada Martinez, Instituto de Astrofisica de Andalucia - CSIC.

# Contents

# List of Figures

# Chapter 1

# Introduction

## 1.1 The ΛCDM model

Most of the Physics community seems to agree in a standard cosmological picture of the Universe called the ΛCDM paradigm (from Λ Cold Dark Matter). This scenario, based on General Relativity, is now capable to explain in general terms the observations, as well as to reconcile them with a congruent theoretical picture of the Universe as a whole and of its evolution. In the ΛCDM paradigm, the geometry of the Universe is flat (i.e. euclidean) and its energy-density is distributed at present in ∼4% baryonic matter, ∼23% of still unknown non-baryonic dark matter and roughly 73% of a even more mysterious dark energy (see Table 1.1 for a complete list of the most recent determination of the model parameters). This paradigm is settled in the Big Bang scenario, in which the Universe had a beginning in time and is as a system evolving from a highly compressed state existing around $10^{10}$ years ago. The Big Bang theory has its roots in the important discoveries of E. Hubble in the 1920s, who realized that all galaxies seem to move away from us. The Big Bang theory, and more in general, the ΛCDM scenario, has survived to all kinds of tests and observations until now. Indeed, this huge theoretical and observational effort to refute the model has derived in a even stronger and extremely sophisticated cosmological scenario, that allows us to explain in a satisfactory way the thermal history, relic background radiation, abundance of elements, large scale structure (LSS) and many other properties of the Universe. Nevertheless, our knowledge is still partial, and there are indeed a lot of open questions that the model will have to face in the coming years.

The existence of Dark Matter seems to be settled down by many observational

Table 1.1 Cosmological parameters from 7-year WMAP data.

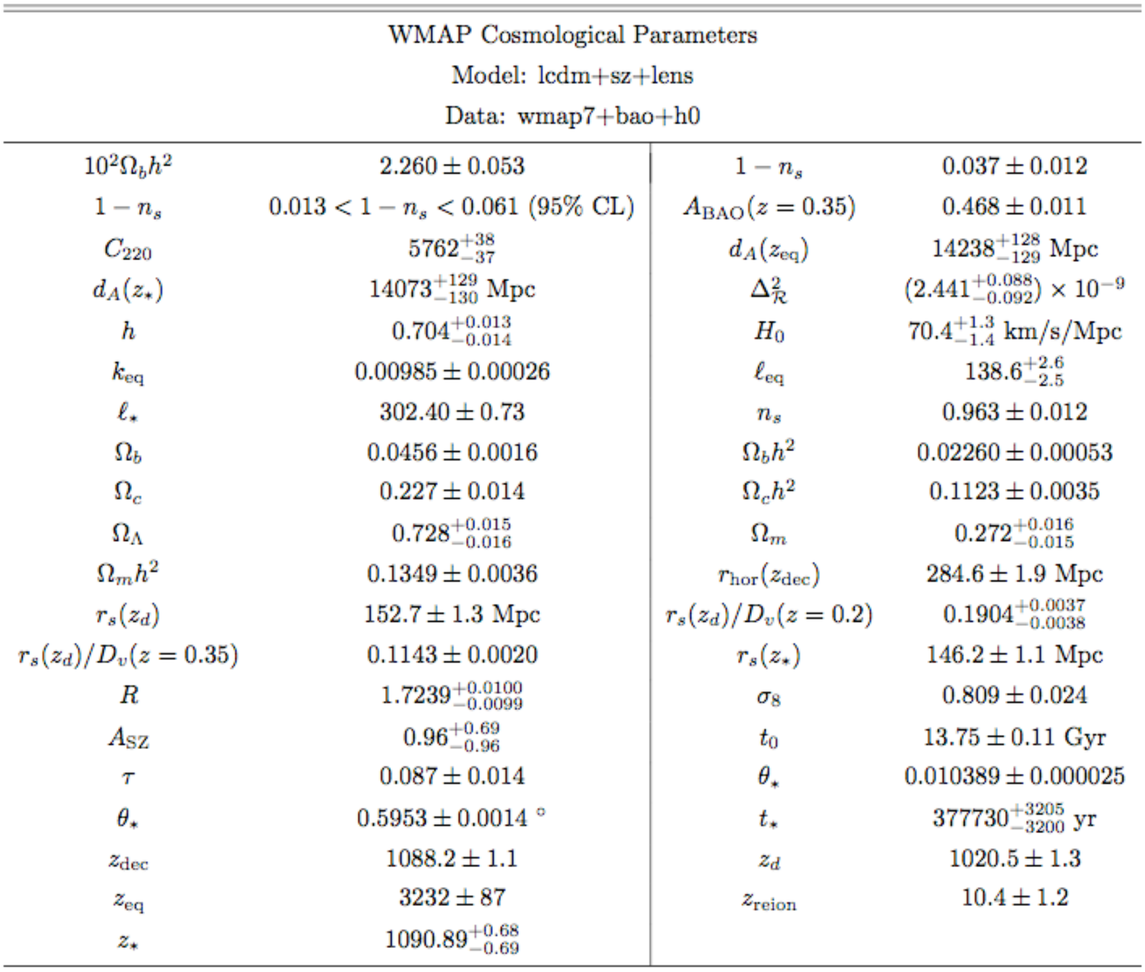

WMAP Cosmological Parameters
Model: lcdm+sz+lens
Data: wmap7+bao+h0

| | | | |
|---|---|---|---|
| $10^2\Omega_b h^2$ | $2.260 \pm 0.053$ | $1 - n_s$ | $0.037 \pm 0.012$ |
| $1 - n_s$ | $0.013 < 1 - n_s < 0.061$ (95% CL) | $A_{\mathrm{BAO}}(z = 0.35)$ | $0.468 \pm 0.011$ |
| $C_{220}$ | $5762^{+38}_{-37}$ | $d_A(z_{\mathrm{eq}})$ | $14238^{+128}_{-129}$ Mpc |
| $d_A(z_*)$ | $14073^{+129}_{-130}$ Mpc | $\Delta^2_{\mathcal{R}}$ | $(2.441^{+0.088}_{-0.092}) \times 10^{-9}$ |
| $h$ | $0.704^{+0.013}_{-0.014}$ | $H_0$ | $70.4^{+1.3}_{-1.4}$ km/s/Mpc |
| $k_{\mathrm{eq}}$ | $0.00985 \pm 0.00026$ | $\ell_{\mathrm{eq}}$ | $138.6^{+2.6}_{-2.5}$ |
| $\ell_*$ | $302.40 \pm 0.73$ | $n_s$ | $0.963 \pm 0.012$ |
| $\Omega_b$ | $0.0456 \pm 0.0016$ | $\Omega_b h^2$ | $0.02260 \pm 0.00053$ |
| $\Omega_c$ | $0.227 \pm 0.014$ | $\Omega_c h^2$ | $0.1123 \pm 0.0035$ |
| $\Omega_\Lambda$ | $0.728^{+0.015}_{-0.016}$ | $\Omega_m$ | $0.272^{+0.016}_{-0.015}$ |
| $\Omega_m h^2$ | $0.1349 \pm 0.0036$ | $r_{\mathrm{hor}}(z_{\mathrm{dec}})$ | $284.6 \pm 1.9$ Mpc |
| $r_s(z_d)$ | $152.7 \pm 1.3$ Mpc | $r_s(z_d)/D_v(z = 0.2)$ | $0.1904^{+0.0037}_{-0.0038}$ |
| $r_s(z_d)/D_v(z = 0.35)$ | $0.1143 \pm 0.0020$ | $r_s(z_*)$ | $146.2 \pm 1.1$ Mpc |
| $R$ | $1.7239^{+0.0100}_{-0.0099}$ | $\sigma_8$ | $0.809 \pm 0.024$ |
| $A_{\mathrm{SZ}}$ | $0.96^{+0.69}_{-0.96}$ | $t_0$ | $13.75 \pm 0.11$ Gyr |
| $\tau$ | $0.087 \pm 0.014$ | $\theta_*$ | $0.010389 \pm 0.000025$ |
| $\theta_*$ | $0.5953 \pm 0.0014\ ^\circ$ | $t_*$ | $377730^{+3205}_{-3200}$ yr |
| $z_{\mathrm{dec}}$ | $1088.2 \pm 1.1$ | $z_d$ | $1020.5 \pm 1.3$ |
| $z_{\mathrm{eq}}$ | $3232 \pm 87$ | $z_{\mathrm{reion}}$ | $10.4 \pm 1.2$ |
| $z_*$ | $1090.89^{+0.68}_{-0.69}$ | | |

evidences. The natural question now is which candidates are able to account for the huge fraction of the total content of the Universe predicted to be in the form of dark matter (DM). Up to now, a plethora of DM candidates have been proposed. For example, MACHOs, or Massive Compact Halo Objects, which are still baryonic DM in the form of faint stars or stellar remnants. However, we now know that they do not exist in sufficient quantity to completely resolve the DM challenge. It seems necessary to make use of physics beyond the Standard Model of Particle Physics, where good non-baryonic DM candidates arise that fulfill all the cosmological requirements. The most popular are probably the neutralinos and the axions, both of them proposed for other reasons in extensions of the Standard Model of particle physics. Ordinary massive neutrinos are too light to be cosmologically significant, though sterile neutrinos remain a possibility. Other candidates include primordial black holes, non-thermal WIMPzillas, and Kaluza-Klein particles. For a detailed picture, see e.g. Bergström (2000), Bertone et al. (2005) or Steffen (2009).

A good DM particle candidate should fulfill a series of important properties (Baltz 2004; Taoso et al. 2008) in order to provide a convincing explanation to all the observed phenomenology: 1. It should be weakly interacting to ordinary matter and electrically neutral, i.e. with neither electromagnetic nor strong interactions. 2. It should be long-lived enough for having been present since the early Universe, when the particles were created. 3. It has to be cold. 4. It must be massive enough to account for the measured $\Omega_m$. 5. It must be consistent with observations (BBN, relic density, stellar evolution, LSS...) and present constraints (direct and indirect detections; see Section 1.3). These particles are known as Weakly Interacting Massive Particles or, simply, WIMPs.

As also discussed in Baltz (2004), the mass range of the proposed non-baryonic DM candidates covers at least ∼90 orders of magnitude in mass (from e.g. "fuzzy" CDM to WIMPzillas); unfortunately astrophysical observations do not help in constraining this huge mass range. However, the energy scale ∼ 100 GeV is of special interest for the DM problem, as we will describe in next sections. In the following, I will briefly present some of the preferred DM candidates at present. Again, I refer to Bergström (2000), Bertone et al. (2005), Buckley et al. (2008), Steffen (2009) for detailed reviews on each of the candidates presented below as well as on other plausible scenarios.

- Neutrinos: In the past, neutrinos were considered excellent DM candidates for their "undisputed virtue of being known to exist" (Bergström 2000). However, neutrinos are simply not abundant enough to be the dominant DM component: from the analysis of CMB anisotropies, combined with LSS data, we know that $\Omega_\nu h^2 < 0.0065$ (95% confidence limit). Furthermore, they are hot (HDM), which is disfavored by current observations. Effectively, being relativistic collisionless particles, neutrinos erase fluctuations below a scale of ∼40 Mpc ($m_\nu$/30 eV) (Bond et al. 1980), which would imply a top-down hierarchical scenario for the formation of structures in the Universe, contrary to present trends.

- Sterile neutrinos: they have also been proposed as CDM; they are similar to standard neutrinos, but without Standard Model weak interactions apart from mixing and can be much heavier. Proposed as DM candidates by Dodelson & Widrow (1994), stringent cosmological and astrophysical constraints on sterile neutrinos come from the analysis of their cosmological abundance and the study of their decay products (Abazajian et al. 2001).

- Axions: the existence of axions requires physics beyond the Standard Model of particle physics, since they were introduced in an attempt to solve the problem of strong CP violation. Laboratory searches, stellar cooling and the dynamics of supernova 1987A constrain axions to be very light ($\lesssim 0.01$ eV). Since axions couple weakly to the rest of matter, they were not produced in thermal equilibrium in the early Universe; therefore, despite their light masses, they can behave as CDM. Their relic abundance matches the DM cosmological density for masses around 10 $\mu$eV (although this value is quite uncertain due to the uncertainties in the production mechanisms).

- Kaluza-Klein particles: if our four-dimensional space-time is embedded in a higher dimensional space, accessible only at very small length or very high energy scales, excitations of Standard Model states along the orthogonal dimensions (called Kaluza-Klein excitations) may be viable DM candidates as well and act therefore as WIMPs (e.g. Servant & Tait 2003). Masses around 1 TeV provide reasonable relic densities from thermal freeze-out.

- SUSY candidates: as discussed above, the Standard Model does not provide a viable DM candidate. Supersymmetry (SUSY) is capable to provide good DM candidates with all the needed characteristics enumerated above, and moreover they provide a solution to the hierarchy problem (why the expected mass of the Higgs particle is so low).

  The most preferred DM candidates that arises in the context of SUSY are:

  Neutralinos: probably considered the best WIMP candidate, and the preferred and most widely studied as well. In SUSY, if one postulates a conserved quantity arising from some new symmetry (R-parity), the lightest supersymmetric particle (LSP) is stable and would provide a natural candidate for DM. In fact, as pointed out e.g. in Buckley et al. (2008), R-parity conservation is introduced into SUSY not to solve the DM problem, but rather to ensure the stability of the proton. In many regions of supersymmetric parameter space, the LSP is the neutralino, a Majorana particle (its own antiparticle) that is the lightest supersymmetric partner to the electroweak and Higgs bosons.

Axinos: if the axions proposed to solve the strong CP problem exist and in addition SUSY is valid, the axion will naturally have as a partner the axino. Their mass ranges between the eV and the GeV scale, and they can be efficiently produced through thermal and non-thermal processes in the early Universe under the form of cold, warm or even hot DM (see e.g. Choi & Roszkowski 2005; Covi et al. 2004). In particular, axinos CDM is achieved for masses $\geq 100$ keV.

Gravitinos: they are the superpartner of the graviton. It was the first SUSY particle considered for the DM problem (Pagels & Primack 1982). In models where the gravitino is the LSP, it is often quite light (keV), and would thus be warm (WDM). In Cosmology, the overproduction of gravitinos can be problematic, though the difficulties can be circumvented (Kawasaki & Moroi 1995). Gravitinos at the weak scale, whose relic density would be obtained through the decays of the next lightest superpartner, are also an interesting possibility (Feng et al. 2003).

As a final remark, it is important to note here that the total amount of DM in the Universe could be constituted by several particle species of those given above. Indeed, we already know that standard neutrinos contribute to DM, but cannot account for all of it. A detailed discussion on the detection prospects of a subdominant density component of DM can be found for example in Duda et al. (2003).

## 1.2 Cosmological N-body Simulations

Structure formation in the Universe is a non-linear process. Hence, analytical methods are limited to obtain a deep understanding of the process itself and the final states of the development of a density perturbation ongoing gravitational collapse. Early attempts by Holmberg (1941) anticipated the extensive use of $N$-body simulations in the era of numerical analysis using computers. The first $N$-body codes were created (Aarseth 1963) and the development of numerical simulations remained bound to that of the computational power. Nowadays this is still true, with the ubiquitous presence of parallel coding, which extends the possibilities of present computers by just adding a large number of them, instead of focusing on the individual power of each processor. This way current $N$-body codes take advantage of this new way of using computers to make simulations more efficient in terms of running time.

The most widely adopted approach to the problem of LSS formation involves the use of $N$-body cosmological simulations (see Bagla 2005 for a review). In Cosmology, the evolution of structure is often approximated with non-linear gravitational clustering from specified initial conditions of DM particles and depending on the properties in which one is interested, sometimes it is refined by introducing the effects of gas dynamics, chemistry, radiative transfer and other astrophysical processes. Basically, these simulations consist of a cubic box also known as simulation box which represents a region in the Universe which does not suffer from boundary effects as periodic boundary conditions are implemented. The density field is represented by discrete tracers called particles. Of course, the more particles there are in a simulation, the highest the resolution in it. This usually puts the hardest constraint when designing a simulation for given computational resources. On the other hand, sometimes it is not necessary to resolve individual collapsed objects (known as dark matter halos) with many particles per halo but it is convenient to have good halo statistics. This way, the simulation volume is set, in such a way that the particles now have a higher mass so that the mean matter density in the box matches that of the Universe $\rho_m = \Omega_m \rho_c$.

Many simulations, as most of the ones we used in this research (which were run and provided by our collaborators Anatoly Klypin, Stefan Gottlöber, Gustavo Yepes and Yehuda Hoffman, some of these simulations are part of the CLUES project[1]), only contain the dark matter component which is the dominant matter component in the Universe, and therefore these simulations include only the gravitational force. Incorporating baryons in the simulations dramatically increases their complexity and hence they usually represent small volumes with an individual halo. A large effort is being carried out at present by several groups in order to successfully implement them in the simulations, since they are expected to be crucial in the understanding of astrophysical processes such as galaxy formation.

Another interesting group of cosmological simulations consist of those implementing observational constraints from the Local Universe, which are usually known as constrained realizations (an example is shown in Figure 1.2). The initial conditions of these simulations are created using the algorithm of Hoffman & Ribak (1991) to constrain ran-

---

[1] `http://www.clues-project.org/`

dom Gaussian fields. This algorithm is based on the formalism of the Wiener filter (Zaroubi et al. 1995, see applications in Kravtsov et al. 2002 and Klypin et al. 2003). In this method, the peculiar velocity field and the density field at present are assumed to be related using linear theory of gravitational instability. The reconstruction of present fields using this method will be more accurate if the filter is applied at the scales where the linear theory is approximately valid. The large scale fluctuations in these fields are then extrapolated back in time using again linear theory to obtain the initial conditions of the simulation. In the case of the simulation set of the CLUES project, the observational data is obtained from the MARKIII catalog (Willick et al. 1997) and the SBF catalog (Tonry et al. 2001). Peculiar velocities remain almost unaffected by non-linear effects and they can be used directly as constraints in the linear theory. For the highest resolution simulations they also include the galaxy catalog of the Local Volume from Karachentsev et al. (2004). The restrictions in the velocity field are complemented with constraints in the density field from the X-ray galaxy cluster catalog of Reiprich & Böhringer (2002). The output of these simulations at redshift $z = 0$ return a cosmological volume in which the largest scales are dominated by the imposed constraints, whereas the random component from the cosmological model will be more evident at smaller scales. This makes the actual output present some differences with what one could expect, in particular at the smallest scales. This issue can only be solved by running at low resolution a large number of simulations with a different seed which changes the random component, and re-simulating the most realistic ones.

$N$-body cosmological simulations based on the $\Lambda$CDM paradigm are in good agreement with a wide range of observations, such as the abundance of clusters at $z \leq 1$ and the galaxy-galaxy correlation functions (see e.g. Primack 2003 for a review of CDM). However, there are important discrepancies. For example, the number of satellite halos in Milky Way-sized galaxies, as predicted by simulations, exceeds the number of observed dwarf galaxies (Moore et al. 1999, Klypin et al. 1999). The rotation curves of low surface brightness (LSB) disk galaxies point to DM distributions with constant density cores rather than the cuspy profiles preferred by $N$-body simulations (see e.g. Flores & Primack 1994; McGaugh & de Blok 1998). As for the angular momentum of DM halos, in simulations gas cools at early time into small mass halos, leading to massive low-angular momentum cores in conflict with the observed exponential disks (Bullock et al. 2001). However, astrophysical processes such as major mergers and astrophysical feedback might help to solve these problems (Vitvitska et al. 2002). The low efficiency of gas cooling and star formation may decrease the number

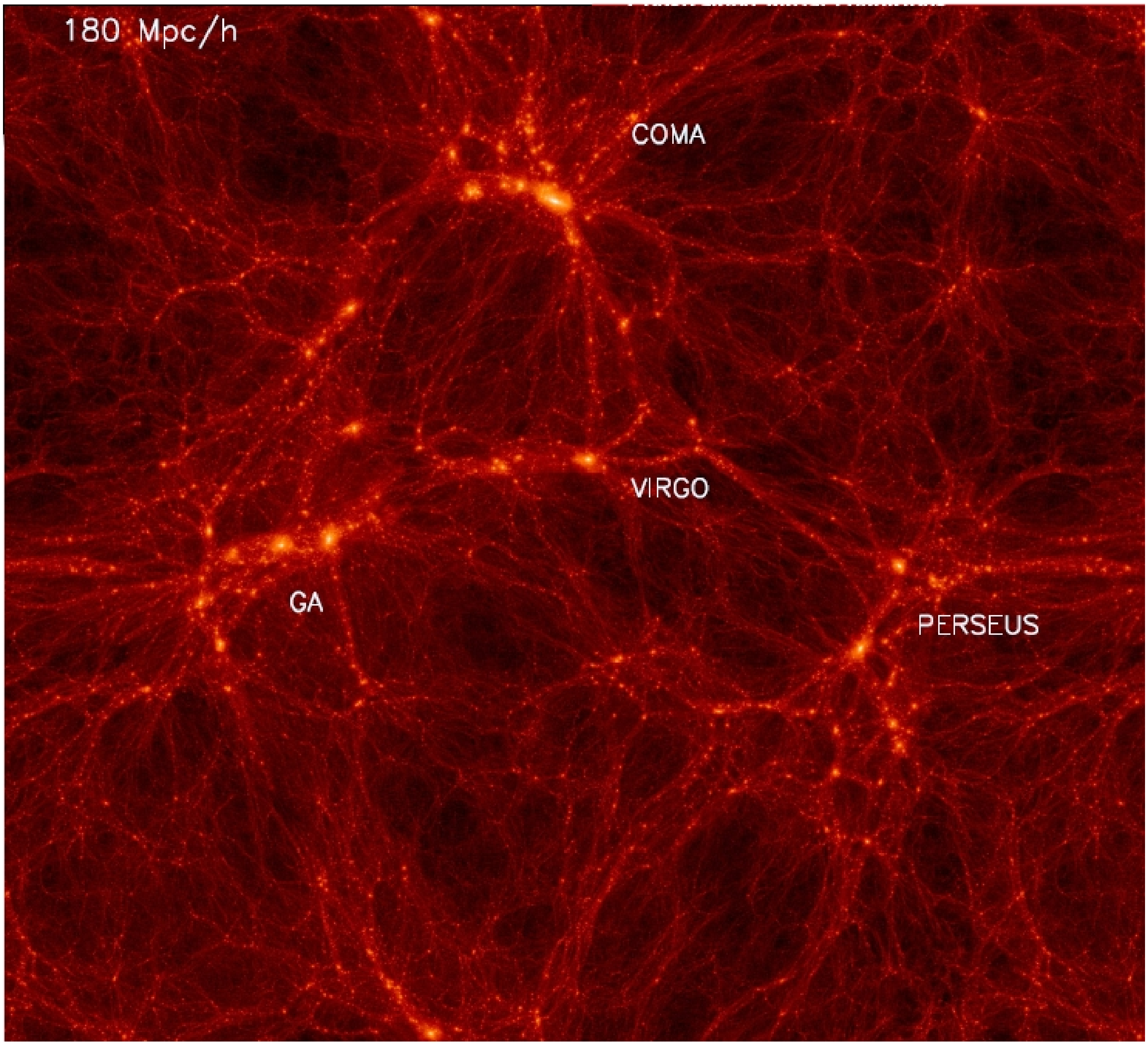

Figure 1.1 Constrained cosmological simulation BOX160CR. The resulting matter distribution from the simulation consists of a filamentary structure surrounded by large voids, which is known as the cosmic web. Large clusters are located at the intersection of these filaments. In this constrained simulation of $160h^{-1}$Mpc on a side, we can also identify known large overdense regions in the Local Universe, such as the Great Attractor, or Perseus-Pisces, Coma, and Virgo clusters. These are labeled in this plot which shows a slice of the dark matter distribution in the simulation centered in the Supergalactic plane.

of satellites in Milky Way-sized galaxies (e.g. Moore et al. 2006) as well as tidal stripping (e.g. Kravtsov et al. 2004). Furthermore, new ultra-faint dwarf galaxies recently detected with SDSS data seems to importantly alleviate the discrepancy between CDM predictions and observations (Simon & Geha 2007). The measurements of the LSB galaxies rotation curves may suffer of observational biases, for example due to the fact that DM halos are triaxial rather than spherically symmetric (Hayashi et al. 2007). Moreover, small deviations of the primordial power spectrum from scale invariance, the presence of neutrinos (Hofmann et al. 2001) or astrophysical processes (e.g. Weinberg & Katz 2002) can sensibly affect the halo profiles.

## 1.3 DM searches

There is a huge effort and an enormous array of experiments trying to detect DM at present. The detection techniques are typically divided in direct and indirect. Direct DM searches are based on the elastic scattering of DM particles on target nuclei, for which nuclei recoil are expected. On the other hand, indirect DM searches try to detect self-annihilation products of DM particles in high DM density environments.

An additional strategy for DM searches is the direct production of DM particles in laboratory experiments (typically at accelerators). In SUSY, as superparticles (sparticles) are expected to be very massive, they can only be tested at powerful particle accelerators, like the Large Hadron Collider (LHC). There is the hope that some of these sparticles can be definitely discovered by these experiment, providing also in this way evidence for grand unification and string theory. In the following I will briefly describe the direct and indirect detection techniques.

Direct DM searches try to detect DM particles by measuring nuclear recoils produced by DM scattering. This should be possible if our own Milky Way is filled with WIMPs as expected, since many of them should pass through the Earth and should weakly interact with ordinary matter. The key ingredients for the calculation of the signal in direct detection experiments are the density and the velocity distribution of WIMPs in the solar neighborhood as well as the WIMP-nucleon scattering cross section. From this information we can evaluate the rate of events expected in an experiment (i.e. WIMP-nucleon scattering events) per unit time and per unit detector material mass. As for present bounds and current experiments, most of them based on the detection of DM particles through their elastic scattering with nuclei, such as CDMS (The CDMS Collaboration: Ahmed et al. 2009), XENON (The XENON100 Collaboration: Aprile et al. 2010), ZEPLIN (Alner et al. 2007),

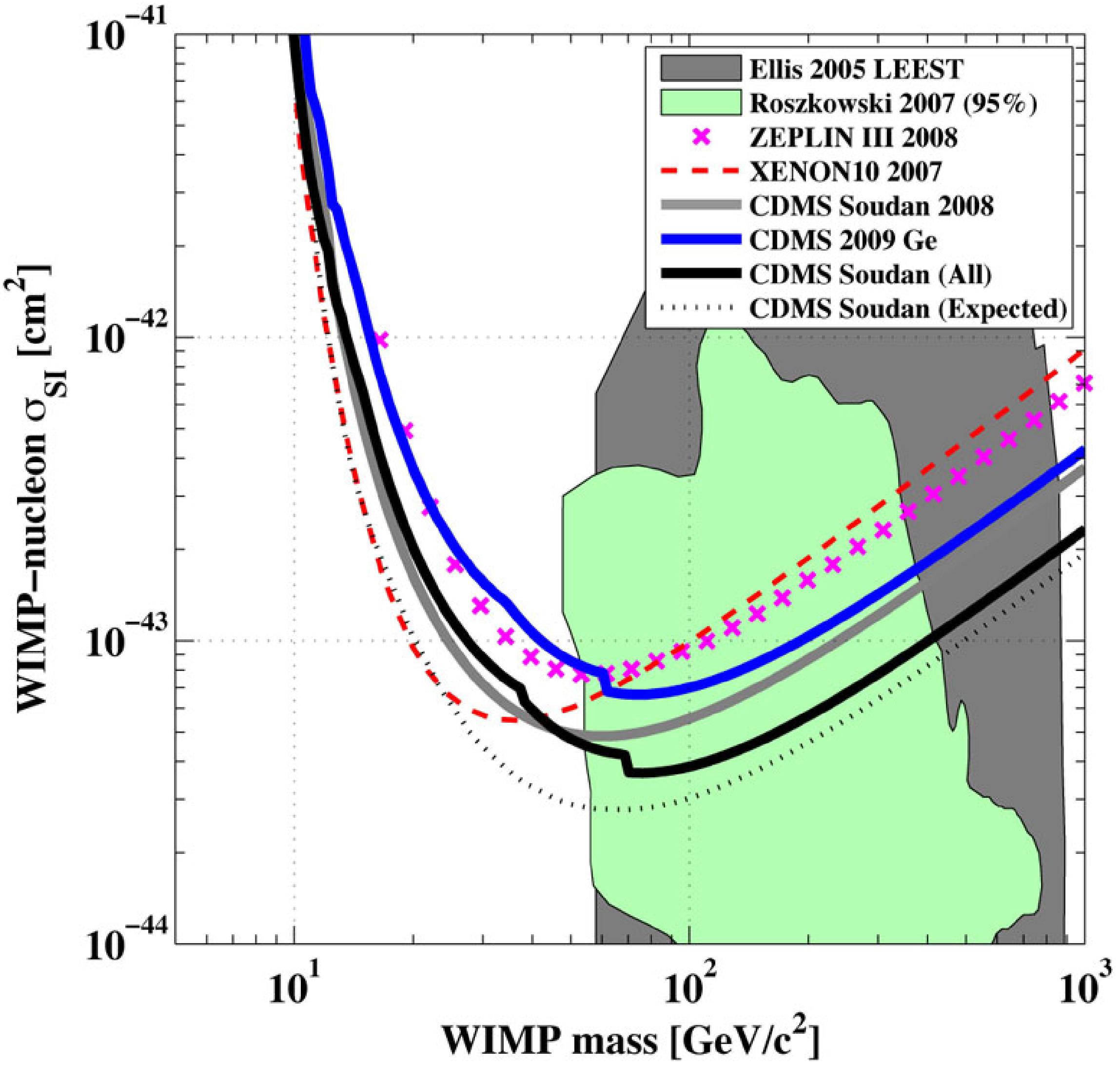

Figure 1.2 90% C.L. upper limits on the WIMP-nucleon spin-independent cross section as a function of WIMP mass. The solid black line shows the combined limit for the full data set recorded by the CDMS collaboration. Prior results from CDMS, EDELWEISS II, XENON10, and ZEPLIN III are shown for comparison. The shaded regions indicate allowed parameter space calculated from certain Minimal Supersymmetric Models. Taken from (The CDMS Collaboration: Ahmed et al. 2009).

EDELWEISS (Sanglard et al. 2005), CRESST (Angloher et al. 2005), CoGeNT (Aalseth et al. 2008), DAMA/LIBRA (Bernabei et al. 2008), COUPP (Behnke et al. 2008), WARP

(Warp Collaboration et al. 2008), and KIMS (Lee et al. 2007). Current constraints on the WIMP-nucleon spin-independent elastic scattering cross section, as a function of the WIMP mass are shown in Fig. 1.2. There are also other experiments that try to discriminate the expected DM signal against the natural background by means of an annual modulation of the measured event rate, based on the fact that the Earth rotation around the Sun should produce a modulation in the velocity of DM particles (Drukier et al. 1986). This is indeed the kind of search carried out by the DAMA Collaboration, although other experiments that could explore the same region of the parameter space than DAMA found null results (EDELWEISS Collaboration: Benoit et al. 2002; Akerib et al. 2003). This comparison, however, is model-dependent, so it should be taken carefully.

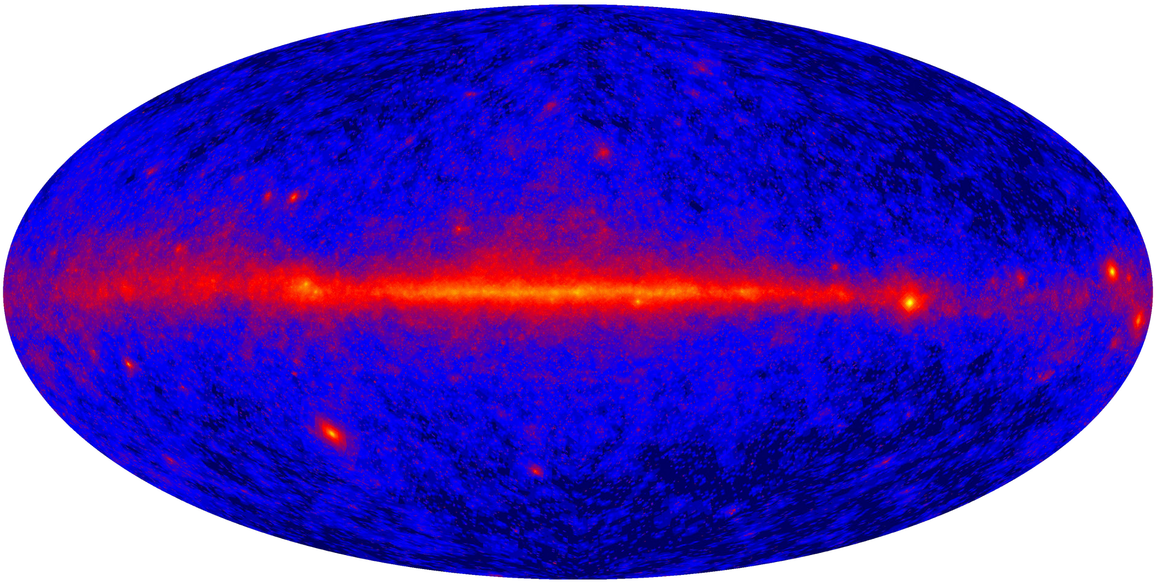

Figure 1.3 Gamma-ray all-sky map of 1-year data using Fermi satellite.

Indirect DM searches consist on detecting the radiation produced in DM annihilations, i.e. the products of WIMP annihilations, such us gamma-rays, neutrinos, positrons, electrons and antiprotons. The flux of this radiation is proportional to the annihilation rate, which in turn is proportional to the squared DM density; this means that the best places to look for DM in the Universe will be those with the highest DM concentrations. Distance is also very important, since high DM dominated systems that are located too far from us will yield too low DM annihilation fluxes at Earth. Having both considerations in mind, it is clear that the Galactic Center should be a very good candidate, but dwarf spheroidal galax-

Figure 1.4 MAGIC stereoscopic Čerenkov telescope at La Palma, Spain.

ies satellites of the Milky Way, and nearby galaxy clusters arise as very good candidates for DM searches as well. Current $\gamma$-ray experiments like IACTs (such as MAGIC, HESS and VERITAS, see Figure 1.4) together with Fermi satellite (see Figure 1.3) are reaching for the first time sensitivities good enough to be able to test some of the allowed and preferred scenarios (i.e. obeying WMAP constraints, using well-motivated DM density profiles and SUSY as the particle physics model). The situation is expected to be even better when new generation telescopes enter in operation in the near future (CTA, AGIS...). Moreover, the recent detection of an excess of high-energy (10–100 GeV) positrons over the standard expectation from galactic cosmic-ray models by the PAMELA experiment (Adriani et al. 2009), triggered an interest in the possibility that these positrons originate from DM in the Milky Way. Interestingly, if this were the case, DM would need to pair-annihilate or to decay into hard leptonic final states — both to prevent over-producing antiprotons and to yield enough high-energy positrons. In turn, this is an interesting scenario for $\gamma$-ray searches, since hard final state leptons yield an unmistakable hard bremsstrahlung $\gamma$-ray spectrum (Pinzke et al. 2009).

While it is possible that the LHC will provide evidence for SUSY, it seems clear that a combination of laboratory detection not only with direct but also with indirect $\gamma$-ray DM searches will be required in order to successfully scan the whole allowed SUSY parameter space, and to truly assess that a new particle detected by any of these methods really constitutes the enigmatic and long-awaited to be discovered DM.

# Chapter 2

# Motivation and main objectives

The main aim of this Thesis is to provide the Astrophysics and Cosmology community with predictions related to the way that matter distributes in the Universe. In the first part, we focus on intrinsic properties of the structure of dark matter halos spanning a large range of masses, from those hosting dwarf galaxies (with masses around $10^{10}h^{-1}M_{\odot}$) to the largest collapsed objects at present, which host clusters of galaxies (with masses of roughly $10^{14}h^{-1}M_{\odot}$ and larger). Our main purpose here is to derive how matter distributes around the center of those collapsed objects (i.e. the density profile) as well as to study other kinematical properties such as the radial velocity profile, the velocity dispersion, or the velocity anisotropy. All these quantities are derived theoretically using high-resolution $N$-body numerical cosmological simulations that reproduce the collapsed objects for a given set of cosmological parameters, such as the matter (dark+baryonic) density, the curvature of the universe, or the fluctuations in the density field. It is remarkable that these predictions are relevant themselves and indeed necessary for experiments of direct and indirect dark matter detection. In the former, an important assumption for their viability is the amount of dark matter in the vicinity of the Sun. In the case of indirect detection, one must know in advance the integrated distribution of the square of the dark matter density (in the case of annihilation), in order to get an input for the self-interaction rate in any particular object or target, which is related to how many events should one observe from these interactions, especially if dark matter self-annihilates.

The main results of this first part however, is not that related to dark matter detectability but with the theory of structure formation, which is the basis for any solid prediction for dark matter searches. The matter distribution in the Universe is a continuous density field in which we can find large overdensities (dark matter halos) coming from gravitational collapse of primordial fluctuations. Structure formation in the cold dark matter (CDM) cosmology is hierarchical, i.e. the smallest structures are formed at earlier stages of structure formation and the larger objects are formed through accretion and mergers of smaller ones. Therefore, the collapsed objects contain a lot of substructure due to accretion and mergers, although some of these substructures are disrupted due to dynamical friction. Hence we get the picture of a clumpy Universe. This makes the matter associated to a collapsed object to be distributed in such a way that it is difficult to define a boundary in which the matter outside this boundary does not belong to the halo. If we need to establish a systematic definition, the problem is even worse, specially in numerical cosmological simulations where dark matter halos are usually defined as spheres enclosing a given (arbitrary) overdensity, or a set of particles linked if the distance between them is less than a given linking length. In order to measure the mass of the halo using a less arbitrary and more physically motivated definition, we choose to focus on a well defined transition: the (spherically averaged) radial velocity of dark matter halos is close to zero in the inner regions, which is an indication that they are in internal equilibrium. However, at some critical distance this is no longer true, and the radial velocity becomes positive (for low mass halos such as those hosting dwarf or even Milky-Way size galaxies) or negative (for high mass halos such as those associated to galaxy clusters). To identify unambiguously this transition despite the numerical uncertainties, we had to average over many halos with similar masses, but in any case we were able to assess how the mass using this definition compares for different redshifts with the spherical overdensity definition, and which differences arise when computing quantities which depend directly on the chosen definition, such as the abundance of dark matter halos of a given mass, also known as the halo mass function. This work was presented in a paper titled ”The virialized mass of dark matter halos” by Cuesta et al. (see Appendix A.1). Results are summarized and discussed in Section 3.1.1.

The internal properties of dark matter halos that we analyse using these cosmological $N$-body simulations are also interesting for other applications, such as gravitational lensing. The deflection of a background light when passing close to a massive object is related to the mass distribution in it. Hence, we focus our interest in an accurate description of the density profile of objects spanning the same mass range as above. Current cosmological simulations provide a general consensus that the density profile is well assessed using the NFW profile (Navarro et al. 1996). However, this equation cannot hold true at large distances from the halo center, as it tends to zero with an asymptotical power-law behavior beyond the virial radius of the halo. In gravitational lensing this virial radius has very little significance, as the actual matter distribution is continuous and do not show any clear boundary. For this reason we derive an extension of the NFW profile which is also valid for large distances from the center of the collapsed object. We also put some effort to keep this formula simple so that the interesting quantities for gravitational lensing are easy to compute. This work was presented in a paper titled "The density profile of dark matter halos beyond the virial radius" by Tavio et al. (see Appendix A.2). Results are summarized and discussed in Section 3.1.2.

In the second part of the thesis we deal with the multi-messenger approach of observing the Universe at very high energies. Imaging Atmospheric Čerenkov Telescopes such as MAGIC, HESS and VERITAS, together with the Fermi satellite, now offer an unprecedented view of the gamma-ray sky. These telescopes not only identify and analyse the powerful sources that can be observed at these energies, but also open a window for indirect detection of dark matter. The extragalactic distribution of dark matter in large scales should follow closely the distribution of luminous matter, contrary to what happens at low scales in which the physics of the baryonic component may determine if a galaxy succeed to form. However, this description of the dark matter distribution will not be complete unless we also choose a cosmological model consistent with the observations to fill the Universe with the unobserved dark structures. In this spirit, constrained cosmological simulations are able to solve this issue. The initial conditions of the simulation are set up in such a way that they implement observational constraints at present. These constraints are related to the spatial distribution of large clusters the large scale distribution of galaxies, and the peculiar velocity field. In this way we obtain a numerical realization of the Local Universe which is consistent not only with the cosmological model but also with the observational constraints. Such a realization is an excellent test bed for indirect detection of dark matter candidates in particle physics. In particular, the flux of decay products from dark matter is proportional to the dark matter density, and the flux of annihilation products from dark matter is proportional to the dark matter density squared. Hence, we find that the computation of the density and density squared all-sky maps from constrained simulations is a novel but very promising technique that can serve as an input for testing different particle physics models using known computer codes such as DarkSUSY (Gondolo et al. 2004). Moreover, the Fermi satellite is currently performing an all-sky 5-years survey, which offers an unique opportunity to compare with our predictions. This will help to identify any possible detection of dark matter from large structures in the Local Universe, and in the case of no detection, to put constraints on properties of the DM particle such as the mass and the cross section. An interesting topic is the detection of extragalactic structure and the luminosity of large scale filaments and galaxy clusters from dark matter gamma rays for both decaying and annihilating dark matter. Fermi has good prospects to detect this radiation for the case of decaying dark matter, and hence a quantitative analysis to predict how strong this detection could be, is mandatory. This work was presented in the paper titled "Dark matter annihilation and decay in the Local Universe: CLUES from Fermi" by Cuesta et al. (see Appendix A.3). Results are summarized and discussed in Section 3.2.1.

Gamma rays, however, are not the only high energy particles that reach the Earth's orbit. Ultra-high energy cosmic rays (UHECRs), i.e. particles with an energy above one million times the sensitivity of Fermi, reflect the power of the most energetic events in the Universe. Unfortunately, the UHECR flux is very low with a steep energy spectrum. Unveiling the origin of these particles is currently a challenge and will represent a major breakthrough in high-energy Astrophysics. Recent measurements of the properties of the atmospheric particle showers induced by UHECRs at the highest energies reveal that these particles are unlikely to be composed of protons only or heavy (iron-like) nuclei. We explore this fact by suggesting that the UHECRs are CNO-like nuclei which have the interesting property that the suppression in the energy spectrum due to interactions with the CMB (also known as the GZK cutoff), which has been detected by large arrays of Čerenkov telescopes such as Auger or HiRes, occurs at lower distances from the UHECR source. Hence, it is interesting to estimate the probability of chance correlation between the arrival directions of these cosmic ray events, and the angular positions of nearby objects. Here we use the catalog of nearby galaxies of Karachentsev et al. (2004), which comprises galaxies closer than roughly 10 Mpc. Obviously, not all the galaxies will be hosting UHECR accelerators, and thus our ignorance on the boosting process prevent us from selecting a non-contaminated sample. In any case, Auger results on the composition of UHECRs together with the detection of the GZK cutoff makes this possibility worth a closer analysis. This work was presented in the paper titled "The correlation of UHECRs with nearby galaxies in the Local Volume" by Cuesta & Prada (see Appendix A.4). Results are summarized and discussed in Section 3.2.2.

Finally, we add in Appendix B some other work that I did during the completion of the research that leads to this PhD Thesis, although they are not directly related with the mainstream topics discussed here.

# Chapter 3

# Discussion of main results

In this Chapter we present the main results of the Thesis. These are divided in two parts: the first block contains the results that we want to highlight as those related with the main objectives of the Thesis as described before, i.e. the properties of virialized halos and the detectability of the underlying dark matter large-scale structures from high-energy gamma-rays and cosmic-rays. On the other hand, the second one describes those results that do not share this connection with the main topics, but they were developed during the PhD as parallel projects.

In Appendix A, I include the publications for both the first part of the Thesis: "The virialized mass of dark matter haloes" (Cuesta et al. 2008b), "The density profile of dark matter haloes beyond the virial radius" (submitted), and for the second part of the Thesis: "Dark matter annihilation and decay in the Local Universe: CLUES from Fermi" (submitted), and "The correlation of UHECRs with nearby galaxies in the Local Volume" (submitted). In Appendix B I attached the corresponding publications from other research projects in which I participated during the completion of the PhD: "The alignment of dark matter halos with the Cosmic Web" (Patiri et al. 2006), and "Spin alignment of dark matter haloes in the shells of the largest voids" (Cuesta et al. 2008a).

## 3.1 The properties of virialized DM halos

### 3.1.1 The virialized mass of dark matter halos

Virial mass is used as an estimator for the mass of a dark matter halo. However, the commonly used constant overdensity criterion does not reflect the dynamical structure of halos. Here, we analyse dark matter cosmological simulations in order to obtain properties of halos of different masses focusing on the size of the region with zero mean radial velocity. Dark matter inside this region is stationary (see Figure 3.1 and Figure 3.2), and thus the mass of this region is a much better approximation for the virial mass. We call this mass the static mass to distinguish from the commonly used constant overdensity mass. We also study the relation of this static mass with the traditional virial mass, and we find that the matter inside galaxy-sized halos ($\mathrm{M} \simeq 10^{12}\mathrm{M}_\odot$) is underestimated by the virial mass by nearly a factor of 2. At $z \simeq 0$, the virial mass is close to the static mass for cluster-sized halos ($\mathrm{M} \simeq 10^{14}\mathrm{M}_\odot$). The same pattern – large halos having $M_{vir} > M_{static}$ – exists at all redshifts, but the scale mass $M_0 = M_{vir} = M_{static}$ decreases dramatically with increasing redshift: $M_0(z) \simeq 3 \times 10^{15} h^{-1} M_\odot (1+z)^{-8.9}$. The mass accretion history using this mass estimator is also compared with the traditional virial mass accretion history. This is shown in Figure 3.4.

When rescaled to the same $M_0$ halos clearly demonstrate a self-similar behavior, which in a statistical sense gives a relation between the static and virial mass (see Figure 3.3). To our surprise, we find that the abundance of halos with a given static mass, i.e. the static mass function, is very accurately fitted by the Press & Schechter approximation (Press & Schechter 1974) at $z = 0$, but this approximation breaks at higher redshifts $z > 1$. Instead, the virial mass function is well fitted as usual by the Sheth & Tormen approximation (Sheth & Tormen 1999) even at $z \simeq 2$.

We find an explanation why the static radius can be two to three times larger as compared with the constant overdensity estimate. The traditional estimate is based on the top-hat model, which assumes a constant density and no rms velocities for the matter before it collapses into a halo. Those assumptions fail for small halos, which find themselves in an environment where density is falling off well outside the virial radius and random velocities grow due to other halos. Applying the non-stationary Jeans equation, we find that the role of the pressure gradients is significantly larger for small halos. At some moment, it gets too large and stops the accretion.

Our more realistic (physical) estimate of the halo mass might be crucial for some areas in cosmology which are sensitive to accurate values of the mass of dark matter halos. For example, our results may be relevant for understanding the galaxy formation processes that happen inside dark matter halos. Indeed, semi-analytical models of galaxy formation (e.g. Croton et al. 2006) might need to assess the impact of their predictions when the virial mass is no longer used. If the static mass and its evolution are used, one may get a more realistic picture of the structure formation process drawn from cosmological simulations. Moreover, recipes for star formation, active galactic nuclei and supernova feedback and merging of galaxies are often taken from quantities of their corresponding dark matter halos, such as their mass. Thus, the conclusions (e.g. color–magnitude diagram, evolution of the stellar mass, etc.) from the analysis of these simulations using semi-analytical models of galaxy formation may be biased due to an underestimation of the mass associated to a halo if the former virial mass is considered, especially for the galaxy-sized halos such as the host of the Milky Way as we have reported in this work.

The precise determination of the halo mass function, in terms of the static mass, can also be very relevant. Mass function of cluster sized halos must be predicted with special accuracy because the number density of galaxy clusters is a probe of fundamental cosmological parameters, such as dark energy. This is very important since the evolution of the mass function of galaxy clusters is taken as an almost direct measurement of the equation of state of dark energy $w = P/\rho$ (The Dark Energy Survey Collaboration 2005) and any statistically significant deviations in the measurements of the mass function of clusters from the predictions of the $\Lambda$CDM model may be and likely will be interpreted as deviations of the dark energy from a simple cosmological constant.

Other possible observational implications of this work also deserve further investigation. It is noteworthy that the transition mass of $\sim 5 \times 10^{12} h^{-1} M_{\odot}$, that separates the infall and outflow regimes, is similar to the mass scale found by Dekel & Birnboim (2006). Dekel & Birnboim (2006) argue that below $M \simeq 10^{12} M_{\odot}$ the efficient early star formation may occur due to cold flows, as thermal pressure is not large enough to avoid the gas accretion from the outer gas reservoir to the inner core of the halo. On larger scales, the heating due to virial shocks may shutdown the star formation. This different behavior of the gas around dark matter halos in simulations above and below this mass scale was proposed by Dekel & Birnboim (2006) as an explanation for the bimodality observed in many properties of galaxies such as the bimodality seen in the color distribution of Sloan Digital Sky Survey

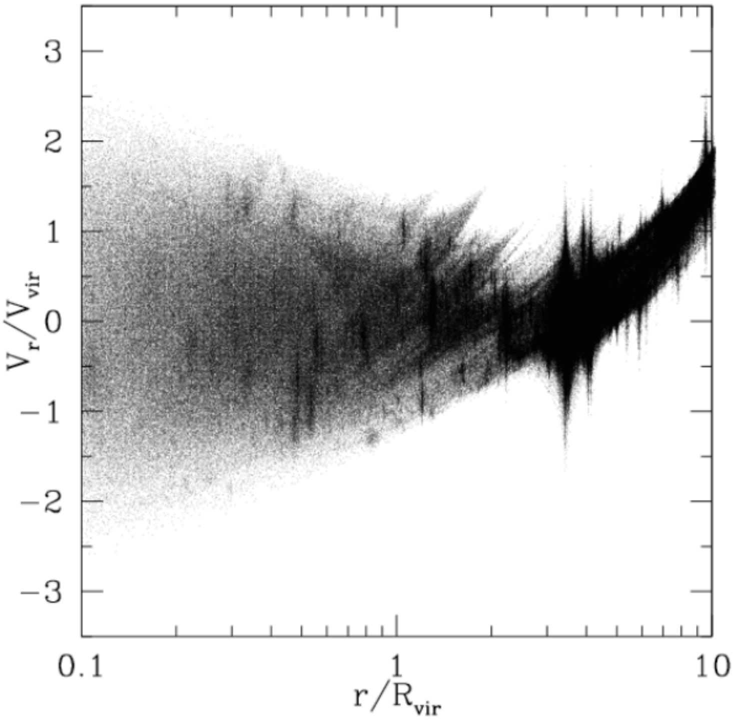

Figure 3.1 Phase-space diagram for the particles in dark matter halos. Here we show a galactic-sized halo ($M_{vir} = 1.4 \times 10^{12} h^{-1} M_{\odot}$). Clusters clearly show strong infall pattern around the virial radius, whereas this is not observed in smaller sized halos.

field galaxies. Thus, a given velocity pattern of infall or outflow in a dark matter halo of mass above and below $10^{12} h^{-1} M_{\odot}$ may be correlated with the fact that the galaxy within the halo belongs to the blue cloud or the red color sequence, respectively. Yet, this is only a speculation which remains to be investigated.

However, the mass scale for transition between infall and outflow is the same as the mass scale at which baryonic matter cannot penetrate the inner parts of the halo. At first glance, this is just a matter of coincidence, as for higher redshifts the transition mass would be well below the mass scale of Dekel & Birnboim (2006). Still, it is an interesting question whether the halos experiencing infall of the dark matter also host galaxies, which grow fast by accreting baryons in their central regions. Such correlations between galaxies and their host halos could unveil some of the relations between dark and baryonic matter, and hence cast some light in the evolution of galaxies in the expanding Universe.

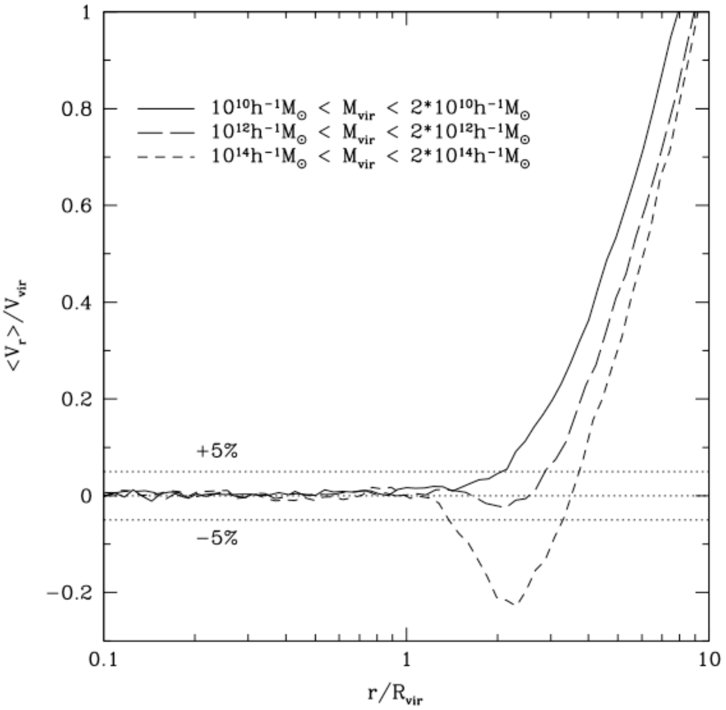

Figure 3.2 Mean radial velocity for three different mass bins. The profiles were obtained by averaging over hundreds of distinct halos on each mass bin. In dotted lines is shown the selected threshold delimiting the static region (5 per cent of the virial velocity). Cluster-sized halos display a region with strong infall (dashed line). In contrast, low-mass halos (solid line) and galactic halos (long-dashed line) do not show infall at all but a small outflow preceding the Hubble flow.

### 3.1.2 The density profile of dark matter halos beyond the virial radius

We present an approximation for the average density profile of dark matter halos in the ΛCDM cosmological model, which is accurate to within 10–15% even for large radial distances from $0.05R_{vir}$ up to $10R_{vir}$ for halo masses ranging from $10^{11.5}$ to $10^{15.0}h^{-1}M_\odot$. We propose a modified form of the Navarro, Frenk & White (Navarro et al. 1996, NFW hereafter) approximation: $\rho(\mathrm{r}) = \rho_{NFW}(r) + A(r/Rvir)^{-1} + B(1 + r/Rvir)^{-1} + \bar{\rho}$ (see Figure 3.5). This generalized expression, which is applicable to the external regions of dark matter halos, only very slightly affects the density in the inner regions of halos. The strong correlation among the different parameters in the model allows us to describe the profile

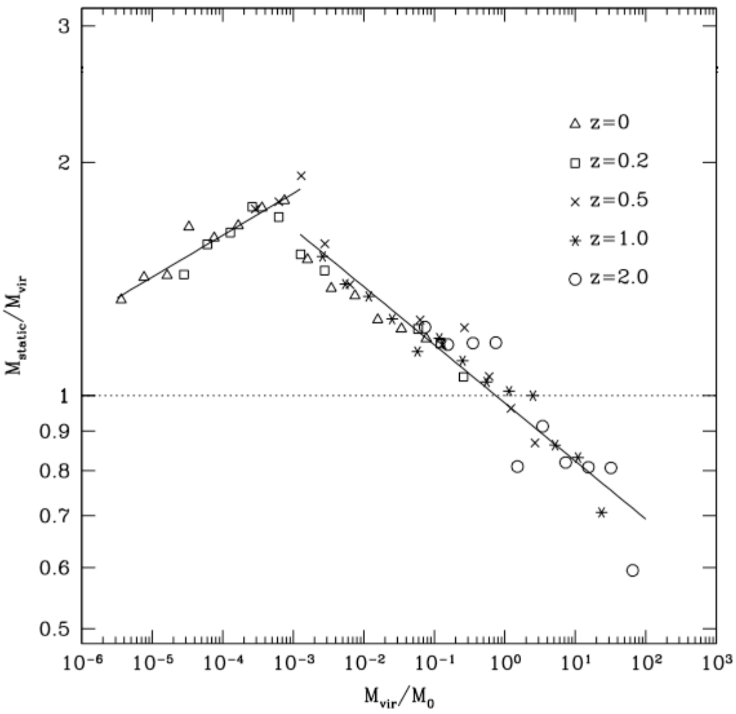

Figure 3.3 The halo static mass – virial mass relation at different redshifts. The ratio $M_{static}/M_{vir}$ increases due to reduced outflow up to the first appearance of infall, making this ratio decrease. The solid line represents a fit to two power laws at both sides of the transition mass. The time dependence of the $M_{static}$–$M_{vir}$ relation is encoded in the mass scale $M_0$.

in terms of just one parameter: the virial mass. We note that other approximations found in the literature will prove to be useful to describe, with high accuracy, the halo density profile up to the virial radius. Yet, most of them fail when they are applied to fit the outer regions, where the mass predicted by extrapolation of these profiles is far below the actual mass in these regions.

We integrate our density profile to derive the enclosed mass in a sphere of a given radius and compare it with the NFW results. We find that the NFW underestimates the enclosed mass by more than 50% at $10R_{vir}$, whereas our model reproduces the results from numerical simulations to within 2% accuracy even at this distance (see Figure 3.6). We also use this new approximation to study the weak gravitational lensing and to obtain an analytic expression for the tangential shear. This allows us to quantify the contribution to the shear

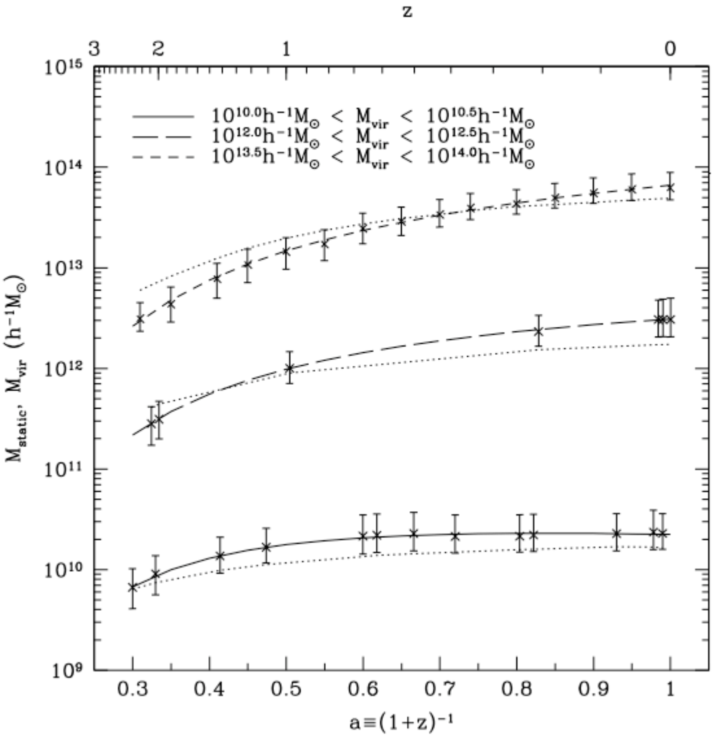

Figure 3.4 The mass accretion history of dark matter halos. The evolution of the static mass is indicated by the crosses and the error bars, with their corresponding fit to our model (solid, long-dashed and dashed lines for low-mass, galaxy-sized and cluster-sized halos, respectively), while the dotted line shows the evolution of the virial mass, according to the parametrization by Wechsler et al. (2002). The static mass inside low-mass halos is nearly constant from $z$=0.5 to 0. On the other hand, galaxy-sized halos increase their static mass even steeper than their virial mass, due to relaxation around halos. Clusters are accreting mass, but also incorporating some of the recently virialized mass from their surroundings.

from the outer regions of the density profile. For the first time we calculate the difference between the tangential shear calculated via the NFW profile and the corresponding result when the external regions of halos in cosmological simulations are taken into account. We find a 4% difference for all the mass ranges under study.

In order to build the numerical mean density profiles, we averaged over many hundreds of halos from high-resolution cosmological simulations so that the profiles corre-

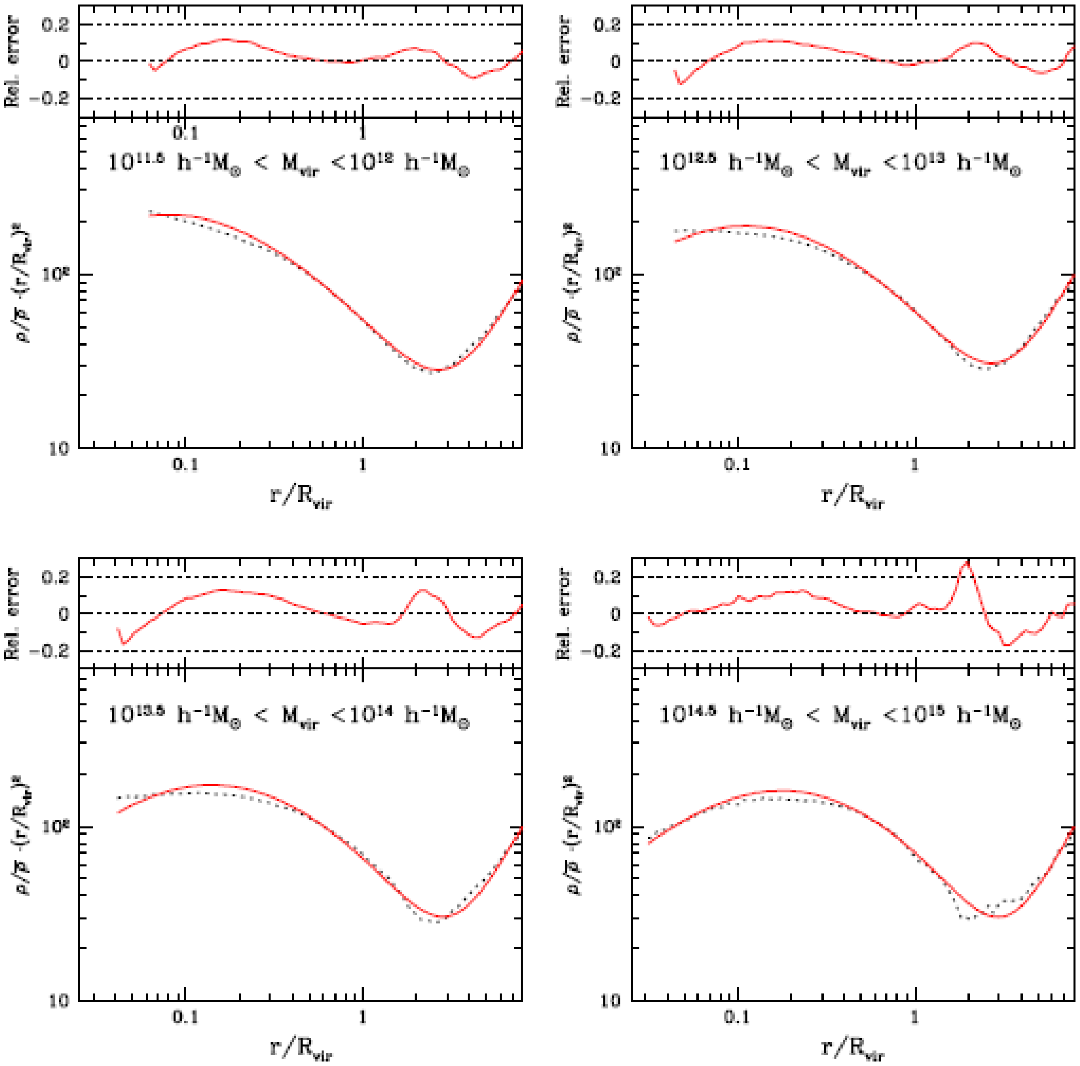

Figure 3.5 Average density profiles in four different halo mass ranges. The solid line represents the best-fit of our approximation to the numerical density profile (dotted line). The deviation around $r = r_s$ is inherited to the NFW profile, which is about the same amount of the deviation at the transition to the outer regions of the halo at 2–3$R_{vir}$.

sponding to most of our mass bins are entirely unaffected by statistics. This procedure for averaging density profiles is analogue to the stacking method, used in observational studies like the one by Mandelbaum et al. (2008) to infer the density profile of a cluster of galaxies. This similarity is useful for the comparison of the results from cosmological simulations to the real data.

There are two main discrepancies from the numerical density profile which have a different origin: whereas the overestimation around $r = r_s$ is inherited from NFW profile, the overestimation just beyond the virial radius suggests that our model is not able to reproduce the steepest region. This steep region just outside Rvir is more pronounced for most massive halos, suggesting a depletion of the halo outskirts due to dark matter infall (Prada et al. 2006, Cuesta et al. 2008b). The presence of our additional terms with respect to the NFW formula has only a very small influence on the inner regions of the density profile, so that our approximation can also be considered as an extension of the NFW profile.

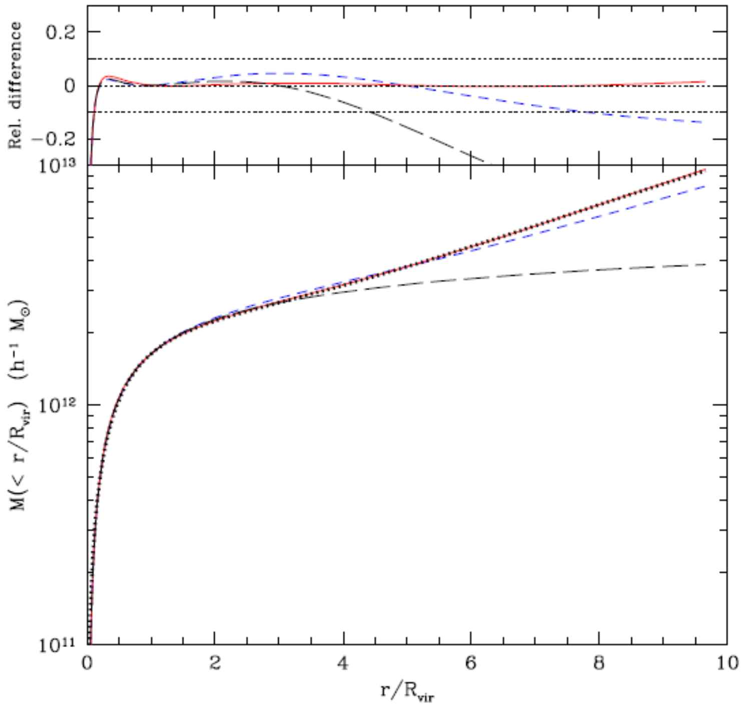

Figure 3.6 Enclosed mass in a sphere of radius $r$ versus $r/R_{vir}$ for the average halo with $M_{vir} \simeq 10^{12} h^{-1} M\odot$. The dotted curve represents the simulation data, long dashed and short dashed lines show the plain NFW and the modified NFW profile (i.e. NFW plus the mean matter density $\bar{\rho}$) respectively. The solid line is our approximation. Top panel represents the relative errors with respect to the simulation data.

Our estimations of the cumulative mass are especially interesting for new measurements of the enclosed mass beyond virial radius in X-ray clusters (George et al. 2009), where plain NFW is still used even at $r > 1Rvir$. While current observations cannot distinguish between modified NFW and our approximation, in the near future they should be able to find the need for adding the mean matter density term to the density profile.

The small difference between the tangential shear calculated using our approximation and the one derived from the NFW profile could provide an observational test for the validity of our approximation, which has been derived from the results of cosmological $N$–body simulations. Although present resolution of weak lensing experiments prevents us from drawing a robust conclusion, the stacking of different observations should prove that this approximation, which includes the contribution of external regions, is more realistic than most of the so far proposed density profiles, which do not account for them.

## 3.2 Signals from the large-scale structures

### 3.2.1 Dark matter annihilation and decay in the Local Universe

We present all-sky Fermi maps of extragalactic $\gamma$-rays coming from dark matter annihilation and decay (see Figure 3.7). The dark matter distribution is obtained from a constrained cosmological simulation of the Local Universe provided by the CLUES project. The dark matter density and density squared fields are then taken as inputs for the Fermi observation simulation tool to predict the $\gamma$-ray photon counts that Fermi will detect in a 5-year all-sky survey. Signal-to-noise sky maps have also been obtained by adopting the current Galactic and isotropic diffuse background models released by the Fermi Collaboration (see Figure 3.8 and Table 3.1).

We find the first theoretical evidence that point out the possibility for Fermi to detect $\gamma$-ray emission from extragalactic large structures, such as nearby galaxy clusters and filaments (e.g. Virgo and Coma), in particular for decaying dark matter models fitting the positron excess as measured by PAMELA. Yet, most of the results presented here are conservative since no boost from unresolved dark matter substructures, or any other enhancement like Sommerfeld effect or adiabatic contraction, is included.

The Fermi Collaboration has started to severely constrain models of annihilating DM that could explain the PAMELA positron excess (Yin et al. 2009, Ibarra & Tran 2009,

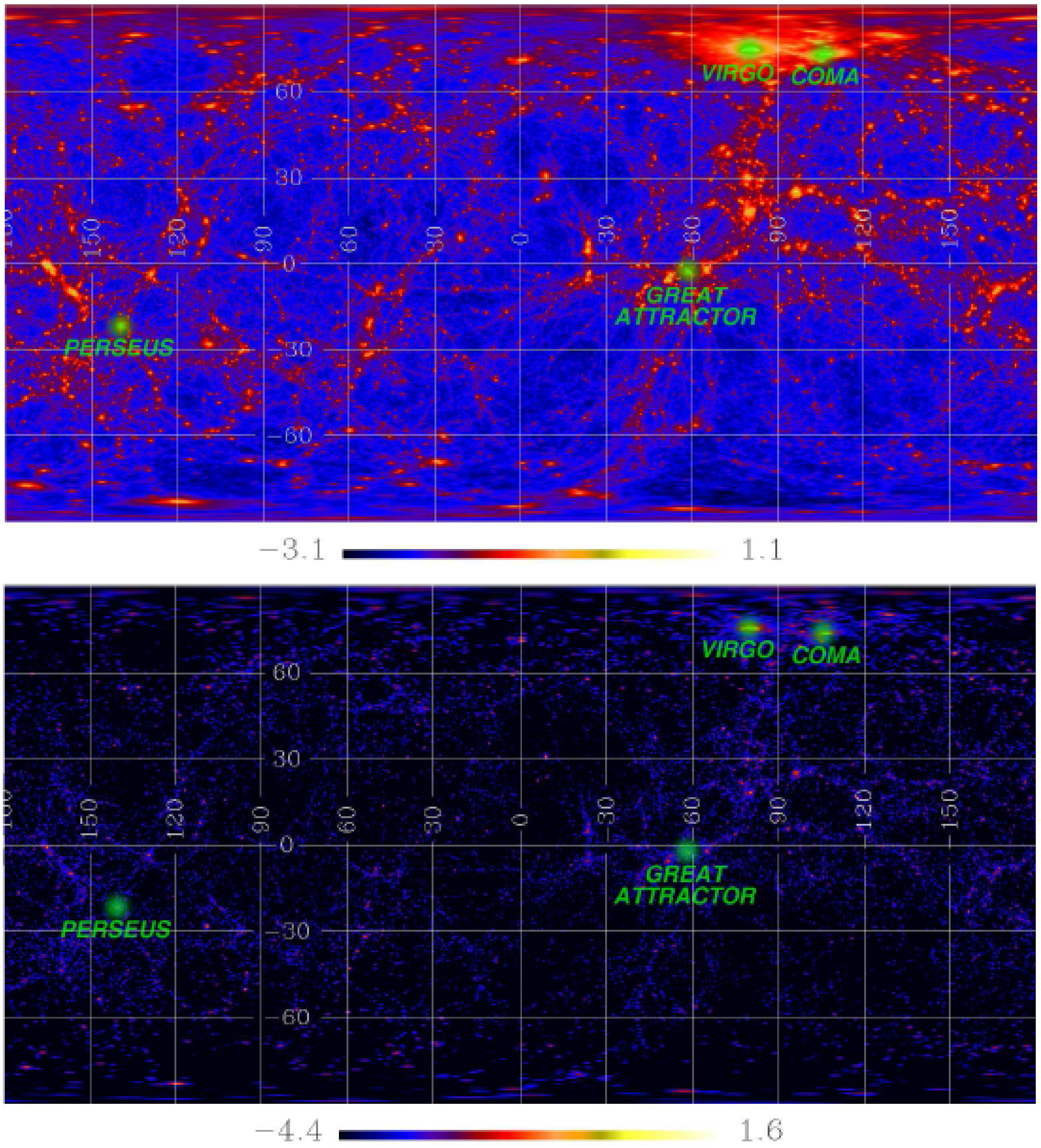

Figure 3.7 DM distribution in the Local Universe constrained cosmological simulation Box160CR. These all-sky maps are Cartesian projections in Galactic coordinates. Left panel shows the density distribution, whereas the right panel displays the distribution of density squared. The maps are color-coded according to the log10 of the DM flux, and units are $GeV cm^{-3} kpc sr^{-1}$ for decay map and $GeV^2 cm^{-6} kpc sr^{-1}$ for the annihilation map. Large structures reproduced by this simulation such as Virgo, Coma, and Perseus clusters, together with the Great Attractor, are labeled.

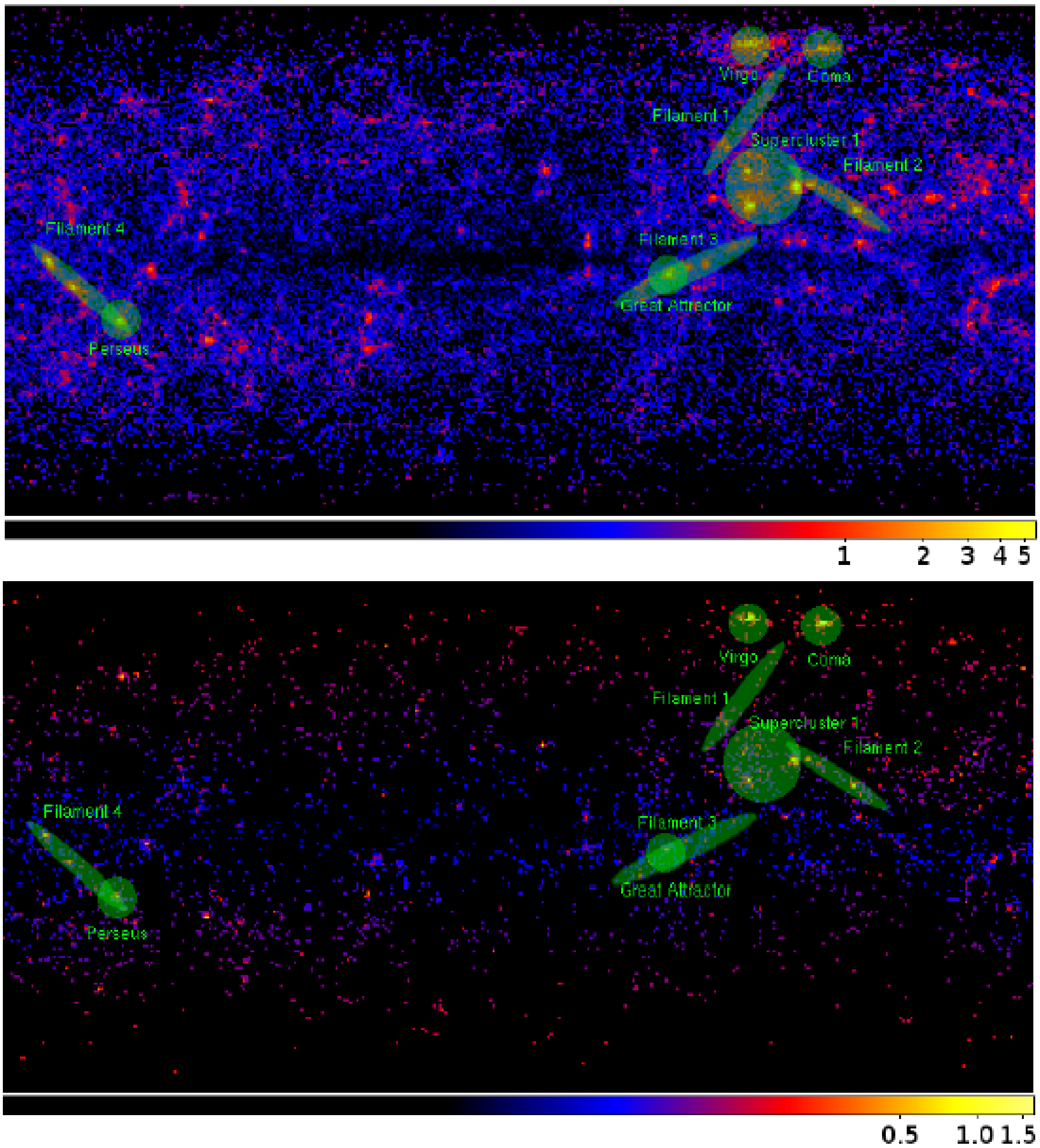

Figure 3.8 S/N all-sky maps from Fermi simulations for DM $\gamma$-rays in the energy range 100MeV–10GeV built from the Box160CR constrained simulation of the Local Universe. $\gamma$-rays from DM decay (left) and annihilation (right) are shown for the $b\bar{b}$ channel model (see text for details).

Table 3.1. S/N, photon counts and backgrounds in Fermi simulations.

| Object | $b\,\bar{b}$ channel | | | | $\mu^+\mu^-$ channel | | | | background |
|---|---|---|---|---|---|---|---|---|---|
| | ann | | dec | | ann | | dec | | |
| Coma 1 deg | 2.981 | (20) | 2.981 | (20) | 0.567 | (3) | 1.078 | (6) | 25 |
| Coma 2 deg | 2.592 | (31) | 4.061 | (52) | 0.371 | (4) | 1.331 | (15) | 112 |
| Coma 5 deg | 1.542 | (39) | 4.976 | (135) | 0.203 | (5) | 1.542 | (39) | 601 |
| Virgo 1 deg | 2.739 | (15) | 3.133 | (18) | 0.000 | (0) | 0.485 | (2) | 15 |
| Virgo 2 deg | 2.858 | (28) | 5.371 | (61) | 0.471 | (4) | 1.444 | (13) | 68 |
| Virgo 5 deg | 1.818 | (42) | 7.700 | (203) | 0.269 | (6) | 2.189 | (51) | 492 |
| Perseus 1 deg | 1.144 | (12) | 5.642 | (74) | 0.493 | (5) | 1.841 | (20) | 98 |
| Perseus 2 deg | 0.700 | (14) | 5.646 | (128) | 0.253 | (5) | 1.518 | (31) | 386 |
| Perseus 5 deg | 0.386 | (20) | 4.542 | (245) | 0.116 | (6) | 1.187 | (62) | 2665 |
| GAttractor 1 deg | 0.280 | (8) | 2.686 | (80) | 0.105 | (3) | 0.935 | (27) | 807 |
| GAttractor 2 deg | 0.211 | (13) | 2.581 | (162) | 0.049 | (3) | 0.696 | (43) | 3777 |
| GAttractor 5 deg | 0.136 | (23) | 2.157 | (367) | 0.041 | (7) | 0.538 | (91) | 28572 |
| Filament1, $d = 65\mathrm{Mpc}/h$ | 0.224 | (14) | 4.515 | (292) | 0.128 | (8) | 1.348 | (85) | 3891 |
| Filament2, $d = 40\mathrm{Mpc}/h$ | 0.752 | (67) | 9.317 | (871) | 0.191 | (17) | 2.589 | (233) | 7869 |
| Filament3, $d = 65\mathrm{Mpc}/h$ | 0.351 | (84) | 4.862 | (1174) | 0.121 | (29) | 1.181 | (283) | 57127 |
| Filament4, $d = 55\mathrm{Mpc}/h$ | 0.576 | (91) | 8.380 | (1358) | 0.184 | (29) | 2.065 | (328) | 24904 |
| Supercluster1, $d = 45\mathrm{Mpc}/h$ | 0.911 | (144) | 12.598 | (2066) | 0.254 | (40) | 3.334 | (531) | 24829 |

Note. — The S/N ratio and number of photon counts (in brackets) in the 1 GeV – 10 GeV energy range for our different DM models. For cluster regions, three different radii are considered (1, 2, and 5 degrees). Filaments 1 to 4 represent elongated regions connected to these clusters which are potentially interesting due to their high S/N. Median distance of the halos belonging to the filaments is indicated. Supercluster1 is a collection of massive halos which accidentally lie along the line-of-sight. Background counts from the Galactic plus extragalactic diffuse in the same regions are also listed.

Profumo & Jeltema 2009). On the other hand, the case of decaying DM has comparatively received considerably smaller attention. Not only does the parameter space range for decaying DM appears at present to be much more generous than that for pair-annihilation, given the less stringent currently available $\gamma$-ray constraints, but from a theoretical standpoint, decaying DM with a lifetime in the correct range is a generic prediction of many theories beyond the Standard Model of particle physics. In this case, we find that filamentary regions, together with large superclusters, provide an interesting chance of detection in the case of DM decay, in particular if the selected sky area under analysis covers the whole overdense region.

These conclusions should be complemented by an analysis of the galactic components, mainly from DM subhalos like those hosting the DM-rich dwarf spheroidal galaxies around the Milky Way. This is discussed in a recent work by Anderson et al. (2010). Moreover, these results on DM search will benefit from additional hints from the study of the angular power spectrum of the $\gamma$-ray flux (e.g. Fornasa et al. 2009, Hensley et al. 2009). Finally, we find that Fermi will be able to place strong constraints on DM nature by measuring the $\gamma$-ray emission from both galactic and extragalactic objects, and the theoretical expectations from the results presented here should provide the astroparticle community with the most interesting structures to detect the elusive DM particle.

### 3.2.2 The correlation of UHECRs with nearby galaxies in the Local Volume

We explore the possibility of a local origin for ultra high energy cosmic rays (UHECRs). Using the catalog of Karachentsev et al. (2004) including nearby galaxies with distances less than 10Mpc (Local Volume), we search for a correlation with the sample of UHECR events released so far by the Pierre Auger collaboration (see Figure 3.9). The counterpart sample selection is performed with variable distance and luminosity cuts which extract the most likely sources in the catalog. The probability of chance correlation after penalizing for scans is 0.96%, which corresponds to a correlation signal of $2.6\sigma$. We find that the parameters that maximize the signal are $\psi = 3.0°$, $D_{max} = 4$Mpc and $M_B = -15$ for the maximum angular separation between cosmic rays and galaxy sources, maximum distance to the source, and sources brighter than B-band absolute magnitude respectively (see Figure 3.10).

This implies a preference for the UHECRs arrival directions to be correlated with the nearest and most luminous galaxies in the Local Volume, while the angular distance between the cosmic ray events and their possible sources is similar to that found by The Pierre Auger Collaboration using active galactic nuclei (AGNs) within 70-100Mpc instead of local galaxies. We note that nearby galaxies with $D < 10$ Mpc show a similar correlation with UHECRs as compared to well-known particle accelerators such as AGNs, although less than 20% of cosmic ray events are correlated to a source in our study. However, the observational evidence for mixed composition in the high-energy end of the cosmic ray spectrum supports the possibility of a local origin for UHECRs, as CNO nuclei can travel only few Mpc without strong attenuation by the GZK effect, whereas the observed suppression in the energy spectrum would require more distant sources in the case of pure proton composition interacting with the CMB.

This analysis is highly motivated in the light that a mixed CNO (as opposed to pure proton) composition of UHECRs, which is the preferred scenario indicated by current data, could not survive the GZK cutoff unless the sources are located in the Local Volume. Therefore, any correlation with these nearby sources would explain both composition and correlation at the same time.

The similar value of the chance correlation found by The Pierre AUGER Collaboration: Abraham et al. (2008) with the AGNs in the Véron-Cetty catalog (Véron-Cetty & Véron 2006) and the one we find here is an indication that there is no clear source of the UHECRs, and finding a lower value of the probability of chance correlation does not guarantee that this is actually the preferred source as compared to other sources which present similar values of $P_{chance}$. This was already noticed even in early papers such as Tinyakov & Tkachev (2001), and in any case it seems unlikely to get a $> 3.3\sigma$ detection (Kashti & Waxman 2008). Interestingly, most of the objects in the catalog of Karachentsev et al. (2004) which correlate with Auger events, are already included in the AGN catalog, which has around 30 objects with $D < 10$Mpc. This may indicate that the relation between nearby galaxies and UHECRs found in our work could be inherited from the The Pierre AUGER Collaboration: Abraham et al. (2008) result. In any case, the so-called AGN hypothesis has proven to be controversial (Gorbunov et al. 2008, Moskalenko et al. 2009), stressed by the deficit of events from the direction of the Virgo supercluster. On the other hand, the correlation with the distribution of luminous matter seems to be well established (Kashti & Waxman 2008), without making any reference to any particular source which can accelerate

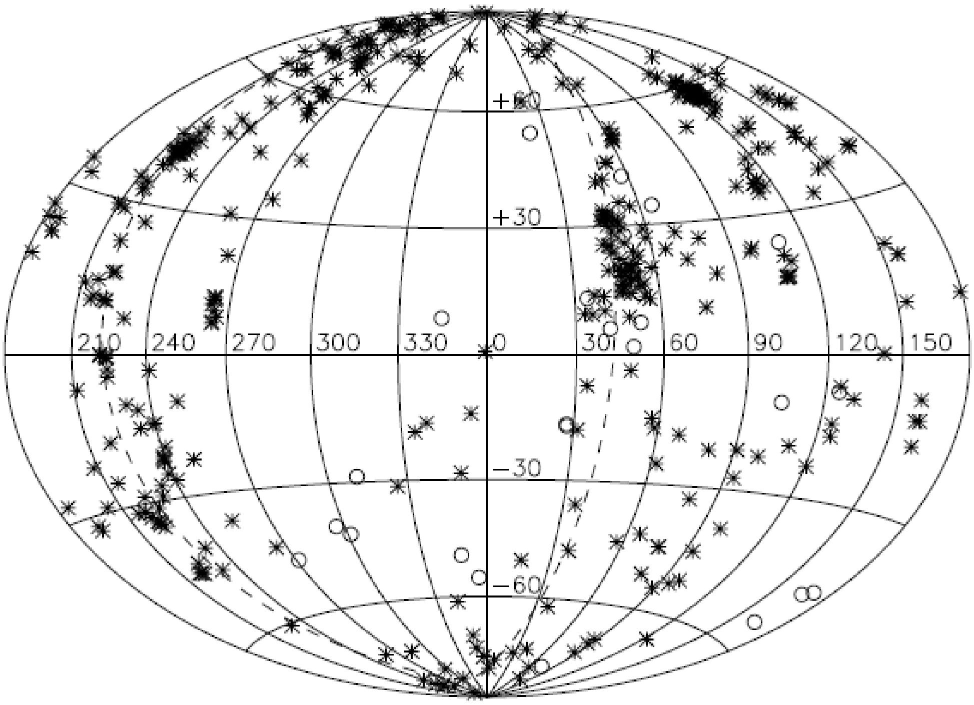

Figure 3.9 The spatial distribution in galactic coordinates of cosmic-ray arrival directions (circles) and nearby galaxies from the catalog of Karachentsev et al. (2004) (stars) shown in Aitoff projection. The Supergalactic plane is also shown with dashed line for reference.

particles up to these energies.

Surprisingly, most of the objects in the Karachentsev et al. (2004) catalog which correlate with the UHECR sample (with the exception of NGC300) are located in a small region in the sky, with Supergalactic coordinates $150^\circ <$ SGL $< 165^\circ$ and $-10^\circ <$ SGB $< -5^\circ$. This region is near the Supergalactic plane, pointing to preferential arrival directions from nearby galaxies located in a high density region. Future measurements and hopefully the next data release with a total of 58 events as announced in The Pierre Auger Collaboration: J. Abraham et al. (2009) will help to clarify the origin of nearby and distant UHECRs, which will allow to study more in detail the acceleration physics behind them.

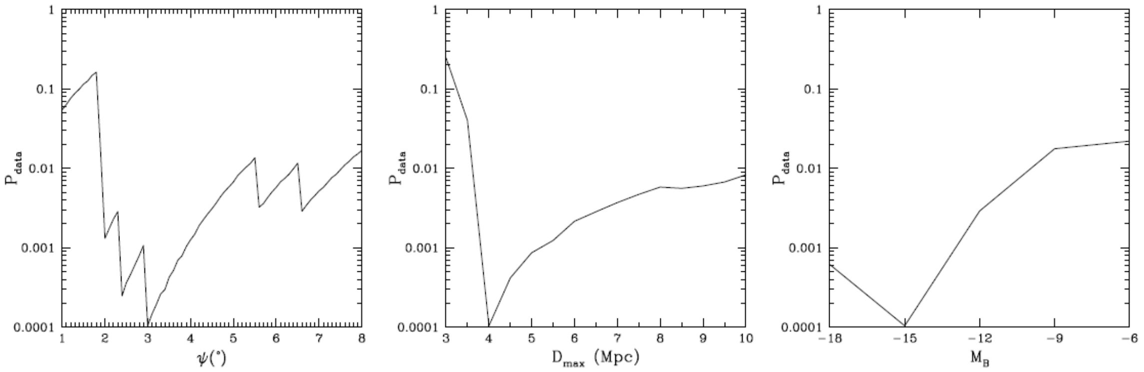

Figure 3.10 The chance correlation probability as a function of each one of the scan parameters, holding the other two fixed at their minimum of $P_{data}$. Left panel : Angular separation. Middle panel : Maximum galaxy distance $D_{max}$. Right panel : Maximum absolute magnitude in the $B$-band.

## 3.3 Other Results

We now summarize some other results that, although they are not fully related with the main topic of this Thesis, they were obtained during its completion.

### 3.3.1 The alignment of dark matter halos with the cosmic web

We have also investigated the orientation of the axes and angular momentum of dark matter halos with respect to their neighboring voids using high-resolution $N$-body cosmological simulations. We find that the minor axis of a halo tends to be aligned along the line joining the halo with the center of the void and that the major axis tends to lie in the plane perpendicular to this line. However, we find that the angular momentum of a halo does not have any particular orientation. These results may provide information about the mechanisms whereby the large-scale structure of the universe affects galaxy formation, and they may cast light on the issue of the orientation of galaxy disks with respect to their host halos.

We clearly see that halos are not randomly oriented within the shells of voids. The major axis of a halo tends to lie along the plane perpendicular to the radial direction; i.e., there is an excess of halos with a angles near 90°. On the contrary, the minor axis tends to point to the direction of the center of the void. There is a marginal orientation of the middle axis toward the plane perpendicular to the radial direction. However, we do not see any particular orientation of the halo angular momentum with respect to the large-scale structure, confirming recent results also obtained from $N$-body simulations using similar methodology (Heymans et al. 2006).

To test the robustness of our results, we have conducted several tests. First of all, we have analyzed the orientations of dark matter halos selected as described above, but in this case we used "fake" voids; i.e., we randomly placed spheres of fixed radius over the sample and calculated the angles between the axis (and angular momentum) of the dark matter halos located in the shells of these fake voids and the direction to their center.

As expected, we found that the angles of the halos chosen to be in the shells of random spheres are uniformly distributed; i.e., they follow a sine distribution. Moreover, we applied two different statistical tests: the average of the cosine test and a standard Kolmogorov-Smirnov (K-S) test. If the angles are randomly distributed, the average of the cosine of these angles is 0.5, so that the bigger the deviation is from this value, the larger will be the effect.

From these results, we conclude that we can reject with high confidence (more than 7 $\sigma$) the null hypothesis (i.e., the axes of dark matter halos are randomly distributed) for the halos in the shells of voids. As expected, the results of the statistical test for the halos located in the shells of the random spheres show that the orientation of these halos is compatible with the random distribution.

On the other hand, we used our data to gain some insight into the nature of the internal alignment of the minor axis with angular momentum found in previous works (e.g., Bailin & Steinmetz 2004, Bailin & Steinmetz 2005). We selected those halos for which both directions form an angle smaller that 20°. For these halos, we found that the alignment between the minor axis and the radial direction of the void is weaker than for randomly chosen halos, quite compatible with a random distribution.

Comparing these results with the observed tendency for the spin of spiral galaxies to point along the plane perpendicular to the direction of the center of the void found by Trujillo et al. (2006), three scenarios are possible: (1) The non-isotropy of the orientation of the spin of the galaxies is entirely induced by the halo alignments, (2) both alignments are two effects with a common origin (namely, the tidal field in the shells of voids), or (3) a combination thereof. In the first scenario the probability distribution for the angle between the major axis of the host halo and the spin of their galaxy is independent of the angle between the spin and the radial direction of the void.

In this case, this probability distribution may be uniquely determined by comparing the distribution of the angle between the major axis and the radial direction with that of the angle between the spin of the galaxies and the radial direction. This would imply that the spin is very closely aligned with the major axis of the host halo. However, recent hydrodynamical simulations (Bailin et al. 2005) do not show this effect (they found that the spin of galaxies is uncorrelated with the halo). Therefore, the other two scenarios seem more plausible.

### 3.3.2 Spin alignment of dark matter halos in the shells of the largest voids

Using the high-resolution cosmological $N$-body simulation MareNostrum universe we study the orientation of shape and angular momentum of galaxy-size dark matter halos around large voids. We find that halos located on the shells of the largest cosmic voids have angular momenta that tend to be preferentially perpendicular to the direction that joins the center of the halo and the center of the void. This alignment has been found in spiral galaxies around voids using galaxy redshift surveys. We measure for the first time the strength of this alignment, showing how it falls off with increasing distance to the center of the void. We also confirm the correlation between the intensity of this alignment and the halo mass. The analysis of the orientation of the halo main axes confirms the results of previous works. Moreover, we find a similar alignment for the baryonic matter inside dark matter halos, which is much stronger in their inner parts.

The possibility of isotropic orientations has been rejected at $7\sigma$ confidence level. This result is in qualitative agreement with and is likely to be related to the observational result of Trujillo et al. (2006) for spiral galaxies using large galaxy surveys. The alignment of dark matter collapsed structures with the large-scale structure finds a natural explanation in the context of the Tidal Torque Theory (TTT). The different components of the angular momentum vector present a dispersion which is not isotropic: there is a marked asymmetry between the dispersion in the direction of maximum compression as compared to that in the direction of maximum expansion (Betancort-Rijo & Trujillo 2009). Therefore, very low density regions such as large voids are suitable to study this effect as they are surrounded by a region with a large tidal field, causing the anisotropy in the shear tensor we are measuring in this work. It is worth noting that this effect is not due to accretion of matter along filaments. Large voids are surrounded by a complex filamentary network of matter (Colberg et al. 2005) which could represent a preferential direction of infall (but see Vitvitska et al. 2002). This accretion generates angular momentum pointing perpendicular to the filament in which the halos are embedded, which could be either the direction to the center of the void but could also be perpendicular to it, resulting in no preferential orientation of angular momentum. Therefore, the anisotropic dispersion in the angular momentum vector seems more plausible in order to explain of this effect.

This is the first time that this alignment has been found in cosmological simulations using halos in the shells of voids with no pre-selection of the halos, in contrast to previous results. The poor halo statistics in the simulation box, the small number of particles in halos, and even an overestimation of the error bars are likely to be the causes of the non-detection of this effect in Patiri et al. (2006) and Heymans et al. (2006). Brunino et al. (2007) did not succeed in finding this alignment either, and concluded that the distribution of angular momentum vectors is compatible with isotropy for their total dark matter halo sample. This is somewhat surprising since they used the Millennium Simulation which exceeds the resolution of the MareNostrum universe simulation used here, having both the same box size. However, we have checked that the uncertainties in the orientation of the vectors used here are small enough to ensure the veracity of these results. We recall that the halos used here are chosen to be well resolved and their directions are determined to within an angle of 13°. Indeed, it can be proven that this small uncertainty in the angle measurement makes the uncertainty in the parameter $p$ we use to quantify the strength of the alignment be negligible. It is very likely that the linking length (and hence the overdensity) used to identify the halos in the simulation box makes the results to differ.

Shape alignment of halos in the surface of large voids is further confirmed, as shown previously by Patiri et al. (2006). Minor axis is found to be preferentially aligned with the direction to the center of the void and major axis tends to be aligned with the orthogonal direction. These results are also robust with respect to the shape of the void. Using an ellipsoidal void catalog and measuring angles with respect to the radial and the normal direction we do not find any difference compared to the results obtained using spherical voids for the orientation of the main axes and angular momentum. Hence, we do not find that the shape of the void is meaningful for this purpose.

# Chapter 4

# Conclusions and future work

## 4.1 Conclusions

In this Thesis we have provided the Astrophysics and Cosmology community with predictions related to the way that matter is distributed in the Universe. These predictions are focused on the possible detection of dark matter particles in the next few years thanks to current and new experiments. In particular, we have shown some results which reveal internal properties (both structural and kinematical) of the dark matter halos which are of interest for direct and indirect dark matter detection searches as well as for the interpretation of weak gravitational lensing measurements. Yet, indirect dark matter detection may involve an all-sky analysis of the extragalactic structures present in the nearby Universe. In this respect, we also have shown some results which are focused on the relation between the Large Scale Structure of the Universe and the multi-messenger high energy Astrophysics. In particular, we have shown some connections between the gamma ray sky and the decay and annihilation of dark matter in the Local Universe, as well as the possible correlation of ultra high energy cosmic rays with these structures. Overall, this work offers a complete analysis of the signals pursued by some of the present and upcoming experiments which are on the quest for a theory beyond the Standard Model.

The main conclusions of this Thesis are given below for each of the different sections discussed in the previous Chapter. I will briefly summarize the strong points of this research:

### 4.1.1 The virialized mass of dark matter halos

We use a set of high-resolution $N$-body cosmological simulations for the analysis of the mass inside the region of dark matter halos with no net infall or outflow velocities, i.e. the static region. Halos show a typical radial velocity pattern that depends on their mass: low-mass halos tend to display a region with outflow in their surroundings, while cluster-sized halos show a prominent infall velocity pattern. Galaxy-sized halos show an intermediate pattern with a sharper transition between the static region and the Hubble flow. We find that the former virial radius tends to underestimate the size of the region with zero mean radial velocity for halos with masses $10^{10}h^{-1}M_{\odot} < M_{vir} < 10^{14}h^{-1}M_{\odot}$ at $z = 0$. The mass inside this static region can be about a factor of 2 larger than the former virial mass, when the threshold defining the static radius is 5 per cent of the virial velocity $V_{vir} = \sqrt{GM_{vir}/R_{vir}}$. Lower values of the threshold ($\lesssim$ 1 per cent) may lower this factor. However, we observe a clear trend in the $M_{static}/M_{vir}$ versus $M_{vir}$ relation which remains unchanged with this threshold: for low-mass halos, this ratio is an increasing function of $M_{vir}$ due to the reduction in the outflow. On the other hand, high-mass halos show a larger infall for larger $M_{vir}$, making this ratio to decrease. The maximum occurs at $M_{vir} \simeq 5 \times 10^{12}h^{-1}M_{\odot}$, where the size of the static region is the largest in units of $R_{vir}$.

The redshift evolution of the $M_{static}$–$M_{vir}$ relation turns out to be very weakly redshift-dependent from $z = 2$ to 0 when appropriate variables are used. This dependence on the redshift is encoded as an evolving mass scale $M_0$ which indicates the approximate mass at which $M_{static} = M_{vir}$ in the declining part of the relation. We also derive the mass evolution of dark matter halos. The static mass of low-mass halos is nearly constant from $z = 0.5$ to 0. Galaxy-sized halos keep growing at present, but the reason here is not the decreasing background density of the expanding Universe. Instead, the relaxation of the matter in the surroundings of these halos is incorporating mass at even a higher rate than the unphysical growth of the virial mass. The same stands for clusters, although the static and virial mass are not very different at present.

The mass function of objects whose mass is defined in the way presented here resembles that of Press & Schechter in the range of mass we have studied, but only at $z = 0$. At higher redshifts, the static mass function deviates significantly from it. In any case, it seems clear that when the virial mass is used, the number density of dark matter halos of a given mass at $z = 0$ might be underestimated in the mass range $10^{10}h^{-1}M_{\odot} <$

$M_{vir} < 10^{14} h^{-1} M_{\odot}$.

### 4.1.2 The density profile of dark matter halos beyond the virial radius

In this part we have presented a simple approximation for the DM density profiles of halos with masses ranging from $10^{11.5}$ to $10^{15.0} h^{-1} M_{\odot}$, which is valid even beyond the virial radius up to $\sim 10 R_{vir}$. The expression we are suggesting here is $\rho(s) = \rho_s / cs(1+cs)^2 + (b_1/s + b_2/(s+1) + 1)\bar{\rho}$, where $s = r/R_{vir}$. This approximation is an extension of the NFW formula but includes two additional parameters. We have shown that these parameters are very well correlated with the virial mass, so that the density profile is effectively just a function of $M_{vir}$. This parametrization for the average density profile is accurate to within 10–15% in the range from $0.05 R_{vir}$ to $10 R_{vir}$. The halo-dark matter correlation function is related in a straightforward way to the average density profile. In this function, the transition from the one-halo term to the two-halo term is present before $10 R_{vir}$, however our approximation has turned out to be a reasonable description of the DM distribution even at these distances. At larger distances our model shows deviations around 20% in the range $10$–$30 R_{vir}$ just before entering the asymptotic regime. These deviations are caused by our additional $(r/R_{vir})^{-1}$ terms which improve the fit in the interesting region below $10 R_{vir}$ where the density is much higher. In any case, we must remark that our approximation implements the correct asymptotic behavior: the density profile tends to the asymptotic value of the mean matter density of the Universe. The cumulative mass inside a sphere of a given radius is underestimated by more than 50% at $10 R_{vir}$ by the NFW formula. On the contrary, it is much better approximated (to within 12%) when the NFW profile is modified by addition of the mean matter density, although with our model the difference with numerical density profiles is reduced even up to 1% in the range $1$–$9 R_{vir}$.

We have also presented an application for our approximation in the context of mass estimation using gravitational lensing effect. We derived expressions for tangential shear corresponding to different regions around the halo, which are in turn related to the different terms in our approximation. The contribution from the outer regions is small as compared to the contribution of the inner region, as expected. We calculated the difference between this tangential shear and the one derived from the NFW profile as a function of distance, showing that the inclusion of the outer regions produces a difference around 4%.

### 4.1.3 Dark matter annihilation and decay in the Local Universe

In this part we have presented Fermi maps of extragalactic $\gamma$-rays coming from DM annihilation and decay, which are made publicly available at the following URL: `http://www.clues-project.org/articles/darkmattermaps.html`. DM distribution is taken from a constrained cosmological simulation of the Local Universe Box160CR by the CLUES project. This distribution is then taken as an input for the Fermi observation simulation to obtain the all-sky distribution of $\gamma$-ray photon counts that would be measured by Fermi in a 5-year survey. Galactic and isotropic $\gamma$-ray diffuse backgrounds are also taken into account to get reliable results. This allows us to get S/N all-sky maps to estimate the possibility of detection of $\gamma$-rays from DM in such a survey using the Fermi satellite. We adopted two different particle physics models: a DM particle annihilating (decaying) primarily to a $b\bar{b}$ final state, and a DM model giving a good fit to the local positron fraction measured by PAMELA and the total electron spectrum measured by Fermi with annihilation (decay) to a $\mu^+\mu^-$ final state and a particle mass of 1.6 TeV. In the case of DM annihilation through the $b\bar{b}$ channel, we find that large objects with high galactic latitude present a good chance to be detected with a S/N ratio of around 3 for Virgo and Coma clusters. These values, as the whole analysis, assume no boost from DM halo substructures, which may enhance these values an order of magnitude or more (between 10 and 200, according to Kuhlen et al. 2008 and Springel et al. (2008)). Besides, we find that the S/N is not a strong function of the area of the analyzed region, which allows for considering large apertures without significant penalty in the results. This is especially interesting for Virgo cluster, being very close to us.

### 4.1.4 The correlation of UHECRs with nearby galaxies in the Local Volume

We have explored the possibility of the correlation of nearby galaxies from the catalog of Karachentsev et al. (2004) with ultra high energy cosmic ray events from the Pierre Auger Collaboration (The Pierre AUGER Collaboration: Abraham et al. 2008). The analysis of the data concludes a $2.6\sigma$ correlation between both samples. There are 5 out of 27 correlating events, while 0.5 should be expected on average in the case of isotropic flux. Due to the small number of correlating events, we cannot specify the scan parameters a priori, thus making our results sensitive to the negative impact of a posteriori anisotropy searches. The probability of chance correlation due to isotropic flux after penalizing for scans is $P_{chance} = 0.96 \times 10^{-2}$, rejecting the hypothesis of isotropy of arrival directions of UHECRs at 99% confidence level. For comparison, the same result before penalizing for scans is $\sim 1 \times 10^{-4}$ which is similar to the $\sim 2 \times 10^{-4}$ result (with scan parameters set a priori) from the correlation found by The Pierre Auger Collaboration (2008) with the AGNs in the Véron-Cetty catalog (Véron-Cetty & Véron 2006), and stronger than the revised value of $\sim 6 \times 10^{-3}$ when they include the new UHECR events from 1 September 2007 to 31 March 2009 (The Pierre Auger Collaboration: J. Abraham et al. 2009). The small number of correlating events with nearby galaxies might also point to the possibility of the absence of UHECR accelerators in our local environment, although there is no definitive answer yet.

## 4.2 Future Work

During my first postdoctoral position I plan to focus my research activities on different aspects of the nature of dark matter and dark energy. I plan to exploit the huge amounts of data from current large-scale galaxy surveys such as BOSS, from the complementary point of view of theory, by means of the analysis of state-of-the-art cosmological simulations. In addition, I will also continue my work on dark matter detectability studies. I will mention few other projects which are interesting for me to continue working in the future.

One of the most exciting science projects in the next years is the possible detection of dark matter. This detection has turned out to be elusive in both direct detection experiments (nuclear recoil experiments) and indirect detection experiments (gamma rays from dark matter annihilation). The allowed parameter space is still large, and Čerenkov telescopes and the Fermi satellite are already on the quest for the detection of an excess of these gamma rays. I believe it is therefore relevant to know in advance which sources are the best candidates to be studied. It is important as well to know how the predicted angular power spectrum from dark matter annihilation should be, and if there is any feature that could provide a clear signature of this effect (e.g. Hensley et al. 2009). Hence, I am planning to continue my work on the analysis of constrained simulations of the Local Universe, which have proven to be a very convenient tool in order to reproduce the observed large structures and complement the smaller scales with a distribution of dark matter halos following a given cosmological model. The combination of the maps shown in this Thesis with those from high-resolution simulations of a Milky Way halo (Kuhlen et al. 2008, Springel et al. (2008), see also Figure 4.1), makes us possible to produce an all-sky map of the expected signal from dark matter annihilation which is more complete and is potentially interesting for analysis of the anisotropic contribution of dark matter to the $\gamma$-ray sky.

I am also interested in improving my work on the properties of virialized regions of dark matter halos. Recent cosmological simulations have achieved an unprecedented level of resolution, and individual halos and their substructures are better resolved with at least 2 orders of magnitude better in number of particles as compared to my previous analyses. I want to explore the connection between the turnaround radius, the standard virial radius, and the radius of the sphere with no net infall or outflow for different halo masses and redshifts. Some collaborators have developed an interesting theoretical framework in which we can deal this issue, and try to learn more about which radius is best in terms of defining the halo mass and hence the mass accretion history, which has a potential impact on Halo Occupation Distribution methods connecting the assembly history of observed galaxies with that of cold dark matter halos in cosmological simulations. I can definitely contribute on a sharper connection using this analytical description.

The imaging data from SDSS Final Data Release has a huge potential for cosmological studies using photometric redshifts. I believe it is necessary to exploit this window of opportunity before large photometric surveys like DES, LSST or Pan-STARRS are able to get significant results, and make it clear in advance their possibilities and the limitations they need to overcome to complement the results from spectroscopic surveys like BOSS. In this context, it is my intention to continue working on the analysis of the baryonic acoustic feature in the matter power spectrum using photometric redshifts. The Luminous Red Galaxy (LRG) catalog, which comprises more than one million LRGs with constraints following the 2SLAQ selection (Cannon et al. 2006), doubles the statistics in the analysis of Padmanabhan et al. (2007), and the effect of cosmic variance in the survey area is reduced due to larger sky coverage (see Figure 4.2). Their redshift distributions have been estimated, and the theoretical angular power spectra for different sets of cosmological parameters have been computed. I am particularly interested in the analysis of the impact that different photometric redshift codes have in the final result, which is a matter of concern for the above mentioned surveys. The photometric pipeline has been modified over time as well, and hence I am interested in exploring its relevance on the values and uncertainties of the

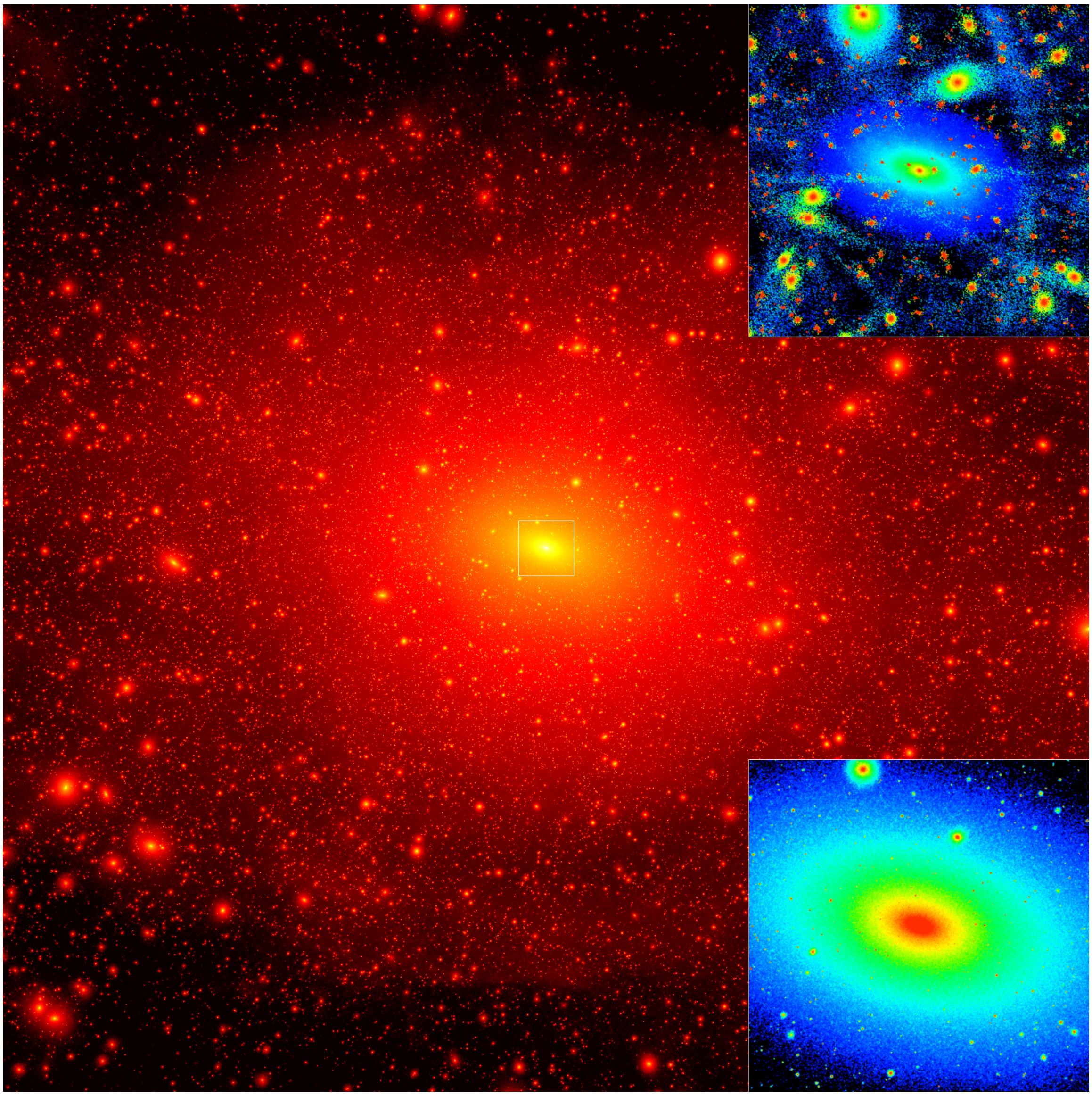

Figure 4.1 Projected dark matter density-square map of "Via Lactea II". An 800 kpc cube is shown. The insets focus on an inner 40 kpc cube, in local density (bottom), and in local phase space density (top). The Via Lactea II simulation has a mass resolution of 4,100 $M_\odot$ and a force resolution of 40 pc. The mass within 402 kpc (the radius enclosing 200 times the mean matter density) is $1.9 \times 10^{12} M_\odot$. Taken from Diemand et al. (2008).

derived cosmological parameters.

I am also interested on the use of statistics of large voids with radius larger than

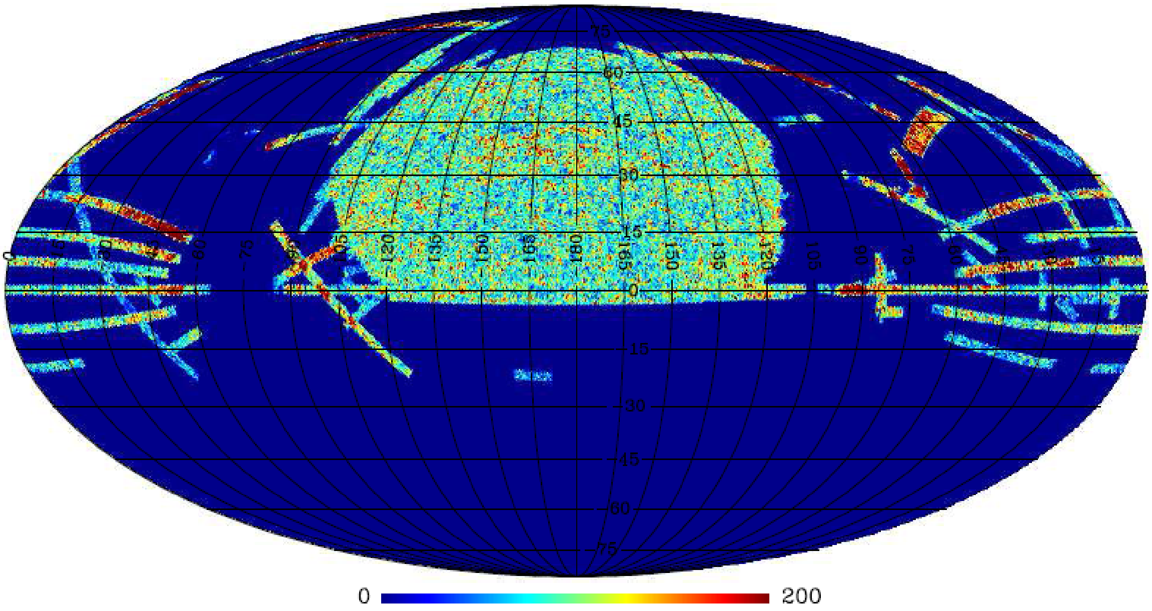

Figure 4.2 Number density of LRGs using SDSS-DR6 data release. Units are galaxies per square degree.

a few Mpc, in order to measure the equation of state of Dark Energy using Cosmological Simulations. This project, in collaboration with Juan Betancort, Santiago Patiri and Francisco Prada deserves particular attention as the statistics of large voids are not very sensitive to redshift distortions as compared to other cosmological probes. I believe it is interesting to assess how well this proxy of dark energy performs in terms of precision and accuracy, as large voids detected by large galaxy surveys might be used in the future as a complementary probe to type Ia Supernovae or Baryon Acoustic Oscillations.

The potential of 21-cm cosmology seems now out of question, and I am also willing to collaborate with Jose Alberto Rubiño and Francisco Prada on the use of kinetic Sunyaev-Zel'dovich signal and its cross-correlation with maps of the 21-cm line of neutral Hydrogen in order to constrain the primordial matter power spectrum. This approach, which might be possible using surveys by large arrays like SKA or ALMA, needs to be explored in terms of reliability and quality of the predictions by future measurements.

The so-called "missing satellites problem" is a longstanding issue which could be alleviated by future observations of very faint dwarf galaxies orbiting the Milky Way. However, there are some important theoretical aspects that may provide an explanation, at least for the absence of dwarf galaxies very close to the Milky Way. The analysis of survival of substructure in halo mergers is very important, in particular the influence of tidal shocking and the effect of disk shocking on the final abundance of substructures near the disk, which needs to be studied in detail. The statistics and final distribution of satellites after the merging of the parent halos, is relevant not only in the context of the missing satellites problem, but also in the context of gravitational lensing. The presence of a high-mass fraction of substructures around galaxies is able to produce anomalies on the flux ratios of multi-lensed images. Although there are recent studies on this topic (e.g. Xu et al. 2009), the effect of the disk has not been quantified yet.

## 4.3 Experience and skills

During my PhD I had the opportunity to work on both theoretical and observational projects. On the theoretical side, most of my results required extensive analysis of dark matter structures in Cosmological simulations. For instance, I have worked on very different topics like the orientation of the shape and spin of dark matter halos ("The Alignment of Dark Matter Halos with the Cosmic Web" by Patiri, Cuesta, Prada, Betancort-Rijo and Klypin, ApJL 652,75, 2006 and "Spin alignment of dark matter halos in the shells of the largest voids" by Cuesta, Betancort-Rijo, Gottlöber, Patiri, Yepes and Prada, MNRAS 385,867, 2008) and the properties of the virialized regions of dark matter halos ("The virialized mass of dark matter haloes" by Cuesta, Prada, Klypin and Moles, MNRAS 389,385, 2008), which is my most cited paper. These works made me become familiar with GADGET and ART snapshots, write subroutines to analyse the data, use visualization codes like Ifrit or PMViewer to help me with the analysis, and generate plots with IDL, GNUPlot or SuperMongo. Recently I have submitted a paper exploring the possibility of a local origin for Auger ultra-high energy cosmic rays ("The correlation of UHECRs with nearby galaxies in the Local Volume" by Cuesta and Prada, submitted to MNRAS), which has also been my first result in which I had to use parallel computing with OpenMP. I have been working on the analysis of the gamma-ray flux from dark matter annihilation in large structures using Constrained Simulations of the Local Universe ("Dark matter annihilation and decay in the Local Universe: CLUES from Fermi", submitted to Astrophysical Journal Letters), which requires efficient parallelization of the analysis code, and also uses HealPix as a tool to visualize the results. A last project I want to finish before I receive my PhD is related with the survival of dark matter substructures in halo mergers and the influence of the galaxy disk. This work is done in collaboration with Lars Hernquist and Elena D'Onghia at the Institute for Theory and Computation at Harvard-Smithsonian Center for Astrophysics. On the observational side, I worked with David Schlegel and Nikhil Padmanabhan on the detection of the acoustic peak using photometric redshifts from SDSS final data release. I could get familiar with tools like SDSS Skyserver, and make a photometric selection of Luminous Red Galaxies at different redshift ranges. Although this work has not been published yet, some of the results using the LRG catalog have already appeared in a publication (Hodge et al., AJ 138,900, 2009).

I have also participated in four important schools that provided me with some of the skills described above. The first one is the very successful Summerschool on Supercomputational Cosmology in Potsdam (speakers included: Anatoly Klypin, Andrey Kravtsov, Volker Springel, Nick Gnedin), where I learnt during four weeks the basic aspects of code parallelization (MPI/OpenMP), Cosmological Hydrodynamical simulations, Radiative Transfer, Visualization, and even I wrote my own Particle-Mesh code with cosmological initial conditions. Another important School is the Canary Islands Winterschool on CMB in Tenerife (with a large number of speakers, including Wayne Hu and Licia Verde), which introduced me to one of the most active fields in Modern Cosmology, and also had the opportunity of using standard cosmological packages like CAMB, CosmoMC, or HealPix. The two latest schools I have attended are the ASTROSIM and the UCSC-HIPACC Summer Schools on AstroComputing, in which we were trained on the underlying details of different numerical techniques in Astrophysical and Cosmological simulations, and the practical use of well-known software packages which implement these different techniques.

My scientific training and research activity has profited from my participation in many relevant conferences and workshops. To mention some of them, I attended to the "Galaxy Growth in a Dark Universe" in Heidelberg, "Next Generation of Computational Models of Baryonic Physics in Galaxy Formation" in Zurich, "Spectroscopy in Cosmology and Galaxy Evolution 2005-2010" in Granada (also as LOC), "Surveys and Simulations of Large-Scale Structure" in Berkeley, "ASTROSIM Meeting on Computational Cosmology" in Granada (also as LOC), "BOSS Target Selection Meeting" in Berkeley and Salt Lake City, "Santa Cruz Galaxy Workshop" in Santa Cruz, "Unveiling the mass: Extracting and Interpreting Galaxy Masses" in Kingston, "The local universe: from dwarf galaxies to galaxy clusters" in Jablonna, and "MultiDark Consolider Workshop" in Madrid and Santander.

Short-term visits to world-class research centers are an important experience for my PhD. In 2008, I spent four months in Lawrence Berkeley National Laboratory, working with David Schlegel, Nikhil Padmanabhan, and Martin White. For my 2009 visit, I'm currently staying in Harvard-Smithsonian Center for Astrophysics to work in a project with Lars Hernquist and Elena D'Onghia. The academic life in both research centers is scientifically motivating, thanks to the large number of seminars, group meetings, and journal clubs.

Finally, I want to mention that some results from my research would not have been possible without the use of large supercomputational facilities. I acknowledge the use of Columbia/Pleiades at NASA Ames, Odyssey at CfA, Riemann at Berkeley Lab, Erebos at AIP, and x4600 at CICA.

# Bibliography

Aalseth, C. E. et al. 2008, Physical Review Letters, 101, 251301

Abazajian, K., Fuller, G. M., & Patel, M. 2001, Phys. Rev. D, 64, 023501

Adriani, O. et al. 2009, Nature, 458, 607

Akerib, D. S. et al. 2003, Phys. Rev. D, 68, 082002

Alner, G. J. et al. 2007, Astroparticle Physics, 28, 287

Anderson, B., Kuhlen, M., Johnson, R., Madau, P., & Diemand, J. 2010, ArXiv e-prints

Angloher, G. et al. 2005, Astroparticle Physics, 23, 325

Bagla, J. S. 2005, Current Science, 88, 1088

Bailin, J., Kawata, D., Gibson, B. K., Steinmetz, M., Navarro, J. F., Brook, C. B., Gill, S. P. D., Ibata, R. A., Knebe, A., Lewis, G. F., & Okamoto, T. 2005, ApJ, 627, L17

Bailin, J. & Steinmetz, M. 2004, ApJ, 616, 27

—. 2005, ApJ, 627, 647

Baltz, E. A. 2004, ArXiv Astrophysics e-prints

Behnke, E. et al. 2008, Science, 319, 933

Bergström, L. 2000, Reports on Progress in Physics, 63, 793

Bernabei, R., Belli, P., Cappella, F., Cerulli, R., Dai, C. J., D'Angelo, A., He, H. L., Incicchitti, A., Kuang, H. H., Ma, J. M., Montecchia, F., Nozzoli, F., Prosperi, D., Sheng, X. D., & Ye, Z. P. 2008, European Physical Journal C, 167

Bertone, G., Hooper, D., & Silk, J. 2005, Phys. Rep., 405, 279

Betancort-Rijo, J. E. & Trujillo, I. 2009, ArXiv e-prints

Bond, J. R., Efstathiou, G., & Silk, J. 1980, Physical Review Letters, 45, 1980

Brunino, R., Trujillo, I., Pearce, F. R., & Thomas, P. A. 2007, MNRAS, 375, 184

Buckley, J., Byrum, K., Dingus, B., Falcone, A., Kaaret, P., Krawzcynski, H., Pohl, M., Vassiliev, V., & Williams, D. A. 2008, ArXiv e-prints

Bullock, J. S., Dekel, A., Kolatt, T. S., Kravtsov, A. V., Klypin, A. A., Porciani, C., & Primack, J. R. 2001, ApJ, 555, 240

Cannon, R. et al. 2006, MNRAS, 372, 425

Choi, K. & Roszkowski, L. 2005, in American Institute of Physics Conference Series, Vol. 805, Particles, Strings, and Cosmology, ed. K. Choi, J. E. Kim, & D. Son, 30–36

Colberg, J. M., Krughoff, K. S., & Connolly, A. J. 2005, MNRAS, 359, 272

Covi, L., Roszkowski, L., Ruiz de Austri, R., & Small, M. 2004, Journal of High Energy Physics, 6, 3

Croton, D. J., Springel, V., White, S. D. M., De Lucia, G., Frenk, C. S., Gao, L., Jenkins, A., Kauffmann, G., Navarro, J. F., & Yoshida, N. 2006, MNRAS, 365, 11

Cuesta, A. J., Betancort-Rijo, J. E., Gottlöber, S., Patiri, S. G., Yepes, G., & Prada, F. 2008a, MNRAS, 385, 867

Cuesta, A. J., Prada, F., Klypin, A., & Moles, M. 2008b, MNRAS, 389, 385

Dekel, A. & Birnboim, Y. 2006, MNRAS, 368, 2

Diemand, J., Kuhlen, M., Madau, P., Zemp, M., Moore, B., Potter, D., & Stadel, J. 2008, Nature, 454, 735

Dodelson, S. & Widrow, L. M. 1994, Physical Review Letters, 72, 17

Drukier, A. K., Freese, K., & Spergel, D. N. 1986, Phys. Rev. D, 33, 3495

Duda, G., Gelmini, G., Gondolo, P., Edsjö, J., & Silk, J. 2003, Phys. Rev. D, 67, 023505

EDELWEISS Collaboration: Benoit, A. et al. 2002, Physics Letters B, 545, 43

Feng, J. L., Rajaraman, A., & Takayama, F. 2003, Phys. Rev. D, 68, 063504

Flores, R. A. & Primack, J. R. 1994, ApJ, 427, L1

Fornasa, M., Pieri, L., Bertone, G., & Branchini, E. 2009, Phys. Rev. D, 80, 023518

George, M. R., Fabian, A. C., Sanders, J. S., Young, A. J., & Russell, H. R. 2009, MNRAS, 395, 657

Gondolo, P., Edsjö, J., Ullio, P., Bergström, L., Schelke, M., & Baltz, E. A. 2004, Journal of Cosmology and Astro-Particle Physics, 7, 8

Gorbunov, D., Tinyakov, P., Tkachev, I., & Troitsky, S. 2008, Soviet Journal of Experimental and Theoretical Physics Letters, 87, 461

Hayashi, E., Navarro, J. F., & Springel, V. 2007, MNRAS, 377, 50

Hensley, B. S., Siegal-Gaskins, J. M., & Pavlidou, V. 2009, ArXiv e-prints

Heymans, C., White, M., Heavens, A., Vale, C., & van Waerbeke, L. 2006, MNRAS, 371, 750

Hoffman, Y. & Ribak, E. 1991, ApJ, 380, L5

Hofmann, S., Schwarz, D. J., & Stöcker, H. 2001, Phys. Rev. D, 64, 083507

Holmberg, E. 1941, ApJ, 94, 385

Ibarra, A. & Tran, D. 2009, Journal of Cosmology and Astro-Particle Physics, 2, 21

Karachentsev, I. D., Karachentseva, V. E., Huchtmeier, W. K., & Makarov, D. I. 2004, AJ, 127, 2031

Kashti, T. & Waxman, E. 2008, Journal of Cosmology and Astro-Particle Physics, 5, 6

Kawasaki, M. & Moroi, T. 1995, Progress of Theoretical Physics, 93, 879

Klypin, A., Hoffman, Y., Kravtsov, A. V., & Gottlöber, S. 2003, ApJ, 596, 19

Klypin, A., Kravtsov, A. V., Valenzuela, O., & Prada, F. 1999, ApJ, 522, 82

Kravtsov, A. V., Gnedin, O. Y., & Klypin, A. A. 2004, ApJ, 609, 482

Kravtsov, A. V., Klypin, A., & Hoffman, Y. 2002, ApJ, 571, 563

Kuhlen, M., Diemand, J., & Madau, P. 2008, ApJ, 686, 262

Lee, H. S. et al. 2007, Physical Review Letters, 99, 091301

Mandelbaum, R., Seljak, U., & Hirata, C. M. 2008, Journal of Cosmology and Astro-Particle Physics, 8, 6

McGaugh, S. S. & de Blok, W. J. G. 1998, ApJ, 499, 41

Moore, B., Diemand, J., Madau, P., Zemp, M., & Stadel, J. 2006, MNRAS, 368, 563

Moore, B., Ghigna, S., Governato, F., Lake, G., Quinn, T., Stadel, J., & Tozzi, P. 1999, ApJ, 524, L19

Moskalenko, I. V., Stawarz, L., Porter, T. A., & Cheung, C. C. 2009, ApJ, 693, 1261

Navarro, J. F., Frenk, C. S., & White, S. D. M. 1996, ApJ, 462, 563

Padmanabhan, N. et al. 2007, MNRAS, 378, 852

Pagels, H. & Primack, J. R. 1982, Physical Review Letters, 48, 223

Patiri, S. G., Cuesta, A. J., Prada, F., Betancort-Rijo, J., & Klypin, A. 2006, ApJ, 652, L75

Pinzke, A., Pfrommer, C., & Bergström, L. 2009, Physical Review Letters, 103, 181302

Prada, F., Klypin, A. A., Simonneau, E., Betancort-Rijo, J., Patiri, S., Gottlöber, S., & Sanchez-Conde, M. A. 2006, ApJ, 645, 1001

Press, W. H. & Schechter, P. 1974, ApJ, 187, 425

Primack, J. R. 2003, Nuclear Physics B Proceedings Supplements, 124, 3

Profumo, S. & Jeltema, T. E. 2009, Journal of Cosmology and Astro-Particle Physics, 7, 20

Reiprich, T. H. & Böhringer, H. 2002, ApJ, 567, 716

Sanglard, V. et al. 2005, Phys. Rev. D, 71, 122002

Servant, G. & Tait, T. M. P. 2003, Nuclear Physics B, 650, 391

Sheth, R. K. & Tormen, G. 1999, MNRAS, 308, 119

Simon, J. D. & Geha, M. 2007, ApJ, 670, 313

Springel, V., White, S. D. M., Frenk, C. S., Navarro, J. F., Jenkins, A., Vogelsberger, M., Wang, J., Ludlow, A., & Helmi, A. 2008, Nature, 456, 73

Steffen, F. D. 2009, European Physical Journal C, 59, 557

Taoso, M., Bertone, G., & Masiero, A. 2008, Journal of Cosmology and Astro-Particle Physics, 3, 22

The CDMS Collaboration: Ahmed, Z. et al. 2009, ArXiv e-prints

The Dark Energy Survey Collaboration. 2005, ArXiv Astrophysics e-prints

The Pierre AUGER Collaboration: Abraham, J. et al. 2008, Astroparticle Physics, 29, 188

The Pierre Auger Collaboration: J. Abraham et al. 2009, ArXiv e-prints

The XENON100 Collaboration: Aprile, E. et al. 2010, ArXiv e-prints

Tinyakov, P. G. & Tkachev, I. I. 2001, Soviet Journal of Experimental and Theoretical Physics Letters, 74, 445

Tonry, J. L., Dressler, A., Blakeslee, J. P., Ajhar, E. A., Fletcher, A. B., Luppino, G. A., Metzger, M. R., & Moore, C. B. 2001, ApJ, 546, 681

Trujillo, I., Carretero, C., & Patiri, S. G. 2006, ApJ, 640, L111

Véron-Cetty, M. & Véron, P. 2006, A&A, 455, 773

Vitvitska, M., Klypin, A. A., Kravtsov, A. V., Wechsler, R. H., Primack, J. R., & Bullock, J. S. 2002, ApJ, 581, 799

Warp Collaboration et al. 2008, Astroparticle Physics, 28, 495

Wechsler, R. H., Bullock, J. S., Primack, J. R., Kravtsov, A. V., & Dekel, A. 2002, ApJ, 568, 52

Weinberg, M. D. & Katz, N. 2002, ApJ, 580, 627

Willick, J. A., Courteau, S., Faber, S. M., Burstein, D., Dekel, A., & Strauss, M. A. 1997, ApJS, 109, 333

Xu, D. D., Mao, S., Wang, J., Springel, V., Gao, L., White, S. D. M., Frenk, C. S., Jenkins, A., Li, G., & Navarro, J. F. 2009, MNRAS, 398, 1235

Yin, P., Yuan, Q., Liu, J., Zhang, J., Bi, X., Zhu, S., & Zhang, X. 2009, Phys. Rev. D, 79, 023512

Zaroubi, S., Hoffman, Y., Fisher, K. B., & Lahav, O. 1995, ApJ, 449, 446

## Appendix A

# Main publications

### A.1 The virialized mass of dark matter halos

Mon. Not. R. Astron. Soc. **389,** 385–397 (2008) doi:10.1111/j.1365-2966.2008.13590.x

# The virialized mass of dark matter haloes

A. J. Cuesta,[1★] F. Prada,[1] A. Klypin[2] and M. Moles[1]

[1] *Instituto de Astrofísica de Andalucía (CSIC), Camino Bajo de Huétor 50, E-18008 Granada, Spain*
[2] *Department of Astronomy, New Mexico State University, Las Cruces, NM 88001, USA*

Accepted 2008 June 12. Received 2008 June 12; in original form 2007 November 12

## ABSTRACT

Virial mass is used as an estimator for the mass of a dark matter halo. However, the commonly used constant overdensity criterion does not reflect the dynamical structure of haloes. Here, we analyse dark matter cosmological simulations in order to obtain properties of haloes of different masses focusing on the size of the region with zero mean radial velocity. Dark matter inside this region is stationary, and thus the mass of this region is a much better approximation for the virial mass. We call this mass the static mass to distinguish from the commonly used constant overdensity mass. We also study the relation of this static mass with the traditional virial mass, and we find that the matter inside galaxy-sized haloes ($M \approx 10^{12}\,\mathrm{M}_{\odot}$) is underestimated by the virial mass by nearly a factor of 2. At $z \approx 0$, the virial mass is close to the static mass for cluster-sized haloes ($M \approx 10^{14}\,\mathrm{M}_{\odot}$). The same pattern – large haloes having $M_{\mathrm{vir}} > M_{\mathrm{static}}$ – exists at all redshifts, but the transition mass $M_0 = M_{\mathrm{vir}} = M_{\mathrm{static}}$ decreases dramatically with increasing redshift: $M_0(z) \approx 3 \times 10^{15} h^{-1}\,\mathrm{M}_{\odot}\,(1+z)^{-8.9}$. When rescaled to the same $M_0$ haloes clearly demonstrate a self-similar behaviour, which in a statistical sense gives a relation between the static and virial mass. To our surprise, we find that the abundance of haloes with a given static mass, i.e. the static mass function, is very accurately fitted by the Press & Schechter approximation at $z = 0$, but this approximation breaks at higher redshifts $z \simeq 1$. Instead, the virial mass function is well fitted as usual by the Sheth & Tormen approximation even at $z \lesssim 2$. We find an explanation why the static radius can be two to three times larger as compared with the constant overdensity estimate. The traditional estimate is based on the top-hat model, which assumes a constant density and no rms velocities for the matter before it collapses into a halo. Those assumptions fail for small haloes, which find themselves in an environment where density is falling off well outside the virial radius and random velocities grow due to other haloes. Applying the non-stationary Jeans equation, we find that the role of the pressure gradients is significantly larger for small haloes. At some moment, it gets too large and stops the accretion.

**Key words:** methods: *N*-body simulations – galaxies: haloes – cosmology: theory – dark matter – large-scale structure of Universe.

## 1 INTRODUCTION

The currently accepted paradigm of hierarchical clustering (White & Rees 1978; Blumenthal et al. 1984) provides a picture of the assembly of dark matter haloes in which more massive haloes are formed through merging and accretion of smaller ones. This picture is supported, for example, by recent observations of ongoing mergers in clusters (e.g. van Dokkum et al. 1999; Rines, Finn & Vikhlinin 2007). The theoretical framework of the cold dark matter (CDM) has been proved successful in the description of the structure formation in the Universe from tiny fluctuations in the primordial density field [see Primack (2003) for a review]. This model has received support from many different observations, in particular of the gravitational lensing effect (Smith et al. 2001; Guzik & Seljak 2002; Kneib et al. 2003; Hoekstra, Yee & Gladders 2004; Sheldon et al. 2004; Mandelbaum et al. 2006), cosmic microwave background (Spergel et al. 2007), the abundance of clusters (Pierpaoli, Scott & White 2001; Gladders et al. 2007) and satellite dynamics (Zaritsky & White 1994; Prada et al. 2003). Cosmological simulations with ever increasing resolution play important role by making accurate predictions of different properties of dark matter haloes. Results of those simulations are used by other methods. For example, semi-analytical models of galaxy formation either have

---

★E-mail: ajcv@iaa.es

been incorporated into *N*-body simulations or use statistics such as halo mass function and merging trees, which were calibrated and tested using the simulations (e.g. Somerville & Primack 1999; Croton et al. 2006). The simulations reveal important information about the internal structure of dark matter haloes (e.g. Navarro et al. 1997; Bullock et al. 2001a; Taylor & Navarro 2001) which is reflecting their underlying dynamics.

Many results of simulations implicitly use some definition of what is the size and mass of a collapsed dark matter halo. The problem is that there is no well-defined boundary of a halo: density field is smooth around the halo. The common prescription for this boundary (and hence the mass belonging to the halo) is defined through the spherical collapse model (Gunn & Gott 1972; Gunn 1977). The size of the halo at redshift $z$ is given by the half of the radius of the spherical shell at turnaround which is collapsing at that redshift. This is the *virial radius*. Thus, it is very common to measure the mass of haloes in cosmological simulations taking the particles inside a sphere of fixed spherical overdensity or to take those particles that are connected by an inter-particle separation below a given value (the friends-of-friends algorithm). We note that there is little justification for using the top-hat collapse model. Haloes do not collapse from perfect spherical homogeneous distribution. The environment of haloes is typically very non-spherical with most of accretion happening from few elongated filaments. The random velocities of the accreted matter also cannot be neglected. As the fluctuations collapse, the dark matter, which is being accreted, increases its rms velocities. This effective pressure should affect the accretion rate. The only motivation for using the top-hat model comes from simulations. Indeed, early simulations indicated that the radius of overdensity 178 is close to the virial radius (Cole & Lacey 1996): 'the radius $r_{178}$ approximately demarcates the inner regions of haloes at $r \lesssim r_{178}$ which are in approximate dynamical equilibrium from the outer regions at $r \gtrsim r_{178}$ which are still infalling'. Thus, the radius of overdensity 200 (≈178) became the virial radius. The reason why this was a good approximation is simply coincidental: the early simulations were mostly done for cluster-sized haloes and, indeed, for those masses the virial radius is close to the radius of overdensity 200. The early models were flat models without the cosmological constant. Models with the cosmological constant have produced significant confusion in the community. The top-hat model must be modified to incorporate the changes due to the different rate of expansion and due to the different rate of growth of perturbations (see Primack 1997). That path produced the so-called virial radius, which for the standard cosmological model gives the radius of overdensity relative to matter of about 340 (Bullock et al. 2001b). Still, a large group of cosmologists uses the old overdensity 200 relative to the critical density even for the models with the cosmological constant.

In this paper, we cast some light on this subject by searching for a physical extent of dark matter haloes, which is related to the physical processes that occur around collapsed structures. Prada et al. (2006) provided first results, which indicated that spherically averaged, mean radial velocity profiles show an inner region in which there is no net infall or outflow. The size of this region in virial units is mass-dependent: for galactic-sized haloes, it may even reach three times the virial radius. We use this result to study the properties of the mass inside this region and, in particular, to determine the redshift evolution of such mass. Recent effort (Wechsler et al. 2002; Zhao et al. 2003) has been devoted to the analysis of the evolution of virial mass inside dark matter haloes, sometimes referred to as the mass accretion history. However, the picture presented in these works has been recently put into question. The analysis of the mass inside a fixed physical radius has revealed that galaxy-sized haloes experience unphysical growth of their virial mass (Diemand, Kuhlen & Madau 2007). The mean background density decreases as the Universe expands, making the virial radius to increase even in the case of no accretion or mergers. This is clearly an artefact of the definition. Other works realized this issue, for example, the evolution of the spin parameter when the matter inside a fixed radius is taken into account differs from that when using the evolving $R_{\rm vir}$ instead (D'Onghia & Navarro 2007). On the other hand, there is another effect apart from accretion and merging, which has not been taken into account: haloes may also grow via relaxation of the surrounding regions near them. This is an important effect as it is a reflection of the dynamical processes which are turning non-virialized mass in the outskirts of a halo into the mass associated to it. Moreover, the long-term evolution of dark matter haloes shows an interesting feature for ΛCDM cosmologies: their mass turns out to converge to an asymptotic value which depends on the definition of mass, as pointed out by Busha et al. (2005). Thus, it is desirable that the mass of a halo is measured using virialization-based criteria (see Macciò, Murante & Bonometto 2003 for an interesting approach), instead of using boundaries of a given overdensity.

The interest of the measurement of the physical mass associated to dark matter haloes is not only theoretical. Indeed, it may have a great impact on the number of collapsed objects in a given range of mass, i.e. the mass function (White 2001). Besides, it is of great importance for the process of formation and evolution of galaxies, and, hence, it is relevant for the results obtained from semi-analytical modelling of galaxy formation (e.g. Croton et al. 2006) to predict the main properties of observed galaxies. Thus, it turns out to be mandatory to bring attention on the mass belonging to a halo, if accurate predictions of the physics behind galaxies from cosmological simulations are to be drawn.

This paper is organized as follows. In Section 2, we describe the set of cosmological simulations used in our analysis and the properties of the halo samples. In Section 3, we present the definition of static mass and how it is related to objects of different sizes. A brief analysis of equilibrium in this context is presented in Section 4. The scaling properties of the static to virial mass relation with redshift are shown in Section 5, together with a simple model derived from this scaling relation. We obtain the static mass function and compare it with analytical models in Section 6. In Section 7, we present the evolution of the static mass tracking the halo progenitors. We discuss our results in Section 8 and present our conclusions in Section 9.

## 2 *N*-BODY SIMULATIONS AND HALO SELECTION

We use four different high-resolution ΛCDM simulations, which were run using the Adaptive Refinement Tree (ART) code (Kravtsov, Klypin & Khokhlov 1997). These cosmological simulations are selected in order to span a broad range of halo masses with very good statistics of the number of haloes. The values of the cosmological parameters are $\Omega_0 = 0.3$, $\Omega_{\rm bar} = 0.045$, $\Omega_\Lambda = 0.7$, $\sigma_8 = 0.9$ and $h = 0.7$. Main simulation parameters may be found in Table 1.

The resolution and the halo mass range covered by these simulations allow us to perform a detailed analysis of the properties of dark matter haloes with very good statistics. Dark matter haloes are identified using the Bound Density Maxima (BDM) halo finder (Klypin et al. 1999). In order to resolve the inner structure and dynamics of dark matter haloes, only haloes which enclose more than

**Table 1.** The main parameters of the cosmological simulations.

| | Box80S | Box80G | Box120 | Box250c |
|---|---|---|---|---|
| Box size ($h^{-1}$ *Mpc*) | 80 | 80 | 120 | 250 |
| Mass of a particle ($h^{-1}$ M$_\odot$) | $4.91 \times 10^6$ | $3.18 \times 10^8$ | $1.07 \times 10^9$ | $9.67 \times 10^9$ |
| Spatial resolution ($h^{-1}$kpc) | 0.52 | 1.2 | 1.8 | 7.6 |
| Number of particles | 159.8M | $512^3$ | $512^3$ | $512^3$ |

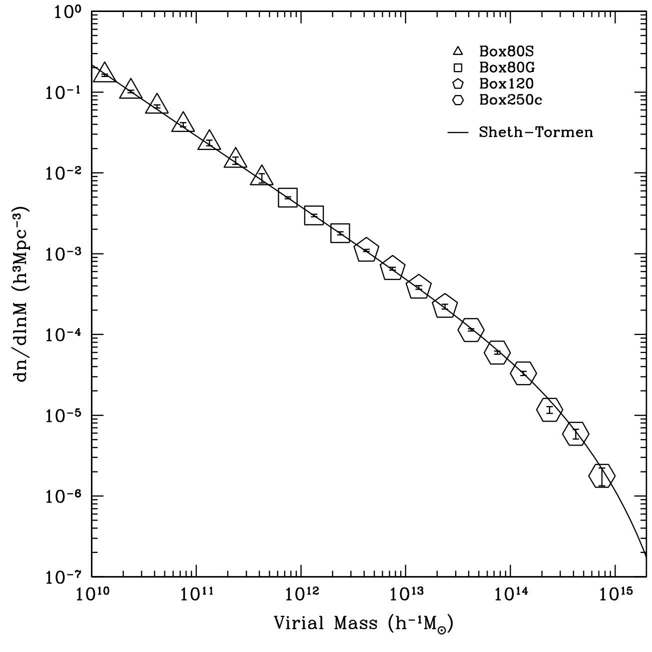

**Figure 1.** The virial mass function using cosmological simulations listed in Table 1. The error bars inside the symbols represent the Poissonian error. The analytical mass function of Sheth and Tormen provides a very good fit for our data.

2000 particles inside the virial radius at $z = 0$ were chosen. We take into account all the mass (both bound and unbound particles) inside the virial radius of the halo. This radius is defined here as the radius of the sphere enclosing an overdensity given by Bryan & Norman (1998), i.e.

$$\Delta_c = 18\pi^2 + 82x - 39x^2 \quad x \equiv \Omega(z) - 1. \qquad (1)$$

In Fig. 1, we plot the virial mass function of dark matter haloes over five orders of magnitude. Here, the error bars represent the Poissonian error, showing very good statistics for all except for the highest mass bins. The different symbols show which simulation is used for each mass bin. The relation between mass bins and simulations depends on the fact that we only choose haloes enclosing more than 2000 particles inside the virial radius at $z = 0$. If two different simulations pass this constraint, then we choose the one with highest statistics. As previously shown (e.g. Sheth, Mo & Tormen 2001), the virial mass function in cosmological simulations is well fitted by the Sheth and Tormen function if $a \simeq 0.707$ (Sheth & Tormen 1999, hereafter ST) in the mass range under study. These four simulations, as mentioned above, cover a broad range in mass, from $10^{10}h^{-1}$ M$_\odot$ low-mass haloes to cluster-sized haloes with nearly $10^{15}h^{-1}$ M$_\odot$.

In order to select a sample of haloes for our analysis, we take all the haloes whose centres are not inside the virial radius of a larger halo (hereafter *distinct* haloes). This criterion reduces strong environmental effects: internal dynamics of haloes are less affected by massive neighbours.

## 3 STATIC MASS OF DARK MATTER HALOES

In this section, we introduce and motivate our definition of static mass. When using cosmological simulations, it is common to define the mass belonging to dark matter haloes in terms of a given spherical overdensity or inter-particle distance. However, so far, it is computationally challenging to define a real virial mass, i.e. the mass which is showing features of statistical equilibrium, for a large number of haloes. This has to be kept in mind if accurate results are to be found, although there is some kind of agreement between different definitions based on overdensity (White 2001). A particular case in which an overdensity-based definition may fail in providing a faithful description of dark matter haloes is the mass accretion history. Fig. 2 clearly demonstrates this. Here, we show the evolution of the density profile of a very high resolution (more than two million particles inside the virial radius) galaxy-sized halo from our cosmological simulation Box20, which has a better spatial (0.152 $h^{-1}$ kpc) and mass resolution ($6.14 \times 10^5 h^{-1}$ M$_\odot$, using 8.98M particles) with the same cosmological parameters as the simulations mentioned above. It is clear that the density profile does not evolve in a significant way from $z = 1$ to 0, as already pointed out by

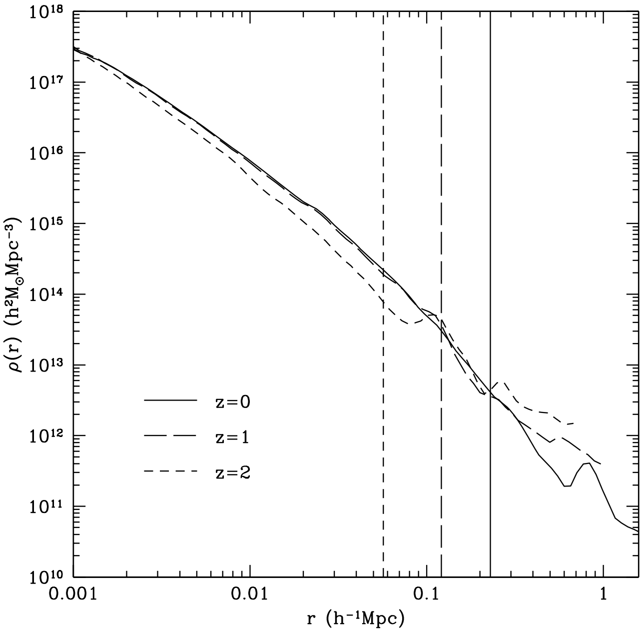

**Figure 2.** Evolution of the density profile for a galactic-sized halo. The vertical lines mark the virial radius at each redshift. The change in the virial radius by a factor of 2 since redshift $z = 1$ gives a false impression of a strong evolution of the halo. Yet, there was very little evolution in the physical density in this halo since $z = 1$.

Diemand et al. (2007). None the less, the virial radius varies by about a factor of 2 as marked with vertical lines in Fig. 2. This growth of the virial radius is obviously an artefact of overdensity-based mass that does not reflect the real accretion of mass in the halo but the evolution of the mean matter density of the Universe, $\rho_{\rm m}(z) = (1+z)^3\rho_{\rm m,0}$.

Therefore, a detailed analysis of the structure of dark matter haloes may prove to be valuable in the search for the virialized regions of the haloes. For example, the study of the radial phase-space diagram provides some insights on halo structure. In Fig. 3, we show the radial velocity pattern of dark matter particles inside haloes of different masses taken from our simulation boxes. The top, middle and bottom panels are for a low-mass halo with $M_{\rm vir} = 2.9 \times 10^{11} h^{-1}\,{\rm M}_{\odot}$, a galactic-sized halo of mass $M_{\rm vir} = 1.4 \times 10^{12} h^{-1}\,{\rm M}_{\odot}$ and a cluster-sized halo with $M_{\rm vir} = 1.3 \times 10^{15}\ h^{-1}\,{\rm M}_{\odot}$, respectively. About 20 per cent randomly selected particles are shown for the low-mass halo and the galactic-sized halo, and 100 per cent for the cluster-sized halo. The structure of haloes in phase space is already discussed in Busha et al. (2005). In the inner parts, the average radial velocities are zero. Around the virial radius, there are some signs of infall or outflow, as it will be discussed below. At large distances, the Hubble flow is the most remarkable feature, except for some spikes showing the presence of neighbouring haloes. This plot shows a substantial difference in the structure of dark matter haloes associated with different masses. Although the transition from the inner region to the Hubble flow shows monotonically increasing radial velocity in the low-mass and the galactic-sized halo, the situation is different for clusters where there is a significant tail in the velocity distribution with large negative velocities (also see fig. 3 in Busha et al. 2003). This infall is altering the equilibrium of the particle distribution in the halo, and hence that region is no longer virialized, as already pointed out by Macciò et al. (2003). This suggests a natural choice for the boundary of a dark matter halo, which is defined by the innermost radius in which mean radial velocity is equal to zero. In practice, we use a small threshold in order to reduce the effects of the statistical noise. The deviation of the spherically averaged radial velocity profile from zero is a signature of non-virialization. For this reason, the zero-velocity radius is defining the mass, which is associated to a halo. This radius will be hereafter referred to as the static radius, and the mass inside a sphere of this radius as the static mass of the halo.

Although the threshold in the mean radial velocity is somewhat arbitrary and may affect our results, we take advantage of the good statistics in our simulation boxes to reduce this threshold to only 5 per cent of the virial velocity $V_{\rm vir} \equiv \sqrt{GM_{\rm vir}/R_{\rm vir}}$ of the halo. This allows us to get acceptable signal-to-noise ratios in the average profiles for all the mass ranges under study, without considerable overestimation of the virialized region.

Individual haloes usually have similar radial profiles at a given range of mass. Thus, the analysis of the average halo profiles is reasonable. The radial profile of a given physical quantity is then obtained by getting the median value of this quantity over all the haloes in the sample for a given mass bin. This is done for every radial bin, which are logarithmically separated for convenience. For the innermost radial bins, there is an additional constraint: the median profile is representative of the halo sample at a radial distance $R$ only if a large fraction (about 80 per cent) of the haloes in this sample contain at least 200 particles (Klypin et al. 2001) inside the sphere of radius $R$.

As mentioned above, there is an important mass dependence in the radial velocity distribution of the haloes. The analysis of the median radial velocity profile reveals a prominent infall for cluster-sized haloes and a notable outflow for low-mass haloes, whereas galaxy-sized haloes show a balanced situation between infall and outflow (see Prada et al. 2006 for more details). This is represented in Fig. 4. This general trend is dividing the total sample in two sets of haloes: those which are exceeding the threshold from below (infall) and those which exceed it from above (outflow).

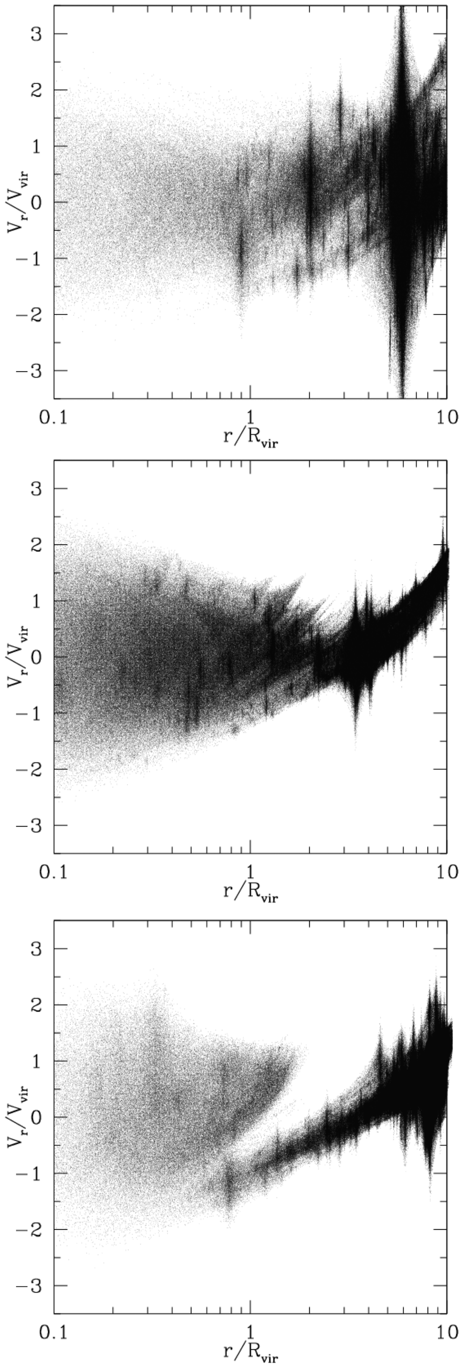

**Figure 3.** Phase-space diagram for the particles in dark matter haloes. The top panel represents a low-mass halo ($M_{\rm vir} = 2.9 \times 10^{11} h^{-1}\,{\rm M}_{\odot}$) and the central panel displays a galactic-sized halo ($M_{\rm vir} = 1.4 \times 10^{12} h^{-1}\,{\rm M}_{\odot}$), whereas the bottom panel shows a cluster-sized halo ($M_{\rm vir} = 1.3 \times 10^{15} h^{-1}\,{\rm M}_{\odot}$). Clusters clearly show strong infall pattern around the virial radius, whereas this is not observed in smaller sized haloes.

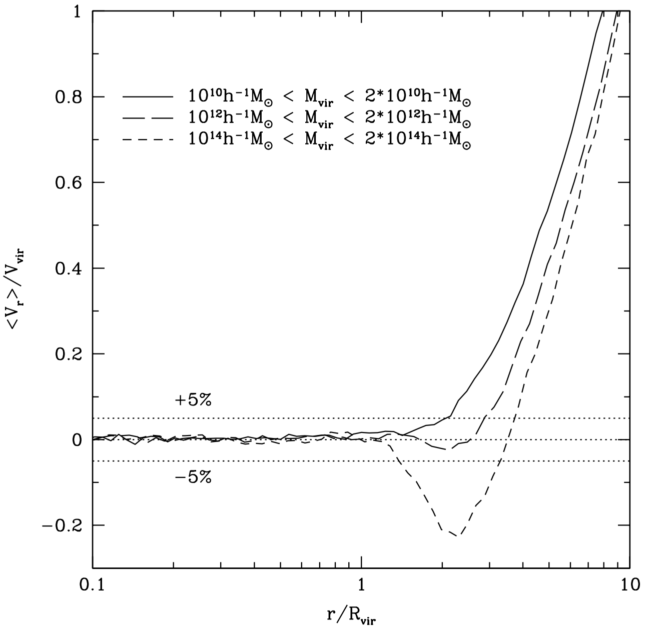

**Figure 4.** Mean radial velocity for three different mass bins. The profiles were obtained by averaging over hundreds of distinct haloes on each mass bin. In dotted lines is shown the selected threshold delimiting the static region (5 per cent of the virial velocity). Cluster-sized haloes display a region with strong infall (dashed line). In contrast, low-mass haloes (solid line) and galactic haloes (long-dashed line) do not show infall at all but a small outflow preceding the Hubble flow.

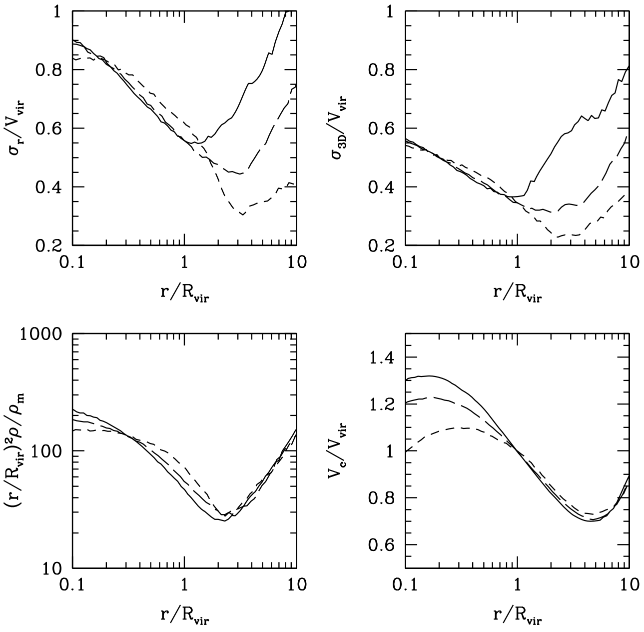

**Figure 5.** Median profiles for the same halo mass bins as in Fig. 4. These profiles show how the behaviour of haloes depends on the halo mass. Top left panel: radial velocity dispersion. Top right panel: 3D velocity dispersion. Bottom left: density profile. Bottom right: circular velocity profile. The different line styles represent the same mass bins as in Fig. 4.

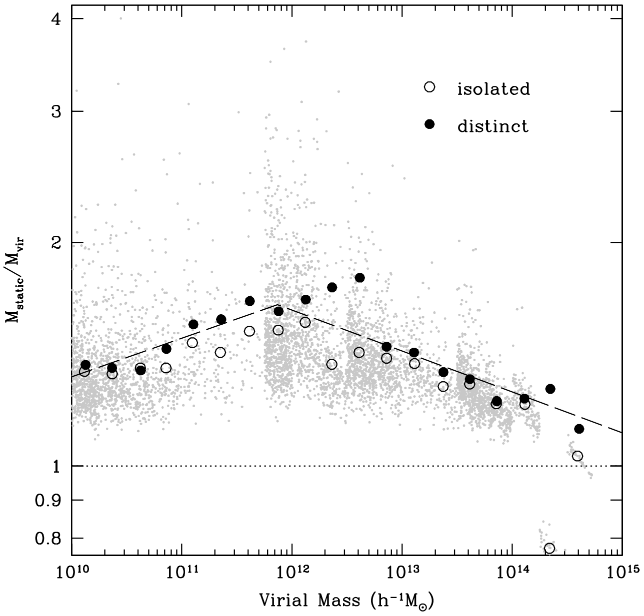

**Figure 6.** The halo static mass – virial mass relation at $z = 0$. Dots show the relation for individual isolated haloes. Circles show this relation for isolated (open) and distinct (solid) median haloes at different mass bins. The ratio $M_{\rm static}/M_{\rm vir}$ increases due to reduced outflow up to the first appearance of infall, making this ratio decrease. The dashed line shows the approximation to two power laws connected where they cross each other; the parameters are those listed in Table 2.

Other properties of haloes also depend on halo mass. Fig. 5 shows some of them for the same mass bins as in Fig. 4. Upper panels represent the radial and 3D velocity dispersions [see also Wojtak et al. (2005) for an extensive analysis of radial velocity moments in massive haloes and Wojtak et al. (2008) for a phenomenological model which describes these]. The radial velocity dispersion for haloes with higher concentration has a larger inner value in terms of the virial velocity (Łokas & Mamon 2001). In the outer region, there is a local minimum, which radius and magnitude also show dependence on halo mass. In the bottom left panel, we show the median density profiles multiplied by $(r/R_{\rm vir})^2$ in order to make more clear any change in their logarithmic slope. At smaller distances $r < 0.1R_{\rm vir}$ (not shown in the figure), curves start to decline because the slope is getting smaller than $-2$. It is also notable that beyond 1–2 $R_{\rm vir}$, the density profiles do not decrease as $r^{-3}$ as for the Navarro, Frenk & White (NFW) density profile. For a detailed parametrization far beyond $R_{\rm vir}$, see Tavío et al. (in preparation). Finally, the bottom right panel shows the radial profile of the circular velocity, which by definition coincides with the virial velocity at $r = R_{\rm vir}$. The maximum of this profile is again mass-dependent, as it is somewhat related to the inner concentration.

The analysis of the mean radial velocity profiles over all masses (similar to those in Fig. 4) allows us to draw the relation between the static mass and the virial mass. This relation is shown in Fig. 6. Solid circles represent the $M_{\rm static}/M_{\rm vir}$ ratio for the median profile built from all distinct haloes, while open circles show the same ratio for the median profile of isolated haloes. The isolation criteria here are that the nearest neighbour of a halo is farther than three times the sum of the virial radii of both haloes. The uncertainty on this relation is difficult to estimate, as static masses could not be obtained for individual haloes. Our radial velocity profiles are too noisy (because of infalling and outflowing subhaloes) to distinguish the static region, and hence we stacked these profiles in order to analyse them. Thus, we calculate the halo-to-halo variation of this relation by measuring for each halo the mass inside the median

**Table 2.** Parameters of the approximation of the $M_{\rm static}/M_{\rm vir}$ ratio as a function of the virial mass.

| Region | Mass range | $\alpha$ | $\beta$ |
|---|---|---|---|
| 1 | $1.0 \times 10^{10} \leq M_{\rm vir}/h^{-1}\,{\rm M}_{\odot} \leq 7.4 \times 10^{11}$ | $\alpha_1 = +0.052 \pm 0.005$ | $\beta_1 = -0.40 \pm 0.05$ |
| 2 | $7.4 \times 10^{11} \leq M_{\rm vir}/h^{-1}\,{\rm M}_{\odot} \leq 5.0 \times 10^{14}$ | $\alpha_2 = -0.055 \pm 0.009$ | $\beta_2 = +0.87 \pm 0.12$ |

static radius. In this way, we obtain the $M_{\rm static}/M_{\rm vir}$ ratio for isolated haloes, shown in this figure as dots. The distribution of this ratio has a long tail to large values of this ratio due to surrounding neighbours, which are inside the median static radius. Again, these unrealistic values of $M_{\rm static}/M_{\rm vir}$ are due to the lack of a reliable determination of the static mass for individual haloes. There are no large differences between distinct and isolated haloes (except for those bins with poor statistics), so we take the $M_{\rm static}/M_{\rm vir}$ relation for distinct haloes, as the isolation criteria reduce their number drastically.

The dependence of this relation with the virial mass is straightforward. The outflow in low-mass haloes is less prominent with increasing mass, and hence the ratio $M_{\rm static}/M_{\rm vir}$ increases. A drop in this ratio occurs due to the transition to infall around $5 \times 10^{12}$ $h^{-1}\,{\rm M}_{\odot}$, and then it decreases due to higher infall with increasing virial mass. As it may be readily checked in Fig. 4, the lowest mass in which infall takes place is very threshold-dependent. To alleviate this, we assume that this relation is a continuous function which is fairly well approximated by two power laws:

$$\log_{10}(M_{\rm static}/M_{\rm vir}) = \begin{cases} \alpha_1 \log_{10}(M_{\rm vir}) + \beta_1 & \text{region 1} \\ \alpha_2 \log_{10}(M_{\rm vir}) + \beta_2 & \text{region 2,} \end{cases} \qquad (2)$$

where the mass is measured in units of $h^{-1}\,{\rm M}_{\odot}$. In Table 2, we list the values of the best-fitting parameters for $\alpha$ and $\beta$.

Interestingly, concentration of individual dark matter haloes decreases with static mass, in a similar way as it does with $M_{\rm vir}$. This makes the ratio $M_{\rm static}/M_{\rm vir}$ non-sensitive to halo concentration. Again, the static mass of individual haloes is estimated by measuring the mass inside their median static radius corresponding to its virial mass bin as in Fig. 6. The $M_{\rm static}(c)$ dependence is similar to $M_{\rm vir}(c)$ because $M_{\rm static}$ is close to $M_{\rm vir}$ (the difference is less than a factor of 2 in the mass range under study). Hence, the correlations involving the logarithm of the mass can only change their zero-point by $\sim$0.3 if we use the static mass instead of the virial mass. The values of the parameter $\alpha$ in Table 2 suggest that the slope would also present a small change of $\sim$5 per cent which might be important in some correlations. In the particular case of the correlation between halo mass and halo concentration (e.g. Macciò et al. 2007), the replacement of virial mass to static mass introduces a modification which is small enough so that this correlation remains almost entirely unaffected.

## 4 ANALYSIS OF EQUILIBRIUM

Haloes of different mass clearly show very different structure. At small ($r < R_{\rm vir}$) distances, the main differences are due to the differences in concentration. The haloes inside the virial radius are nearly in equilibrium (with possible exception of the most massive clusters). At larger distances, the differences are more complicated. Fig. 4 and similar results in Prada et al. (2006) demonstrate that haloes of small mass have static radius a few times larger than the formal virial radius. To make things even more complicated, the small haloes do not have an infall region. We can try to somewhat clarify the situation by applying the Jeans equation. In order to do this, we first need to measure the velocity anisotropy $\beta = 1 - \sigma_t^2/(2\sigma_r^2)$.

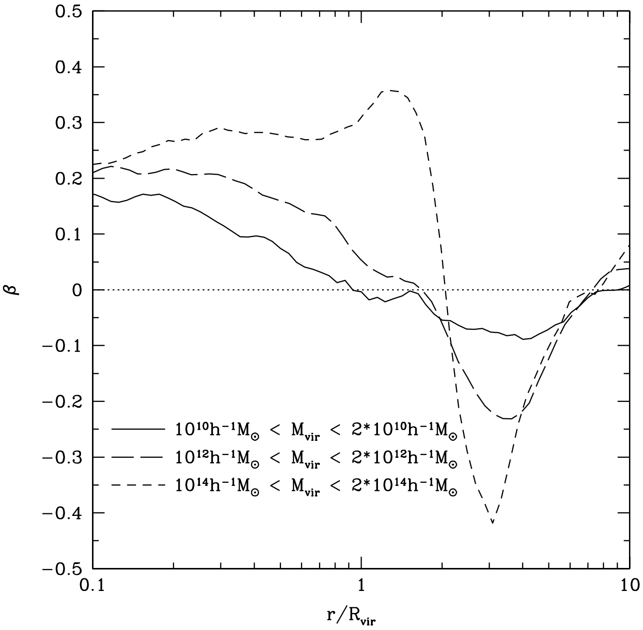

**Figure 7.** Velocity anisotropy profile for the same mass bins as in Figs 4 and 5. In the inner region, the velocity anisotropy is preferentially radial. It changes to nearly isotropic in the outer regions with $R \approx (1 - 2)R_{\rm vir}$ followed by preferentially tangential at larger distances.

In Fig. 7, we show the median radial profile for $\beta$ for the same mass bins as in Fig. 4. Inside the virial radius $\beta$ is positive. Cluster-mass haloes have a familiar behaviour: $\beta$ increases with distance and gets to $\beta \approx 0.3$–0.4 around the virial radius. The real surprise came for the small galaxy-sized haloes. After initial increase, $\beta$ reaches maximum $\beta \approx 0.2$ and then declines with distance. It goes almost to zero at $r = (1 - 2)R_{\rm vir}$. At larger distances, the velocity anisotropy is negative and approaches zero at very large distances. We should note that $\beta = 0$ does not mean nearly circular orbits. Orbits of dark matter particles or satellites are typically very elongated even for isotropic velocity ellipsoid: axial ratios are typically 1:4–1:5 for $\beta = 0$ and the NFW profile.

Why do small haloes not have a turn-around radius followed by an infall region? The top-hat model of non-linear evolution is supposed to provide a reasonable description of what happens at large distances. Yet, it seems to be failing qualitatively for galaxy-sized haloes, which do not have infall region and even show an outflow. Haloes are complex systems: they are not spherically symmetric and may have substantial substructure. Still, the spherically symmetric non-stationary Jeans equation is an undeniably significant improvement as compared with the top-hat model. The Jeans equation provides a simple approximation for the haloes. Assuming spherical symmetry, the non-stationary Jeans equation can be

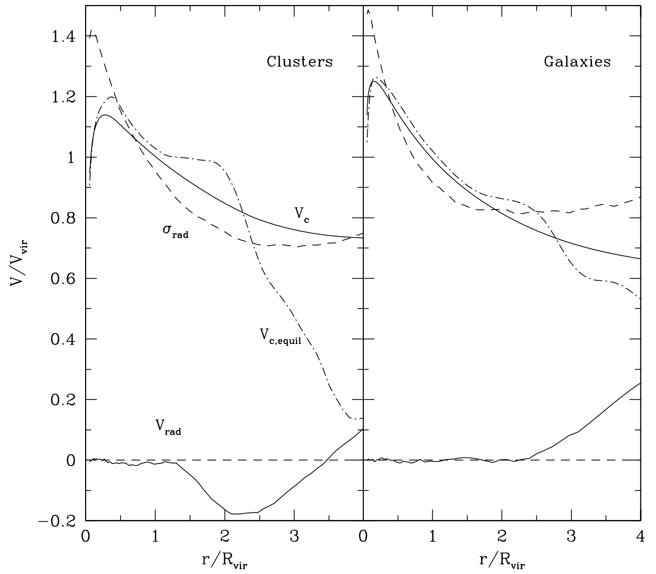

**Figure 8.** Different velocity components for cluster-sized haloes (left-hand panel; $M_{\rm vir} \approx 2 \times 10^{14} h^{-1}\,{\rm M}_{\odot}$) and galaxy-sized haloes (right-hand panel; $M_{\rm vir} \approx 10^{12} h^{-1}\,{\rm M}_{\odot}$). The dot–dashed curves show the predictions $v_{\rm c,equil}$ of stationary Jeans equation (4). The stationary solution closely follows the real circular velocity up to $(2-2.5)R_{\rm vir}$ for galaxy-sized haloes. It falls below $v_{\rm c}$ at larger distances indicating significant non-stationary effects. The situation with clusters is different: the central virialized region is surrounded by a shell where virialization is happening ($v_{\rm c,equil} > v_{\rm c}$) followed by the region where $v_{\rm c,equil} < v_{\rm c}$ (see text for details).

written in the following form:

$$\frac{r}{\rho}\frac{\mathrm{d}(\rho v_{\rm r})}{\mathrm{d}t} + \sigma_{\rm r}^2\left[\frac{\mathrm{d}\ln(\rho\sigma_{\rm r}^2)}{\mathrm{d}\ln r} + 2\beta\right] = v_{\rm c}^2(r), \tag{3}$$

where $v_{\rm r}$ is the radial velocity and $v_{\rm c}^2(r) = GM(<r)/r$. When the rms velocities $\sigma_{\rm r}$ are negligible, equation (3) is the normal equation of motion. Assuming a small initial perturbation and the Hubble flow, we recover the top-hat model. Yet, the haloes do not have small rms velocities even well outside the formal virial radius. Fig. 8 illustrates the point. Even for the massive haloes, which typically dominate their environment, the rms velocities are relatively large. The effect is even stronger for less massive haloes. Another important component is the density gradient. Fig. 2 shows that the density gradients exist at very large distances: at many virial radii. At $z = 2$, the density was on average steeply declining well outside its virial radius.

The left-hand side of the Jeans equation has two terms. The first term describes non-stationary effects. It is the dominant term at early stages of evolution. The second term is related with the pressure gradient. It dominates in the virial part of the halo. If the system is stationary, the second term must be equal to the square of the circular velocity in the right-hand side of the Jeans equation. We can call this term the equilibrium circular velocity:

$$v_{\rm c,equil}^2 = \sigma_{\rm r}^2\left[\frac{\mathrm{d}\ln(\rho\sigma_{\rm r}^2)}{\mathrm{d}\ln r} + 2\beta\right]. \tag{4}$$

We plot $v_{\rm c,equil}$ in Fig. 8. For galaxy-sized haloes (right-hand panel) in the inner region $r < (2-2.5)R_{\rm vir}$, the term is very close to the right-hand side of the Jeans equation, which means that the system is nearly in virial equilibrium. At larger distances, the term falls short of the circular velocity: the halo is out of equilibrium.

For clusters (left-hand panel), the equilibrium is only in the central $r < R_{\rm vir}$ region. Just outside of this region at $r = (1-2)R_{\rm vir}$, the equilibrium term $v_{\rm c,equil}$ is substantially above the circular velocity $v_{\rm c}$. At the same range of radii, the infall velocity is clearly detected. The upturn in the $v_{\rm c,equil}$ is the cumulative result of two effects: increase in the slope of the density profile and substantial change in the velocity anisotropy. The same trend exists in the case of small haloes, but it is barely visible. At larger distances $r > 2R_{\rm vir}$, the equilibrium term $v_{\rm c,equil}$ falls below the circular velocity.

Our analysis of the Jeans equation shows that the mean radial velocity is a good indicator of the virialization of a halo and that the low-mass haloes are nearly in virial equilibrium well beyond formal $R_{\rm vir}$.

## 5 EVOLUTION AND SCALING OF HALO MASSES

Dark matter haloes grow by accreting mass from their outskirts. Haloes with small mass grow very slow at late times. Thus, in the past they must have experienced a remarkable infall, which has created extended virialized regions surrounding the haloes at present. In this section, we study how this process of building of halo exterior was happening. For this reason, we analyse our simulations at different redshifts. We then take the median of different halo properties using the same mass bins as in previous sections with masses ranging from $10^{10}$ to $10^{15} h^{-1} M_{\rm vir}$. As expected, the statistics in each mass bin are smaller at higher redshifts. Using these data, we calculate the relation between static and virial mass for $z = 0$– 2. When doing this analysis, we take every halo at a given redshift without considering their relation with the final haloes at $z = 0$. The result is shown in Fig. 9, where we plot only the mass bins with enough statistics. At $z = 0$, the $M_{\rm static}/M_{\rm vir}$ ratio increases with mass. Then, it reaches maximum and starts to decline at large masses. Because of mass resolution, we do not see the rising part of $M_{\rm static}/M_{\rm vir}$ ratio at large redshifts, but the declining branch of the

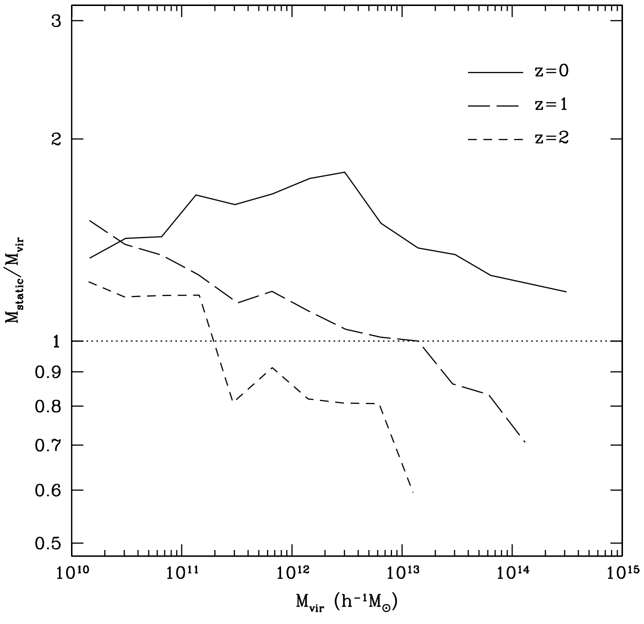

**Figure 9.** The static to virial mass relation from $z = 2$ to 0, taking into account every halo at a given redshift. Large haloes having $M_{\rm static} < M_{\rm vir}$ exist at all redshifts, but the transition mass decreases with increasing redshift.

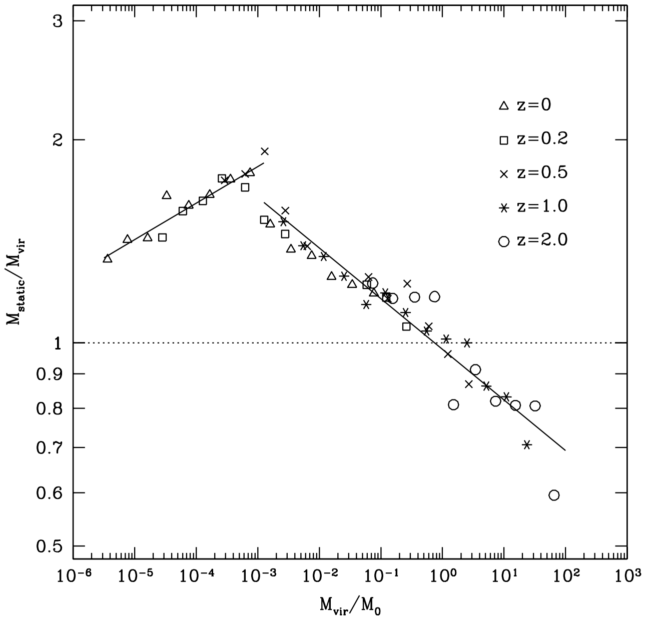

**Figure 10.** Same as Fig. 9, but scaled to the mass $M_0$ in which the fit of the smooth decline in $M_{\rm static}/M_{\rm vir}$ to a power law is equal to one. The time dependence of the $M_{\rm static}$–$M_{\rm vir}$ relation is encoded in the mass scale $M_0$. The solid line represents a fit to a power law at both sides of the transition mass (see equation 5).

curve is better resolved, and we clearly see that the ratio gets below unity at large masses.

It suggests that the relation between static and virial mass is essentially scale-free for different redshifts up to $z = 2$. In order to test this hypothesis, we approximate the declining part of this relation by a power law $M_{\rm static}/M_{\rm vir} = CM_{\rm vir}^{\alpha}$, and then find the crossing point: $M_{\rm static} = M_{\rm vir}$. This solution $M_0 = M_0(z)$ allows us to scale the static to virial mass relation for different redshifts. The results clearly overlap, indicating that there is a universal ($z$-independent) static to virial mass relation shown in Fig. 10. This plot shows that the static to virial mass ratio is well fitted by two power law with different slopes:

$$\frac{M_{\rm static}}{M_{\rm vir}} = \begin{cases} 10^{+0.423\pm0.021}\ x^{+0.054\pm0.005} & x < 10^{-3} \\ 10^{-0.010\pm0.005}\ x^{-0.075\pm0.004} & x > 10^{-3}, \end{cases} \qquad (5)$$

where $x \equiv M_{\rm vir}/M_0$. This relation allows us to convert the virial mass, which is easier to be computed accurately in numerical simulations, to the static mass. In order to have a complete description of this relation for any redshift, the redshift dependence of the mass scale $M_0(z)$ remains to be determined. Although this dependence may suffer from the scatter in the determination of the static mass, it seems clear from Fig. 11 that there is an approximate power-law dependence $M_0(a) = M_0(a = 1)a^{\gamma}$, from $z = 2$ to 0. The best fit to our data[1] is given by

$$M_0 \simeq (2.8 \pm 0.8) \times 10^{15} a^{8.9\pm0.4} h^{-1}\,{\rm M}_{\odot}. \qquad (6)$$

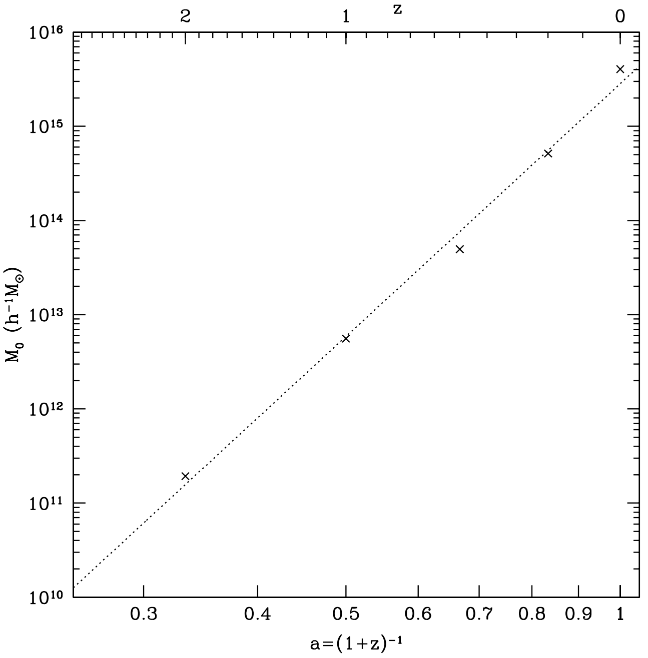

**Figure 11.** The evolution of the mass scale $M_0$. This behaviour is approximately fitted by a power law, $M_0 \simeq 2.8 \times 10^{15} a^{8.9} h^{-1}\,{\rm M}_{\odot}$ (see text for details).

It is worth pointing out that the absence of explicit redshift dependence in the relation between static and virial mass when the variable $M_{\rm vir}/M_0$ is used allows an analytic and straightforward derivation of the relation between both mass accretions, i.e. taking the logarithmic derivative in equation (5) and using equation (6) we obtain

$$\frac{\dot{M}_{\rm static}}{M_{\rm static}} = (1+\alpha)\,\frac{\dot{M}_{\rm vir}}{M_{\rm vir}} - \frac{\alpha\gamma}{a}, \qquad (7)$$

where the dot refers to the derivative with respect to the scalefactor $a$. However, this equation is no longer valid near the transition mass, where this derivative is not finite.

Despite the fact that the mass scale $M_0$ is not motivated by the physics of the formation of dark matter haloes (as opposed to, for example, $M_*$), it is the best way we found to encode the redshift dependence of $M_{\rm static}/M_{\rm vir}$. We have also explored the relation of this ratio with $\nu = \delta_{\rm c}/\sigma(M, z)$. However, we found a wider scatter for a given value of $\nu$, with lower values of the ratio for increasing redshift, in particular for $\nu > 1$.

## 6 MASS FUNCTION

The relation between the static and the virial mass is not monotonic, as we have shown before. This implies a change in the shape and in the amplitude of the distribution of the number density of haloes with a given mass, i.e. the mass function. As the virial mass is calculated accurately for all the haloes in our simulations, we may also obtain their static mass directly from the conversion formula given in equation (5). This allows us to estimate the static mass function of dark matter haloes and compare it to the virial mass function. We obtain very similar results taking the virial mass bins in Fig. 10 and then shifting them according to their corresponding value of the ratio $M_{\rm static}/M_{\rm vir}$. The results are presented in Fig. 12. In spite of the fact that the mass function of ST provides a very good fit for the virial mass (as shown in Fig. 1 for the case of $z = 0$), we find that this analytic model is not a good description for the static mass function. Moreover, some authors using different definitions of virialized halo have already shown the presence of significant

---

[1] We want to emphasize that halo virial mass is defined here with an overdensity criterion which evolves with time, as detailed in Section 2. The choice of non-evolving overdensity criterion will imply a change in the $M_0(z)$ relation.

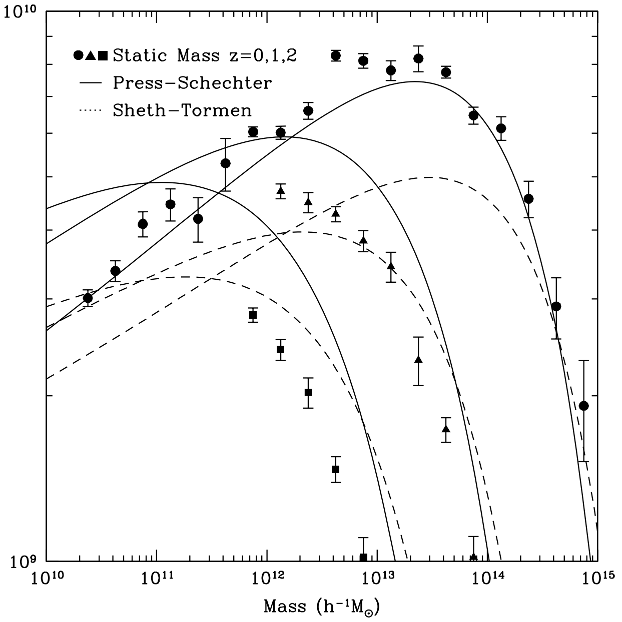

**Figure 12.** The static mass function obtained from individual haloes using equation (5) (solid circles for $z = 0$, triangles for $z = 1$ and squares for $z = 2$). Error bars show the Poissonian error only (not including the uncertainty in the $M_{\rm static}$–$M_{\rm vir}$ relation). Solid and dashed lines show the PS and ST mass function, respectively. Surprisingly, the PS mass function provides a very good fit to our data at $z = 0$. On the other hand, the mass function at higher redshifts deviates from the PS analytic model.

departures from the Sheth & Tormen function (see e.g. Macciò et al. 2003).

Surprisingly, the mass function of Press & Schechter (1974) approximates really well our data at $z = 0$ in the mass range under study. In order to test robustness of our estimates of the static mass function, we changed different parameters (e.g. changed the threshold to $0.1V_{\rm vir}$ in algorithm of detecting the static radius). Results are stable. We leave for future the investigation of the static mass function at its high-mass end (Betancort-Rijo & Montero-Dorta 2006), because the poor statistics for the highest mass bins here prevent us from drawing any conclusion about it. The redshift evolution of the mass function is also shown in Fig. 12. We realize that the static mass function deviates from the corresponding Press & Schechter function at $z = 1$ and 2 so it is no longer described by this model. None the less, it is interesting that we can still recover the agreement with Press & Schechter by an overall increase in the static mass. This shift could be accounted for by the scatter in the $M_0(z)$ relation, which is very similar to this deviation. However, it is not clear whether this deviation is an artefact due to resolution effects, so this remains as an open issue.

## 7 EVOLUTION OF THE MAJOR HALO PROGENITOR

We are now in a position to study the evolution of the mass, i.e. the mass accretion history, of dark matter haloes in cosmological simulations. So, we need to track the set of haloes identified by BDM at $z = 0$ back in time and then measure their static mass. Here, we use a method similar to that in Ascasibar, Hoffman & Gottlöber (2007). First of all, we pick up a sample of a few hundreds of particles around the density maximum of every halo at $z = 0$. These particles are then tracked back to the highest redshift available in our cosmological simulation. Although it may occur that these particles no longer belong to the same object at that redshift, we take the particle that has a minimum sum of squared distances to the others in the sample, as an initial guess for the centre of the protohalo. Finally, we calculate the centre of mass around this position iteratively using the whole set of particles in the simulation box. After a few iterations, we obtain the centre of the primordial peak of density which corresponds to our halo at $z = 0$. We then label some particles around this centre. This new set of particles will help us, by the calculation of their centre of mass, to identify at every redshift the position of the halo which encloses them. Hence this halo, as the offspring of the main primordial peak corresponding to the halo at present, will be referred to as the halo major progenitor.

In our analysis, we study the evolution of the progenitors from three different mass bins at $z = 0$: low-mass haloes ($10^{10.0}$–$10^{10.5}h^{-1}\,{\rm M}_\odot$), galactic-sized haloes ($10^{12.0}$–$10^{12.5}h^{-1}\,{\rm M}_\odot$) and cluster-sized haloes ($10^{13.5}$–$10^{14.0}h^{-1}\,{\rm M}_\odot$). These ranges are selected in order to study the dependence of mass on our results with very good statistics: each bin contains more than a thousand of haloes. This allows us to calculate with good accuracy the median profiles for different physical quantities at every redshift from $z = 0$ to $\simeq 2$. We keep this as the maximum redshift analysed here because the median radial profile is no longer well resolved (i.e. with more than 200 particles for the majority of the haloes) in the inner regions for higher redshifts. Thus, we cannot determine the size of the virialized region and hence cannot go further in redshift.

The evolution of the mean radial velocity profile for the median halo is displayed in Fig. 13. Here, we show that the time sequence suggested in Busha et al. (2005) for cluster-sized haloes takes place even for low-mass haloes: the mean radial velocity profile experiences infall in their outer parts while forming. Just after the infall is finished, there is an epoch in which some outflow appears, followed by a final profile with an inner virialized region and the Hubble flow.[2] Moreover, the time-scale of this sequence seems to be mass-dependent: the analysis of Busha et al. (2005) finds this sequence in the future for cluster-sized haloes, whereas low-mass haloes are already in the outflow phase at present. Galaxy-sized haloes are now experiencing neither infall nor outflow, so the virialized region is reaching a maximum in units of the virial radius, as already shown in Fig. 6.

This evolution is reflected in the redshift dependence of the static radius. In Fig. 14, we illustrate the evolution of the ratio of static to virial radius. It is clear from this plot that low-mass haloes have already formed (the infall stopped when the maximum ratio took place) and they are even losing some of their virialized mass at present. Galaxy-sized haloes are reaching now this maximum, but for cluster-sized haloes the infall has not even finished.

The static mass accretion history is presented in Fig. 15. The solid, long-dashed and short-dashed lines show the evolution of the static mass of the median halo for three different mass bins, while the dotted line corresponds to their virial mass. The error bars are estimated using the halo-to-halo variation, calculating the mass inside the median virial radius for each dark matter halo, and taking the central 68 per cent of these values. Neither the uncertainty in the virial radius nor the scatter in the static versus virial mass relation was taken into account. In spite of the scatter, some conclusions

---

[2] This final state agrees with the picture shown by other different analyses of halo virialization, in which virial parameters are ill-defined in merging events but there is a general trend for the virial ratio $2E_{\rm kin}/|E_{\rm pot}|$ to approach unity at present (e.g. Hetznecker & Burkert 2006).

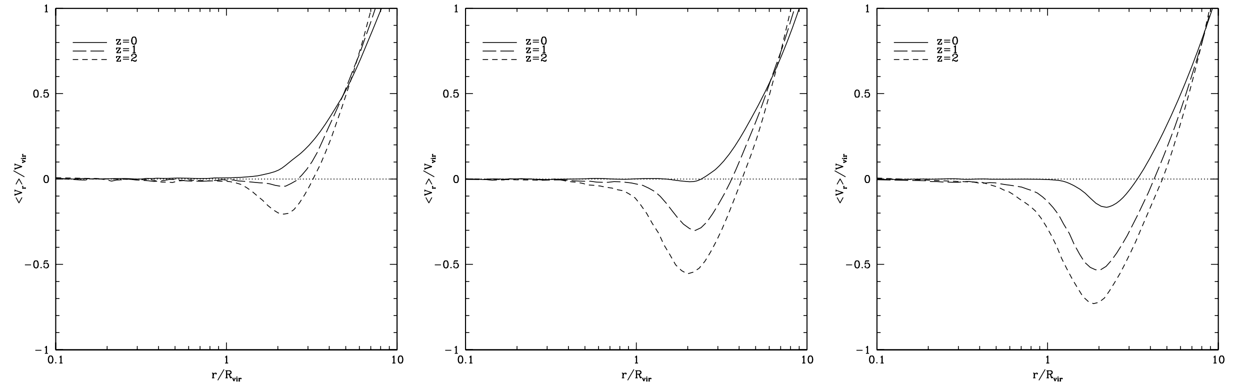

**Figure 13.** The evolution of the mean radial velocity profile from $z = 2$ to 0. Left-hand panel: low-mass haloes. Middle panel: galactic-sized haloes. Right-hand panel: cluster-sized haloes. The sequence followed by low-mass haloes has hardly started by cluster-sized haloes.

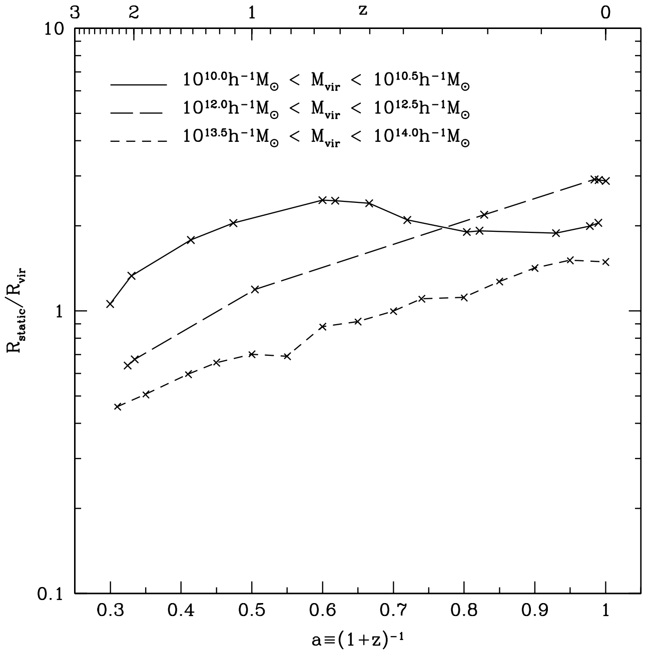

**Figure 14.** The static to virial radius as a function of the redshift. It appears that this ratio behaves differently for each mass bin. The mass bins are the same as those in Fig. 13. Low-mass haloes have reduced their static region in units of $R_{\rm vir}$ due to recent outflow. On the other hand, galaxy-sized haloes are reaching a maximum on this ratio. Cluster-sized haloes continue increasing this ratio as the infall is less prominent.

may be drawn from this plot. The recent assembly history is very mass-dependent: low-mass haloes hardly experienced a change in their mass since $z = 1$, and their virial mass is underpredicting the average amount of matter inside them since $z \simeq 2$. On the other hand, galactic-sized haloes have been increasing their static mass up to the present epoch, most likely due to halo relaxation. This process is responsible of the largest difference between the static and the virial mass at $z = 0$: the mass inside the virialized region is about a factor of 2 larger than the virial mass. Finally, cluster-sized haloes are still increasing their mass at present, but the difference with respect to the virial mass is not so large. In fact, around $z = 0.5$ both static and virial mass should have been very similar. In contrast, it is likely that they differ significantly at higher redshift.

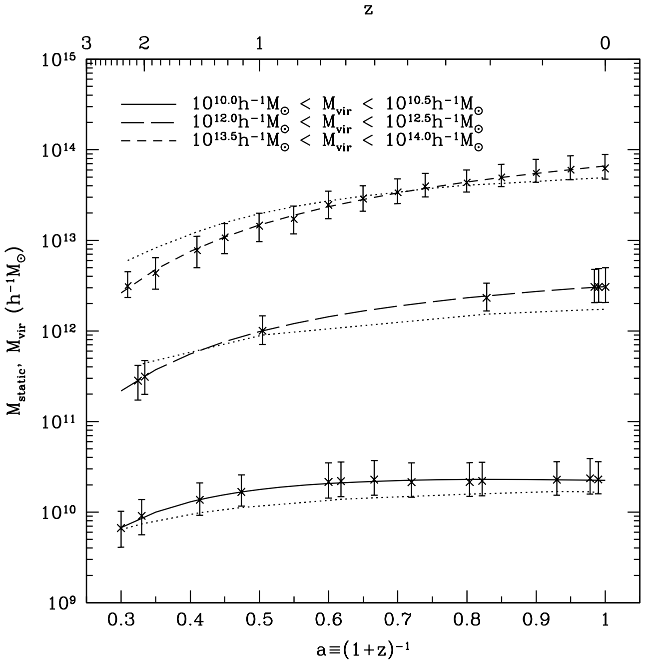

**Figure 15.** The mass accretion history of dark matter haloes. The evolution of the static mass is indicated by the crosses and the error bars, with their corresponding fit to equation (9) (solid, long-dashed and dashed lines for low-mass, galaxy-sized and cluster-sized haloes, respectively), while the dotted line shows the evolution of the virial mass, according to the parametrization by Wechsler et al. (2002). The mass bins are the same as those in Fig. 13. The static mass inside low-mass haloes is nearly constant from $z = 0.5$ to 0. On the other hand, galaxy-sized haloes increase their static mass even steeper than their virial mass, due to relaxation around haloes. Clusters are accreting mass, but also incorporating some of the recently virialized mass from their surroundings.

We find for our median profiles that the function proposed in equation (3) in Wechsler et al. (2002) for the virial mass, $M_{\rm vir}(a) = M_{\rm vir}(a = 1)\ \exp(-\delta z)$, provides an excellent fit for the accretion history of the virial mass from $z = 2$ to 0. However, if we include this relation in our model given by equation (7), and solve the differential equation, we obtain

$$\frac{M_{\rm static}(a)}{M_{\rm static}(a = 1)} = \frac{\exp^{-(1+\alpha)\delta z}}{a^{\alpha\gamma}} \tag{8}$$

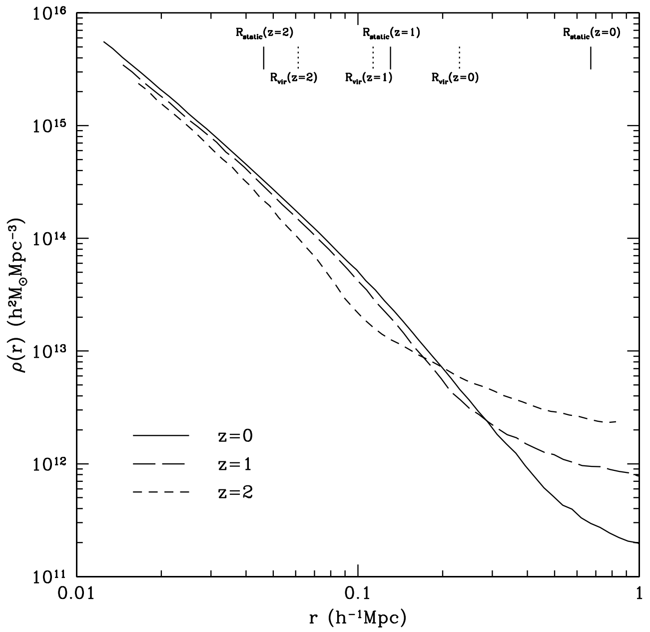

**Figure 16.** The evolution of the median density profile from $z = 2$ to 0 for galactic-sized haloes. As shown in Fig. 2 for individual haloes, there has been very little change in this profile from $z = 1$ up to the present epoch. The vertical dotted lines mark the virial radii at $z = 2$ (left-hand side), $z = 1$ (middle) and $z = 0$ (right-hand side). Static radii are shown with vertical solid lines. The growth of the static radius in Milky Way sized haloes from $z = 1$ to 0 is not due to accretion but virialization of the surrounding regions of the halo.

which fails to reproduce the evolution of the static mass when the discontinuity of the static versus virial mass relation takes place. This is reasonable as equation (7) is obtained when all the haloes (not just the progenitors of the haloes at $z = 0$) are taken into account. None the less, this starting point suggests the functional dependence of this evolution, so that a fit of the data to

$$M_{\mathrm{static}}(z) = M_{\mathrm{static}}(z = 0)(1 + z)^{-\beta} \mathrm{e}^{-\alpha z}, \qquad (9)$$

where both $\alpha$ and $\beta$ are free parameters, provides a better description of the data. This function is very similar to that corresponding to the virial mass, but there is an extra factor that enhances the fit, in particular, for low-mass haloes.

As we pointed out above, the recent increase in the mass of galactic-sized haloes is mainly due to virialization of mass surrounding them. In Fig. 16, we display the evolution of the density profile for the median galactic-sized halo, which is similar to the profile for individual haloes as shown in Fig. 2. Only small variations in the density profile occur for the median galactic halo from $z = 1$ to 0, which correspond to a small variation of the mass inside a physical radius. However, these haloes experience an important growth of their static mass due to the expansion of the virialized region, as is clear from Fig. 13.

## 8 DISCUSSION

A more realistic (physical) estimate of the halo mass might be crucial for some areas in cosmology which are sensitive to accurate values of the mass of dark matter haloes. For example, our results may be relevant for understanding the galaxy formation processes that happen inside dark matter haloes. Indeed, semi-analytical models of galaxy formation (e.g. Croton et al. 2006) might need to assess the impact of their predictions when the virial mass is no longer used. If the static mass and its evolution are used, one may get a more realistic picture of the structure formation process drawn from cosmological simulations. Moreover, recipes for star formation, active galactic nuclei and supernova feedback and merging of galaxies are often taken from quantities of their corresponding dark matter haloes, such as their mass. Thus, the conclusions (e.g. colour–magnitude diagram, evolution of the stellar mass, etc.) from the analysis of these simulations using semi-analytical models of galaxy formation may be biased due to an underestimation of the mass associated to a halo if the former virial mass is considered, especially for the galaxy-sized haloes such as the host of the Milky Way as we have reported in this work.

The precise determination of the halo mass function, in terms of the static mass, can also be very relevant. Mass function of cluster-sized haloes must be predicted with special accuracy because the number density of galaxy clusters is a probe of fundamental cosmological parameters, such as dark energy. This is very important since the evolution of the mass function of galaxy clusters is taken as an almost direct measurement of the equation of state of dark energy $\omega = P/\rho$ (The Dark Energy Survey Collaboration 2005) and any statistically significant deviations in the measurements of the mass function of clusters from the predictions of the $\Lambda$CDM model may be and likely will be interpreted as deviations of the dark energy from a simple cosmological constant.

Other possible observational implications of this work also deserve further investigation. It is noteworthy that the transition mass of $\simeq 5 \times 10^{12} h^{-1}\,\mathrm{M}_\odot$, that separates the infall and outflow regimes, is similar to the mass scale found by Dekel & Birnboim (2006). Dekel & Birnboim (2006) argue that below $M \lesssim 10^{12}\,\mathrm{M}_\odot$ the efficient early star formation may occur due to cold flows, as thermal pressure is not large enough to avoid the gas accretion from the outer gas reservoir to the inner core of the halo. On larger scales, the heating due to virial shocks may shutdown the star formation. This different behaviour of the gas around dark matter haloes in simulations above and below this mass scale was proposed by Dekel & Birnboim (2006) as an explanation for the bimodality observed in many properties of galaxies such as the bimodality seen in the colour distribution of Sloan Digital Sky Survey field galaxies. Thus, a given velocity pattern of infall or outflow in a dark matter halo of mass above and below $10^{12} h^{-1}\,\mathrm{M}_\odot$ may be correlated with the fact that the galaxy within the halo belongs to the blue cloud or the red colour sequence, respectively. Yet, this is only a speculation which remains to be investigated. However, the mass scale for transition between infall and outflow is the same as the mass scale at which baryonic matter cannot penetrate the inner parts of the halo. At first glance, this is just a matter of coincidence, as for higher redshifts the transition mass would be well below the mass scale of Dekel & Birnboim (2006). Still, it is an interesting question whether the haloes experiencing infall of the dark matter also host galaxies, which grow fast by accreting baryons in their central regions.

Such correlations between galaxies and their host haloes could unveil some of the relations between dark and baryonic matter, and hence cast some light in the evolution of galaxies in the expanding Universe.

## 9 CONCLUSIONS

In this paper, we use a set of high-resolution *N*-body cosmological simulations for the analysis of the mass inside the region of dark matter haloes with no net infall or outflow velocities, i.e. the static region. Haloes show a typical radial velocity pattern that depends on their mass: low-mass haloes tend to display a region with outflow in their surroundings, while cluster-sized haloes show a prominent infall velocity pattern. Galaxy-sized haloes show an intermediate pattern with a sharper transition between the static region and the Hubble flow. We find that the former virial radius tends to underestimate the size of the region with zero mean radial velocity for haloes with masses $10^{10}h^{-1}\,\mathrm{M}_{\odot} < M_{\mathrm{vir}} \lesssim 10^{14}h^{-1}\,\mathrm{M}_{\odot}$ at $z = 0$. The mass inside this static region can be about a factor of 2 larger than the former virial mass, when the threshold defining the static radius is 5 per cent of the virial velocity $V_{\mathrm{vir}} = \sqrt{(GM_{\mathrm{vir}}/R_{\mathrm{vir}})}$. Lower values of the threshold ($\lesssim$1 per cent) may lower this factor. However, we observe a clear trend in the $M_{\mathrm{static}}/M_{\mathrm{vir}}$ versus $M_{\mathrm{vir}}$ relation which remains unchanged with this threshold: for low-mass haloes, this ratio is an increasing function of $M_{\mathrm{vir}}$ due to the reduction in the outflow. On the other hand, high-mass haloes show a larger infall for larger $M_{\mathrm{vir}}$, making this ratio to decrease. The maximum occurs at $M_{\mathrm{vir}} \simeq 5 \times 10^{12}h^{-1}\,\mathrm{M}_{\odot}$, where the size of the static region is the largest in units of $R_{\mathrm{vir}}$.

The mass function of objects whose mass is defined in the way presented here resembles that of Press & Schechter in the range of mass we have studied, but only at $z = 0$. At higher redshifts, the static mass function deviates significantly from it. This disagreement could be accounted for by the scatter in $M_0(z)$, although it seems more likely that the resemblance with Press & Schechter at $z = 0$ is due to coincidence (in both shape and amplitude to within $\sim$20 per cent) of the ratio $f_{\mathrm{PS}}/f_{\mathrm{ST}}$ with $M_{\mathrm{static}}/M_{\mathrm{vir}}$. Whatever may be the case, this resemblance is theoretically unexpected because the Sheth & Tormen function, which fits very well the mass function for virial masses, is derived from a more realistic approach (ellipsoidal collapse). In any case, it seems clear that when the virial mass is used, the number density of dark matter haloes of a given mass at $z = 0$ might be underestimated in the mass range $10^{10}h^{-1}\,\mathrm{M}_{\odot} < M_{\mathrm{vir}} \lesssim 10^{14}h^{-1}\,\mathrm{M}_{\odot}$.

The redshift evolution of the $M_{\mathrm{static}}$–$M_{\mathrm{vir}}$ relation turns out to be very weakly redshift-dependent from $z = 2$ to 0 when appropriate variables are used. This dependence on the redshift is encoded as an evolving mass scale $M_0$ which indicates the approximate mass at which $M_{\mathrm{static}} = M_{\mathrm{vir}}$ in the declining part of the relation. By doing this, it is straightforward to derive from this relation a differential equation for the evolution of the static mass, provided that the evolution of $M_{\mathrm{vir}}$ and of $M_0$ is already known. As we have shown in this paper, the evolution of the mass scale has an acceptable fit to a power law: $M_0 \simeq 2.8 \times 10^{15}\,a^{8.9}h^{-1}\,\mathrm{M}_{\odot}$. On the other hand, the evolution of the virial mass $M_{\mathrm{vir}}$ of the major progenitor is well described by an exponential law in $z$, as claimed by Wechsler et al. (2002). Once we have fixed the evolution of $M_{\mathrm{vir}}$ and of $M_0$, we solve this differential equation and we find a simple model for the evolution of the static mass of the major progenitor, i.e. $M_{\mathrm{static}}(z) = M_{\mathrm{static}}(z = 0)(1 + z)^{-\beta}\mathrm{e}^{-\alpha z}$, which turns out to be a very good fit to our data. In any case, there is a different behaviour for the evolution of the static mass in different mass bins. The static mass of low-mass haloes is nearly constant from $z = 0.5$ to 0. Galaxy-sized haloes keep growing at present, but the reason here is not the decreasing background density of the expanding Universe. Instead, the relaxation of the matter in the surroundings of these haloes is incorporating mass at even a higher rate than the unphysical growth of the virial mass. The same stands for clusters, although the static and virial mass are not very different at present.

The mean radial velocity profile (averaged over a halo mass bin) evolves in the way found by Busha et al. (2005) for cluster-sized haloes: while the halo is forming, it accretes mass from its surroundings via infall, which is being reduced with time. This is followed by a period of outflow of unbound matter, and a final configuration thereafter consisting in a static region whose size is independent of time. Although the simulation used in that paper was evolved until $a = 100$, and our halo sample was instead tracked up to redshift $z = 0$, we find a situation that is consistent with this picture. Moreover, we find that the time-scale of this sequence is different for each mass bin: low-mass haloes at present are in the outflow phase, but cluster-sized haloes are still in their infall phase. Interestingly, galactic-sized haloes are experiencing a transition (infall to outflow) epoch at $z = 0$.

## ACKNOWLEDGMENTS

AJC and FP thank the Spanish MEC under grant PNAYA 2005-07789 for their support. AK acknowledges support from NASA and NSF grants to NMSU. AJC acknowledges the financial support of the MEC through Spanish grant FPU AP2005-1826. We thank Juan Betancort-Rijo for valuable discussion and useful comments in this work, and Douglas Rudd for suggesting some points which improved the text. We do appreciate the useful feedback from the anonymous referee. AJC also thanks the Helmholtz Institute for Supercomputational Physics for their outstanding Summerschool 2006 in Supercomputational Cosmology. Computer simulations were done at the LRZ Munich, NIC Julich and NASA Ames.

## REFERENCES

Ascasibar Y., Hoffman Y., Gottlöber S., 2007, MNRAS, 376, 393
Betancort-Rijo J. E., Montero-Dorta A. D., 2006, ApJ, 650, L95
Blumenthal G. R., Faber S. M., Primack J. R., Rees M. J., 1984, Nat, 311, 517
Bryan G. L., Norman M. L., 1998, ApJ, 495, 80
Bullock J. S., Dekel A., Kolatt T. S., Kravtsov A. V., Klypin A. A., Porciani C., Primack J. R., 2001a, ApJ, 555, 240
Bullock J. S., Kolatt T. S., Sigad Y., Somerville R. S., Kravtsov A. V., Klypin A. A., Primack J. R., Dekel A., 2001b, MNRAS, 321, 559
Busha M. T., Adams F. C., Wechsler R. H., Evrard A. E., 2003, ApJ, 596, 713
Busha M. T., Evrard A. E., Adams F. C., Wechsler R. H., 2005, MNRAS, 363, L11
Cole S., Lacey C., 1996, MNRAS, 281, 716
Croton D. J. et al., 2006, MNRAS, 365, 11
Dekel A., Birnboim Y., 2006, MNRAS, 368, 2
Diemand J., Kuhlen M., Madau P., 2007, ApJ, 667, 859
D'Onghia E., Navarro J. F., 2007, MNRAS, 380, L58
Gladders M. D., Yee H. K. C., Majumdar S., Barrientos L. F., Hoekstra H., Hall P. B., Infante L., 2007, ApJ, 655, 128
Gunn J. E., 1977, ApJ, 218, 592
Gunn J. E., Gott J. R. I., 1972, ApJ, 176, 1
Guzik J., Seljak U., 2002, MNRAS, 335, 311
Hetznecker H., Burkert A., 2006, MNRAS, 370, 1905
Hoekstra H., Yee H. K. C., Gladders M. D., 2004, ApJ, 606, 67
Klypin A., Gottlöber S., Kravtsov A. V., Khokhlov A. M., 1999, ApJ, 516, 530
Klypin A., Kravtsov A. V., Bullock J. S., Primack J. R., 2001, ApJ, 554, 903
Kneib J.-P. et al., 2003, ApJ, 598, 804
Kravtsov A. V., Klypin A. A., Khokhlov A. M., 1997, ApJS, 111, 73
Łokas E. L., Mamon G. A., 2001, MNRAS, 321, 155
Macciò A. V., Murante G., Bonometto S. P., 2003, ApJ, 588, 35
Macciò A. V., Dutton A. A., van den Bosch F. C., Moore B., Potter D., Stadel J., 2007, MNRAS, 378, 55
Mandelbaum R., Seljak U., Kauffmann G., Hirata C. M., Brinkmann J., 2006, MNRAS, 368, 715
Navarro J. F., Frenk C. S., White S. D. M., 1997, ApJ, 490, 493
Pierpaoli E., Scott D., White M., 2001, MNRAS, 325, 77

Prada F. et al., 2003, ApJ, 598, 260
Prada F., Klypin A. A., Simonneau E., Betancort-Rijo J., Patiri S., Gottlöber S., Sanchez-Conde M. A., 2006, ApJ, 645, 1001
Press W. H., Schechter P., 1974, ApJ, 187, 425
Primack J. R., 1997, preprint (astro-ph/9707285)
Primack J. R., 2003, Nucl. Phys. B Proc. Suppl., 124, 3
Rines K., Finn R., Vikhlinin A., 2007, ApJ, 665, L9
Sheldon E. S. et al., 2004, AJ, 127, 2544
Sheth R. K., Tormen G., 1999, MNRAS, 308, 119 (ST)
Sheth R. K., Mo H. J., Tormen G., 2001, MNRAS, 323, 1
Smith D. R., Bernstein G. M., Fischer P., Jarvis M., 2001, ApJ, 551, 643
Somerville R. S., Primack J. R., 1999, MNRAS, 310, 1087
Spergel D. N. et al., 2007, ApJS, 170, 377
Taylor J. E., Navarro J. F., 2001, ApJ, 563, 483
The Dark Energy Survey Collaboration, 2005, preprint (astro-ph/0510346)
van Dokkum P. G., Franx M., Fabricant D., Kelson D. D., Illingworth G. D., 1999, ApJ, 520, L95
Wechsler R. H., Bullock J. S., Primack J. R., Kravtsov A. V., Dekel A., 2002, ApJ, 568, 52
White M., 2001, A&A, 367, 27
White S. D. M., Rees M. J., 1978, MNRAS, 183, 341
Wojtak R., Łokas E. L., Gottlöber S., Mamon G. A., 2005, MNRAS, 361, L1
Wojtak R., Lokas E. L., Mamon G. A., Gottloeber S., Klypin A., Hoffman Y., 2008, MNRAS, 388, 815
Zaritsky D., White S. D. M., 1994, ApJ, 435, 599
Zhao D. H., Mo H. J., Jing Y. P., Börner G., 2003, MNRAS, 339, 12

This paper has been typeset from a TEX/LATEX file prepared by the author.

## A.2 The density profile of dark matter halos beyond the virial radius

Mon. Not. R. Astron. Soc. **000**, 000–000 (0000) Printed 21 July 2008 (MN LaTeX style file v2.2)

# The dark outside: the density profile of dark matter haloes beyond the virial radius

Hugo Tavío,[1,2,3]* Antonio J. Cuesta[1], Francisco Prada,[1] Anatoly A. Klypin[4],
Miguel A. Sánchez-Conde[1]
[1] *Instituto de Astrofísica de Andalucía (CSIC), Camino Bajo de Huétor 50, E-18008 Granada, Spain.*
[2] *Instituto de Enseñanza Secundaria "José Cadalso", c/Castiella s/n, San Roque (Cádiz), Spain.*
[3] *Escuela Politénica Superior de Algeciras. Universidad de Cádiz, Avda. Ramón Pujol s/n 11202 Algeciras (Cádiz), Spain.*
[4] *Astronomy Department, New Mexico State University, MSC 4500, P.O.Box 30001, Las Cruces, NM, 880003-8001, USA.*

21 July 2008

## ABSTRACT

We present an approximation for the average density profile of dark matter haloes in the ΛCDM cosmological model, which is accurate to within 10–15% even for large radial distances from $0.05R_{\rm vir}$ up to $10R_{\rm vir}$ for halo masses ranging from $10^{11.5}$ to $10^{15.0}\ h^{-1}M_{\odot}$. We propose a modified form of the Navarro, Frenk & White (NFW) approximation: $\rho(r) = \rho_{\rm NFW}(r) + A(r/R_{\rm vir})^{-1} + B(1 + r/R_{\rm vir})^{-1}$. This generalized expression, which is applicable to the external regions of dark matter haloes, only very slightly affects the density in the inner regions of haloes. The strong correlation among the different parameters in the model allows us to describe the profile in terms of just one parameter: the virial mass. We integrate our density profile to derive the enclosed mass in a sphere of a given radius and compare it with the NFW results. We find that the NFW underestimates the enclosed mass by more than 50% at $10R_{\rm vir}$, whereas our model reproduces the results from numerical simulations to within 2% accuracy even at this distance. We also use this new approximation to study the weak gravitational lensing and to obtain an analytic expression for the tangential shear. This allows us to quantify the contribution to the shear from the outer regions of the density profile. For the first time we calculate the difference between the tangential shear calculated via the NFW profile and the corresponding result when the external regions of haloes in cosmological simulations are taken into account. We find a 4% difference for all the mass ranges under study.

**Key words:** dark matter – galaxies: haloes – large-scale structure of Universe – cosmology: theory – methods: $N$-body simulations – methods: statistical

## 1 INTRODUCTION

Measurements of the mass distribution of dark matter (DM) haloes are essential for the theory of structure formation. This issue has been addressed in two ways: observational and theoretical. The observational measurements have profited from recent gravitational lensing studies and also from measurements of galactic dynamics using large scale and massive galaxy surveys (e.g. Mandelbaum et al. 2006, Prada et al. 2003). Theoretical estimates made substantial progress thanks to recent advances in both top-hat gravitational collapse models and fully non-linear evolution via $N$-body simulations (e.g. Sánchez-Conde et al. 2007, Ascasibar et al. 2007, Diemand et al. 2007).

Cosmological $N$-body simulations have been extensively used in order to provide predictions for the structure of DM haloes in the hierarchical clustering scenario. The Navarro, Frenk & White (NFW) density profile has become a convenient formula for the description of DM haloes in a broad mass range. This profile provides a reasonable fit for the halo density distribution, despite that many other functions have been suggested in order to improve accuracy (Moore et al. 1998, Sérsic 1968, Einasto 1965 profiles, see also Merritt et al. 2005 for reference). Nevertheless, the NFW density profile (Navarro et al. 1997) was proposed and contrasted to fit the inner regions of DM haloes roughly up to the virial radius, where haloes are expected to be in equilibrium (Cole & Lacey 1996). Therefore, it was not expected that the NFW analytical profile will describe the external density profile properly. Our aim here is to extend the va-

---

* E-mail: htavio@iaa.es

lidity of this approximation to describe the outer regions of DM haloes. Moreover, recent works (see Prada et al. 2006, Cuesta et al. 2007, Diemand et al. 2007) have shown that the DM virialized regions extend well beyond the formal virial radius especially for low-mass haloes. This reinforces our interest in studying haloes beyond the virial radius.

On the other hand, current observational techniques allow us to measure the mass distribution around galaxies and clusters at large distances. The dynamics of satellite galaxies (e.g. Zaritsky & White 1994; Zaritsky et al. 1997; Prada et al. 2003; Brainerd 2004; Conroy et al. 2007) provide strong constraints on the shape of the density profiles of DM haloes in the outer regions. Another technique which has proven its usefulness despite its recent development, is the analysis of the weak lensing effect in gravitational lensing theory (e.g. Mellier 1999; Bartelmann & Schneider 2001; Hoekstra et al. 2004 Heymans et al. 2006; Massey et al. 2007). In both observational techniques, the external regions under study are often beyond the virial radius. Yet, the use of the NFW profile to model observations is still very common in the determination of DM halo mass. Although the NFW profile is a great improvement as compared to the isothermal profile to describe for example the weak lensing observations (e.g. Mandelbaum et al. 2006b), it is not suitable for extrapolation at large distances beyond the virial radius. The study of the physical processes occurring in the external regions of DM haloes will provide unique insight into our understanding of the formation of DM haloes. A good example is the recent observational work by George et al. 2008 who measured temperature and density profiles beyond the virial radius of a cluster and this allowed them to produce improved constraints on the mass and gas fraction profiles. A first step in this direction is the study of average density profiles in the outer regions of DM haloes in cosmological simulations.

In this paper, we present an approximation for the density profile of DM haloes well beyond the virial radius, obtained from high resolution cosmological simulations. This approximation focuses on the external regions of the haloes as an extension of the NFW formula that fits well the inner regions. We took the NFW model as our starting point because of its simplicity and with the aim to derive an expression which is easy to implement in many of the applications mentioned above. In order to describe representative DM halo density profiles and compare them with our approximation, we average over many individual density profiles for a given mass range. Hence, our conclusions apply for the ensemble of haloes of a given mass, with a halo-to-halo mass dependent scatter. As it is already known from the early work of Navarro et al. (1996), individual haloes at a given range of mass usually show a similar profile. Thus, the analysis of average halo density profiles happens to be a reasonable option for our purposes.

The approximation presented in this paper includes free parameters which have to be fixed for a given mass range. However, we will also study some correlations among them and prove that only one parameter (for example the virial mass) is enough in order to provide a high quality fitting function for the inner and outer regions. Moreover, our approximation can be useful to obtain a suitable formula to describe the projected mass density of average DM haloes. We determine with this formula the tangential shear associated to gravitational lensing. We also have compared our results with those obtained using the NFW formula, in order to assess its validity at large distances from the halo centre.

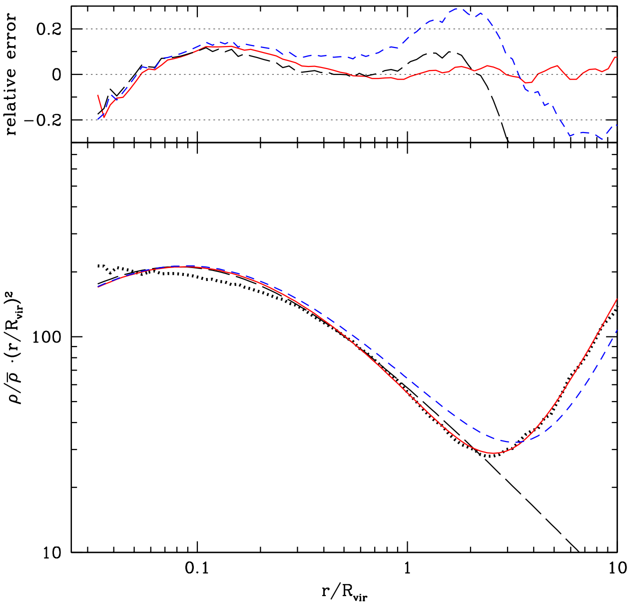

**Figure 1.** Average matter density profile for a Milky Way size DM halo. The numerical profile given by cosmological simulations (dotted line) is compared to the fit to the NFW model (Eq. 2, long dashed line), the mean matter density of the Universe (Eq. 8, short dashed line), and our model (Eq. 12, solid line). The upper panel shows the relative error for each approximation with respect to the numerical profile.

The paper is organized as follows. In Section 2, we introduce our approximation that describes the density profiles of DM haloes well beyond $R_{\rm vir}$. In Section 3, we fit the numerical density profiles drawn from cosmological simulations. In Section 4, we show the application of our model to the measurement of the tangential shear in gravitational lensing. Finally, we discuss and summarize the main conclusions in Section 5.

## 2 THE THEORETICAL FRAMEWORK

Let us start with a brief review of the NFW approximation for DM haloes in cosmological $N$-body simulations (see also e.g. Łokas & Mamon 2001). This is a simple function which provides a good description for the density profile inside the virial radius. Yet, it turns out to give wrong results for the external regions since it does not take into account the mean matter density of the Universe, which is the main contribution at large distances from the halo centre (see Prada et al. 2006). The analytic expression for the NFW density profile is:

$$\rho_{\rm NFW}(r) = \frac{\rho_s^{\rm NFW}}{(r/r_s)\,(1+r/r_s)^2}. \qquad (1)$$

This formula describes the internal profile region quite well (up to one virial radius approximately) and depends on two parameters: the characteristic density $\rho_s^{\rm NFW}$ and the characteristic scale radius $r_s$. The latter is the radius in which $r^2 \cdot \rho_{\rm NFW}(r)$ reaches its local maximum, i.e. $\frac{d\ \ln\rho(r)}{d\ln r} = -2$, and the former is just given by $\rho_s^{\rm NFW} = 4\rho_{\rm NFW}(r_s)$. The NFW profile may also be described in terms of the virial mass $M_{\rm vir} = M(< R_{\rm vir})$, and the concentration parameter $c \equiv R_{\rm vir}/r_s$. The quantity $R_{\rm vir}$ is the virial radius of the halo, defined as the radius of a sphere enclosing a given overdensity, the value adopted here is $\Delta = 340$. Hence, the relation between the virial radius and the virial mass is $M_{\rm vir} = \frac{4\pi}{3} 340\ \bar\rho\ R^3_{\rm vir}$. The NFW profile can now be written as follows:

$$\rho_{\rm NFW}(s) = \frac{\rho_s^{\rm NFW}}{cs\,(1+cs)^2}. \tag{2}$$

where $s$ is the radial coordinate scaled to $R_{\rm vir}$, i.e. $s \equiv r/R_{\rm vir}$. Note that $\rho_s^{\rm NFW}$ is now a function (in general) of both $c$ and $M_{\rm vir}$. In order to find this function, let us calculate the halo enclosed mass from the density NFW profile:

$$M_{\rm NFW}(s) = \frac{3M_{\rm vir}}{340\bar\rho}\frac{\rho_s^{\rm NFW}}{c^3}\left[\ln(cs+1) - \frac{cs}{cs+1}\right]. \tag{3}$$

Since $M_{\rm vir}$ is defined as the mass inside the virial radius, we have,

$$M(s=1) \equiv M_{\rm vir} \tag{4}$$

It is straightforward to derive the expression for the characteristic density in terms of $c$ and $M_{\rm vir}$. It turns out that $\rho_s^{\rm NFW}$ is actually a function of the concentration parameter only, i.e.:

$$\rho_s^{\rm NFW} = \frac{340}{3}\,c^3 g(c)\bar\rho \tag{5}$$

where the function $g$ is defined as follows:

$$g(x) \equiv \frac{1}{\ln(x+1) - x/(x+1)} \tag{6}$$

Therefore, the mass inside a sphere of a given radius is completely given by the virial mass of the halo and its concentration:

$$\frac{M(s)}{M_{\rm vir}} = g(c)\left[\ln(cs+1) - \frac{cs}{cs+1}\right] = \frac{g(c)}{g(cs)}. \tag{7}$$

To describe the external regions of DM haloes, it is essential to decide the kind of function that must be added to the NFW approximation, in such a way that its contribution can be neglected in the inner parts. A first attempt to improve this fit is proposed in Prada et al. (2006). At very large radii the DM density profile should not tend to zero as the NFW profile does, but instead it should tend to the mean matter density of the Universe. Then, the modified profile is:

$$\rho_{\rm mod}(s) = \frac{\rho_s^{\rm mod}}{cs\,(1+cs)^2} + \bar\rho \tag{8}$$

The parameter $\rho_s^{\rm mod}$ is no longer given by Eq. (5). If we use the condition (4) we obtain in this case:

$$\rho_s^{\rm mod} = 113\,c^3 g(c)\bar\rho = \rho_s^{\rm NFW} - \frac{1}{3}c^3 g(c)\bar\rho \tag{9}$$

In addition, cosmological DM halo density profiles show a tiny or null influence on the concentration parameter at large distances ($r > R_{\rm vir}$), so that the density profile in the halo outskirts can only depend on the remaining parameter $M_{\rm vir}$. Therefore, in order to approximate the transition to the outer regions we add a function $f$ which depends only on $s$ (i.e. on the virial radius, but not on the concentration). This makes $M_{\rm vir}$ the only relevant parameter at large distances from the halo centre. The new density profile approximation that we propose here is a simple extension of the NFW formula, i.e.,

$$\rho(s) = \frac{\rho_s}{cs\,(1+cs)^2} + \bar\rho + f(s)\bar\rho \tag{10}$$

where $f(s)$ is the new function that we are proposing in order to improve the fit to the external parts of DM haloes. We choose the following rational function:

$$f(s) = \frac{b_1}{s} + \frac{b_2}{s+1} \tag{11}$$

There are several reasons for this choice. On the one hand, we aim for a simple formula which allows an easy calculation for the tangential shear. On the other hand, we want to minimize the influence of the new added parameters ($b_1$ and $b_2$) on the internal profile, where the NFW profile is steeper, except for the very inner regions in which NFW and $f(s)$ are both proportional to $r^{-1}$. We thus propose in this work the following model as an approximation of the density profile from the inner regions up to large distances well beyond $R_{\rm vir}$:

$$\rho(s) = \frac{\rho_s}{cs\,(1+cs)^2} + \left(\frac{b_1}{s} + \frac{b_2}{s+1} + 1\right)\bar\rho \tag{12}$$

It is worth noting that the enclosed mass and the characteristic density are now given by these relations:

$$\begin{aligned} M(s) \;&=\; \frac{3\,M_{\rm vir}}{340}\left[\frac{\rho_s}{c^3 g(cs)\bar\rho} + b_1\frac{s^2}{2} + \right. \\ &+\; \left. b_2\left(\ln(s+1) - s + \frac{s^2}{2}\right) + \frac{s^3}{3}\right] \end{aligned} \tag{13}$$

$$\rho_s = \rho_s^{\rm NFW} - \left[\frac{1}{3} + \frac{1}{2}b_1 + \left(\ln 2 - \frac{1}{2}\right)b_2\right]c^3 g(c)\bar\rho \tag{14}$$

Applying the condition (4) to the expression (13) leads to Eq. (14), which quantifies the influence of external parameters $b_1$ and $b_2$ on the value of $\rho_s$. In the case of $b_1 = b_2 = 0$, which is equivalent to $f(s) = 0$, we recover the modified NFW characteristic density $\rho_s^{\rm mod}$.

An example of this new fitting formula for Milky Way size haloes is shown in Figure 1. Here we compare different approximations to fit the numerical density profile. In order to reduce the range of variation along the $y$-axis, we plot the function $(\rho/\bar\rho)\cdot(r/R_{\rm vir})^2$ instead of just $\rho/\bar\rho$. The relative errors for each one of them are also displayed. The numerical profile given by cosmological simulations (dotted line) is compared to the NFW model (Eq. 2), the modified NFW model (NFW plus the mean matter density of the Universe, Eq. 8) and our model (Eq. 12). The fit in the inner part is quite similar for all the models as expected. There is an obvious discrepancy beyond the virial radius between the NFW fit, the modified NFW approach, and the data from numerical simulations. Our model helps to alleviate this disagreement, providing a reasonable fit going from the inner regions to well beyond the virial radius up to $10R_{\rm vir}$.

The description of the DM distribution from small to large distances from the centre of a halo presents an added

**Table 1.** Results of the fitting of our approximation to average halo density profiles in different mass bins. The first column sets the name of the bin, the second shows the number of distinct haloes in each mass range, the third corresponds to the mass range in logarithmic scale, the fourth is the mean virial mass in this range, the fifth the concentration in the NFW model, the sixth, seventh and eighth show the best-fitting values of the parameters of our approximation. The ninth and tenth columns indicate the position of the local extrema in the numerical density profiles.

| Name | Number of haloes | Mass range $\log_{10}(M_{\rm vir}[h^{-1}M_{\odot}])$ | $< M_{\rm vir} >$ $[h^{-1}M_{\odot}]$ | $c_{\rm NFW}$ | $c$ | $b_1$ | $b_2$ | $s_{\rm max}$ | $s_{\rm min}$ |
|---|---|---|---|---|---|---|---|---|---|
| H1 | 3512 | [ 11.5 , 12.0 ) | $5.35 \times 10^{11}$ | 12.99 | 12.43 | -19.00 | 24.17 | 0.080 | 2.623 |
| H2 | 4591 | [ 12.0 , 12.5 ) | $1.64 \times 10^{12}$ | 10.84 | 10.15 | -23.43 | 30.01 | 0.097 | 2.661 |
| H3 | 1719 | [ 12.5 , 13.0 ) | $5.08 \times 10^{12}$ | 9.40 | 8.73 | -27.83 | 34.57 | 0.112 | 2.750 |
| H4 | 4894 | [ 13.0 , 13.5 ) | $1.58 \times 10^{13}$ | 7.99 | 7.19 | -33.87 | 41.61 | 0.134 | 2.797 |
| H5 | 1509 | [ 13.5 , 14.0 ) | $4.82 \times 10^{13}$ | 7.52 | 6.82 | -37.11 | 45.18 | 0.141 | 2.820 |
| H6 | 384 | [ 14.0 , 14.5 ) | $1.48 \times 10^{14}$ | 6.75 | 6.12 | -44.20 | 52.95 | 0.155 | 2.872 |
| H7 | 68 | [ 14.5 , 15.0 ) | $4.47 \times 10^{14}$ | 5.76 | 5.26 | -48.94 | 58.04 | 0.177 | 2.954 |

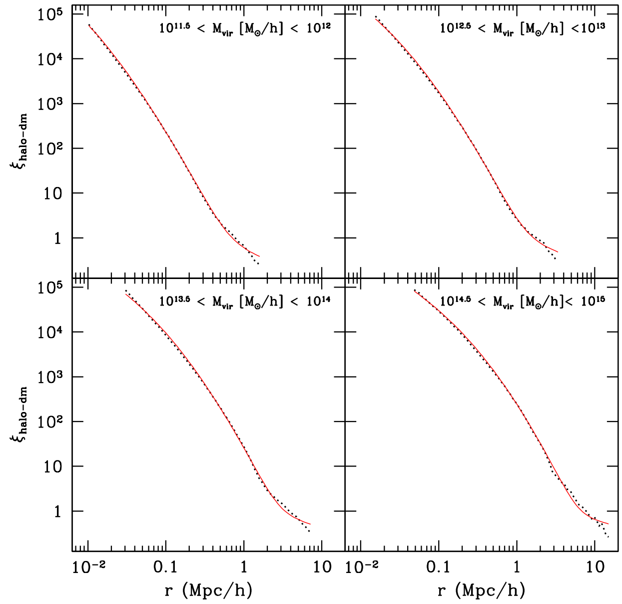

**Figure 2.** Halo-dark matter correlation function $\xi_{\rm Halo-DM}$ for average haloes in four different mass bins. The solid line represents our approximation whereas the dotted curves are the results from numerical simulations.

relevance as it is related to the halo-dark matter correlation function $\xi_{\rm Halo-DM} = \frac{\langle\rho(r)\rangle - \bar{\rho}}{\bar{\rho}}$ (e.g. Hayashi & White 2008). Therefore, our approximation for the density profiles in the outer regions of DM haloes is also showing information about this correlation function. In Figure 2 we display $\xi_{\rm Halo-DM}$ for different bins in the mass range covered in this paper (see Section 3). In this plot we can clearly distinguish between the one-halo term, which corresponds to the halo density profile, and the two-halo term, which corresponds to the distribution of matter in its outskirts. Our approximation provides a reasonable description in both regions.

## 3 FIT TO SIMULATED DENSITY PROFILES

To carry out our analysis we have used several high-resolution cosmological simulations. The initial conditions of these simulations have been set up from the power spectrum corresponding to the ΛCDM model with the following values of the cosmological parameters: $\Omega_m = 0.3$, $\Omega_\Lambda = 0.7$, $h = 0.7$ and $\sigma_8 = 0.9$. We used three different boxes whose size is 80, 120 and 250 $h^{-1}$Mpc. The mass resolution in these boxes is $3.14 \times 10^8$, $1.06 \times 10^9$ and $9.59 \times 10^9 h^{-1}M_\odot$ respectively, and the space resolution is 1.2, 1.8 and 7.6 $h^{-1}$kpc, respectively. The final output of the simulation is obtained by tracking the evolution of $512^3$ particles in each box to $z = 0$, using the $N$-body code ART (Kravtsov et al. 1997). The collapsed DM haloes are detected using Bound Density Maxima halofinder (BDM).

We use mean halo density profiles averaged over seven different virial mass bins ranging from $5.35 \times 10^{11} h^{-1}M_\odot$ to $4.47 \times 10^{14} h^{-1}M_\odot$. There is a total of 17,220 haloes in all simulation boxes but we constrain this sample with the following selection criterion in order to select distinct haloes: the centre of all selected haloes must be further than the virial radius of every halo with higher mass. This criterion reduces the number of haloes to 16,679 (see Cuesta et al. 2007 for details on this halo sample).

Figure 3 shows the best fit provided by our approximation to some average density profiles from simulations. In this plot we can see that there are deviations of the order of 15–20% at the position $s_{\rm max}$ of the local maximum of $\rho(r) \cdot r^2$. This deviation is inherited from the NFW model, where the fit to numerical density profiles usually show a noticeable disagreement at $r = r_s$. However, the transition from the internal to external regions at 2–3$R_{\rm vir}$ of the halo displays a similar difference due to the fact that our simple model is not able to reproduce the steepest region in the density profile. In Table 1 we give the results of the best fit of our model to the simulated average halo density profile for the seven different mass bins.

It is interesting to keep in mind the halo-to-halo variation of DM density profiles. This has been shown for example in Prada et al. (2006). In Figure 4 we show the root mean square in $\rho(r)$ normalized to the density profile itself. Although only small variations (at the level of 20–30%) are present inside $R_{\rm vir}$ among different haloes, the density profiles show fluctuations larger than twice the density profile itself beyond $2R_{\rm vir}$. Haloes corresponding to small masses present a larger scatter.

A regression analysis between the parameters in our approximation allows us to find that there are strong cor-

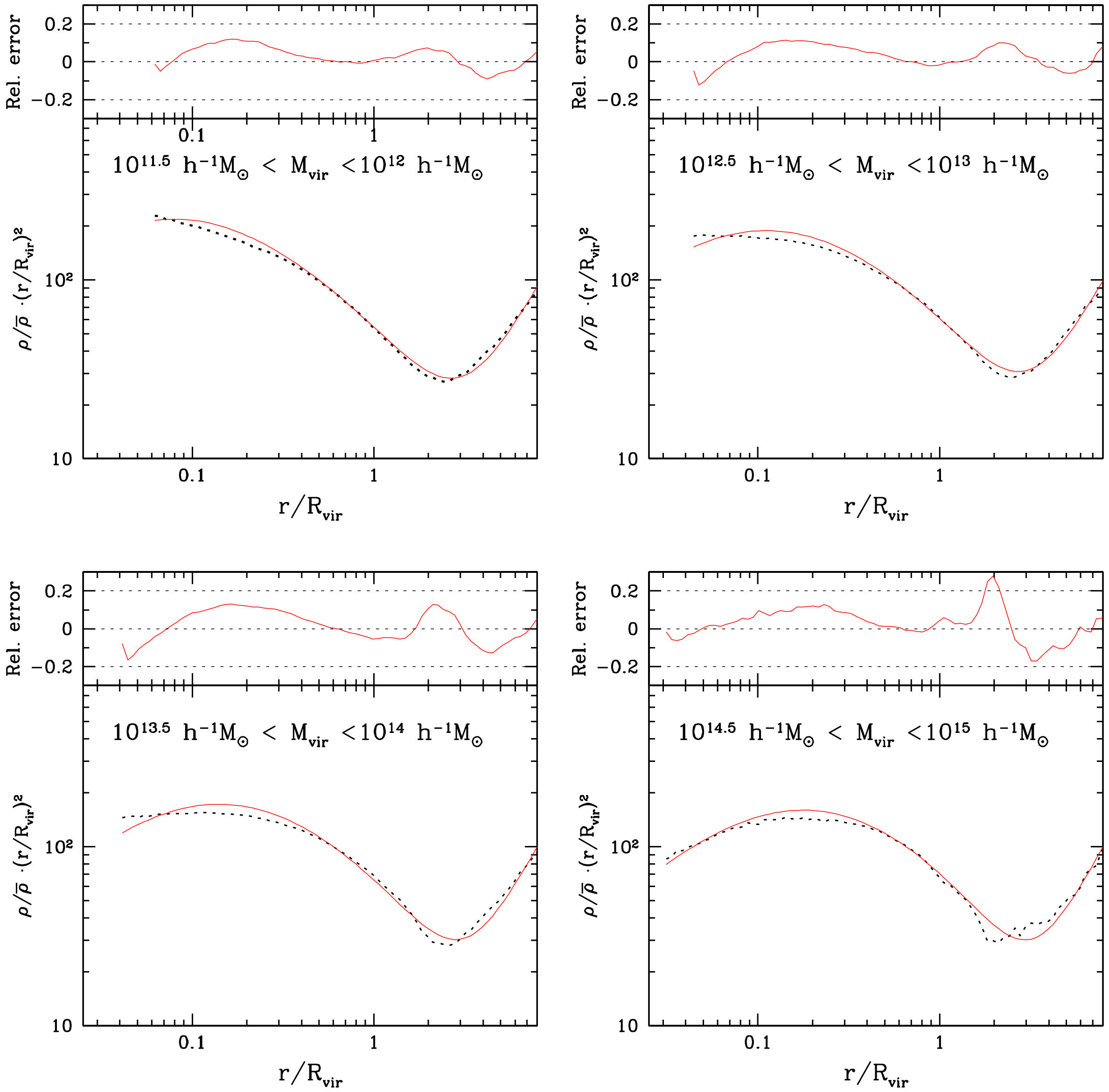

**Figure 3.** Average density profiles in four different halo mass ranges. The solid line represents the best-fit of our approximation to the numerical density profile (dotted line). The deviation around $r = r_s$ is inherited to the NFW profile, which is about the same amount of the deviation at the transition to the outer regions of the halo at 2–$3R_{\rm vir}$.

relations among them. These results are shown in Table 2. An interesting correlation occurs between the NFW concentration (hereafter $c_{\rm NFW}$) and the parameter $c$ in our model. This tight relation motivates the search for an interpretation of this parameter. We recall that in the NFW model the concentration is related to the radius in which the function $\rho(r) \cdot r^2$ presents its maximum, i.e. $s_{\rm max} = 1/c_{\rm NFW}$. It is tempting to explore whether the parameter $c$ in our model admits a similar interpretation. The condition $d/ds\left(s^2 \cdot \rho/\bar{\rho}\right) = 0$ is a sixth degree polynomial equation with two real and positive solutions, $s_{\rm max}$ and $s_{\rm min}$, corresponding to the local maximum and minimum of this function respectively. The numerical solutions for $s_{\rm max}$ and $s_{\rm min}$ are shown in the last two columns of Table 1. The correlation between $c_{\rm NFW} = 1/s_{\rm max}$ and $c$ turns out to be:

$$\frac{1}{s_{\rm max}} = 0.967(\pm 0.004) \cdot c + 0.53(\pm 0.03) \qquad (15)$$

with a Pearson correlation coefficient of $1 - r^2 = 7.3 \times 10^{-5}$ showing this evident connection. This means that our parameter $c$, which is no longer related to the position of the local maximum of $\rho(r)r^2$ due to the addition of $f(s)$, still

**Table 2.** Results from the regression analysis. The first two columns display the name of the correlated variables (dependent and independent variable respectively). In the remaining columns, the value of Pearson's correlation coefficient, the coefficients of the regression equations and their standard deviations are shown. In the first four rows a linear regression is performed between both variables ($y = mx + n$), whereas in the last two rows a quadratic relationship is shown ($y = px^2 + mx + n$).

| y | x | $r^2$ | $n$ | $\sigma_n$ | $m$ | $\sigma_m$ | $p$ | $\sigma_p$ |
|---|---|---|---|---|---|---|---|---|
| $c_{\rm NFW}$ | $c$ | 0.9985 | 0.66 | 0.15 | 1.00 | 0.02 | - | - |
| $\log(c_{\rm NFW})$ | $\log(M_{\rm vir})$ | 0.9857 | 2.44 | 0.08 | -0.115 | 0.006 | - | - |
| log c | $\log(M_{\rm vir})$ | 0.9788 | 2.50 | 0.11 | -0.122 | 0.008 | - | - |
| $b_1$ | $b_2$ | 0.9994 | 2.9 | 0.4 | -0.890 | 0.0010 | - | - |
| $b_2$ | $c$ | 0.9904 | 121 | 8 | -15 | 2 | 0.58 | 0.11 |
| $b_1$ | $c$ | 0.9905 | -107 | 8 | 14 | 2 | -0.56 | 0.10 |

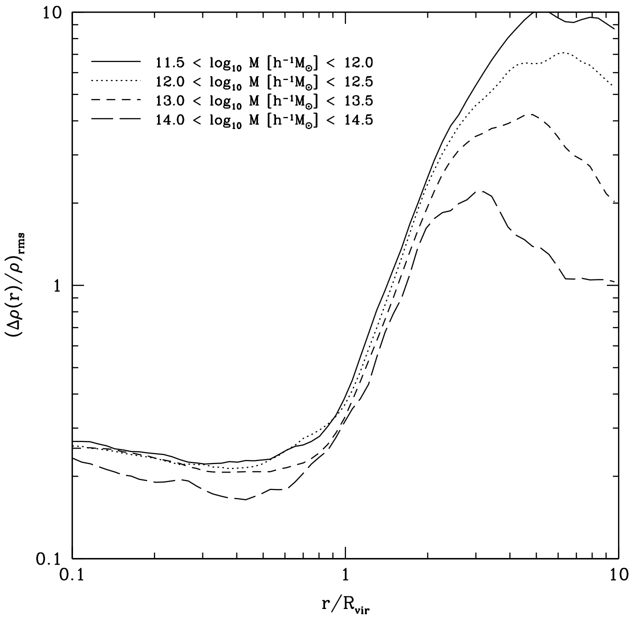

**Figure 4.** Halo-to-halo variation of DM density profiles in four different mass bins. Whereas the fluctuations compared to the magnitude of the density profile are small below $1R_{\rm vir}$, they become very large around $r \gtrsim 2R_{\rm vir}$. At large distances, this scatter is higher for decreasing halo mass. This effect is not an artifact of the different behaviour of mean density profile at large distances, but the intrinsic scatter due to halo environment.

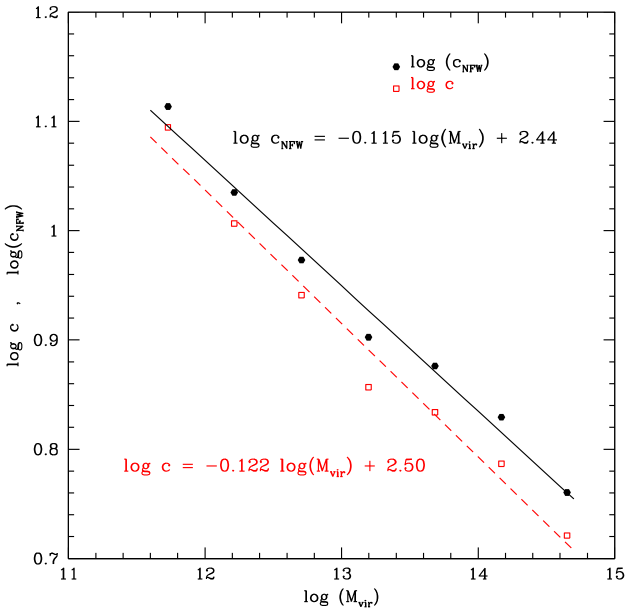

**Figure 5.** The correlation between the average virial mass in the mass bins under study and the concentration parameters, i.e. both the usual NFW concentration (solid circles) and the $c$ in our approximation (open circles). Solid and dashed lines represent the best fit to a power-law for $c_{\rm NFW}(M_{\rm vir}$ and $c(M_{\rm vir}$, respectively.

retains its original interpretation, with only a small variation in its value. The function $f(s)$ has therefore very little influence in the inner regions, i.e. in the NFW term of our approximation.

The correlation between the NFW concentration and the virial mass is already well-known (e.g. Macciò et al. 2007). Therefore, the relationship between our parameter $c$ and $M_{\rm vir}$ is straightforward as shown in Figure 5 for our sample average halo profiles. This correlation is extremely useful as it will allow us to derive simple mathematical expressions for the outer density profile in terms of the parameter $c$, which would be more complicated if they are written in terms of the virial mass. However, it is important to remark that this choice is just for our convenience, as we know that the parameter $c$ has no effect in the outer halo regions.

Something more surprising arises when we examine the relation among the fitted parameters $b_1$, $b_2$ and $c$ (as it can be readily seen from the last two rows in Table 2). This allows us to remove two parameters from our density model (Eq. 12) as $b_1$ and $b_2$ can be expressed in terms of $c$ with little scatter.

Thus, taking into account that the parameters $\rho_s$, $b_1$ and $b_2$ are a function of $c$, expression (12) turns into:

$$\begin{aligned}\frac{\rho(s)}{\bar\rho} &= \frac{\rho_s(c)/\bar\rho}{cs\ (cs+1)^2} + \frac{b_1(c)}{s} + \frac{b_2(c)}{s+1} + 1 = \\ &= \underbrace{\frac{\rho_s/\bar\rho}{cs\ (cs+1)^2}}_{\text{internal}} + \underbrace{\frac{(b_1+b_2)s+b_1}{s(s+1)}}_{\text{middle}} + \underbrace{1}_{\text{external}} \qquad (16)\end{aligned}$$

where $\rho_s(c)/\bar\rho$, $b_1(c)$ and $b_2(c)$ are no longer free parameters but fixed in terms of $c$. This dependence is determined by

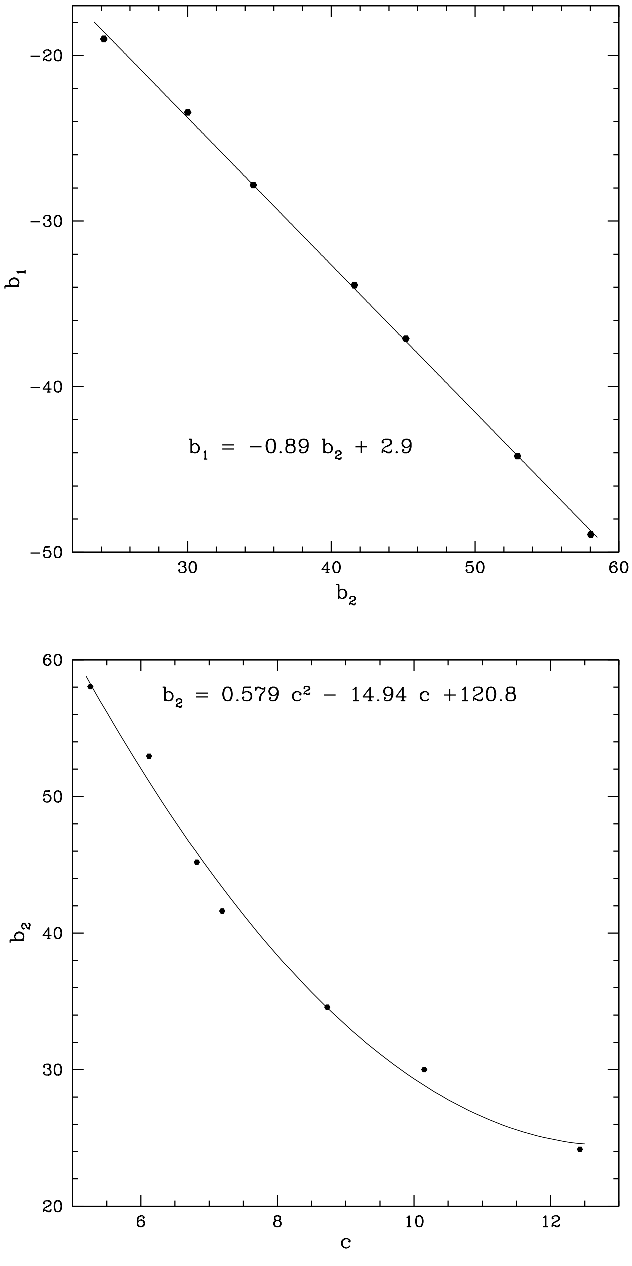

**Figure 6.** *Top panel*: correlation between the parameters $b_1$ and $b_2$ in our approximation. There is a tight linear correlation between both parameters which describe the outskirts of the density profile, so our model gains simplicity. *Bottom panel*: correlation between the parameters $b_2$ and $c$ in our approximation. Although a linear regression fails in order to find a correlation of this two parameters, the quadratic regression works reasonably well.

the expression (14) and the values shown in the last two rows in Table 2, i.e.,

$$\begin{array}{rclll} \rho_s/\bar{\rho}(c) & = & 0.167\,c^2 & -4.12\,c & +143.4 \\ b_2(c) & = & 0.579\,c^2 & -14.94\,c & +120.8 \\ b_1(c) & = & -0.558\,c^2 & +14.02\,c & -107.4 \end{array} \qquad (17)$$

**Table 3.** Results of the constrained fitting of our approximation to halo density profiles. As opposed to Table 1, here $c$ is the only free parameter, whereas the values of $b_1(c)$ and $b_2(c)$ are obtained using Eq. (17) for the best-fit value of $c$. We include the fourth and fifth column to allow direct comparison with Table 1.

| Name | $M_{\rm vir}$ ($M_\odot$/h) | c | $b_1(c)$ | $b_2(c)$ |
|---|---|---|---|---|
| H1 | $5.35 \times 10^{11}$ | 12.42 | -19.32 | 24.60 |
| H2 | $1.64 \times 10^{12}$ | 10.12 | -22.66 | 28.95 |
| H3 | $5.08 \times 10^{12}$ | 8.77 | -27.37 | 34.35 |
| H4 | $1.58 \times 10^{13}$ | 7.12 | -35.89 | 43.82 |
| H5 | $4.82 \times 10^{13}$ | 6.80 | -37.89 | 46.02 |
| H6 | $1.48 \times 10^{14}$ | 6.17 | -42.17 | 50.70 |
| H7 | $4.47 \times 10^{14}$ | 5.26 | -49.12 | 58.27 |

It is important to realize that Eq. (16) has been grouped in such a way that each term is related to a region of the halo density profile (internal, middle and external, respectively).

After the elimination of $b_1$ and $b_2$, we obtain again the best-fit for the only free parameter $c$, taking into account that now the values of $b_1$ and $b_2$ are fixed and can be obtained using Eq. (17). We note that Eq. (17) implicitly includes the correlation between $c$ and $M_{\rm vir}$, as the use of the parameter $c$ instead of $M_{\rm vir}$ makes this expression much simpler. We have chosen this form for our mere convenience although $c$ has nothing to do with the outer halo regions. The results are given in Table 3, where the fourth and fifth column allows a comparison with Table 1. Only small differences about few per cent are present between the best-fit values for $b_1$ and $b_2$ in Table 1 and the new results for the best-fit value of $c$ in Table 3.

Apart from the discrepancies already shown in Figure 3, we also note that the slope in the density profiles from the simulations tends to be shallower as compared to our approximation starting around 8 virial radii. We therefore address the issue of the range of validity of our approximation. In order to study this, we will use a density profile which extends up to nearly 30 virial radii (see Fig. 7).

At these very large distances we are able to analyse the asymptotic behaviour of both numerical and approximated density profiles. To this aim, it is more useful to use the function $y = (\rho/\bar{\rho})\ s$ since we can study its oblique asymptote. If we multiply Eq. (12) by $s$ we obtain that the asymptotic behaviour is:

$$y = s + b_1 + b_2 \qquad (18)$$

The leading term at large distances corresponds to the trend of the density profile to have the same value as the mean matter density in the Universe, but there is also a dependence on the coefficients $b_1$ and $b_2$. In Figure 8 we can also see that this dependence makes our approximation slightly shifted by a constant value $b_1 + b_2$ with respect to the data from cosmological simulations. This means that the $\mathcal{O}(1/r)$ terms in our approximation are still important in the range from 10 to $\sim 30R_{\rm vir}$ just before entering the asymptotic regime where the density profile tends to the constant mean matter density $\bar{\rho}$.

This shows the limitations of our approximation: while it provides a reasonable fit up to 10 virial radii, the goodness

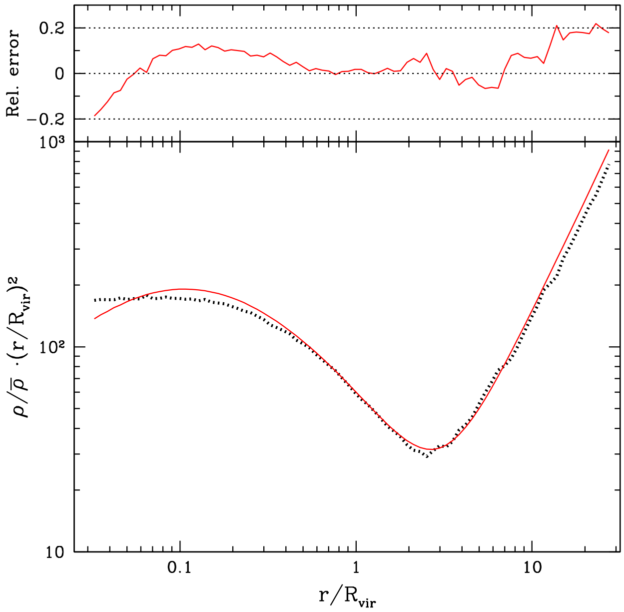

**Figure 7.** The density profile of an average halo with $M_{\rm vir} \simeq 5{\times}10^{12}\ h^{-1}M_{\odot}$ up to nearly $30R_{\rm vir}$. Although our approximation implements the right trend at large distances from the halo centre, residuals of the order of $1/r$ are amplified since the density profile is multiplied here by $r^2$.

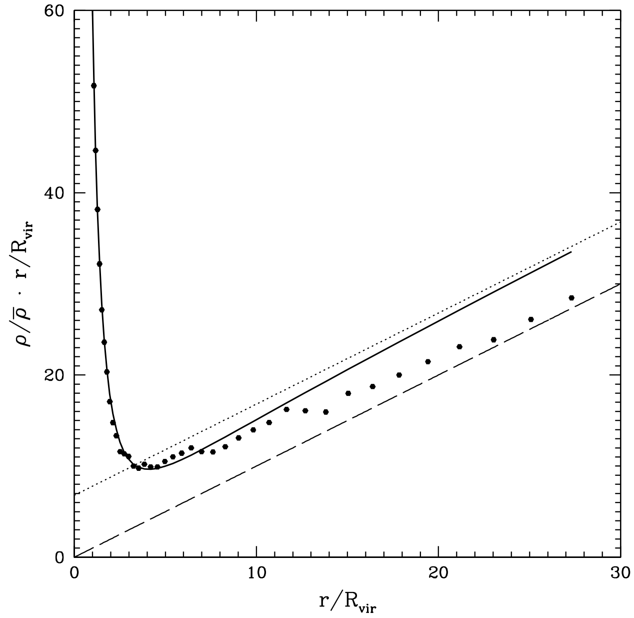

**Figure 8.** The density profile $\rho/\bar{\rho}$ times $r/R_{\rm vir}$ versus $r/R_{\rm vir}$ for our approximation (solid line) and the data from numerical simulations (solid circles). The dashed and the dotted lines represent the oblique asymptotes which correspond to our fit and the simulation data, respectively. The vertical shift between both asymptotes shows the presence of $1/r$ errors in our approximation.

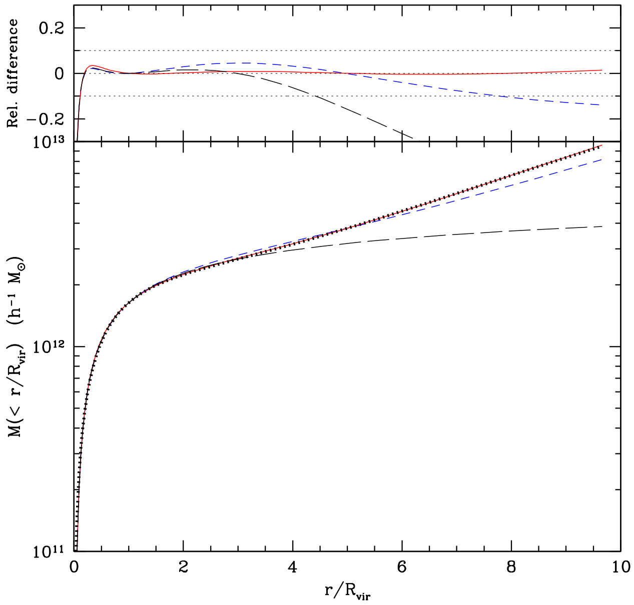

**Figure 9.** Enclosed mass in a sphere of radius $r$ versus $r/R_{\rm vir}$ for the average halo with $M_{\rm vir} \simeq 10^{12}h^{-1}M_{\odot}$. The dotted curve represents the simulation data, long dashed and short dashed lines show the plain NFW and the modified NFW profile (i.e. NFW plus the mean matter density $\bar{\rho}$) respectively. The solid line is our approximation. Top panel represents the relative errors with respect to the simulation data.

of the fit is not so good at larger distances. This is mainly due to the simplicity of the approximation, which is one of the premises in our model. Of course, we can always add more rational terms to our function $f$ but this would complicate the model and the interpretation of the different terms. However, the density at distances larger than $10R_{\rm vir}$ is similar to the mean matter density, e.g. $\rho(s > 8) < 1.5\bar{\rho}$. With this in mind, we can calculate the enclosed mass in a sphere of a given radius, and compare with our approximation (see Figure 9). We can see that even comparing with the modified NFW density profile (i.e. NFW plus the mean matter density in the Universe), our approximation is a significant improvement regarding the enclosed mass. While the modified NFW profile can overestimate the enclosed mass by 5% at $3R_{\rm vir}$, and underestimate it by 10% at $8R_{\rm vir}$, our approximation keeps this uncertainty below 2% even at $10R_{\rm vir}$, which makes our simple model more than enough for this application. On the contrary, the plain NFW profile is not suitable beyond $4R_{\rm vir}$ in order to estimate the enclosed mass, as the estimated mass falls short by more than a factor of two with respect to the data from the simulations at $10R_{\rm vir}$ (see Figure 9).

## 4 APPLICATION TO GRAVITATIONAL LENSING

One of the most relevant experimental techniques for determining the distribution of dark matter is based on the gravitational lensing effect (for some specific applications, see e.g.

Gavazzi et al. 2003, Broadhurst et al. 2005, Johnston et al. 2007, Mandelbaum et al. 2006, Mandelbaum et al. 2008). In these observations the quantity in which we are interested is the tangential shear $\gamma_t$, which describes the image elongation perpendicular to the line connecting the image from the source and the distorting lens. This quantity is related with the surface mass density $\Sigma$ (projected on the lens plane, which is perpendicular to the trajectory of the incoming ray), through the following formula:

$$\gamma_t(R) = \frac{\Delta\Sigma}{\Sigma_{crit}} = \frac{\bar{\Sigma}(<R) - \Sigma(R)}{\Sigma_{crit}} \tag{19}$$

where $R$ is the radial coordinate projected on the plane of the lens (impact parameter). $\bar{\Sigma}(<R)$ is the mean surface density enclosed in a radius $R$, and $\Sigma_{crit}$ is the critical surface density, which depends from the distance between the lens and the source, i.e.,

$$\Sigma_{crit} = \frac{c^2}{4\pi G}\,\frac{D_S}{D_L D_{LS}} \tag{20}$$

where $D_S$, $D_L$ and $D_{LS}$ are the distance to the source, the distance to the lens, and the distance between the source and the lens, respectively.

In fact, the quantity which can be observed is the shear in units of critical density $\Delta\Sigma(R)$. We can derive its expression using our approximation for the dark matter halo density profile.

The surface mass density is given by the following formula, i.e. the projection of the volume density $\rho(r)$ in the line of sight:

$$\Sigma(R) = 2\int_R^{+\infty} \rho(r)\frac{r}{\sqrt{r^2 - R^2}}\;dr. \tag{21}$$

instead, the mean surface density is defined as follows:

$$\bar{\Sigma}(<R) = \frac{1}{R}\int_0^R \Sigma(R')\;dR'. \tag{22}$$

For simplicity in our calculations, we use distances which are scaled to the virial radius ($s \equiv \frac{r}{R_{\rm vir}}$; $S \equiv \frac{R}{R_{\rm vir}}$). Therefore, the last two equations transform into:

$$\Sigma(S) = 2R_{\rm vir}\int_S^{+\infty} \rho(s)\frac{s}{\sqrt{s^2 - S^2}}\;ds \tag{23}$$

$$\bar{\Sigma}(<S) = \frac{1}{S}\int_0^S \Sigma(S')\;dS' \tag{24}$$

where we choose for $\rho(s)$ our approximation for the density profile given by Eq. (16), in which $b_1$ and $b_2$ are functions which depend on our parameter $c$ as explained in the previous section, i.e.,

$$\rho(s) = \underbrace{\frac{\rho_s}{cs\,(1+cs)^2}}_{\rho_{int}(s)} + \underbrace{\frac{b_1(c)}{s}\bar{\rho} + \frac{b_2(c)}{s+1}\bar{\rho}}_{\rho_{mid}(s)} + \bar{\rho} \tag{25}$$

Now we compute the tangential shear for this density profile. As we can separate the contributions from different terms in Eq. (25) due to linearity of the integrals in the definition of the shear, we will calculate each term (i.e. the internal, the middle region and the contribution from background density) separately. The last term has associated a trivial contribution, because it is a known fact that for any homogeneous density field the tangential shear is null. Therefore, in the case of the background density we obtain $\Delta\Sigma_b(S) = 0$.

### 4.1 Internal tangential shear

The first term in this equation is formally identical to the NFW model and the surface mass density $\Sigma$ for this model has already been determined by Bartelmann (1996):

$$\Sigma_{int}(S) = \frac{2\rho_s R_{\rm vir}}{c}\int_S^{+\infty} \frac{ds}{(cs+1)^2\sqrt{s^2 - S^2}} \tag{26}$$

$$\Sigma_{int}(S) = \begin{cases} \frac{2\rho_s\;R_{\rm vir}}{c}\,\frac{1-\phi(cS)}{c^2S^2-1} & \text{if} \quad S \neq \frac{1}{c} \\ \\ \frac{2\rho_s\;R_{\rm vir}}{3c} & \text{if} \quad S = \frac{1}{c} \end{cases} \tag{27}$$

where $\phi$ is given by:

$$\phi(x) = \begin{cases} \frac{\text{atanh}\sqrt{1-x^2}}{\sqrt{1-x^2}} & 0 < x < 1 \\ \\ 1 & x = 1 \\ \\ \frac{\text{arctan}\sqrt{x^2-1}}{\sqrt{x^2-1}} & x > 1 \end{cases} \tag{28}$$

On the other hand, we get from the calculation of the mean surface density:

$$\bar{\Sigma}_{int}(<S) = \frac{2\rho_s R_{\rm vir}}{c}\begin{cases} \int_0^S \frac{1-\phi(cS')}{c^2S'^2-1}dS' & 0 < S < 1/c \\ \\ 1/c & S = 1/c \\ \\ \frac{1}{c} + \int_{1/c}^S \frac{1-\phi(cS')}{c^2S'^2-1}dS' & S > 1/c \end{cases} \tag{29}$$

and hence we can write this in terms of $\phi$, i.e.:

$$\bar{\Sigma}_{int}(<S) = \frac{2\rho_s\;R_{\rm vir}}{c}\;\phi(cS). \tag{30}$$

Therefore the tangential shear $\Delta\Sigma_{int}(S) = \bar{\Sigma}_{int}(<S) - \Sigma_{int}(S)$ is:

$$\Delta\Sigma_{int}(S) = \frac{2\rho_s R_{\rm vir}}{c}\begin{cases} \frac{c^2S^2\phi(cS)-1}{c^2S^2-1} & S \neq 1/c \\ \\ 2/3 & S = 1/c \end{cases} \tag{31}$$

So, if we introduce for our convenience the function $\psi$ defined as follows:

$$\psi(x) = \begin{cases} \frac{x^2\phi(x)-1}{x^2-1} & x \neq 1 \\ \\ 2/3 & x = 1 \end{cases} \tag{32}$$

We can simply write the tangential shear for the internal region in this form:

$$\Delta\Sigma_{int}(S) = \frac{2\rho_s\;R_{\rm vir}}{c}\;\psi(cS) \tag{33}$$

### 4.2 Middle tangential shear

The second and third terms in the equation (25) represent the contribution from the intermediate region of the density profile to the tangential shear. For $\rho_{mid}(s) = \left(\frac{b_1(c)}{s} + \frac{b_2(c)}{s+1}\right)\bar{\rho}$ the surface density is:

$$\begin{aligned}\Sigma_{mid}(S) &= 2R_{\rm vir}\bar{\rho}\int_S^{\infty}\frac{(b_1(c)+b_2(c))\ s\ ds}{(s+1)\sqrt{s^2-S^2}}\\ &= 2R_{\rm vir}\bar{\rho}\left[(b_1+b_2)\lim_{\xi\to+\infty}\ln\frac{\sqrt{\xi^2-S^2}+\xi}{S}+\phi(S)\right]\end{aligned}$$

where $\phi(s)$ is defined in the same way as above, and for the mean surface density we get:

$$\begin{aligned}\bar{\Sigma}_{mid}(<S) &= 2R_{\rm vir}\bar{\rho}\Bigg[(b_1+b_2)+\\ &+\ (b_1+b_2)\lim_{\xi\to\infty}\ln\frac{\sqrt{\xi^2-S^2}+\xi}{S}+\frac{b_1}{S}\int_0^S\phi(S')\ dS'\Bigg]\end{aligned}$$

The tangential shear from the intermediate region is therefore:

$$\Delta\Sigma_{mid}(S) = 2R_{\rm vir}\bar{\rho}\left[b_1+b_2\left(1+\phi(S)-\frac{1}{S}\int_0^S\phi(S')dS'\right)\right] \quad (34)$$

Unfortunately there is no primitive function for $\phi$ which could be written in terms of elementary functions. Nevertheless, it is possible to find a fitting function for it. We will fit $\frac{1}{S}\int_0^S\phi(S')dS'-\phi(S)$ over the interval $s\in[0,10]$ using the function $\frac{1}{1+(x/a)}$. The result is:

$$\frac{1}{S}\int_0^S\phi(S')dS'-\phi(S)\approx\frac{1}{1+(\frac{S}{4.8})}. \quad (35)$$

We are now in a position to write down the complete expression of the tangential shear in units of the critical density for our model, i.e.,

$$\Delta\Sigma(S) = 2R_{\rm vir}\bar{\rho}\left[\frac{\rho_s}{\bar{\rho}\ c}\psi(cS)+b_1+b_2\left(\frac{S}{4.8+S}\right)\right]. \quad (36)$$

We can now compare this tangential shear with that one given by the NFW model (which is formally identical to $\Delta\Sigma_{int}(S)$, except that we have to replace $\rho_s$ and $c$ by $\rho_s^{\rm NFW}$ and $c_{\rm NFW}$ respectively):

$$\Delta\Sigma_{\rm NFW}(S) = \frac{2\rho_s^{\rm NFW}\ R_{\rm vir}}{c_{\rm NFW}}\ \psi(c_{\rm NFW}S) \quad (37)$$

In Figure 10 we show the relative difference between $\Delta\Sigma_{\rm NFW}(S)$ (which does not account for external region of the halo) and $\Delta\Sigma(S)$ as given by our model for the different halo mass bins. The differences are small and always below 4%. They are not appreciable at the level of current experimental sensitivity. As expected, the contribution from the matter distribution in the outer regions of DM haloes is small, but for the first time it has been estimated to what extent it may have influence in the measurement of the tangential shear. Besides, we find an obvious trend with halo mass: the difference between both $\Delta\Sigma_{\rm NFW}(S)$ and $\Delta\Sigma(S)$ is higher for most massive haloes.

## 5 DISCUSSION AND CONCLUSIONS

In this paper we have presented a simple approximation for the DM density profiles of haloes with masses ranging from $10^{11.5}$ to $10^{15.0}h^{-1}M_{\odot}$, which is valid even beyond the virial radius up to $\sim 10R_{\rm vir}$. The expression we are suggesting here is $\rho(s)=\frac{\rho_s}{cs(1+cs)^2}+\left(\frac{b_1}{s}+\frac{b_2}{s+1}+1\right)\bar{\rho}$, where $s=r/R_{\rm vir}$. This approximation is an extension of the NFW formula but includes two additional parameters. We have shown that these parameters are very well correlated with the virial mass, so that the density profile is effectively just a function of $M_{\rm vir}$. Other approximations found in the literature will prove to be useful to describe, with high accuracy, the halo density profile up to the virial radius. Yet, most of them fail when they are applied to fit the outer regions, where the mass predicted by extrapolation of these profiles is far below the actual mass in these regions.

The description of DM distribution far away from the halo centre is especially interesting. In particular, the halo–dark matter correlation function is related in a straightforward way to the *average* density profile. Although the transition from the one-halo term to the two-halo term in this correlation function is present before $10R_{\rm vir}$, our approximation has turned out to be a reasonable description of the DM distribution even at these distances. In order to build the numerical mean density profiles, we averaged over many hundreds of haloes from high-resolution cosmological simulations so that the profiles corresponding to most of our mass bins are entirely unaffected by statistics. This procedure for averaging density profiles is analogue to the stacking method, used in observational studies like the one by Mandelbaum et al. (2008) to infer the density profile of a cluster of galaxies. This similarity is useful for the comparison of the results from cosmological simulations to the real data.

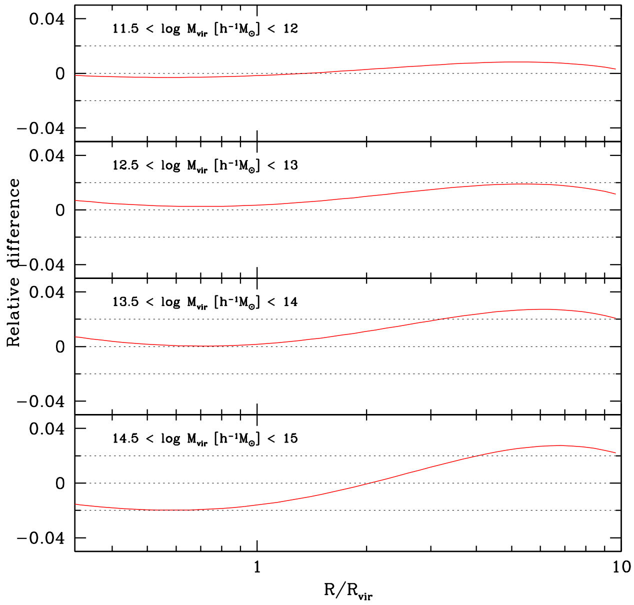

**Figure 10.** The relative difference between the tangential shear (in units of critical surface density) for NFW approximation and our model, $(\Delta\Sigma_{\rm NFW}(S)-\Delta\Sigma(S))/\Delta\Sigma(S)$, in four different mass ranges.

This parametrization for the average density profile is accurate to within 10–15% in the range from $0.05R_{\rm vir}$ to $10R_{\rm vir}$. There are two main discrepancies from the numerical density profile which have a different origin: whereas the overestimation around $r = r_s$ is inherited from NFW profile, the overestimation just beyond the virial radius suggests that our model is not able to reproduce the steepest region. This steep region just outside $R_{\rm vir}$ is more pronounced for most massive haloes, suggesting a depletion of the halo outskirts due to dark matter infall (Prada et al. 2006, Cuesta et al. 2007). The presence of our additional terms with respect to the NFW formula has only a very small influence on the inner regions of the density profile, so that our approximation can also be considered as an extension of the NFW profile. At larger distances our model shows deviations around 20% in the range 10–$30R_{\rm vir}$ just before entering the asymptotic regime. These deviations are caused by our additional $(r/R_{\rm vir})^{-1}$ terms which improve the fit in the interesting region below $10R_{\rm vir}$ where the density is much higher. In any case, we must remark that our approximation implements the correct asymptotic behaviour: the density profile tends to the asymptotic value of the mean matter density of the Universe $\bar{\rho}$.

The cumulative mass inside a sphere of a given radius is underestimated by more than 50% at $10R_{\rm vir}$ by the NFW formula. On the contrary, it is much better approximated (to within 12%) when the NFW profile is modified by addition of the mean matter density, although with our model the difference with numerical density profiles is reduced even up to 1% in the range 1–$9R_{\rm vir}$. This is especially interesting for new measurements of the enclosed mass beyond virial radius in X-ray clusters (George et al. 2008), where plain NFW is still used even at $r > 1R_{\rm vir}$. While current observations cannot distinguish between modified NFW and our approximation, in the near future they should be able to find the need for adding the mean matter density term to the density profile.

We have also presented an application for our approximation in the context of mass estimation using gravitational lensing effect. We derived expressions for tangential shear corresponding to different regions around the halo, which are in turn related to the different terms in our approximation. The contribution from the outer regions is small as compared to the contribution of the inner region, as expected. We calculated the difference between this tangential shear and the one derived from the NFW profile as a function of distance, showing that the inclusion of the outer regions produces a difference around 4% . This small difference could provide an observational test for the validity of our approximation, which has been derived from the results of cosmological $N$–body simulations. Although present resolution of weak lensing experiments prevents us from drawing a robust conclusion, the stacking of different observations should prove that this approximation, which includes the contribution of external regions, is more realistic than most of the so far proposed density profiles, which do not account for them.

HT wants to thank the I.E.S. José Cadalso for allowing him to combine this research with his teaching duties. FP, AJC and MASC thank the Spanish MEC under grant PNAYA 2005-07789 for their support. AK acknowledges support from NASA and NSF grants to NMSU. AJC acknowledges the financial support of the MEC through Spanish grant FPU AP2005-1826. MASC acknowledges the financial support of the CSIC through Spanish grant I3P.

## REFERENCES

Ascasibar Y., Hoffman Y., Gottlöber S., 2007, MNRAS, 376, 393

Bartelmann M., 1996, A&A, 313, 697

Bartelmann M., Schneider P., 2001, Phys. Rep., 340, 291

Brainerd T. G., 2004, ArXiv Astrophysics e-prints (astro-ph/0409381)

Broadhurst T., Takada M., Umetsu K., Kong X., Arimoto N., Chiba M., Futamase T., 2005, ApJ, 619, L143

Cole S., Lacey C., 1996, MNRAS, 281, 716

Conroy C., Prada F., Newman J. A., Croton D., Coil A. L., Conselice C. J., Cooper M. C., Davis M., Faber S. M., Gerke B. F., Guhathakurta P., Klypin A., Koo D. C., Yan R., 2007, ApJ, 654, 153

Cuesta A. J., Prada F., Klypin A., Moles M., 2007, ArXiv e-prints (ArXiv:0710.5520)

Diemand J., Kuhlen M., Madau P., 2007, ApJ, 667, 859

Einasto J., 1965, Trudy Inst. Astrofiz. Alma-Ata, 5, 87

Gavazzi R., Fort B., Mellier Y., Pelló R., Dantel-Fort M., 2003, A&A, 403, 11

George M. R., Fabian A. C., Sanders J. S., Young A. J., Russell H. R., 2008, ArXiv e-prints (ArXiv:0807.1130)

Hayashi E., White S. D. M., 2008, MNRAS, 388, 2

Heymans C., Van Waerbeke L., Bacon D., Berge J., Bernstein G., Bertin E., Bridle S., Brown M. L., Clowe D., Dahle H., Erben T., Gray M., Hetterscheidt M., Hoekstra H. et al., 2006, MNRAS, 368, 1323

Hoekstra H., Yee H. K. C., Gladders M. D., 2004, ApJ, 606, 67

Johnston D. E., Sheldon E. S., Tasitsiomi A., Frieman J. A., Wechsler R. H., McKay T. A., 2007, ApJ, 656, 27

Kravtsov A. V., Klypin A. A., Khokhlov A. M., 1997, ApJS, 111, 73

Łokas E. L., Mamon G. A., 2001, MNRAS, 321, 155

Macciò A. V., Dutton A. A., van den Bosch F. C., Moore B., Potter D., Stadel J., 2007, MNRAS, 378, 55

Mandelbaum R., Seljak U., Cool R. J., Blanton M., Hirata C. M., Brinkmann J., 2006b, MNRAS, 372, 758

Mandelbaum R., Seljak U., Hirata C. M., 2008, ArXiv e-prints (ArXiv:0805.2552)

Mandelbaum R., Seljak U., Kauffmann G., Hirata C. M., Brinkmann J., 2006, MNRAS, 368, 715

Massey R., Rhodes J., Leauthaud A., Capak P., Ellis R., Koekemoer A., Réfrégier A., Scoville N., Taylor J. E., Albert J., Bergé J., Heymans C., Johnston D., Kneib J.-P., Mellier Y. et al., 2007, ApJS, 172, 239

Mellier Y., 1999, ARA&A, 37, 127

Merritt D., Navarro J. F., Ludlow A., Jenkins A., 2005, ApJ, 624, L85

Moore B., Governato F., Quinn T., Stadel J., Lake G., 1998, ApJ, 499, L5+

Navarro J. F., Frenk C. S., White S. D. M., 1996, ApJ, 462, 563

Navarro J. F., Frenk C. S., White S. D. M., 1997, ApJ, 490, 493

Prada F., Klypin A. A., Simonneau E., Betancort-Rijo J., Patiri S., Gottlöber S., Sanchez-Conde M. A., 2006, ApJ, 645, 1001
Prada F., Vitvitska M., Klypin A., Holtzman J. A., Schlegel D. J., Grebel E. K., Rix H.-W., Brinkmann J., McKay T. A., Csabai I., 2003, ApJ, 598, 260
Sánchez-Conde M. A., Betancort-Rijo J., Prada F., 2007, MNRAS, 378, 339
Sérsic J. L., 1968, Atlas de galaxias australes. (Obs. Astron., Univ. Nac. Córdoba)
Zaritsky D., Smith R., Frenk C., White S. D. M., 1997, ApJ, 478, 39
Zaritsky D., White S. D. M., 1994, ApJ, 435, 599

This paper has been typeset from a TEX/ LATEX file prepared by the author.

## A.3 Dark matter annihilation and decay in the Local Universe: CLUES from Fermi

Draft version June 21, 2010
Preprint typeset using LaTeX style emulateapj v. 5/25/10

# DARK MATTER ANNIHILATION AND DECAY IN THE LOCAL UNIVERSE: CLUES FROM FERMI

A. J. Cuesta[1], T. E. Jeltema[2], F. Zandanel[1], S. Profumo[3,4], F. Prada[1,5], G. Yepes[6], A. Klypin[7], Y. Hoffman[8], S. Gottlöber[9], J. Primack[3], M. A. Sánchez-Conde[10] and C. Pfrommer[11]

*Draft version June 21, 2010*

## ABSTRACT

We present all-sky *Fermi* maps of extragalactic $\gamma$-rays coming from dark matter annihilation and decay. The dark matter distribution is obtained from a constrained cosmological simulation of the Local Universe provided by the CLUES project. The dark matter density and density squared fields are then taken as inputs for the *Fermi* observation simulation tool to predict the $\gamma$-ray photon counts that *Fermi* will detect in a 5-year all-sky survey. Signal-to-noise sky maps have also been obtained by adopting the current Galactic and isotropic diffuse background models released by the *Fermi* Collaboration. We find the first theoretical evidence that point out the possibility for *Fermi* to detect $\gamma$-ray emission from extragalactic large structures, such as nearby galaxy clusters and filaments (e.g. Virgo and Coma), in particular for decaying dark matter models fitting the positron excess as measured by PAMELA. Yet, most of the results presented here are conservative since no boost from unresolved dark matter substructures, or any other enhancement like Sommerfeld effect or adiabatic contraction, is included. The analysis of the anisotropy in the angular distribution of this radiation will be shown in an upcoming paper.

*Subject headings:* astroparticle physics – dark matter – large-scale structure of Universe – gamma-rays: diffuse background – methods: numerical

## 1. INTRODUCTION

There are a large number of astrophysical evidences revealing that most of the Universe matter content is in the form of cold dark matter (DM). However, the nature of DM is still one of the most important open questions in modern physics. Many different candidates have been proposed as DM constituents (see Bertone et al. 2005 for a review on candidates, and experimental searches), yet for the time being there is no evidence in favor of any detection. One of the most studied scenarios is that of the super-symmetric weakly interacting massive particles, where $\gamma$-rays are generated as secondary products of the WIMP decay or annihilation of the adopted super-symmetric dark matter candidate (e.g. Bertone 2010). Therefore, $\gamma$-ray observations, being a complementary approach to underground searches, are a powerful tool to study the nature of DM.

At present, the Imaging Čerenkov Atmospheric Telescopes (IACTs such as MAGIC, HESS and VERITAS) together with the recently launched *Fermi* satellite offer a great opportunity to search for the $\gamma$-ray emission due to DM decay or annihilation in the MeV–TeV energy range. The main instrument on board *Fermi* is the Large Area Telescope (LAT), which is designed to explore the entire $\gamma$-ray sky in the 20MeV–300GeV energy range (Atwood et al. 2009). The *Fermi*-LAT collaboration already reported some of their results in this direction, with no detection of DM $\gamma$-ray emission in dwarf spheroidal galaxies (Abdo et al. 2010c, Aharonian et al. 2008), clusters (Ackermann et al. 2010), or spectral features (Abdo et al. 2010a, Abdo et al. 2010b). Čerenkov telescopes did not succeed in DM detection either (e.g. Albert et al. 2008, Aleksić et al. 2010). These studies are focused mainly on DM annihilation.

Despite to these negative results, the recent detection of an excess of high-energy (10-100 GeV) positrons over the standard expectation from galactic cosmic-ray models by the PAMELA experiment (Adriani et al. 2009), triggered an interest in the possibility that these positrons originate from DM in the Milky Way. Interestingly, if this were the case, the DM would need to pair-annihilate or to decay into hard leptonic final states — both to prevent over-producing antiprotons and to yield enough high-energy positrons. In turn, this is an interesting scenario for $\gamma$-ray searches, since hard final state leptons yield an unmistakable hard bremsstrahlung $\gamma$-ray spectrum.

The main aim of this letter is to study the extragalactic DM induced $\gamma$-ray emission in a constrained Local Universe cosmological simulation, as will be observed by the *Fermi* satellite in an all-sky $\gamma$-ray survey. In Section 2, we describe the cosmological simulation used to infer the DM distribution in the Local Universe. In Section 3, the *Fermi* observation simulations and the assumed particle

---

[1] Instituto de Astrofísica de Andalucía (CSIC), E-18008 Granada, Spain. E-mail: ajcv@iaa.es (AJC), fabio@iaa.es (FZ)
[2] UCO/Lick Observatories, Santa Cruz, CA 95064, USA, E-mail: tesla@ucolick.org (TEJ)
[3] Department of Physics, University of California, Santa Cruz, CA 95064, USA
[4] Santa Cruz Institute for Particle Physics, University of California, Santa Cruz, CA 95064, USA
[5] Visiting research physicist at the Santa Cruz Institute for Particle Physics, University of California, Santa Cruz, CA 95064, USA
[6] Universidad Autónoma de Madrid, Grupo de Astrofísica, E-28049 Madrid, Spain
[7] Department of Astronomy, New Mexico State University, Las Cruces, NM 88003-0001, USA
[8] Racah Institute of Physics, Hebrew University, Jerusalem 91904, Israel
[9] Astrophysical Institute Potsdam, 14482 Potsdam, Germany
[10] Instituto de Astrofísica de Canarias, E-38200 La Laguna, Tenerife, Spain
[11] Canadian Institute for Theoretical Astrophysics, Toronto ON, M5S 3H8, Canada

physics models are described. In Section 4 we present the main results from the $\gamma$-ray all-sky maps. We finally discuss the main conclusions of our work in Section 5.

## 2. CONSTRAINED SIMULATIONS OF THE LOCAL UNIVERSE

In order to get a detailed description of the DM density distribution in the Local Universe, we use a high-resolution cosmological simulation box from the CLUES Project[12]. This simulation set fits very well our main goal of getting a realistic local density field which is consistent with the $\Lambda$CDM cosmology (see Yepes et al. 2009 and Gottloeber et al. 2010 for more details). As we want to study extragalactic $\gamma$-rays from large structures such as nearby galaxy clusters, we choose the Box160CR simulation. This is a constrained realization with $1024^3$ particles in a cube of $160h^{-1}$Mpc on a side which was run using the ART cosmological code (Kravtsov et al. 1997). The initial conditions are set assuming WMAP3 cosmology (with $\Omega_m = 0.24$, $\Omega_\Lambda = 0.76$, $\Omega_b = 0.042$, $h = 0.73$, $\sigma_8 = 0.75$, and $n = 0.95$) and implements the constraints from the observed density field so that it reproduces the observed matter distribution in the Local Universe on large scales at redshift $z = 0$ (Hoffman & Ribak 1991, Klypin et al. 2003). In the simulation Box160CR the massive clusters such as Virgo, Coma and Perseus, together with the Great Attractor, are well constrained. Due to non-linear evolution, the final positions of these objects are not exactly at their true (observed) positions, with a typical error around $5h^{-1}$Mpc.

This cosmological simulation allows us to produce all-sky maps of the dark matter density and density squared, which are related to $\gamma$-ray emission due to decay and annihilation, respectively. We follow the method described in Kuhlen et al. (2008) to compute these luminosities. The associated flux is $\sum_i m_p/4\pi d_i^2$ for decay and $\sum_i m_p\rho_i/4\pi d_i^2$ for annihilation, where $m_p$ is the mass of the simulation particle, $\rho_i$ is the density associated to the $i$-th particle, computed using its 32 nearest neighbors, and $d_i$ is the distance to the observer. We bin these fluxes in a Cartesian grid with 3600 and 1800 pixels of galactic longitude and latitude, respectively. This corresponds to an angular resolution of roughly 0.1 deg per pixel, reproducing the best angular resolution that *Fermi* has at its highest accessible energy range.

Due to the finite resolution of the simulation, we cannot resolve the very inner center of DM halos (Kuhlen et al. 2008). For this reason, we may need (if they are underestimated) to correct the flux in every pixel where the center of DM halos lie. We assume a NFW profile (Navarro et al. 1996) for the inner density profile of these halos and we extrapolate it up to the halo center. We note that no boost factor due to DM substructure, or any other effect (such as adiabatic contraction due to the presence of baryons or Sommerfeld enhancement), is included in our analysis.

The resulting all-sky maps are shown in Figure 1, where the position of known objects is indicated. Maps are color-coded according to the logarithmic flux in each 0.1 deg pixel, measured in GeV cm$^{-3}$ kpc sr$^{-1}$ for decay and GeV$^2$ cm$^{-6}$ kpc sr$^{-1}$ for annihilation. These maps are used as input for the *Fermi* satellite observation simulations, which we describe in the following Section.

## 3. FERMI SATELLITE OBSERVATION SIMULATIONS

Using the DM density and density squared maps from the constrained realization as input, we simulate *Fermi*-LAT observations of $\gamma$-ray emission from DM decay and annihilation, respectively, over the full sky for different assumed DM models. The simulated *Fermi*-LAT observations are produced using the `gtobssim` routine, part of the *Fermi* Science Tools package (v9r15p2), which incorporates the *Fermi*-LAT effective area and point spread function and their energy dependence. All simulations are run to generate a 5-year observation in the default scanning mode and using the current release of the LAT instrument response functions (P6_V3_DIFFUSE).

In the present study, we specifically adopt two example final states through annihilation or decay of the DM particle, chosen to be representative of more general classes of DM models. The first model features a DM particle with a mass of 1.6 TeV yielding a pair of $\mu^+\mu^-$, which was shown to fit accurately the PAMELA data in Papucci & Strumia (2010). The decay lifetime was tuned to $\tau \simeq 3 \times 10^{26}$ s to match the observed positron fraction excess. Given that the energy loss time scales for high-energy electrons and positrons produced by muon decays are much shorter than the diffusion time scales in the structures we consider here, we neglect diffusion, and also calculate the emission of said electrons and positrons via inverse Compton up-scattering of CMB photons. This yields a significant low-energy component, extending all the way up to energies relevant to the *Fermi* telescope (Profumo & Jeltema 2009). We also consider a second, more conventional model, inspired by what it is expected in e.g. supersymmetric models with very weak $R$-parity violation and a bino-like lightest supersymmetric particle. We thus consider a 100 GeV neutralino yielding a pair of quark-antiquarks (of $b$ flavor, for definiteness). In this case, the produced electrons-positrons are too soft to give any significant inverse Compton emission. We fix the lifetime of the DM in this case to be a few times larger than current limits (see below), and set it to $\tau \simeq 10^{26}$ s.

Since our primary goal is to compare local structures in terms of the best location to look for a signal from dark matter, all four of the *Fermi* simulations (annihilation to $b\bar{b}$, decay to $b\bar{b}$, annihilation to $\mu^+\mu^-$, decay to $\mu^+\mu^-$) are normalized to give the same total $\gamma$-ray flux from DM integrated over the full sky of $9 \times 10^{-8}$ photons cm$^{-2}$ s$^{-1}$. This number was chosen in order to obtain good statistics to compare between different extragalactic structures. For annihilation to $b\bar{b}$, this flux corresponds to an annihilation cross-section of $10^{-23}$cm$^3$s$^{-1}$, such that the brightest clusters are expected to be detectable above the diffuse $\gamma$-ray backgrounds (Ackermann et al. 2010). For annihilation to $\mu^+\mu^-$, the same total flux corresponds to an annihilation cross-section of $5.8 \times 10^{-23}$cm$^3$s$^{-1}$, which gives a good fit to the PAMELA positron excess. We note that these values are close to the cross-section limits in Ackermann et al. (2010). However, since we have not included the effects of DM substructure in the simulated maps, this normalization could alternatively be thought of as a lower annihilation cross-section with the potential order of magnitude boosts from substructure (e.g. Kuhlen et al. 2008, Springel et al. 2008). In

---

[12] http://clues-project.org

the case of DM decay, the lifetimes are above the current limits derived from other $\gamma$-ray studies (see e.g. Papucci & Strumia 2010).

We also include in the simulations realistic treatments of both the Galactic and isotropic diffuse backgrounds. In particular, the $\gamma$-ray emission from the Galaxy is quite variable across the sky, an important consideration when comparing the expected signals from known objects. For example, structures lying at low Galactic latitudes like the Great Attractor will have much higher $\gamma$-ray backgrounds than high latitude objects like the Virgo cluster. We simulated 5-year *Fermi* observations of the Galactic and isotropic diffuse backgrounds using the current background models released by the *Fermi* Collaboration[13] (`gll_iem_v02.fit` and `isotropic_iem_v02.txt`, respectively). The output background map is then used to compute signal-to-noise ($S/N$) all-sky maps, detailed in the next Section.

## 4. RESULTS

In Figure 2 we show our main result: the S/N prediction for the extragalactic $\gamma$-ray emission in the 100MeV–10GeV energy range from DM in the Local Universe, as it would be seen by the *Fermi* satellite after 5-years of observations. This is the first time that a realistic (constrained) cosmological simulation is used to generate maps that are not only consistent with the currently accepted cosmology but also with the observed Local Universe. The maps correspond to the S/N for DM annihilation (right panel) and decay (left panel) assuming a particle mass of 100 GeV which annihilates or decays through the $b\bar{b}$ channel. The S/N is defined as the signal over the square root of the signal plus the background $\gamma$-ray emission. Pixels are binned in squares of 1 deg which matches the *Fermi*-LAT PSF at around 1 GeV as well as the typical size in the sky of nearby clusters.

In order to make a quantitative analysis of DM detectability in large nearby structures, we computed in Table 1 the photon number counts and signal-to-noise from annihilation and decay in the 1 GeV–10 GeV energy range, for both the $b\bar{b}$ and $\mu^+\mu^-$ channels. This choice of energy range maximizes the S/N ratio as compared to the 100MeV–10GeV range, as the Fermi-LAT sensitivity is significantly worse at lower energies. Interestingly, for the clusters shown in Table 1 (Virgo, Coma, Perseus, and the Great Attractor), the S/N values do not present a steep decline with distance from the cluster center. Also, with the assumed parameters for DM cross section, these values would imply an optimistic conclusion of DM being detected in some of these objects. Again, we recall that we came to this conclusion without including substructures or any other mechanisms that may act as boosts of the expected DM flux.

It is important to note that according to Table 1 the most promising clusters are Virgo and Coma. The former, however, has not been considered by the *Fermi* collaboration in their recent DM works, likely due to the presence of M87, which is a powerful $\gamma$-ray source. Yet, as the S/N in Virgo cluster does not decrease very strongly with the aperture from the cluster center, it seems to be a promising object to be used for DM studies.

Besides, we highlight that in the case of DM decay, the filamentary structure of the cosmic web constitutes an even more interesting target. In this case the $\gamma$-ray luminosity is just proportional to the enclosed mass, whereas this is not true for annihilation. This makes massive extragalactic objects offer the best chance for detection (see Table 1). Large filaments of DM match and even exceed the values of S/N as compared to those in large clusters. Superclusters such as the region marked in Figure 2 show even more significant values. Hence, these features of the Large-Scale Structure of the Universe may prove to be a very promising way to detect decaying DM with *Fermi*.

## 5. DISCUSSION AND CONCLUSION

In this letter we have presented *Fermi* maps of extragalactic $\gamma$-rays coming from DM annihilation and decay, which are made publicly available at the following URL: `http://dae47.iaa.es:8080/fermimaps/`. DM distribution is taken from a constrained cosmological simulation of the Local Universe Box160CR by the CLUES project. This distribution is then taken as an input for the *Fermi* observation simulation to obtain the all-sky distribution of $\gamma$-ray photon counts that would be measured by *Fermi* in a 5-year survey. Galactic and isotropic $\gamma$-ray diffuse backgrounds are also taken into account to get reliable results. This allows us to get S/N all-sky maps to estimate the possibility of detection of $\gamma$-rays from DM in such a survey using the *Fermi* satellite. We adopted two different particle physics models: a DM particle annihilating (decaying) primarily to a $b\bar{b}$ final state, and a DM model giving a good fit to the local positron fraction measured by PAMELA and the total electron spectrum measured by *Fermi* with annihilation (decay) to a $\mu^+\mu^-$ final state and a particle mass of 1.6 TeV.

In the case of DM annihilation through the $b\bar{b}$ channel, we find that large objects with high galactic latitude present a good chance to be detected with a S/N ratio of around 3 for Virgo and Coma clusters. These values, as the whole analysis, assume no boost from DM halo substructures, which may enhance these values an order of magnitude or more (between 10 and 200, according to Kuhlen et al. 2008 and Springel et al. 2008). Besides, we find that the S/N is not a strong function of the area of the analyzed region, which allows for considering large apertures without significant penalty in the results. This is especially interesting for Virgo cluster, being very close to us.

The *Fermi* Collaboration has started to severely constrain models of annihilating DM that could explain the PAMELA positron excess (Yin et al. 2009, Ibarra & Tran 2009, Profumo & Jeltema 2009). On the other hand, the case of decaying DM has comparatively received considerably smaller attention. Not only does the parameter space range for decaying DM appears at present to be much more generous than that for pair-annihilation, given the less stringent currently available $\gamma$-ray constraints, but from a theoretical standpoint, decaying DM with a lifetime in the correct range is a generic prediction of many theories beyond the Standard Model of particle physics. In this case, we find that filamentary regions, together with large superclusters, provide an interesting chance of detection in the case of DM decay, in particular if the selected sky area under analysis covers the whole overdense region.

These conclusions should be complemented by an anal-

---

[13] http://fermi.gsfc.nasa.gov/ssc/data/access/lat/BackgroundModels.html

TABLE 1
S/N, photon counts and backgrounds in Fermi simulations.

| Object | $b\bar{b}$ channel ann | | $b\bar{b}$ channel dec | | $\mu^+\mu^-$ channel ann | | $\mu^+\mu^-$ channel dec | | background |
|---|---|---|---|---|---|---|---|---|---|
| Coma 1 deg | 2.981 | (20) | 2.981 | (20) | 0.567 | (3) | 1.078 | (6) | 25 |
| Coma 2 deg | 2.592 | (31) | 4.061 | (52) | 0.371 | (4) | 1.331 | (15) | 112 |
| Coma 5 deg | 1.542 | (39) | 4.976 | (135) | 0.203 | (5) | 1.542 | (39) | 601 |
| Virgo 1 deg | 2.739 | (15) | 3.133 | (18) | 0.000 | (0) | 0.485 | (2) | 15 |
| Virgo 2 deg | 2.858 | (28) | 5.371 | (61) | 0.471 | (4) | 1.444 | (13) | 68 |
| Virgo 5 deg | 1.818 | (42) | 7.700 | (203) | 0.269 | (6) | 2.189 | (51) | 492 |
| Perseus 1 deg | 1.144 | (12) | 5.642 | (74) | 0.493 | (5) | 1.841 | (20) | 98 |
| Perseus 2 deg | 0.700 | (14) | 5.646 | (128) | 0.253 | (5) | 1.518 | (31) | 386 |
| Perseus 5 deg | 0.386 | (20) | 4.542 | (245) | 0.116 | (6) | 1.187 | (62) | 2665 |
| GAttractor 1 deg | 0.280 | (8) | 2.686 | (80) | 0.105 | (3) | 0.935 | (27) | 807 |
| GAttractor 2 deg | 0.211 | (13) | 2.581 | (162) | 0.049 | (3) | 0.696 | (43) | 3777 |
| GAttractor 5 deg | 0.136 | (23) | 2.157 | (367) | 0.041 | (7) | 0.538 | (91) | 28572 |
| Filament1, $d = 65\mathrm{Mpc}/h$ | 0.224 | (14) | 4.515 | (292) | 0.128 | (8) | 1.348 | (85) | 3891 |
| Filament2, $d = 40\mathrm{Mpc}/h$ | 0.752 | (67) | 9.317 | (871) | 0.191 | (17) | 2.589 | (233) | 7869 |
| Filament3, $d = 65\mathrm{Mpc}/h$ | 0.351 | (84) | 4.862 | (1174) | 0.121 | (29) | 1.181 | (283) | 57127 |
| Filament4, $d = 55\mathrm{Mpc}/h$ | 0.576 | (91) | 8.380 | (1358) | 0.184 | (29) | 2.065 | (328) | 24904 |
| Supercluster1, $d = 45\mathrm{Mpc}/h$ | 0.911 | (144) | 12.598 | (2066) | 0.254 | (40) | 3.334 | (531) | 24829 |

Note. — The S/N ratio and number of photon counts (in brackets) in the 1 GeV – 10 GeV energy range for our different DM models. For cluster regions, three different radii are considered (1, 2, and 5 degrees). Filaments 1 to 4 represent elongated regions connected to these clusters which are potentially interesting due to their high S/N. Median distance of the halos belonging to the filaments is indicated. Supercluster1 is a collection of massive halos which accidentally lie along the line-of-sight. Background counts from the Galactic plus extragalactic diffuse in the same regions are also listed.

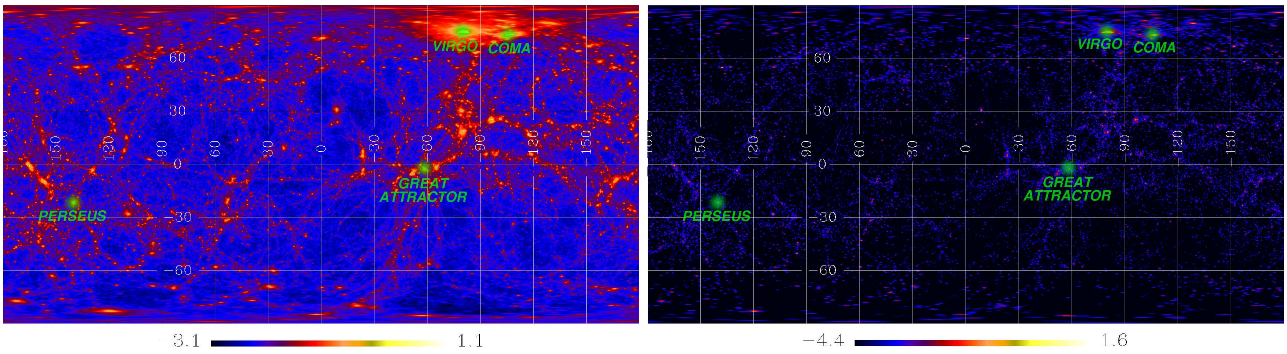

Fig. 1.— DM distribution in the Local Universe constrained cosmological simulation Box160CR. These all-sky maps are Cartesian projections in Galactic coordinates. Left panel shows the density distribution, whereas the right panel displays the distribution of density squared. The maps are color-coded according to the $\log_{10}$ of the DM flux, and units are GeV cm$^{-3}$ kpc sr$^{-1}$ for decay map and GeV$^2$ cm$^{-6}$ kpc sr$^{-1}$ for the annihilation map. Large structures reproduced by this simulation such as Virgo, Coma, and Perseus clusters, together with the Great Attractor, are labeled.

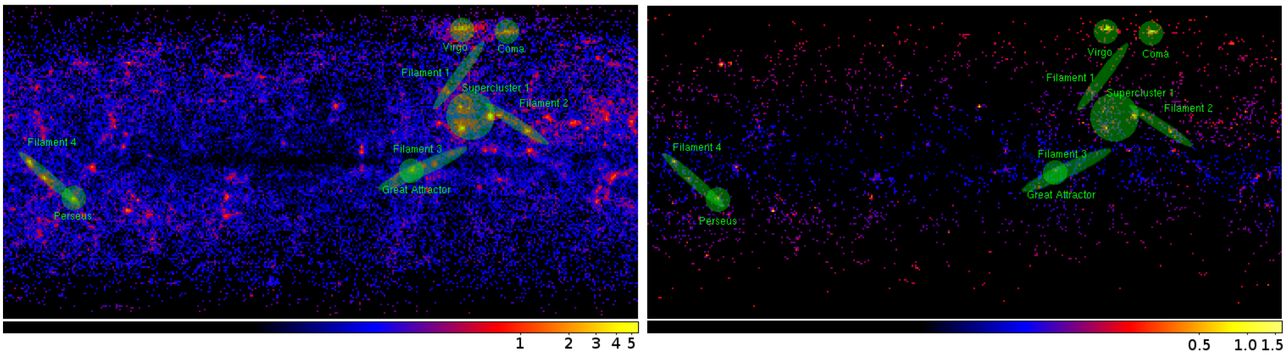

Fig. 2.— S/N all-sky maps from *Fermi* simulations for DM $\gamma$-rays in the energy range 100MeV–10GeV built from the Box160CR constrained simulation of the Local Universe. $\gamma$ rays from DM decay (left) and annihilation (right) are shown for the $b\bar{b}$ channel model (see text for details).

ysis of the galactic components, mainly from DM subhalos like those hosting the DM-rich dwarf spheroidal galaxies around the Milky Way. This is discussed in a recent work by Anderson et al. (2010). Moreover, these results on DM search will benefit from additional hints from the study of the angular power spectrum of the $\gamma$-ray flux (e.g. Fornasa et al. 2009, Hensley et al. 2009). A careful analysis of the anisotropies in the extragalactic diffuse radiation from DM annihilation and decay using constrained simulations of the Local Universe will be presented in an upcoming paper.

Finally, we find that *Fermi* will be able to place strong constraints on DM nature by measuring the $\gamma$-ray emission from both galactic and extragalactic objects, and the theoretical expectations from the results presented in this letter should provide the astroparticle community with the most interesting structures to detect the elusive DM particle.

A.J.C. thanks support of the MEC through Spanish grant FPU AP2005-1826. We thank the support of the Spanish MICINNs Consolider-Ingenio 2010 Programme under grant MULTIDARK CSD2009-00064 and ASTROMADRID (S2009/ESP-146). GY acknowledges support of MICINN (Spain) through research grants FPA2009-08958 and AYA2009-13875-C03-02. *Fermi*-LAT simulation tools were provided by the *Fermi*-LAT collaboration and the *Fermi* Science Support Center.

## REFERENCES

Abdo, A. A. et al. 2010a, Journal of Cosmology and Astro-Particle Physics, 4, 14
—. 2010b, Physical Review Letters, 104, 091302
—. 2010c, ApJ, 712, 147
Ackermann, M. et al. 2010, ArXiv e-prints
Adriani, O. et al. 2009, Nature, 458, 607
Aharonian, F. et al. 2008, Astroparticle Physics, 29, 55
Albert, J. et al. 2008, ApJ, 679, 428
Aleksić, J. et al. 2010, ApJ, 710, 634
Anderson, B., Kuhlen, M., Johnson, R., Madau, P., & Diemand, J. 2010, ArXiv e-prints
Atwood, W. B. et al. 2009, ApJ, 697, 1071
Bertone, G. 2010, Cambridge University Press
Bertone, G., Hooper, D., & Silk, J. 2005, Phys. Rep., 405, 279
Fornasa, M., Pieri, L., Bertone, G., & Branchini, E. 2009, Phys. Rev. D, 80, 023518
Gottloeber, S., Hoffman, Y., & Yepes, G. 2010, ArXiv e-prints
Hensley, B. S., Siegal-Gaskins, J. M., & Pavlidou, V. 2009, ArXiv e-prints
Hoffman, Y. & Ribak, E. 1991, ApJ, 380, L5
Ibarra, A. & Tran, D. 2009, Journal of Cosmology and Astro-Particle Physics, 2, 21
Klypin, A., Hoffman, Y., Kravtsov, A. V., & Gottlöber, S. 2003, ApJ, 596, 19
Kravtsov, A. V., Klypin, A. A., & Khokhlov, A. M. 1997, ApJS, 111, 73
Kuhlen, M., Diemand, J., & Madau, P. 2008, ApJ, 686, 262
Navarro, J. F., Frenk, C. S., & White, S. D. M. 1996, ApJ, 462, 563
Papucci, M. & Strumia, A. 2010, Journal of Cosmology and Astro-Particle Physics, 3, 14
Profumo, S. & Jeltema, T. E. 2009, Journal of Cosmology and Astro-Particle Physics, 7, 20
Springel, V., White, S. D. M., Frenk, C. S., Navarro, J. F., Jenkins, A., Vogelsberger, M., Wang, J., Ludlow, A., & Helmi, A. 2008, Nature, 456, 73
Yepes, G., Martínez-Vaquero, L. A., Gottlöber, S., & Hoffman, Y. 2009, in AIPC Series, Vol. 1178, The CLUES project: Constrained Local UniversE Simulations, ed. C. Balazs & F. Wang, 64–75
Yin, P., Yuan, Q., Liu, J., Zhang, J., Bi, X., Zhu, S., & Zhang, X. 2009, Phys. Rev. D, 79, 023512

## A.4 The correlation of UHECRs with nearby galaxies in the Local Volume

Mon. Not. R. Astron. Soc. **000**, 000–000 (0000) Printed 14 October 2009 (MN LaTeX style file v2.2)

# The correlation of UHECRs with nearby galaxies in the Local Volume

Antonio J. Cuesta[1,2⋆] and Francisco Prada[1]

[1] *Instituto de Astrofísica de Andalucía (CSIC), Camino Bajo de Huétor 50, E-18008 Granada, Spain*

[2] *Visiting Scholar, Institute for Theory and Computation, Harvard-Smithsonian Center for Astrophysics, Cambridge, MA 02138*

14 October 2009

## ABSTRACT

We explore the possibility of a local origin for ultra high energy cosmic rays (UHECRs). Using the catalogue of Karachentsev et al. including nearby galaxies with distances less than 10Mpc (Local Volume), we search for a correlation with the sample of UHECR events released so far by the Pierre Auger collaboration. The counterpart sample selection is performed with variable distance and luminosity cuts which extract the most likely sources in the catalogue. The probability of chance correlation after penalizing for scans is 0.96%, which corresponds to a correlation signal of $2.6\sigma$. We find that the parameters that maximize the signal are $\psi = 3.0^\circ$, $D_{\max} = 4$Mpc and $M_{\rm B} = -15$ for the maximum angular separation between cosmic rays and galaxy sources, maximum distance to the source, and sources brighter than $B$-band absolute magnitude respectively. This implies a preference for the UHECRs arrival directions to be correlated with the nearest and most luminous galaxies in the Local Volume, while the angular distance between the cosmic ray events and their possible sources is similar to that found by The Pierre Auger Collaboration using active galactic nuclei (AGNs) within 70-100Mpc instead of local galaxies. We note that nearby galaxies with $D < 10$Mpc show a similar correlation with UHECRs as compared to well-known particle accelerators such as AGNs, although less than 20% of cosmic ray events are correlated to a source in our study. However, the observational evidence for mixed composition in the high-energy end of the cosmic ray spectrum supports the possibility of a local origin for UHECRs, as CNO nuclei can travel only few Mpc without strong attenuation by the GZK effect, whereas the observed suppression in the energy spectrum would require more distant sources in the case of pure proton composition interacting with the CMB.

**Key words:** cosmic rays – methods: statistical

## 1 INTRODUCTION

Ultra-high energy cosmic rays (UHECRs) may become a complementary probe of some astrophysical objects in addition to observations in multiple wavelengths. In fact, the detection of these particles with enough statistics would represent the awake of the development of multi-messenger astrophysics. The Pierre Auger observatory in Malargüe, Argentina (see Abraham et al. 2004) has devoted a large effort in the construction of an unprecedented array of water Čerenkov tanks covering an area of ∼3,000 km$^2$, together with four fluorescence telescopes which allow for increased accuracy in energy measurements. This effort has proven to be fruitful as the first relevant results were obtained even before the completion of the entire experiment array. In particular, the unprecedented statistics on the detection of ultra-high energy cosmic rays above 10EeV=$10^{19}eV \simeq 1J$ with arrival directions measured with an accuracy better than 1° has allowed to search for possible astrophysical sources of these particles with higher reliability than previous experiments (e.g. Finley & Westerhoff 2004).

By the end of 2007, the Pierre Auger Collaboration concluded that the arrival directions of UHECRs above 55EeV correlate with the positions of nearby active galactic nuclei (AGN), or other objects which trace, in the same way as AGNs, the Large Scale Structure of the Universe (The Pierre Auger Collaboration 2007, The Pierre Auger Collaboration 2008). Statistics of these cosmic ray events has doubled since then (from 27 to 58 events), and yet the correlation with these objects has not strengthened as compared to previous estimations (The Pierre Auger Collaboration 2009b). This supports the

⋆ E-mail: ajcv@iaa.es

fact that this scenario is not the only one which can reproduce the observed data, although increasing statistics of UHECR events may be able to finally disentangle their real origin. Expectations in the cosmic-ray community are optimistic, and as stated in Olinto et al. (2009), this issue may find a solution in the next decade.

Indeed, there has been a plethora of studies in the literature trying to find out a correlation of the UHECRs with other candidate sources such as particular objects like galaxy clusters, GRBs or other potential hosts of energetic phenomena (e.g. Pierpaoli & Farrar 2005, Murase et al. 2008, Ghisellini et al. 2008) and structures like the Supergalactic Plane (Stanev 2008). Some of these works did report a similar significance as compared to the Auger result on the correlation with the angular positions of nearby AGNs. These similar values of the probability of chance correlation failed to discriminate with enough robustness between different cosmic-ray acceleration sites. In order to get stronger conclusions from this scarce set of UHECR events, there have been several efforts on the development of new methods to estimate the chance probability of correlation in the case of isotropic flux with potential sources (Ave et al. 2009, The Pierre Auger Collaboration 2009b). Despite all these efforts, there is no preferred candidate source yet.

Therefore, any complementary information from other measurements, like the shape of the energy spectrum, or the composition of these cosmic rays, plays now a decisive role. For example, interactions with CMB photons via the Greisen-Zatsepin-Kuzmin effect (Greisen 1966, Zatsepin & Kuz'min 1966) are expected to decimate the statistics of the UHECRs arriving to the Earth as a function of their composition and travel distance (e.g. Cronin 2005, Olinto et al. 2009). Recent claims of a detection of this GZK cutoff (Abbasi et al. 2008, Abraham et al. 2008) raises the question of how far away these cosmic accelerators must be located in order to present the observed suppression. Besides, simple considerations regarding the coincidence of the GZK and UHECR clustering energies point to the fact that the composition of UHECRs must deviate from pure proton composition and tend to be CNO–like (Dermer 2008), which is favoured by observations (Bellido et al. 2009, Unger et al. 2009, The Pierre Auger Collaboration 2009a). As CNO nuclei can travel shorter distances as compared to protons, this sets a strong limit on the distance of UHECR sources, without suffering from the large deflection angles by the galactic magnetic field in the case of iron nuclei (Takami & Sato 2009).

In this paper we address the possibility of a local origin for the Auger UHECRs. We use the only data published so far in The Pierre Auger Collaboration (2008), which comprises 27 UHECR events detected prior to 1 September 2007, with energies above 57EeV (which has been revised to 55EeV due to new calibration procedures). This energy scale turns out to be however very interesting in the search for these comic ray sources, as Mollerach et al. (2009) showed that the clustering above this energy is statistically significant. Most of the recent studies, including The Pierre Auger Collaboration (2008), have focused so far on sources located as far as $75 - 100$Mpc, which corresponds to the GZK horizon for protons. Here we assess if there is any correlation signal with nearby objects with distance $D < 10$Mpc (Local Volume) which is roughly the GZK horizon for CNO nuclei. In order to explore this hypothesis, we take advantage of the Local Volume catalogue of galaxies of Karachentsev et al. (2004), which is about 70–80% complete up to 8Mpc. This allows us to evaluate the likelihood of galaxies in the Local Volume as UHECR accelerator sites.

This paper is organized as follows: in Section 2 we describe the methodology used in our analysis and the catalogue of nearby galaxies in the Local Volume. In Section 3 we present the results of the chance probability of the correlation of UHECRs with these objects. We discuss our results and conclude in Section 4.

## 2 METHODOLOGY

In this paper we compare the distribution of UHECR arrival directions from The Pierre Auger Collaboration (2008) with the positions on the sky of nearby galaxies from the catalogue of Karachentsev et al. (2004). This catalogue comprises 451 neighbouring galaxies up to an estimated distance of $D \lesssim 10$Mpc or a radial velocity $V_{\rm LG} < 550$km s$^{-1}$ with respect to the Local Group centroid. In Figure 1 we represent an Aitoff projection of the angular distribution of cosmic-ray arrival directions (circles) together with the locations of all the galaxies in the whole Karachentsev et al. (2004) Local Volume catalogue (stars), both in galactic coordinates. The Supergalactic plane is also shown with dashed line for reference. As expected, a large number of nearby galaxies in the catalogue are clustered near the Supergalactic plane. This makes these particular sources good candidates for cosmic ray accelerators, as the arrival directions of UHECRs seem to be correlated with this plane (see Stanev 2008). In particular, there are a large number of these UHECR events which are clustered near the Supergalactic plane at the location of Centaurus A, as previously pointed out by The Pierre Auger Collaboration (2008) and confirmed in The Pierre Auger Collaboration (2009b), although some studies conclude that this region is unlikely to be a significant source of UHECRs (Croston et al. 2009).

The information available in the catalogue of Karachentsev et al. (2004) includes the absolute magnitude in the $B$-band and real distance information of the galaxies therein. This allows us to select the nearest and most luminous galaxies, which might be associated to the highest UHECR flux provided that there is a correlation between $B$-band luminosity and cosmic ray acceleration power. Hence, the relevant quantities we choose to conform our parameter space are: the angular separation $\psi$ between cosmic-ray events and galaxy sources, the threshold in the distance to the candidate sources $D_{max}$, and the maximum absolute magnitude in $B$-band $M_{\rm B}$. We did not study any dependence in energy of cosmic-ray events, as the data released by the Auger collaboration in 2007 only included 27 events, which is too sparse to make sub-samples with different energies. We show in Table 1 the values in the parameter space explored in our study for these three parameters $\psi$, $D_{max}$ and $M_{\rm B}$. We note that the most finely scanned quantity is the angular separation $\psi$, which is related to the deflection angle by the intervening magnetic fields. The small number of galaxies in the catalogue of Karachentsev et al. (2004) do not allow to perform a fine slicing in all the three parameters simultaneously, so we choose $\Delta\psi = 0^\circ.1$ for comparison

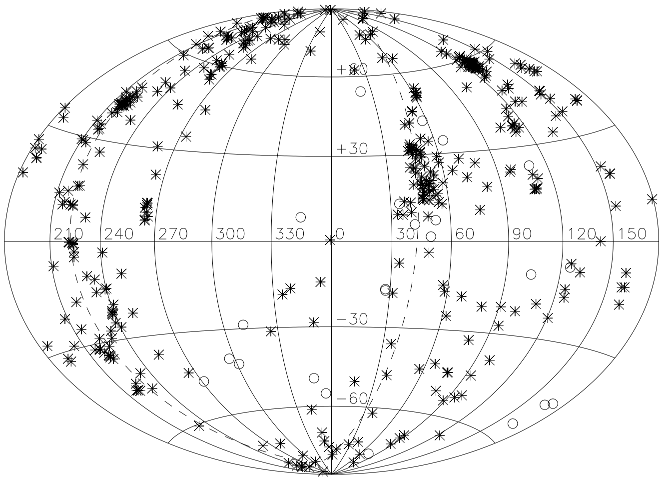

**Figure 1.** The spatial distribution in galactic coordinates of cosmic-ray arrival directions (circles) and nearby galaxies from the catalogue of Karachentsev et al. 2004 (stars) shown in Aitoff projection. The Supergalactic plane is also shown with dashed line for reference.

**Table 1.** Parameter space explored in this study. We show the minimum and maximum values, $X_{\rm min}$ and $X_{\rm max}$, as well as the scanning step $\Delta X$, for the three parameters explored in our study, i.e., $\psi$, $D_{max}$ and $M_{\rm B}$(see text for details).

| Quantity $X$ | $\psi$ (°) | $D_{\rm max}$ (Mpc) | $M_{B,{\rm max}}$ |
|---|---|---|---|
| $X_{\rm min}$ | 1.0 | 3.0 | −18 |
| $X_{\rm max}$ | 8.0 | 10.0 | −6 |
| $\Delta X$ | 0.1 | 0.5 | 3 |

with Fig. 3 in The Pierre Auger Collaboration (2008), and took several slices in distance and luminosity. The sampled values according to Table 1 extends over a grid of only 5,325 points in this space, which is computationally inexpensive.

In order to have an estimation of the probability of rejecting the null hypothesis (i.e. that the UHECRs in our sample show a distribution compatible with isotropy), we need to calculate the probability of correlation with a possible isotropic flux, following The Pierre Auger Collaboration (2008). Provided that a particular combination of values for our three parameters can show a pronounced minimum in this probability, we have to explore the full parameter space so that we can study the case in which isotropy seems to be unlikely. Therefore, for each set of values of our parameters we evaluate the probability of isotropic flux associated to (at least) $N_{\rm corr}$ correlated source–cosmic ray event pairs. This is given as expected by the binomial distribution:

$$P_{\rm data} = \sum_{j>N_{\rm corr}}^{N_{\rm tot}} \binom{N_{\rm tot}}{j} p^j (1-p)^{N_{\rm tot}-j} \qquad (1)$$

where $p$ is the probability that an event drawn from isotropy correlates with a galaxy within $\psi$, using the subsample given by the other two parameters. To make this more clear, let us assume that the observatory has uniform exposure for the entire sky. In this case the circles in the sky of radius $\psi$ around galaxies in the catalogue which are brighter than $M_{\rm B}$ and nearer than $D_{\rm max}$ define an area which is a fraction $p$ of the full $4\pi$ sr sky. The value of $p$ is estimated by MonteCarlo sampling of the sphere, calculating the fraction of points whose distance to a galaxy in the catalogue is smaller than a given angle $\psi$. For very small values of $\psi$, this estimation is straightforward as the areas covered by individual galaxies do not overlap, and hence the total area is equal to the number of galaxies $N$ times the area covered by the spherical cap subtended by the angle $\psi$, i.e. $0.5N(1-\cos\psi)$. On the other hand, for large values of $\psi$ or large number of galaxies, the area around individual galaxies will overlap and this approximation is no longer valid, so a numerical estimation is needed. In the general case, we also need to take into account the declination dependence on the exposure due to partial sky coverage by the observatory. This is done by generating events according to the relative exposure distribution $\omega(\delta)$. The number of points we used in the MonteCarlo sampling of the sphere is $10^6$ so we have a $10^{-3}$ uncertainty on the determination of $p$ for each node in the grid of the parameter space.

## 3 RESULTS

We now apply the method described in the previous Section to calculate the probability in the case of isotropic flux of $N_{\rm corr}$ correlated source–cosmic ray event pairs, as a function of the parameters $\psi$, $D_{max}$ and $M_B$. A full exploratory scan is performed over the entire parameter space, and as a result we find that this probability reaches its absolute minimum (hereafter $P_{\rm data}$) at cosmic ray event deflections below $\psi = 3.0°$ and galaxies accelerating UHECRs with distances below $D_{\rm max} = 4$Mpc and brighter than $M_{\rm B}$=-15. This implies a preference for the UHECRs arrival directions to be correlated with the nearest and most luminous galaxies in the catalogue, while the angular distance between the cosmic ray events and their possible sources is similar to that found by The Pierre Auger Collaboration (2008) using AGNs instead of local galaxies. In order to visualize the dependence of this probability with individual parameters, we refer to Figure 2. Here we display the chance probability of correlation with the Auger UHECRs above $E > 55$EeV as a function of each one of the scan parameters, keeping the other two parameters fixed at the absolute minimum of the probability of isotropic flux. When the angular distance $\psi$ varies, we find several local minima, although the region in which the chance correlation probability is below 0.1% is in the range of 2–4°. On the other hand, the behaviour with the other two scan parameters is quite robust with a single minimum, although this is also due to the coarseness in the scanning values in this case. Nevertheless, it seems clear that including distant and intrinsically faint sources decreases the correlation signal. Moreover, given the value of $\psi$ the deflection of cosmic ray trajectories due to intervening magnetic fields is not large, suggesting that these events are light nuclei, as suggested by The Pierre Auger Collaboration (2008).

As shown in Figure 2, the probability at the absolute minimum is $P_{\rm data} = 1.1 \times 10^{-4}$. This signal is similar to the previous result of The Pierre Auger Collaboration (2008), who found $P_{\rm data} = 2 \times 10^{-4}$, and even stronger than the revised result by The Pierre Auger Collaboration (2009b), who found that $P_{\rm data} = 6 \times 10^{-3}$ for the correlation with

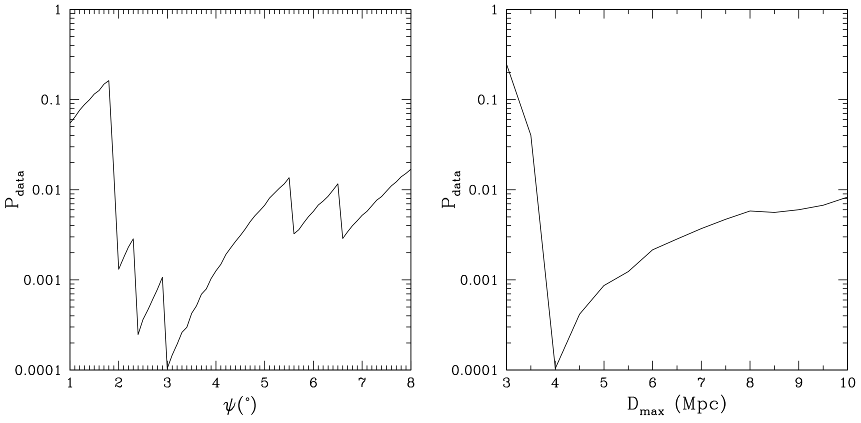

**Figure 2.** The chance correlation probability as a function of each one of the scan parameters, holding the other two fixed at their minimum of $P_{\rm data}$. *Left panel*: Angular separation $\psi$. *Middle panel*: Maximum galaxy distance $D_{max}$. *Right panel*: Maximum absolute magnitude in the $B$-band.

AGNs up to 75Mpc. Nevertheless, our result is not free from the negative impact of trial factors in a posteriori anisotropy searches, as it was not tested on an independent data set with the scan parameters specified a priori. For reference, the Auger result including all the 27 events is $P_{\rm data} = 4.6 \times 10^{-9}$. Also, our value is very sensitive to the low number of correlating events at this minimum (five cosmic rays associated to four sources), so removing one UHECR can boost $P_{\rm data}$ to $1.10 \times 10^{-3}$. However, it is important to note that Eq. (1) is not the true probability of chance correlation due to isotropic flux, as pointed out by Finley & Westerhoff (2004). Although this exploratory scan is useful in order to detect the location of the strongest potential correlation signal, the fact that we have chosen our parameters in such a way to get the minimum value of this probability has to be taken into account. In order to correct the value $P_{\rm data}$ that we have just obtained, we need to include a probability penalty due to parameter selection. This is fixed by performing $n_{\rm MC}$ MonteCarlo realizations of the cosmic-ray data set, which are drawn from a isotropic distribution but they are also selected in such a way that they mimic the events which the Pierre Auger Observatory might detect, due to declination dependence of the exposure. Therefore, the mock cosmic ray data set assume isotropic flux but the probability of a given arrival direction $(\alpha, \delta)$ is proportional to the exposure function of the Auger observatory on that position (see e.g. Cuoco et al. 2006).

The isotropic samples are obtained as usual by generating random points on the sphere, i.e. picking uniformly distributed random numbers in $\sin\delta$ and $\alpha$, so that the number density of points is completely homogeneous over the solid angle unit $\mathrm{d}\Omega = \cos\delta \mathrm{d}\delta \mathrm{d}\alpha$. To account for the Auger observed sky, we accept a random point on the sphere if an uniformly distributed random number between 0 and 1 is smaller than the relative exposure $\omega$ normalized by its maximum value $\omega_{\rm max}$, otherwise this point is rejected. According to Sommers (2001), the relative exposure is given by:

$$\omega(\delta) \propto \cos(\lambda)\sin(\alpha_m(\zeta))\cos(\delta) + \alpha_m(\zeta)\sin(\lambda)\sin(\delta) \quad (2)$$

where $\lambda \simeq -35^\circ$ is the latitude corresponding to the location of the Pierre Auger Observatory, $\zeta$ is given by:

$$\zeta \equiv \frac{\cos(\theta_{\rm max}) - \sin(\lambda)\sin(\delta)}{\cos(\lambda)\cos(\delta)} \quad (3)$$

($\theta_{\rm max} = \pi/3$ is the cut in zenith angle $\theta$ of the arrival directions applied by Auger), and $\alpha_m$ is defined as follows:

$$\alpha_m = \begin{cases} \pi & \text{if } \zeta < -1 \\ \arccos\zeta & \text{if } -1 < \zeta < +1 \\ 0 & \text{if } \zeta > +1 \end{cases} \quad (4)$$

Therefore, if we perform the same exploratory scan in the same way as in the beginning of this Section, for each different set $i$ of Monte Carlo generated arrival directions $(i = 1, \ldots, n_{\rm MC})$, we can just count the number of trials $n^*_{\rm MC}$ for which the absolute minimum (over the entire parameter space) of the probability of isotropic flux is lower than the actually observed minimum, $P^i_{\rm min} \leqslant P_{\rm data}$. The chance probability of observing $P_{\rm data}$ is (Finley & Westerhoff 2004):

$$P = \frac{n^*_{\rm MC}}{n_{\rm MC}} \quad (5)$$

We can consider this value as an estimate of the chance probability of correlation due to isotropic flux, as in The Pierre Auger Collaboration (2008). We performed $10^6$ Monte Carlo realizations of the Auger cosmic ray data set, in order to keep our uncertainties below 0.1%. The value we obtain for this probability after correcting for parameter selection is the following one:

$$P_{\rm chance} = (9.6 \pm 1.0) \times 10^{-3} \quad (6)$$

We find that the probability of chance correlation of the highest energy ($E > 55$EeV) Auger events with nearby galaxies from the Karachentsev et al. (2004) catalogue is around 0.96%. This small probability corresponds to a $2.6\sigma$ correlation between both samples. We point out that more than the half of the 27 Auger events above $E > 55$EeV are within $4^\circ$ of a nearby ($D < 10$Mpc) galaxy, which made it worth of exploring. This result goes along the same direction as the previous studies, finding a hint of violation of isotropy in the Auger sample.

There are 5 out of 27 correlating events, while only 0.5 should be expected on average in the case of isotropic flux, as the effective fraction of the sky for the values of the parameters at the minimum is $p = 0.018$. Of course the number of correlating events is much lower than the value found by The Pierre Auger Collaboration (2008) (20 out of 27, with 5.6 expected in the case of isotropic flux), but it should be considered that the effective fraction of the sky covered (at the minimum $P_{\rm data}$) by 442 objects in the Véron-Cetty AGN catalogue with $z \leqslant 0.017$ is much larger ($p \simeq 0.21$) than the 31 objects with our parameters ($p = 0.018$).

The galaxies which correlate with the arrival directions of the cosmic rays, are NGC300 (spiral galaxy type SA), NGC4945 (Sy2), NGC5102 (HII) and NGC5128 (Sy2). With exception of NGC300, they mostly show nuclear activity and both Seyfert galaxies are included in the AGN catalogue used by The Pierre Auger Collaboration (2008). In particular NGC5128, which is associated with 2 cosmic-ray events, is inside the well known Cen A region. Thus, it might happen that the correlation we find could just be inherited by the correlation found by the Auger Collaboration if the latter is finally confirmed. This is reasonable, as only a few tens of AGNs from the Véron-Cetty catalogue are located at a distance of $D <$ 10Mpc, but it is important to keep in mind that CNO UHECRs from larger distances can be heavily suppressed.

## 4 DISCUSSION AND CONCLUSION

We have explored the possibility of the correlation of nearby galaxies from the catalogue of Karachentsev et al. (2004) with ultra high energy cosmic ray events from the Pierre Auger Collaboration. This analysis is highly motivated in the light that a mixed CNO (as opposed to pure proton) composition of UHECRs, which is the preferred scenario indicated by current data, could not survive the GZK cutoff unless the sources are located in the Local Volume. Therefore, any correlation with these nearby sources would explain both composition and correlation at the same time. The analysis of the data concludes a $2.6\sigma$ correlation between both samples. There are 5 out of 27 correlating events, while 0.5 should be expected on average in the case of isotropic flux. Due to the small number of correlating events, we cannot specify the scan parameters a priori, thus making our results sensitive to the negative impact of a posteriori anisotropy searches. The probability of chance correlation due to isotropic flux after penalizing for scans is $P_{\rm chance} = 0.96 \times 10^{-2}$, rejecting the hypothesis of isotropy of arrival directions of UHECRs at 99% confidence level. For comparison, the same result before penalizing for scans is $\sim 1 \times 10^{-4}$ which is similar to the $\sim 2 \times 10^{-4}$ result (with scan parameters set a priori) from the correlation found by The Pierre Auger Collaboration (2008) with the AGNs in the Véron-Cetty catalogue, and stronger than the revised value of $\sim 6 \times 10^{-3}$ when they include the new UHECR events from 1 September 2007 to 31 March 2009 (The Pierre Auger Collaboration 2009b). This is an indication that there is no clear source of the UHECRs, and finding a lower value of the probability of chance correlation does not guarantee that this is actually the preferred source as compared to other sources which present similar values of $P_{\rm chance}$. This was already noticed even in early papers such as Tinyakov & Tkachev (2001), and in any case it seems unlikely to get a $> 3.3\sigma$ detection (Kashti & Waxman 2008). Interestingly, most of the objects in the catalogue of Karachentsev et al. (2004) which correlate with Auger events, are already included in the AGN catalogue, which has around 30 objects with $D <$ 10Mpc. This may indicate that the relation between nearby galaxies and UHECRs found in our work could be inherited from the The Pierre Auger Collaboration (2008) result. In any case, the so-called AGN hypothesis has proven to be controversial (Gorbunov et al. 2008, Moskalenko et al. 2009), stressed by the deficit of events from the direction of the Virgo supercluster. On the other hand, the correlation with the distribution of luminous matter seems to be well established (Kashti & Waxman 2008), without making any reference to any particular source which can accelerate particles up to these energies.

The small number of correlating events with nearby galaxies might also point to the possibility of the absence of UHECR accelerators in our local environment, although there is no definitive answer yet. Surprisingly, most of the objects in the Karachentsev et al. (2004) catalogue which correlate with the UHECR sample (with the exception of NGC300) are located in a small region in the sky, with Supergalactic coordinates $150^\circ < SGL < 165^\circ$ and $-10^\circ < SGB < -5^\circ$. This region is near the Supergalactic plane, pointing to preferential arrival directions from nearby galaxies located in a high density region. Future measurements and hopefully the next data release with a total of 58 events as announced in The Pierre Auger Collaboration (2009b) will help to clarify the origin of nearby and distant UHECRs, which will allow to study more in detail the acceleration physics behind them.

The authors acknowledge support from the Spanish MEC under grant PNAYA 2005-07789. A.J.C. thanks support of the MEC through Spanish grant FPU AP2005-1826. We especially want to thank Vasiliki Pavlidou from CalTech Astronomy Department for useful comments on this paper. This work made extensive use of the x4600 machine at CICA (Spain). We thank Claudio Arjona and Ana Silva at CICA for making this machine available to us.

## REFERENCES

Abbasi R. U. et al., 2008, Physical Review Letters, 100, 101101

Abraham J. et al., 2004, Nuclear Instruments and Methods in Physics Research A, 523, 50

Abraham J. et al., 2008, Physical Review Letters, 101, 061101

Ave M., Cazon L., Cronin J., de Mello Neto J. R. T., Olinto A. V., Pavlidou V., Privitera P., Siffert B. B., Schmidt F., Venters T., 2009, Journal of Cosmology and Astro-Particle Physics, 7, 23

Bellido J. A. for the Pierre Auger Collaboration, 2009, ArXiv e-prints, arXiv:0901.3389

Cronin J. W., 2005, Nuclear Physics B Proceedings Supplements, 138, 465

Croston J. H. et al., 2009, MNRAS, 395, 1999

Cuoco A., D'Abrusco R., Longo G., Miele G., Serpico P. D., 2006, Journal of Cosmology and Astro-Particle Physics, 1, 9

Dermer C. D., 2008, Journal of Physics Conference Series, 120, 062006

Finley C. B., Westerhoff S., 2004, Astroparticle Physics, 21, 359

Ghisellini G., Ghirlanda G., Tavecchio F., Fraternali F., Pareschi G., 2008, MNRAS, 390, L88

Gorbunov D., Tinyakov P., Tkachev I., Troitsky S., 2008, Soviet Journal of Experimental and Theoretical Physics Letters, 87, 461

Greisen K., 1966, Physical Review Letters, 16, 748

Karachentsev I. D., Karachentseva V. E., Huchtmeier W. K., Makarov D. I., 2004, AJ, 127, 2031

Kashti T., Waxman E., 2008, Journal of Cosmology and Astro-Particle Physics, 5, 6

Mollerach S. for the Pierre Auger Collaboration, 2009, ArXiv e-prints, arXiv:0901.4699

Moskalenko I. V., Stawarz L., Porter T. A., Cheung C. C., 2009, ApJ, 693, 1261

Murase K., Ioka K., Nagataki S., Nakamura T., 2008, Phys. Rev. D, 78, 023005

Olinto A. V., Adams J. H., Dermer C. D., Krizmanic J. F., Mitchell J. W., Sommers P., Stanev T., Stecker F. W., Takahashi Y., 2009, Astronomy, 2010, 225

Pierpaoli E., Farrar G., 2005, ArXiv Astrophysics e-prints, astro-ph/0507679

Sommers P., 2001, Astroparticle Physics, 14, 271

Stanev T., 2008, ArXiv e-prints, arXiv:0805.1746

Takami H., Sato K., 2009, ArXiv e-prints, arXiv:0909.1532

The Pierre Auger Collaboration 2007, Science, 318, 938

The Pierre Auger Collaboration 2008, Astroparticle Physics, 29, 188

The Pierre Auger Collaboration: J. Abraham 2009a, ArXiv e-prints, arXiv:0906.2319

The Pierre Auger Collaboration 2009b, ArXiv e-prints, arXiv:0906.2347

Tinyakov P. G., Tkachev I. I., 2001, Soviet Journal of Experimental and Theoretical Physics Letters, 74, 445

Unger M. for the Pierre Auger Collaboration 2009, ArXiv e-prints, arXiv:0902.3787

Zatsepin G. T., Kuz'min V. A., 1966, Soviet Journal of Experimental and Theoretical Physics Letters, 4, 78

# Appendix B

# Other publications

## B.1 The alignment of dark matter halos with the Cosmic Web

The Astrophysical Journal, 652:L75–L78, 2006 December 1

# THE ALIGNMENT OF DARK MATTER HALOS WITH THE COSMIC WEB

Santiago G. Patiri,[1] Antonio J. Cuesta,[2] Francisco Prada,[2] Juan Betancort-Rijo,[1,3] and Anatoly Klypin[4]

*Received 2006 June 18; accepted 2006 October 20; published 2006 November 10*

## ABSTRACT

We investigate the orientation of the axes and angular momentum of dark matter halos with respect to their neighboring voids using high-resolution *N*-body cosmological simulations. We find that the minor axis of a halo tends to be aligned along the line joining the halo with the center of the void and that the major axis tends to lie in the plane perpendicular to this line. However, we find that the angular momentum of a halo does not have any particular orientation. These results may provide information about the mechanisms whereby the large-scale structure of the universe affects galaxy formation, and they may cast light on the issue of the orientation of galaxy disks with respect to their host halos.

*Subject headings:* dark matter — galaxies: halos — large-scale structure of universe — methods: statistical

## 1. INTRODUCTION

The knowledge of the intrinsic alignments of the angular momentum of dark matter halos with respect to their axes and the alignments of these axes with respect to the galaxy disks is of great importance to understanding the processes involved in galaxy formation. Moreover, the alignment of halo axes, the angular momentum, and the galaxy spins with respect to the large-scale structure may provide further clues to this end; for example, they could be determinants to our understanding the origin of the angular momentum of galaxies (see, e.g., Navarro et al. 2004). They also may help us to understand several observational results, like the distribution of galactic satellites (e.g., Zentner et al. 2005; Azzaro et al. 2006a, 2006b), the formation of galactic warps (e.g., Dekel & Shlosman 1983; Toomre 1983; Bailin 2004), and the tidal streams observed, for example, in the Milky Way (e.g., Ibata et al. 2002). Furthermore, they could be a source of contamination in weak-lensing studies (e.g., Heymans et al. 2006).

Dark matter halos are triaxial in general, being defined by their three semiaxes, $a \geq b \geq c$ (Dubinski & Carlberg 1991; Warren et al. 1992; Cole & Lacey 1996; Jing & Suto 2002; Allgood et al. 2006). Recently, some effort has been devoted to measuring their intrinsic alignments with respect to angular momentum. It has been found that the angular momentum of dark matter halos tends to be parallel to their minor axes (Bailin & Steinmetz 2005; Allgood et al. 2006). This situation is typical for rotationally supported objects. However, as dark matter halos are not found to be rotationally supported, this alignment could have a nontrivial origin (Allgood et al. 2006).

On the other hand, the measurement of the alignments of galaxy disks with their host dark matter halos is both theoretical and observationally difficult. Using cosmological hydrodynamic simulations of disk galaxy formation, Bailin et al. (2005) found that the halo minor axis within $0.1R_{\rm vir}$ matches the disk axis. Beyond $0.1R_{\rm vir}$, the halo orientation is uncorrelated with the disk axis. Moreover, Hoekstra et al. (2004), using galaxy-galaxy lensing measurements, find that galaxies (disks plus ellipticals combined) are aligned with the major axis of their dark matter halo. Other works show that the angular momenta of disks and dark matter are not perfectly aligned (van den Bosch et al. 2002; Sharma & Steinmetz 2005). Hence, the final orientation of the galactic disk in a cosmological dark matter halo is still an unresolved problem.

One way of gaining insight into these alignments is to study the alignments of both halos and disks with respect to the large-scale structure. The basic idea is that the angular momentum of halos and galaxies is generated by tidal torques operating on the primordial material destined to form them (Peebles 1969; White 1984). In this scenario, the primordial angular momenta of baryons and dark matter are aligned, and the final galactic angular momentum is a “relic” of the primordial one. According to this, the current misalignment between galactic and dark matter halo angular momenta is due to subsequent tidal torques affecting dark matter halos. However, this scenario could be more complex because in addition to the primordial tidal torques operating on the material that eventually becomes the disk, the mass accretion by the disk is a clumpy and stochastic process (see Vitvitska et al. 2002). Along this line, Navarro et al. (2004) found, using high-resolution numerical simulations, that galaxy disks are rather well aligned with the angular momentum of the surrounding matter at the epoch of turnaround. Bailin & Steinmetz (2005) found that the minor axes of halos of groups and clusters show a strong tendency to lie perpendicular to the direction of filaments. However, it has been suggested that although filaments cause alignments of cluster-size halos, they have no discernible influence on smaller halos (Altay et al. 2006). On the other hand, it has recently been found, using observations from the Two Degree Field Galaxy Redshift Survey and the Sloan Digital Sky Survey, that galactic disk planes tend to be perpendicular to the walls of cosmic voids (Trujillo et al. 2006).

In this Letter, using high-resolution *N*-body simulations, we study the orientation of axes and the angular momentum of galactic-size dark matter halos embedded in the walls of large voids, those with radii larger than 10 $h^{-1}$ Mpc. We discuss the observational implications of our results.

## 2. NUMERICAL SIMULATIONS AND METHODOLOGY

### 2.1. *N-Body Simulations*

We have used for our analysis a high-resolution *N*-body numerical simulation of $512^3$ particles in a box of 120 $h^{-1}$ Mpc

---

[1] Instituto de Astrofísica de Canarias, Calle Vía Láctea, E-38200 La Laguna, Tenerife, Spain; spatiri@iac.es.

[2] Instituto de Astrofísica de Andalucía, CSIC, E-18008 Granada, Spain; ajcv@iaa.es; fprada@iaa.es.

[3] Facultad de Fisica, Universidad de La Laguna, Astrofísico Francisco Sánchez, s/n, La Laguna, Tenerife E-38200, Spain; jbetanco@iac.es.

[4] Astronomy Department, New Mexico State University, MSC 4500, P.O. Box 30001, Las Cruces, NM 880003-8001; aklypin@nmsu.edu.

on a side, assuming the concordance ΛCDM cosmological model ($\Omega_0 = 0.3$, $\Omega_\Lambda = 0.7$, and $H_0 = 100\ h$ km s$^{-1}$ Mpc$^{-1}$ with $h = 0.7$). The simulation was done with the Adaptive Refinement Tree (ART) code (Kravtsov et al. 1997). The force resolution was 1.8 $h^{-1}$ kpc comoving, and the mass of a particle was $1.1 \times 10^9\ h^{-1}$ Mpc. Dark matter halos are identified in the simulation by the Bound Density Maxima (BDM) algorithm (Klypin & Holtzman 1997; Klypin et al. 1999). For more details about this simulation, see Table 1 (L120$_{0.9}$) in Allgood et al. (2006). There is a total of 181,000 halos in the whole simulation box at $z = 0$. However, we limited our analysis to well-resolved halos with more than 1000 particles inside $R_{\rm vir}$ in order to be able to analyze accurately their internal axes and angular momentum orientations.

### 2.2. *Searching for Voids and Halo Sample*

In order to study the alignments of dark matter halos with their surrounding large-scale structure, we searched for large voids in the numerical simulation box using the HB void finder (Patiri et al. 2006). The HB void finder is conceptually simple since it searches for the maximal spheres (with radii larger than a given value) that are empty of halos (with masses larger than some specified value). This code is designed to be accurate and computationally efficient in finding the largest voids in any *point* distribution, like galaxy samples or dark matter halo samples. To search for these voids, the code first generates a sphere of fixed radius randomly located within the sample. We check to see if this sphere is empty of previously selected halos. If so, we increase the size of the sphere until its surface reaches the four nearest halos. This is our void. For a full description of the algorithm, see Patiri et al. (2006).

In the present work, we have searched for voids defined by dark matter halos with masses larger than $1.0 \times 10^{12}\ h^{-1}\ M_\odot$. We choose this mass in order to compare it with the observational results found by Trujillo et al. (2006); i.e., we select the halo mass so that their number density is equal to the number density of galaxies found in the observed galaxy samples (galaxies brighter than $M_{b_J} = -19.4 + 5 \log h$). With these definitions, we found a total of 60 voids with radii larger than 10 $h^{-1}$ Mpc in the whole simulation box. Once we have obtained the voids, we selected the halos located within shells 4 $h^{-1}$ Mpc thick beyond the surface of the void. Also, since we are interested in the orientations of galactic-size halos with respect to their neighboring large-scale structure, we restricted the mass of the halos to be smaller than $1.0 \times 10^{13}\ h^{-1}\ M_\odot$. We detect a total of 1729 halos in this mass range that are located in the shells of large voids. For each of these halos, we obtain their principal axes ($\hat{\boldsymbol{a}}$, $\hat{\boldsymbol{b}}$, and $\hat{\boldsymbol{c}}$) and calculate their angular momentum, in order to measure their orientations with respect to the void centers (see next section).

### 2.3. *Measuring Halo Orientations*

We follow the method presented in Allgood et al. (2006) in order to fit our halos to ellipsoids. First of all, we calculate the *reduced* inertial tensor for all the particles inside $R_{\rm vir}$ as $I_{ij} = \Sigma x_i x_j / r^2$, where the sum is over every particle inside a sphere of radius $R_{\rm vir}$ around the center of the halo. The halo center and $R_{\rm vir}$ are given by our BDM halo finder. The coordinates here are Cartesian, and the denominator (squared distance to halo center) makes the eigenvalues of the tensor, $\lambda_1 > \lambda_2 > \lambda_3$ dimensionless and nonsensitive to particle distances. The axis lengths $a > b > c$ are proportional to the square root of the eigenvalues. After this first step, we iterate this procedure to get more and more approximate ellipsoids that fit our dark matter distribution. To achieve this, we take the eigenvalues that we have just calculated, and we normalize them so that $a = R_{\rm vir}$ and the ratios $c/a$, $b/a$ are preserved. We then take into account every particle inside the ellipsoid (the ones that obey $[(\boldsymbol{r} \cdot \hat{\boldsymbol{a}})/a]^2 + [(\boldsymbol{r} \cdot \hat{\boldsymbol{b}})/b]^2 + [(\boldsymbol{r} \cdot \hat{\boldsymbol{c}})/c]^2 < 1$, with $\hat{\boldsymbol{a}}$, $\hat{\boldsymbol{b}}$, and $\hat{\boldsymbol{c}}$ being the unit eigenvectors), and we calculate the reduced inertial tensor, defined now as

$$I_{ij} = \sum \frac{x_i x_j}{r_e^2}, \quad r_e = a\sqrt{x^2/a^2 + y^2/b^2 + z^2/c^2}. \tag{1}$$

Its diagonalization results in the new eigenvalues and axis lengths. This method is repeated until convergence is achieved in every axis, with a tolerance $\epsilon = 5 \times 10^{-2}$. We stop the fit after just seven iterations since the convergence is usually very fast. The halos that could not be fitted to ellipsoids (∼8%) are therefore rejected.

Once the ellipsoid axes are measured, we calculate in a straightforward way the angle between the vector joining the center of the halo to the center of the void $\boldsymbol{R} = R\hat{\boldsymbol{R}} \equiv \boldsymbol{R}_{\rm halo} - \boldsymbol{R}_{\rm void}$ and the principal halo axes with $\alpha = \arccos|\hat{\boldsymbol{R}} \cdot \hat{\boldsymbol{a}}|$, $\beta = \arccos|\hat{\boldsymbol{R}} \cdot \hat{\boldsymbol{b}}|$, and $\gamma = \arccos|\hat{\boldsymbol{R}} \cdot \hat{\boldsymbol{c}}|$. The 1 $\sigma$ error for the direction of the axes is about 8° (see eq. [5] in Bailin & Steinmetz 2004).

Since the particles inside the ellipsoid are known after the iterative method converges, we can calculate the total angular momentum vector of the halo as

$$\boldsymbol{L} = \sum m\boldsymbol{r} \times \boldsymbol{v}, \tag{2}$$

where $\boldsymbol{r}$ is again the particle position referred to as the center of the halo and $\boldsymbol{v}$ is the particle velocity. Note that we are approximating this center with the real center of mass of the ellipsoid, otherwise there would be nonnegligible additional terms to take into account. Then the angle $\theta$ between $\boldsymbol{L}$ and $\boldsymbol{R}$ is calculated as follows:

$$\theta = \arccos\left|\frac{\boldsymbol{R} \cdot \boldsymbol{L}}{RL}\right|. \tag{3}$$

There are several sources of noise when calculating these angles, so it is not wise to take every halo we have in our sample. In particular, we reject the halos whose axes are determined to within an uncertainty greater than 0.2 rad $\simeq$ 11°. Moreover, we reject halos with degenerate axes since the direction of these axes is ill-defined and arbitrary within a plane (see Jing & Suto 2002). Therefore, we just take halos with axis ratios lower than 0.95, in order to avoid such degeneracy. After all, we have 1187 halos left for our analysis.

We also checked to see if our halos have the expected properties reported in the literature for their axis ratios and the intrinsic alignment of the angular momentum with the direction of principal axes. No discrepancies were found. The mean axis ratios in our mass range are $c/a = 0.64 \pm 0.14$, $b/a = 0.78 \pm 0.15$, and $c/b = 0.82 \pm 0.09$, in agreement with Jing & Suto (2002), Bailin & Steinmetz (2005), and Allgood et al. (2006). The median direction cosines of the angular momentum with the principal axes are $\boldsymbol{L} \cdot \boldsymbol{a} = 0.32$, $\boldsymbol{L} \cdot \boldsymbol{b} = 0.48$, and $\boldsymbol{L} \cdot \boldsymbol{c} = 0.69$, in agreement with the results in Bailin & Steinmetz (2005). About 75% of the halos have an angle between

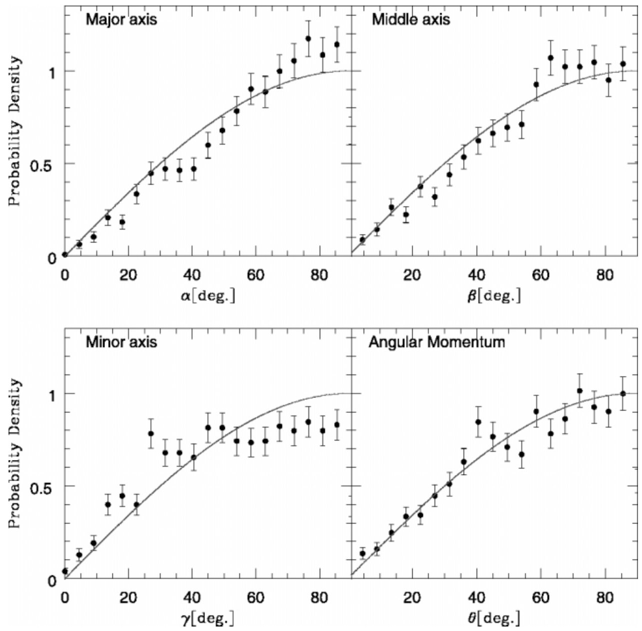

FIG. 1.—Probability density distribution for the angles between the axes (and angular momentum) of the dark matter halos and the vectors pointing to the center of the voids. *Top left panel*: Angle $\alpha$ for the major axis. *Top right panel*: Angle $\beta$ for the middle axis. *Bottom left panel*: Angle $\gamma$ for the minor axis. *Bottom right panel*: Angle $\theta$ for the angular momentum. The error bar on each bin is the Poissonian error. The solid line represents randomly distributed angles (i.e., a sine distribution)

their angular momentum and their major axes greater than 60°, as shown in Gottlöber & Turchaninov (2006).

## 3. RESULTS AND CONCLUSIONS

In Figure 1 we show the orientations of the three halo axes and the angular momentum with the cosmic voids. In the top left panel we show the probability distribution of the angle $\alpha$, which is defined between the major axis of the dark matter halos and the vector pointing to the center of the void (*filled circles*). Similarly, in the top right and bottom left panels we present the angles $\beta$ and $\gamma$, which are the ones between the middle and minor axes with the direction to the center of the void, respectively. Finally, in the bottom right panel we show the angle $\theta$ between the halo angular momentum and the direction to the center of the void. The solid line corresponds to the probability distribution of randomly distributed angles, which is a sine function for geometrical reasons.

In these plots we clearly see that halos are not randomly oriented within the shells of voids. The major axis of a halo tends to lie along the plane perpendicular to the radial direction; i.e., there is an excess of halos with $\alpha$ angles near 90°. On the contrary, the minor axis tends to point to the direction of the center of the void. There is a marginal orientation of the middle axis toward the plane perpendicular to the radial direction. However, we do not see any particular orientation of the halo angular momentum with respect to the large-scale structure, confirming recent results also obtained from *N*-body simulations using similar methodology (Heymans et al. 2006).

To test the robustness of our results, we have conducted several tests. First of all, we have analyzed the orientations of dark matter halos selected as described above, but in this case we used "fake" voids; i.e., we randomly placed spheres of fixed radius over the sample and calculated the angles between the axis (and angular momentum) of the dark matter halos located in the shells of these fake voids and the direction to their center. As expected, we found that the angles of the halos chosen to be in the shells of random spheres are uniformly distributed; i.e., they follow a sine distribution. Moreover, we applied two different statistical tests: the average of the cosine test and a standard Kolmogorov-Smirnov (K-S) test. If the angles are randomly distributed, the average of the cosine of these angles is 0.5, so that the bigger the deviation is from this value, the larger will be the effect. In Table 1 we show the results of the statistical tests. In the upper part of the table we show the results for the mean cosine (the second column) and the probabilities that the results are compatible with isotropy as given by the mean cosine and the K-S tests (the third and fourth columns, respectively) for halos located in the shells of voids. In the lower part of the table we show the same results, but for halos inside the shells of the random spheres (i.e., the fake voids). From these results, we conclude that we can reject with high confidence (more than 7 $\sigma$) the null hypothesis (i.e., the axes of dark matter halos are randomly distributed) for the halos in the shells of voids. As expected, the results of the statistical test for the halos located in the shells of the random spheres show that the orientation of these halos is compatible with the random distribution.

TABLE 1
RESULTS OF THE STATISTICAL TESTS

| Angle | ⟨cos⟩ | ⟨cos⟩ Prob. | K-S Prob. |
|---|---|---|---|
| Halos in Walls of Voids | | | |
| $\alpha$ ...... | 0.459 | $1.13 \times 10^{-8}$ | $5.4 \times 10^{-7}$ |
| $\beta$ ...... | 0.481 | $7.58 \times 10^{-3}$ | $2.0 \times 10^{-3}$ |
| $\gamma$ ...... | 0.556 | $9.19 \times 10^{-15}$ | $9.4 \times 10^{-13}$ |
| $\theta$ ...... | 0.509 | 0.19 | 0.12 |
| Halos in Walls of Random Spheres | | | |
| $\alpha$ ...... | 0.496 | 0.48 | 0.23 |
| $\beta$ ...... | 0.509 | $8.90 \times 10^{-2}$ | $7.80 \times 10^{-2}$ |
| $\gamma$ ...... | 0.492 | 0.19 | 0.10 |
| $\theta$ ...... | 0.502 | 0.69 | 0.57 |

On the other hand, we used our data to gain some insight into the nature of the internal alignment of the minor axis with angular momentum found in previous works (e.g., Bailin & Steinmetz 2004). We selected those halos for which both directions form an angle smaller that 20°. For these halos, we found that the alignment between the minor axis and the radial direction of the void is weaker than for randomly chosen halos, quite compatible with a random distribution.

Comparing these results with the observed tendency for the spin of spiral galaxies to point along the plane perpendicular to the direction of the center of the void found by Trujillo et al. (2006), three scenarios are possible: (1) The nonisotropy of the orientation of the spin of the galaxies is entirely induced by the halo alignments, (2) both alignments are two effects with a common origin (namely, the tidal field in the shells of voids), or (3) a combination thereof. In the first scenario the probability distribution for the angle between the major axis of the host halo and the spin of their galaxy is independent of the angle between the spin and the radial direction of the void. In this case, this probability distribution may be uniquely determined by comparing the distribution of the angle between the major axis and the radial direction with that of the angle between the spin of the galaxies and the radial direction. This would imply that the spin is very closely aligned with the major axis of the host halo. However, recent hydrodynamical simulations (Bailin et al. 2005) do not show this effect (they found that the spin of galaxies is uncorrelated with the halo). Therefore, the other two scenarios seem more plausible.

We thank Conrado Carretero, Stefan Gottlöber, Andrey Kravtsov, and Brant Robertson for useful discussions. S. G. P., A. J. C., F. P., and J. B.-R. thank the Spanish MEC under grant PNAYA 2005-07789 for their support. A. J. C. acknowledges the financial support of the MEC through Spanish grant FPU AP2005-1826.

## REFERENCES

Allgood, B., Flores, R. A., Primack, J. R., Kravtsov, A. V., Wechsler, R. H., Faltenbacher, A., & Bullock, J. S. 2006, MNRAS, 367, 1781
Altay, G., Colberg, J., & Croft, R. 2006, MNRAS, 370, 1422
Azzaro, M., Patiri, S. G., Prada, F., & Zentner, A. R. 2006a, MNRAS, in press (astro-ph/0607139)
Azzaro, M., Zentner, A. R., Prada, F., & Klypin, A. 2006b, ApJ, 645, 228
Bailin, J. 2004, Ph.D. thesis, Univ. Arizona
Bailin, J., & Steinmetz, M. 2004, ApJ, 616, 27
———. 2005, ApJ, 627, 647
Bailin, J., et al. 2005, ApJ, 627, L17
Cole, S., & Lacey, C. 1996, MNRAS, 281, 716
Dekel, A., & Shlosman, I. 1983, in IAU Symp. 100, Internal Kinematics and Dynamics of Galaxies, ed. E. Athanassoula (Dordrecht: Reidel), 187
Dubinski, J., & Carlberg, R. G. 1991, ApJ, 378, 496
Gottlöber, S., & Turchaninov, V. 2006, in Mass Profiles and Shapes of Cosmological Structures, ed. G. A. Mamon et al. (EAS Publ. Ser. 20; Les Ulis: EDP Sciences), 25
Heymans, C., White, M., Heavens, A., Vale, C. & Van Waerbeke, L. 2006, MNRAS, 371, 750
Hoekstra, H., Yee, H. K. C., & Gladders, M. D. 2004, ApJ, 606, 67
Ibata, R. A., Lewis, G. F., Irwin, M. J., & Quinn, T. 2002, MNRAS, 332, 915
Jing, Y. P., & Suto, Y. 2002, ApJ, 574, 538
Klypin, A., & Holtzman, J. 1997, preprint (astro-ph/9712217)
Klypin, A., Kravtsov, A. V., Valenzuela, O., & Prada, F. 1999, ApJ, 522, 82
Kravtsov, A. V., Klypin, A. A., & Khokhlov, A. M. 1997, ApJS, 111, 73
Navarro, J. F., Abadi, M. G., & Steinmetz, M. 2004, ApJ, 613, L41
Patiri, S. G., Betancort-Rijo, J. E., Prada, F., Klypin, A., & Gottlöber, S. 2006, MNRAS, 369, 335
Peebles, P. J. E. 1969, ApJ, 155, 393
Sharma, S., & Steinmetz, M. 2005, ApJ, 628, 21
Toomre, A. 1983, in IAU Symp. 100, Internal Kinematics and Dynamics of Galaxies, ed. E. Athanassoula (Dordrecht: Reidel), 177
Trujillo, I., Carretero, C., & Patiri, S. G. 2006, ApJ, 640, L111
van den Bosch, F. C., Abel, T., Croft, R. A. C., Hernquist, L., & White, S. D. M. 2002, ApJ, 576, 21
Vitvitska, M., Klypin, A. A., Kravtsov, A. V., Wechsler, R. H., Primack, J. R., & Bullock, J. S. 2002, ApJ, 581, 799
Warren, M. S., Quinn, P. J., Salmon, J. K., & Zurek, W. H. 1992, ApJ, 399, 405
White, S. D. M. 1984, ApJ, 286, 38
Zentner, A. R., Kravtsov, A. V., Gnedin, O. Y., & Klypin, A. A. 2005, ApJ, 629, 219

## B.2 Spin alignment of dark matter haloes in the shells of the largest voids

Mon. Not. R. Astron. Soc. **385,** 867–874 (2008) doi:10.1111/j.1365-2966.2008.12879.x

# Spin alignment of dark matter haloes in the shells of the largest voids

Antonio J. Cuesta,[1]⋆ Juan E. Betancort-Rijo,[2,3] Stefan Gottlöber,[4] Santiago G. Patiri,[2]† Gustavo Yepes[5] and Francisco Prada[1]

[1]*Instituto de Astrofísica de Andalucía (CSIC), Camino Bajo de Huétor 50, E-18008 Granada, Spain*
[2]*Instituto de Astrofísica de Canarias, C/Vía Láctea s/n, E-38200 La Laguna, Tenerife, Spain*
[3]*Universidad de La Laguna, Departamento de Astrofísica, Avda. Astrofísico Fco. Sánchez s/n, E-38200 La Laguna, Tenerife, Spain*
[4]*Astrophysikalisches Institut Potsdam, An der Sternwarte 16, D-14482 Potsdam, Germany*
[5]*Universidad Autónoma de Madrid, Grupo de Astrofísica, E-28049 Madrid, Spain*

Accepted 2007 December 13. Received 2007 December 13; in original form 2007 June 19

## ABSTRACT

Using the high-resolution cosmological *N*-body simulation MareNostrum universe we study the orientation of shape and angular momentum of galaxy-size dark matter haloes around large voids. We find that haloes located on the shells of the largest cosmic voids have angular momenta that tend to be preferentially perpendicular to the direction that joins the centre of the halo and the centre of the void. This alignment has been found in spiral galaxies around voids using galaxy redshift surveys. We measure for the first time the strength of this alignment, showing how it falls off with increasing distance to the centre of the void. We also confirm the correlation between the intensity of this alignment and the halo mass. The analysis of the orientation of the halo main axes confirms the results of previous works. Moreover, we find a similar alignment for the baryonic matter inside dark matter haloes, which is much stronger in their inner parts.

**Key words:** methods: *N*-body simulations – methods: statistical – galaxies: haloes – cosmology: theory – dark matter – large-scale structure of Universe.

## 1 INTRODUCTION

Understanding how the angular momentum is distributed over the collapsed structures in the Universe and its connection with the large-scale structure distribution of galaxies at present is a key issue to determine its origin (see Primack 2004, for a review). Furthermore, angular momentum is fundamental in order to explain the structure and dynamics of galaxy discs and hence it is a basic ingredient to determine their evolution and morphology. The currently accepted paradigm for explaining the origin of the angular momentum is the Tidal Torque Theory (Peebles 1969; Doroshkevich 1970; White 1984), hereafter TTT. In this framework, the angular momentum is transferred to the protohalo by the coupling of the quadrupolar inertia tensor and the tidal tensor during the linear regime of growth of density fluctuations. According to TTT, the epoch of turnaround marks a major change in the amount of angular momentum transferred, as this tidal torquing becomes inefficient due to the small size of the halo after it collapses. However, the theory breaks at this epoch as non-linear effects are expected to turn up together with merger and accretion processes. In particular, this causes the dilution of the TTT prediction regarding the spin direction (Porciani, Dekel & Hoffman 2002; Peirani, Mohayaee & de Freitas Pacheco 2004).

None the less, recent observational studies have found a preferential orientation of galaxy discs with respect to their surrounding large-scale structures (Navarro, Abadi & Steinmetz 2004; Trujillo, Carretero & Patiri 2006). Such an alignment is thus expected to be a relic of the alignment already present before the epoch of the turnaround. These works differ both in the methodology and the sample used. For instance, Navarro et al. (2004) used catalogues of nearby galaxies and found an excess of edge-on spiral galaxies highly inclined relative to the supergalactic plane. However, this result has two major drawbacks: the sample is limited to galaxies in the vicinity of the Milky Way, which is not very representative of the overall large-scale structure; and the orientation of the large-scale sheet-like distributions like the supergalactic plane is blurred due to redshift distortion at high distances (which can only be determined by redshift). On the other hand, Trujillo et al. (2006) used the largest galaxy redshift surveys up to date (2dFGRS and SDSS) to get the sample, and searched for large voids in these surveys to identify spatial orientations not relying on the detection of planes. They found that spiral galaxies located on the shells of the largest cosmic voids have rotation axes that lie preferentially on the

---

⋆E-mail: ajcv@iaa.es
†Present Address: Department of Astronomy, Case Western Reserve University, 10900 Euclid Avenue, 44106 Cleveland, OH, USA.

surface of the void. As this paper has been written, it has also been found a correlation between the orientation of galaxy discs and local tidal shears using the Two-Mass Redshift Survey (Lee & Erdogdu 2007).

In addition, *N*-body cosmological simulations have nowadays enough resolution to study whether dark matter haloes also show this alignment. This result is expected as it is commonly assumed that both dark and baryonic matter shared a similar evolution during early epochs and gained the same specific angular momentum before the formation of the disc (e.g. Fall & Efstathiou 1980). However, even in the case of a positive signal, it is expected to be very weak as dark matter haloes are more affected by torques from neighbouring haloes than baryonic matter concentrated in discs. This recently led to numerous studies with a variety of methods to select a homogeneous sample of dark matter haloes with the aim of searching a counterpart of the observational results. For example, in Aragón-Calvo et al. (2007) a multiscale filter is developed in order to distinguish haloes belonging to filaments or walls. This code infers the morphology of the structure surrounding a halo by calculating the relations between the eigenvalues of the Hessian of the density field. In a dynamical approach, Hahn et al. (2007a) use the number of positive eigenvalues of the Hessian of the gravitational potential to classify the environment in which a halo resides. Both papers conclude that haloes in walls have spin vectors that tend to lie in the plane of the host wall, but haloes in filaments show only a weak trend for their angular momenta to be aligned with the filament direction. However, the method proposed by Trujillo et al. (2006) provides a very clean way to characterize the orientation of the large-scale distribution (i.e. the reference direction to measure any kind of alignment) by using the centre of a large void. This method, besides its robustness in observations with respect to redshift distortion, owes its convenience to the well-known fact that the direction of maximum compression (that of the smallest eigenvalue of the deformation tensor) turns out to be very well correlated with the direction to the centre of the void.

The study of this type of alignments is specially interesting in the context of gravitational lensing. A key assumption of this method is that the observed galaxy ellipticity correlations come only from the distortion caused by the gravitational shear, with all the intrinsic terms being negligible (e.g. Heymans et al. 2006). Thus, exploring these cosmological alignments may prove to be useful in order to estimate the contamination from this source in the lensing signal. The importance of angular momentum is also remarkable in semi-analytical modelling of galaxy formation (e.g. Avila-Reese, Firmani & Hernández 1998). The properties of the galactic discs are usually expected to be related to those of the dark matter haloes in which they are embedded (e.g. Mo, Mao & White 1998). However, regarding angular momentum this assumption has been recently questioned (D'Onghia & Navarro 2007).

In this paper, mainly motivated by the observational result found by Trujillo et al. (2006), we use a high-resolution cosmological simulation to study the alignment of shape and angular momentum of galaxy-size dark matter haloes in the shells of large voids. Our simulation provides enough statistics to assess the results in Patiri et al. (2006a) and Brunino et al. (2007) and for the first time to measure the strength of the alignment signal of the angular momentum in these haloes without performing a previous selection of them, as opposed to Brunino et al. (2007).

This work is organized as follows. In Section 2 we describe the cosmological simulation and the methodology. The results are presented in Section 3. We summarize and discuss our conclusions in Section 4.

## 2 MARENOSTRUM UNIVERSE SIMULATIONS AND METHODOLOGY

The cosmological simulation we have used for this study is the *MareNostrum universe* (Gottlöber & Yepes 2007). This non-radiative smoothed particle hydrodynamics (SPH) simulation employs $1024^3$ dark matter particles of mass $8.24 \times 10^9\,h^{-1}\,\mathrm{M}_{\odot}$ and $1024^3$ gas particles of mass $1.45 \times 10^9\,h^{-1}\,\mathrm{M}_{\odot}$ in a box of $500\,h^{-1}$ Mpc on a side. The cosmological model is $\Lambda$CDM with cosmological parameters $\Omega_{\Lambda} = 0.7, \Omega_{\mathrm{m}} = 0.3, \Omega_{\mathrm{bar}} = 0.045, h = 0.7, \sigma_8 = 0.9$ and a slope $n = 1$ for the initial power spectrum. The evolution of the initial conditions was performed by using the TREEPM + SPH code GADGET-2 (Springel 2005). The spatial force resolution was set to an equivalent Plummer gravitational softening of $15\,h^{-1}$ comoving kpc, and the SPH smoothing length was set to the 40th neighbour to each particle. The long-range gravitational force calculation was done by the particle-mesh algorithm using FFT in a homogeneous mesh of $1024^3$ elements.

In this work we use both dark matter and gas particle distributions of this simulation. In order to test the effects of the baryonic component in the results of our analysis, we have also used the results of an *N*-body, dark matter only version of the MareNostrum universe. This simulation has exactly the initial conditions and parameters than the SPH simulation but with $1024^3$ dark matter particles only.

Dark matter haloes are found using a parallel hierarchical friends-of-friends algorithm based on the minimum spanning tree for the particle distribution with linking parameter $b = 0.17$, which corresponds to overdensity $\Delta = 330$ with respect to mean matter density. Using equation (2) in Bailin & Steinmetz (2005), and taking into account that the mean axis ratios for galaxy-size haloes are $c/b \simeq 0.79$ and $b/a \simeq 0.75$, we find that about 65 particles are enough to determine main axes orientations to within 15°. As this is a reasonable resolution, we are restricted to use haloes with $M > 5.4 \times 10^{11}\,h^{-1}\,\mathrm{M}_{\odot}$, so we will choose our lower mass limit above this value. There are 881 861 haloes in the entire simulation box above this mass at $z = 0$, which provides very good statistics for our purposes.

The detection of voids is made using the HB void finder (Patiri et al. 2006a). This code searches for the maximal non-overlapping spheres which are larger than a given radius and empty of objects below a given mass. Those spheres are our voids. We are interested only in large voids, i.e. those with $R_{\mathrm{void}} > 10\,h^{-1}$ Mpc, which characterize the orientation of the large-scale distribution at the position of the halo. We searched for voids defined by haloes with masses larger than $7.95 \times 10^{11}\,h^{-1}\,\mathrm{M}_{\odot}$, whose axes are resolved to within 13°. The mass limit has been chosen to get the same number density of haloes as the number density of galaxies found in the observed galaxy samples of Trujillo et al. (2006) ($n = 5 \times 10^{-3}\,h^3\,\mathrm{Mpc}^{-3}$, which corresponds to galaxies brighter than $M_{b_{\mathrm{J}}} \geqslant -19.4 + 5 \log h$). With this defining mass we found a total of 3047 voids, with a median radius of $11.17\,h^{-1}$ Mpc. For further comparison with the observational result, we look for Milky Way-sized haloes in a shell of $4\,h^{-1}$ Mpc around the surface of each void. We thus remove all the haloes with mass below the defining mass of the voids $7.95 \times 10^{11}\,h^{-1}\,\mathrm{M}_{\odot}$ (which is greater than our resolution limit), and those with mass exceeding $7.95 \times 10^{12}\,h^{-1}\,\mathrm{M}_{\odot}$, so that they are still galaxy size. Considering all these constraints, we are finally left with 88 426 haloes in the shells of voids and in this range of mass for our analysis.

For every halo we calculate its total angular momentum,

$$\boldsymbol{L} = \sum_k m \boldsymbol{r}_k \times \boldsymbol{v}_k, \qquad (1)$$

where $\boldsymbol{r}_k$ has its origin in the centre of mass of the halo and the sum is over every dark matter particle identified by the halo finder as belonging to the halo. The orientation of the angular momentum with the centre of the void is given by the $\theta$ angle derived from

$$\cos\theta = \frac{\boldsymbol{R}\cdot\boldsymbol{L}}{|\boldsymbol{R}||\boldsymbol{L}|}, \qquad (2)$$

where $\boldsymbol{R}$ is the vector linking the centre of mass of the halo with the centre of the void, $\boldsymbol{R} = \boldsymbol{r}_{\rm halo} - \boldsymbol{r}_{\rm void}$. In the same way we use an analogous equation to calculate the angle between $\boldsymbol{R}$ and the major ($\boldsymbol{a}$), middle ($\boldsymbol{b}$) and minor ($\boldsymbol{c}$) halo axis, i.e. the three main axes resulting of the diagonalization of the 'inertia' tensor of haloes in the shells of the voids (the eigenvalues will be referred to as $a$, $b$ and $c$). This tensor is defined as

$$\mathsf{I}_{ij} = \sum_k x_{i,k} x_{j,k}, \qquad (3)$$

where the coordinates $x_i, k$ represent the $i$th component of the position vector of the $k$th particle, measured with respect to the centre of mass of the halo. This sum is again over halo particles (see Patiri et al. 2006b).

**Table 1.** The strength of the alignment of the three main axes and angular momentum vector of haloes (and baryons embedded therein) in a shell of $4\,h^{-1}$ Mpc around large voids, with respect to the direction to the centre of the void. First column shows the average of the cosine of the angles between these vectors and the radial direction $\boldsymbol{R}$. Second and third columns show the value of the parameter $p$ from a fit to equation (4) and using equation (5), respectively. The fourth column shows the goodness of this fit. The last column represents the result of the statistical test for the rejection of the null hypothesis in terms of $N_\sigma$ (see text for details).

| Axis | $\langle\cos\theta\rangle$ | $p_{\rm fit}$ | $p_{\rm estimated}$ | $\frac{\chi^2-N_{\rm d.o.f.}}{\sqrt{2N_{\rm d.o.f.}}}$ | $N_\sigma$ |
|---|---|---|---|---|---|
| | | Dark matter | | | |
| Major | 0.4739 | $1.110 \pm 0.004$ | $1.110 \pm 0.004$ | $+0.06$ | $-26.9$ |
| Minor | 0.5306 | $0.884 \pm 0.003$ | $0.885 \pm 0.003$ | $+0.63$ | $+31.6$ |
| Middle | 0.4945 | $1.023 \pm 0.004$ | $1.022 \pm 0.004$ | $-0.04$ | $-5.7$ |
| $\boldsymbol{L}$ | 0.4926 | $1.029 \pm 0.004$ | $1.030 \pm 0.004$ | $-0.69$ | $-7.6$ |
| | | Gas | | | |
| Major | 0.4639 | $1.154 \pm 0.012$ | $1.156 \pm 0.013$ | $-0.56$ | $-13.1$ |
| Minor | 0.5288 | $0.891 \pm 0.009$ | $0.891 \pm 0.010$ | $-0.36$ | $+10.4$ |
| Middle | 0.5042 | $0.980 \pm 0.010$ | $0.983 \pm 0.011$ | $-1.15$ | $+1.5$ |
| $\boldsymbol{L}$ | 0.4922 | $1.030 \pm 0.011$ | $1.032 \pm 0.011$ | $+3.20$ | $-2.8$ |

## 3 RESULTS

The main results are summarized in Fig. 1 and Table 1. We show in Fig. 1 the probability density distribution of the orientations of the three main axes and angular momentum of haloes in the shells of voids (using a spherical shell of $4\,h^{-1}$ Mpc around the surface of the void), with respect to the direction to the centre of the void. The angles are calculated using equation (2) and the analogous ones for the main axes correspondingly.

We also plot an analytical fit of the probability density distribution (Betancort-Rijo & Trujillo, in preparation) given by the following equation:

$$P(\mu)\,\mathrm{d}\mu \propto \frac{p\,\mathrm{d}\mu}{\left[1+(p^2-1)\mu^2\right]^{3/2}}; \quad \mu \equiv \cos\theta, \qquad (4)$$

where $p$ is a free parameter, related to the ratio between the dispersion in the radial component of the angular momentum vector, and its dispersion in the transverse component. Although this equation was proposed to describe how the orientation of angular momentum is distributed, it proves to be a very good fit for the distribution of the orientations of the halo main axes.

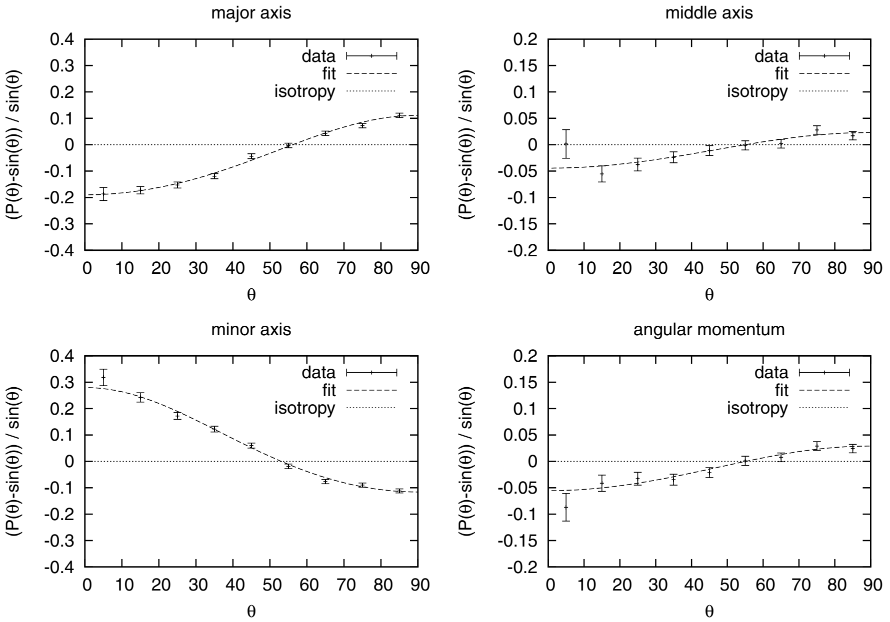

**Figure 1.** Probability density distribution (measured with respect to the case of isotropic orientations) for the angles between the angular momentum of dark matter haloes in the shells of voids, the three principal axes of these haloes, and the direction to the centre of the void. The error bar on each bin represents the Poissonian error. The dashed line shows a fit of the data using equation (4), and the dotted line represents the null hypothesis. Taking haloes in the shells of spheres with randomly distributed centres makes the results agree with isotropy.

The distribution of an isotropic distribution is computed and also shown in Fig. 1. If these vectors have no particular orientation (our null hypothesis), then the expected probability distribution is a sine function. We use this fact to represent the deviation of the probability distributions with respect to the isotropic case, so that the null hypothesis corresponds to the zero level in this plot.

In order to quantify the strength of these alignments, we use the parameter $p$ in equation (4), as previously done by Brunino et al. (2007). The null hypothesis corresponds to $p = 1$, so that $\mu$ is uniformly distributed. Lower and higher values of $p$ correspond to a preferential orientation parallel and perpendicular to the centre of the void, respectively. A good approximation for this parameter in the case $p \simeq 1$ comes from the relation

$$\langle \cos\theta \rangle = \frac{1}{1+p}, \tag{5}$$

where the average is taken over all the halo samples in the shells of voids.

The results presented in Table 1 are for the three main axes and angular momentum of haloes in the shell of $4\,h^{-1}$ Mpc around the surface of the void. The first column shows the result of averaging the cosine values of the angles considered here for our sample of haloes. The second column shows the result of the statistical test performed here, i.e. the average of the cosine test. In the case of isotropic orientations, the average of the cosine is normally distributed with mean 0.5 and variance $1/(12N)$, where $N$ is the number of haloes. Therefore, the bigger is the departure from the mean and the bigger the statistics, the higher the significance of rejecting the null hypothesis, $N_\sigma = \sqrt{12N}(\langle \cos\theta \rangle - 0.5)$. The third column represents the strength of the alignment using the aforementioned parametrization, estimated from a Levenberg–Marquardt fit to our data using equation (4). The fourth column also represents the value of $p$ but this time it is estimated using equation (5). The error bars in this parameter correspond to the 68 per cent confidence level. The last column shows that the value of the reduced $\chi^2$ is indeed near to unity, which proves the goodness of the fit. It is important to remark that the statistical test only quantifies the probability of isotropy in these orientations; the magnitude of the alignment is instead measured by the parameter $p$.

We find for this sample of haloes that the minor axis is preferentially aligned with the direction to the centre of the void, and the major axis is preferentially aligned perpendicular to it. Middle axis also shows an alignment orthogonal to the radial direction, but much weaker than previous one. This confirms the results reported by Patiri et al. (2006b) and Brunino et al. (2007). The same conclusion holds from the analysis of the gas particles embedded in dark matter haloes, although in this case middle axis does not show any significant alignment.

In order to characterize the complete statistical information about the spatial orientation of these haloes, we studied the distribution of the Euler angles. These angles link two orthogonal systems defined at location of each halo in the shell of a void: the one formed by the direction to the centre of the void and any two perpendicular directions that lie in the shell ($\boldsymbol{X}$, $\boldsymbol{Y}$, $\boldsymbol{R}$), and the one formed by the three main axes derived from the diagonalization of the inertia tensor of the halo ($\boldsymbol{a}$, $\boldsymbol{b}$, $\boldsymbol{c}$). The second coordinate system can be obtained from the first by means of a set of three rotations: a rotation of angle $\phi$ about $\boldsymbol{R}$, a rotation of angle $\omega$ about the rotated $\boldsymbol{X}$ axis (which places the $\boldsymbol{R}$ axis in the direction of $\boldsymbol{a}$), and finally a rotation of angle $\psi$ about this $\boldsymbol{a}$ axis, which places the other two in the direction of $\boldsymbol{b}$ and $\boldsymbol{c}$. It is important to remark that $\omega$ is actually the angle between the major axis and the direction to the centre of the void, so we already know its distribution. Moreover, due to the rotational symmetry about the direction $\boldsymbol{R}$ (there is no privileged point in the surface of a sphere), we also know that $\phi$ is uniformly distributed. Thus, for a complete description of the spatial orientation of our haloes we need to find out the distribution of the $\psi$ angle. Obviously if the shape of the haloes were not aligned with any particular direction, $\psi$ would be uniformly distributed. Nevertheless we find that the distribution of this angle is instead well described by (Betancort-Rijo & Trujillo, in preparation)

$$P(\psi)\,\mathrm{d}\psi = \frac{2}{\pi}[1 + \beta\cos(2\psi)]\,\mathrm{d}\psi, \tag{6}$$

where $\beta$ is a free parameter. A fit of our data gives $\beta = -0.093 \pm 0.005$. However, if we select a sample of those haloes whose major axis forms an angle with $\boldsymbol{R}$ above a given value $\omega_0$, this parameter seems to rise. This is an indication that in fact, the distribution of $\psi$ is not independent of this angle, and the complete description of the shape alignment will be given by a more general distribution $P(\omega, \psi)$.

But our most remarkable result is that we find a previously undetected alignment of angular momentum, whose orientation is preferentially perpendicular to the direction to the centre of the void (but not necessarily aligned with the major axis). This is confirmed by the average of the cosine and a Kolmogorov–Smirnov test. Although this alignment is small, both statistical tests agree in rejecting the null hypothesis with a probability corresponding to a significance level of more than $7\sigma$.

Previous studies have not found such an orientation of the angular momentum in the shells of voids, mainly because of the poor halo statistics due to the small simulation box. For instance, the halo sample in Patiri et al. (2006b) consisted of only 1729 objects with which they managed to find $p = 0.96 \pm 0.04$. Despite this value is compatible with our result, it points that angular momentum tends to be aligned with the direction to the centre of the void, which is the opposite of what we find. Box size may also have been the reason why Heymans et al. (2006) could not reject the null hypothesis (causing the error bars to be about a factor of 2 larger than those shown in our Fig. 1), although other factors may have had some influence on their conclusions, like the small number of particles in their haloes or their estimation of error bars via bootstrap method. The case of Brunino et al. (2007) is specially surprising, since having the same box size, the resolution of Millennium Simulation largely exceeds that of this paper. Yet, they still find that the distribution of the angular momentum is compatible with a random orientation. Taking a convenient subsample of haloes they found a significant alignment, but only in one out of the seven radial bins considered. This subsample is obtained selecting haloes with a disc-dominated galaxy at their centre, using semi-analytic galaxy catalogue of Croton et al. (2006). The galaxy must be brighter than $M_K < -23$ and have a bulge to total ratio $0 < B/T < 0.4$. On the contrary, it is noteworthy that no pre-selection was performed for the results presented here.

The likely explanation for this disagreement is that their haloes were identified with the same halo finder but with a linking length which corresponds to an overdensity 900 times the mean matter density, to focus on the core properties of the haloes. Here, we compute main axes and angular momentum of haloes detected with a linking length corresponding to 330 times the mean matter density (see Section 2). For comparison, we show in Table 2 the results of the same analysis as in Table 1 but using a catalogue of haloes in our simulation box defined by an overdensity eight times higher. Although the main axes show a stronger alignment in the inner parts of the halo, it is clear that the alignment of the angular momentum

**Table 2.** Same as Table 1, but the haloes are defined here as enclosing eight times the virial overdensity.

| Axis | $\langle\cos\theta\rangle$ | $p_{\rm fit}$ | $p_{\rm estimated}$ | $\frac{\chi^2-N_{\rm d.o.f.}}{\sqrt{2N_{\rm d.o.f.}}}$ | $N_\sigma$ |
|---|---|---|---|---|---|
| | | Dark matter | | | |
| Major | 0.4702 | $1.125 \pm 0.005$ | $1.127 \pm 0.005$ | $-0.23$ | $-25.2$ |
| Minor | 0.5362 | $0.869 \pm 0.004$ | $0.865 \pm 0.004$ | $+1.00$ | $+30.7$ |
| Middle | 0.4925 | $1.030 \pm 0.005$ | $1.030 \pm 0.005$ | $-1.42$ | $-6.3$ |
| $\boldsymbol{L}$ | 0.5003 | $1.000 \pm 0.005$ | $0.999 \pm 0.005$ | $-0.70$ | 0.2 |
| | | Gas | | | |
| Major | 0.4476 | $1.232 \pm 0.020$ | $1.234 \pm 0.021$ | $-0.65$ | $-12.3$ |
| Minor | 0.5549 | $0.793 \pm 0.013$ | $0.802 \pm 0.014$ | $+2.54$ | $+12.8$ |
| Middle | 0.4926 | $1.029 \pm 0.017$ | $1.030 \pm 0.018$ | $+0.95$ | $-1.7$ |
| $\boldsymbol{L}$ | 0.5015 | $0.988 \pm 0.016$ | $0.994 \pm 0.017$ | $-0.19$ | $+0.4$ |

with the direction to the centre of the void is lost when we focus in the inner parts. The contribution to the angular momentum from the particles in the outer shells of a halo is then fundamental for this conclusion. It is quite remarkable that the gas in the inner part does not show this alignment either, despite the fact that both major and minor axes show an enhanced alignment compared to dark matter haloes.

As a further test of our results we repeated the analysis to obtain the strength of the alignments, by taking haloes in the shells of *fake* voids (i.e. spheres with randomly distributed centres throughout the simulation box). The results for both shape and angular momentum alignment are then compatible with the null hypothesis. To test the effect of baryons in the alignments of dark matter haloes we have analysed the dark matter only version of the MareNostrum universe. The results we obtain for the strength of these alignments are compatible to those listed in the upper (dark matter) part of Tables 1 and 2.

We also studied the dependence of the strength of these alignments when moving outside the surface of the void. The results are shown in Table 3. In this table we show the value of the parameter $p$ estimated using equation (4) along with their error bars, in several different shells surrounding the void. The shells are selected for direct comparison with Brunino et al. (2007). It is clear from the table that the strength of the alignments dilutes as we move outside the surface of the void. The inner shell show a weaker alignment of the angular momentum compared to that work. Instead, this strength declines slower here as we advance to the outer shells. This is in contradiction with the statement in Brunino et al. (2007) suggesting that taking a wide shell can mask this alignment. Interestingly, we find that the alignment of the angular momentum is still significant even at few times $R_{\rm void}$.

The minimum void size $R_{\rm void} > 10\,h^{-1}$ Mpc was chosen in order to mimic the observational result of Trujillo et al. (2006), and it seems reasonable as it is of the order of the scale of non-linearity at present, and hence haloes around voids with this size are embedded into quasi-linear structures which remember the original shape. However, we are in an excellent position to study whether this value is good enough for our analysis. In Fig. 2 we show the dependence of the strength of the alignments on the choice of the void size, in the range of $5 < R_{\rm void} < 15\,h^{-1}$ Mpc. The width of the bins is chosen to be $\Delta\, R_{\rm void} = 2\,h^{-1}$ Mpc. All the haloes in a shell $0.4\, R_{\rm void}$ in width around the surface of the void are taken into account. We find that the alignment decreases considerably with the radius of the void, fading away for $R_{\rm void} < 5\,h^{-1}$ Mpc. On the other hand, large voids are rare and the poor statistics of objects around them increases the uncertainty on the parameter $p$. Therefore, a strong and significant alignment can be found using voids of intermediate size. It is worth noting that if we use the same procedure as above, i.e. all the voids larger than a given minimum size are included into the analysis, the highest signal-to-noise ratio is located around $\lesssim 6\,h^{-1}$ Mpc. As shown in Fig. 3, this ratio declines very steeply with the choice of minimum void size because the decrease in the statistics (and hence the increase in the uncertainty $\Delta\, p$) is much higher than the increase in the strength of the alignment. This result is of interest in observational studies, but it is important to remark that the position of this maximum could be shifted when using redshift space instead of real space.

Some studies have suggested that voids are not generally spherical, so that alignment detections assuming spherical voids should therefore be seen as residual of genuine physical alignments (e.g. Aragón-Calvo et al. 2007). However, using an ellipsoidal void catalogue for the MareNostrum universe we find similar results for the orientation of angular momentum and main axes for the haloes in the shells of those non-spherical voids (see Table 4). Moreover, we find no significant difference between the direction to the centre of the void and the direction perpendicular to the ellipsoid, taking $\boldsymbol{n} \equiv (\boldsymbol{R}\cdot\boldsymbol{a}/a^2,\ \boldsymbol{R}\cdot\boldsymbol{b}/b^2,\ \boldsymbol{R}\cdot\boldsymbol{c}/c^2)$ as the reference direction for angle measurements. Dark matter haloes selected here are located in a shell of $4\,h^{-1}$ Mpc thick around the maximal sphere enclosed into the ellipsoid. In order to study more in depth the relevance of void shape, we studied the probability distribution function of the Euler angle $\phi$. In the case of spherical voids, this angle is uniformly distributed due to the rotational symmetry in the plane tangential to the sphere at the position of the halo. On the other hand, this symmetry is broken in the case of ellipsoidal voids, so the distribution of the

**Table 3.** The strength of dark matter halo alignments measured from parameter $p$ at $1\sigma$ confidence level using different shells around the surface of the void. Recall that the null hypothesis (isotropic orientations) corresponds to $p = 1$. Lower and higher values of $p$ correspond to a preferential orientation parallel and perpendicular to the centre of the void, respectively.

| Shell $R_{\rm void}$ units | Major axis $p$ | Middle axis $p$ | Minor axis $p$ | Angular momentum $p$ | Number of haloes |
|---|---|---|---|---|---|
| $1.00 < R < 1.05$ | $1.138 \pm 0.010$ | $1.022 \pm 0.009$ | $0.865 \pm 0.007$ | $1.046 \pm 0.009$ | 16 406 |
| $1.05 < R < 1.10$ | $1.149 \pm 0.013$ | $1.008 \pm 0.011$ | $0.874 \pm 0.010$ | $1.024 \pm 0.012$ | 9437 |
| $1.10 < R < 1.20$ | $1.115 \pm 0.008$ | $1.019 \pm 0.007$ | $0.883 \pm 0.006$ | $1.021 \pm 0.007$ | 24 329 |
| $1.20 < R < 1.40$ | $1.085 \pm 0.005$ | $1.027 \pm 0.004$ | $0.901 \pm 0.004$ | $1.024 \pm 0.004$ | 66 576 |
| $1.40 < R < 1.80$ | $1.052 \pm 0.003$ | $1.006 \pm 0.003$ | $0.946 \pm 0.002$ | $1.013 \pm 0.003$ | 187 565 |
| $1.80 < R < 2.60$ | $1.025 \pm 0.002$ | $1.008 \pm 0.002$ | $0.969 \pm 0.002$ | $1.009 \pm 0.002$ | 460 592 |
| $2.60 < R < 3.20$ | $1.013 \pm 0.001$ | $1.001 \pm 0.001$ | $0.985 \pm 0.001$ | $1.006 \pm 0.001$ | 555 621 |

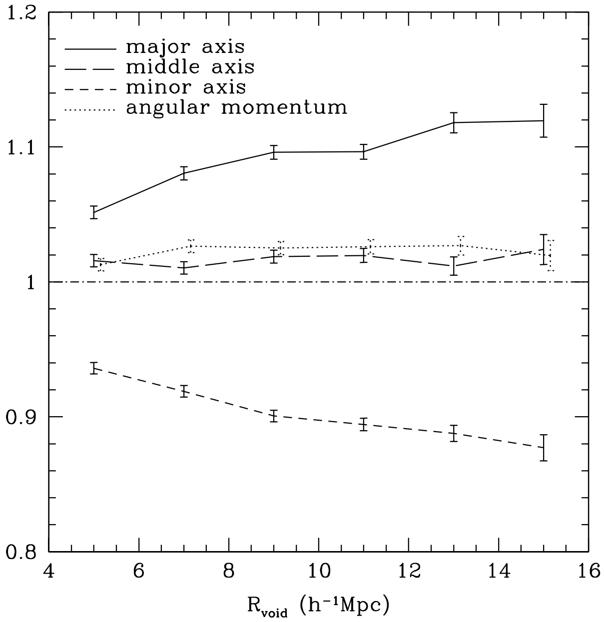

**Figure 2.** The strength of the alignment as a function of the void size, measured over bins of $2\,h^{-1}$ Mpc wide in void radius. The solid, long-dashed and short-dashed lines represent the major, middle and minor axes, respectively. Dotted line represents the angular momentum, which has been slightly shifted to the right-hand side for the sake of clarity. Error bars show the $1\sigma$ uncertainty in the value of the parameter $p$. The dash–dotted line represents the null hypothesis.

$\phi$ angle might be different. However, taking into account that

$$\sin\phi = \frac{\boldsymbol{v}\cdot\boldsymbol{i} - (\boldsymbol{v}\cdot\boldsymbol{R})(\boldsymbol{i}\cdot\boldsymbol{R})}{\sqrt{1-(\boldsymbol{v}\cdot\boldsymbol{R})^2}\sqrt{1-(\boldsymbol{i}\cdot\boldsymbol{R})^2}}, \tag{7}$$

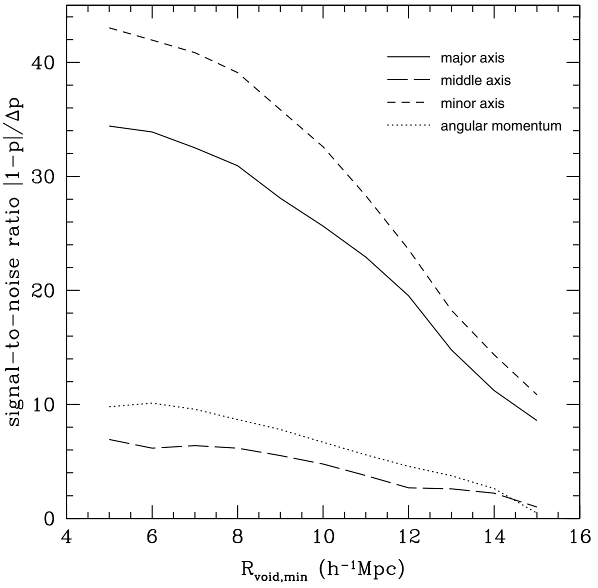

**Figure 3.** The signal-to-noise ratio in the alignments of haloes around voids as a function of the minimum void size. This ratio is estimated by the deviation of the parameter $p$ from the isotropic case $p = 1$, over the uncertainty in this parameter. As in Fig. 2, dotted line represents the angular momentum and the solid, long-dashed and short-dashed lines represent the major, middle and minor axes, respectively.

**Table 4.** Values for the $p$ parameter for the alignment of the three main axes and angular momentum vector with the direction to the centre of the void for haloes in a shell of $4\,h^{-1}$ Mpc using two different void catalogues in the same simulation. For the ellipsoidal void catalogue the results for both the *radial* and the *normal* direction are shown.

| axis | spherical void catalogue | ellipsoidal void catalogue | |
|---|---|---|---|
| | $p$ (using $\boldsymbol{R} \equiv \boldsymbol{n}$) | $p$ (using $\boldsymbol{R}$) | $p$ (using $\boldsymbol{n}$) |
| major | $1.110 \pm 0.004$ | $1.112 \pm 0.004$ | $1.112 \pm 0.004$ |
| minor | $0.884 \pm 0.003$ | $0.886 \pm 0.004$ | $0.887 \pm 0.003$ |
| middle | $1.023 \pm 0.004$ | $1.021 \pm 0.004$ | $1.021 \pm 0.004$ |
| $\boldsymbol{L}$ | $1.029 \pm 0.004$ | $1.028 \pm 0.004$ | $1.029 \pm 0.004$ |

where $\boldsymbol{i}$ is defined in the direction of the major axis of the void and $\boldsymbol{v}$ in the direction of the major axis of the halo, we find $\langle\phi\rangle/(\pi/2) = 0.5001 \pm 0.0009$ in agreement with a uniform distribution.

There also have been recent claims of dependence on the alignment of the angular momentum with the mass of the halo in filaments and walls of the large-scale structure (Aragón-Calvo et al. 2007; Hahn et al. 2007a). In agreement with these papers we find a slight trend of increasing alignment strength with halo mass for our sample. Using a shell of $4\,h^{-1}$ Mpc the haloes near the resolution limit imposed, with $M = 5 \times 10^{11}$–$8 \times 10^{11}\,h^{-1}\,\mathrm{M}_{\odot}$, have a strength value of $p \simeq 1.015$. On the other hand, haloes with masses in the upper limit of the sample $M = 8 \times 10^{12}$–$2 \times 10^{13}\,h^{-1}\,\mathrm{M}_{\odot}$ show evidence of a stronger alignment with $p \simeq 1.060$.

## 4 DISCUSSION AND CONCLUSION

In this paper we have analysed the orientation of main axes and angular momentum of dark matter haloes in the shells of large voids using the MareNostrum universe simulation. The spins of these haloes are preferentially perpendicular to the direction to the centre of the void. The possibility of isotropic orientations has been rejected at $7\sigma$ confidence level. This result is in qualitative agreement with and is likely to be related to the observational result of Trujillo et al. (2006) for spiral galaxies using large galaxy surveys. The alignment of dark matter collapsed structures with the large-scale structure finds a natural explanation in the context of the TTT. The different components of the angular momentum vector present a dispersion which is not isotropic: there is a marked asymmetry between the dispersion in the direction of maximum compression as compared to that in the direction of maximum expansion (Betancort-Rijo & Trujillo, in preparation). Therefore, very low density regions such as large voids are suitable to study this effect as they are surrounded by a region with a large tidal field, causing the anisotropy in the shear tensor we are measuring in this work. It is worth noting that this effect is not due to accretion of matter along filaments. Large voids are surrounded by a complex filamentary network of matter (Colberg, Krughoff & Connolly 2005) which could represent a preferential direction of infall (but see Vitvitska et al. 2002). This accretion generates angular momentum pointing perpendicular to the filament in which the haloes are embedded, which could be either the direction to the centre of the void but could also be perpendicular to it, resulting in no preferential orientation of angular momentum. Therefore, the anisotropic dispersion in the angular momentum vector seems more plausible in order to explain of this effect.

This is the first time that this alignment has been found in cosmological simulations using haloes in the shells of voids with no pre-selection of the haloes, in contrast to previous results. The poor halo statistics in the simulation box, the small number of particles in haloes, and even an overestimation of the error bars are likely to be the causes of the non-detection of this effect in Patiri et al. (2006b) and Heymans et al. (2006). Brunino et al. (2007) did not succeed in finding this alignment either, and concluded that the distribution of angular momentum vectors is compatible with isotropy for their total dark matter halo sample. This is somewhat surprising since they used the Millennium Simulation which exceeds the resolution of the MareNostrum universe simulation used here, having both the same box size. However, we have checked that the uncertainties in the orientation of the vectors used here are small enough to ensure the veracity of these results. We recall that the haloes used here are chosen to be well resolved and their directions are determined to within an angle of 13°. Indeed, it can be proven that this small indetermination in the angle measurement makes the uncertainty in the parameter $p$ be negligible. It is very likely that the linking length (and hence the overdensity) used to identify the haloes in the simulation box makes the results to differ as we have shown in Section 3. The choice of an overdensity 900 times the mean matter density (as opposed to our selection of overdensity 330) allowed them to focus only in the inner parts of the halo, but this may have prevented them from the detection of the alignment of angular momentum we find. This suggests that the particles in the outer shells of the halo are determining in the measurement of the strength of this alignment.

None the less, the claim of Brunino et al. (2007) that they found a significant alignment at the surface of the void, is based only in the choice of a subsample based on a semi-analytic galaxy catalogue. As we have mentioned above, they do not find any preferential orientation in their total sample. Moreover, we find that this alignment is significant even at few times $R_{\rm void}$. The signal decreases with distance to the void centre, which is expected for several reasons: the dispersion in the different components of the angular momentum vector becomes isotropic with increasing distance to the centre of the void. This is due to the less anisotropic tidal field in regions with higher density. Besides, the local density increases at larger distance from the centre of the void, and hence the interaction with neighbouring haloes is stronger, diluting the alignment from the initial torquing.

The choice of the minimum size of the void $R_{\rm void} > 10\,h^{-1}$ Mpc has proven to be reasonable because it is a good compromise between strength of the alignment and statistics. However, we have found that the choice $R_{\rm void} > 6\,h^{-1}$ Mpc is even better for the detection of alignment of dark matter haloes. When including smaller voids, which are more abundant, the statistics of haloes in the sample is highly improved. On the other hand, the alignment of these haloes is much weaker compared to the strength of the haloes around the largest voids: haloes around smaller voids are separated by shorter distances, and thus they are more influenced by interactions. Thus, the best choice is non-trivial and requires from the large amount of data given by cosmological simulations. Prospective observational studies should find this scale useful to get high signal-to-noise ratios in the detection of these alignments.

Our main result that galaxy-size dark matter haloes around voids have spins that lie in the shells of voids is in agreement with that of Aragón-Calvo et al. (2007) if haloes in the shells of void which form large-scale sheets are mainly responsible for this effect. However, Hahn et al. (2007b) found a stronger alignment of haloes in sheets than largely exceed the one presented here. Nevertheless, haloes around voids are located in a less dense environment than actual sheet haloes, which may have influence on their orientation.

Shape alignment of haloes in the surface of large voids is further confirmed, as shown previously by Patiri et al. (2006b). Minor axis is found to be preferentially aligned with the direction to the centre of the void and major axis tends to be aligned with the orthogonal direction. These results are also robust with respect to the shape of the void. Using an ellipsoidal void catalogue and measuring angles with respect to the radial and the normal direction we do not find any difference compared to the results obtained using spherical voids for the orientation of the main axes and angular momentum. Hence, we do not find that the shape of the void is meaningful for this purpose. We also analysed the strength of these alignments in several shells around the surface of the void. Comparing our results with those in Brunino et al. (2007) we find a systematically weaker alignment in the shape orientation of dark matter haloes.

Regarding gas particles, we find that the angular momentum of baryons is oriented with respect to the radial direction with a strength similar to dark matter, even considering the inner parts of the halo. However, in the core of the halo shape alignment for gas particles is enhanced with respect to dark matter. Although this is a remarkable result for its observational implications, the effect of cooling and full-scale star formation in these orientations remains to be investigated.

In addition, we found a slight trend of the alignment of angular momentum with the halo mass, as in Aragón-Calvo et al. (2007). More massive haloes happen to be more aligned with the orthogonal direction. A possible explanation to this fact could be their recent formation, as pointed out by Aragón-Calvo et al. (2007), which makes less massive haloes be more affected by non-linear interactions. It has also been suggested that an alternative explanation is that this effect might be due to the preferred accretion along the filaments (Shaw et al. 2006).

Evolution of this alignment in cosmological simulations has been studied by Hahn et al. (2007b). Unfortunately, it is very difficult to draw a conclusion about the evolution of the alignments from the present data. A deeper analysis of the redshift evolution of the strength of this signal is mandatory to elucidate its origin.

## ACKNOWLEDGMENTS

We thank Barcelona Supercomputer Centre – Centro Nacional de Supercomputación for the computer time awarded to run the MareNostrum universe simulations. The analysis of this simulation has been performed in NIC Jülich. AJC enjoyed the hospitality of the Astrophysical Institute Potsdam where part of this work was carried out. AJC, JEB-R, SGP and FP thank the Spanish MEC under grant PNAYA 2005-07789 for their support. SG acknowledges the support of the European Science Foundation through the ASTROSIM Exchange Visits Programme. GY acknowledges financial support to the Spanish PNFPA2006-01105 and PNAYA2006-15492-C03. AJC appreciates the financial support of the MEC through Spanish grant FPU AP2005-1826. This work was also partially supported by the Acciones Integradas Hispano-Alemanas.

## REFERENCES

Aragón-Calvo M. A., van de Weygaert R., Jones B. J. T., van der Hulst J. M., 2007, ApJ, 655, L5
Avila-Reese V., Firmani C., Hernández X., 1998, ApJ, 505, 37
Bailin J., Steinmetz M., 2005, ApJ, 627, 647
Brunino R., Trujillo I., Pearce F. R., Thomas P. A., 2007, MNRAS, 375, 184
Colberg J. M., Krughoff K. S., Connolly A. J., 2005, MNRAS, 359, 272
Croton D. J. et al., 2006, MNRAS, 365, 11
D'Onghia E., Navarro J. F., 2007, MNRAS, 380, L58
Doroshkevich A. G., 1970, Astrofizika, 6, 581
Fall S. M., Efstathiou G., 1980, MNRAS, 193, 189
Gottlöber S., Yepes G., 2007, ApJ, 664, 117

Hahn O., Porciani C., Carollo C. M., Dekel A., 2007a, MNRAS, 375, 489
Hahn O., Carollo C. M., Porciani C., Dekel A., 2007b, MNRAS, 381, 41
Heymans C., White M., Heavens A., Vale C., van Waerbeke L., 2006, MNRAS, 371, 750
Lee J., Erdogdu P., 2007, ApJ, 671, 1248
Mo H. J., Mao S., White S. D. M., 1998, MNRAS, 295, 319
Navarro J. F., Abadi M. G., Steinmetz M., 2004, ApJ, 613, L41
Patiri S. G., Betancort-Rijo J. E., Prada F., Klypin A., Gottlöber S., 2006a, MNRAS, 369, 335
Patiri S. G., Cuesta A. J., Prada F., Betancort-Rijo J., Klypin A., 2006b, ApJ, 652, L75
Peebles P. J. E., 1969, ApJ, 155, 393
Peirani S., Mohayaee R., de Freitas Pacheco J. A., 2004, MNRAS, 348, 921
Porciani C., Dekel A., Hoffman Y., 2002, MNRAS, 332, 325
Primack J. R., 2004, in Ryder S. D., Pisano D. J., Walker M. A., Freeman K. C., eds, Proc. IAU Symp. 220, Dark Matter in Galaxies. Astron. Soc. Pac., San Francisco, p. 467
Shaw L. D., Weller J., Ostriker J. P., Bode P., 2006, ApJ, 646, 815
Springel V., 2005, MNRAS, 364, 1105
Trujillo I., Carretero C., Patiri S. G., 2006, ApJ, 640, L111
Vitvitska M., Klypin A. A., Kravtsov A. V., Wechsler R. H., Primack J. R., Bullock J. S., 2002, ApJ, 581, 799
White S. D. M., 1984, ApJ, 286, 38

This paper has been typeset from a TEX/LATEX file prepared by the author.